

Interface phenomena in  
 $\text{La}_{1/3}\text{Sr}_{2/3}\text{FeO}_3$  /  $\text{La}_{2/3}\text{Sr}_{1/3}\text{MnO}_3$   
heterostructures  
and  
a quest for p-electron magnetism

Von der Fakultät für Mathematik, Informatik und Naturwissenschaften der RWTH  
Aachen University zur Erlangung des akademischen Grades eines Doktors der  
Naturwissenschaften genehmigte Dissertation

vorgelegt von

Diplom-Physiker

Markus Waschk

aus Witten

Berichter: Univ.-Prof. Dr. rer. nat. Thomas Brückel  
Univ.-Prof. Dr. rer. nat. Larissa Juschkina

Tag der mündlichen Prüfung: 03. November 2017

Diese Dissertation ist auf den Internetseiten der Universitätsbibliothek online verfügbar.



## Zusammenfassung

Übergangsmetalloxide sind aufgrund ihres korrelierten Elektronensystems vielversprechende Kandidaten für neuartige Speicherkonzepte und Sensoren. Bauteile aus solchen Materialien können aus Heterostrukturen bestehen, bei denen die Grenzfläche interessante Eigenschaften aufweist, die im Volumenmaterial nicht gefunden werden können. Beispiele für solche Effekte sind zum einen magnetische Grenzflächen zwischen zwei nicht magnetischen und zum anderen elektrisch leitende Grenzflächen zwischen zwei isolierenden Materialien. Dabei zeigen sie eine hohe Empfindlichkeit auf externe Erregungen, wie zum Beispiel magnetische Felder. Diese Arbeit konzentriert sich auf eine systematische Studie des Systems  $\text{La}_{1/3}\text{Sr}_{2/3}\text{FeO}_3$  (LSFO) und  $\text{La}_{2/3}\text{Sr}_{1/3}\text{MnO}_3$  (LSMO). Dabei weist LSFO eine Vielzahl von spannenden Eigenschaften auf. Neben einem Verwey Übergang, der von einer Widerstandsänderung von acht Größenordnungen begleitet ist, können Ladungsordnung und Antiferromagnetismus beobachtet werden. LSMO hingegen ist ein ferromagnetisches Material, dessen Magnetismus durch epitaktische Verspannungen oder elektronischer Dotierung innerhalb der Grenzfläche stark beeinflusst werden kann. Die Proben in dieser Arbeit wurden mittels einer Kombination aus zwei etablierten Wachstumsmethoden, Molekularstrahlepitaxie und Hochdruckspütern, hergestellt. Anschließend wurden die Proben hinsichtlich ihrer Oberflächenbeschaffenheit, Kristallstruktur und magnetischen Eigenschaften charakterisiert. Es konnte gezeigt werden, dass die Kombination zweier Herstellungsverfahren keinen Einfluss auf die Qualität der Proben hat. Alle untersuchten Proben sind stöchiometrisch und weisen eine gute Kristallinität und geringe Oberflächenrauigkeiten auf. An der Grenzfläche LSMO/LSFO tritt starke Interdiffusion von Eisen in mindestens neun Monolagen des LSMO auf, während das System LSFO/LSMO kein solches Verhalten zeigt und die Interdiffusion auf maximal zwei Atomlagen beschränkt bleibt. Die Unterschiede beider Proben pflanzen sich auch auf die magnetischen Eigenschaften fort. Bei LSMO/LSFO kann eine Erhöhung der Curie Temperatur, sowie eine Reduzierung der Magnetisierung in der Grenzfläche, beobachtet werden. LSMO/LSFO allerdings zeigt ein sehr interessantes Verhalten. Während eine  $M(H)$  Messung bei 10 K einen Exchange Bias Effekt und eine starke Einkühlfeldabhängigkeit der Hysteresenform zeigt, kann bei 110 K eine invertierte Hysterese gemessen werden. Der Magnetismus ist in diesem System homogen über die gesamte magnetische Schicht verteilt.

Ein weiterer Teil der Arbeit widmet sich einer neuen Klasse von magnetischen Materialien, bei denen der Magnetismus von p-Elektronen verursacht wird. Ein solches System ist z.B. dotiertes  $\text{BaTiO}_3$  und wurde von Gruber et al. [1] theoretisch vorausgesagt.  $\text{BaTiO}_3$  ist ein ferroelektrisches Material, das durch das Einfügen von Magnetismus über Dotieratome multiferroische Eigenschaften aufweisen könnte. Dies würde neue Wege für neuartige Speicher schaffen, die deutlich leistungsfähiger bei gleichzeitig reduzierten Energieverbrauch sind. Ein weiteres System aus dieser Klasse wurde von Oja et al. [2] eingeführt. Es basiert auf einer Heterostruktur zweier Materialien die kein magnetisches Übergangsmetallion (3d,4f) besitzen, aber dennoch eine ferromagnetische Grenzfläche aufweisen (z. B.  $\text{KTaO}_3/\text{SrTiO}_3$ ). Da die Realisierung solcher Systeme sehr schwierig ist, werden nur erste Ergebnisse der Probenherstellung beider Systeme gezeigt.



# Abstract

Transition metal oxides (TMO's) show functionalities which make them promising candidates for sensors and storage devices in future information technologies, because of electronic correlations and complex ordering phenomena. Such devices will consist of heterostructures of different TMO's, where interfaces can add additional functionalities, which cannot be found in the individual constituents. The subtle balance between electronic, spin, and lattice degrees of freedom leads to a variety of quantum phenomena in TMO's and results in an extreme sensitivity to external stimuli such as pressure and magnetic fields. The use of thin films increases the plethora of phenomena due to the reduced dimensionality, and epitaxial strain. At the interface completely new phenomena like magnetic interlayers between two non-magnetic layers or metallic behavior between two insulating materials may emerge, which cannot be found in the bulk materials.

The main part of this thesis is an investigation of the system  $\text{La}_{1/3}\text{Sr}_{2/3}\text{FeO}_3$  (LSFO) and  $\text{La}_{2/3}\text{Sr}_{1/3}\text{MnO}_3$  (LSMO). LSFO contains a Verwey transition with a resistivity increase of eight orders of magnitude from 300 K to 10 K, coinciding with an antiferromagnetic and a charge ordering transition. The samples were prepared with two powerful oxide growth methods, the high oxygen pressure sputtering, which was used for the LSMO growth, and a state of the art oxide molecular beam epitaxy system for the LSFO growth. The optimized growth of the individual layers and the heterostructures will be presented in detail. Furthermore, a detailed investigation with regard to structural, magnetic, and electronic properties will be shown.

Single layers as well as heterostructures grow epitaxially on a  $\text{SrTiO}_3$  substrate, in spite of a transfer procedure from one preparation chamber to another under atmosphere, which was necessary for the growth of heterostructures. The stoichiometric samples exhibit a good crystallinity and low surface roughness. However, the interface morphology in the heterostructures depends crucially on the growth order. Significant iron interdiffusion from the pre-deposited LSFO into the LSMO layer to at least nine unit cells is observable for the system LSMO/LSFO, whereas the LSFO deposited on LSMO exhibits a sharp interface with interdiffusion restricted to two unit cells at most.

The differences of the magnetic properties are also remarkable. The LSMO/LSFO sample shows an increased Curie temperature, a reduced interface magnetization, and a vanishing exchange bias effect, which is linked to the interdiffusion. In contrast, the system LSFO/LSMO has a homogeneous magnetization in the whole layer, but the macroscopic magnetization measurements reveal an additional magnetic impurity phase which persists at temperatures higher than 380 K, with a rather high coercive field.  $M(H)$  measurements feature an inverted hysteresis at 110 K and a strong field cooling dependency of the magnetization at 10 K, which includes a significant exchange bias effect.

The second investigated system belongs to a new class of magnetic materials, namely those where magnetism is caused by p-electrons as predicted by Gruber et al. [1] and Oja et al. [2]. These materials provide new routes to future storage devices as one can magnetically dope ferroelectric materials like  $\text{BaTiO}_3$  to achieve artificial multiferroic materials. The realization of such systems seems to be challenging and only initial results of a  $\text{BaTiO}_3$  bulk system and  $\text{KTaO}_3/\text{SrTiO}_3$  heterostructure can be presented.



# Contents

<b>1</b>	<b>Introduction</b>	<b>1</b>
<b>2</b>	<b>Basics</b>	<b>5</b>
2.1	Perovskite structure . . . . .	5
2.2	Crystal field . . . . .	8
2.3	Charge ordering . . . . .	9
2.4	Magnetic interactions . . . . .	10
2.4.1	Superexchange interaction . . . . .	10
2.4.2	Double-exchange interaction . . . . .	10
2.4.3	Exchange bias effect . . . . .	11
2.5	Magnetic anisotropy . . . . .	12
2.5.1	Magnetocrystalline anisotropy . . . . .	12
2.5.2	Shape anisotropy . . . . .	13
2.5.3	Surface anisotropy . . . . .	13
2.5.4	Strain anisotropy . . . . .	13
2.6	Small polaron conduction . . . . .	14
<b>3</b>	<b>Scattering theory</b>	<b>15</b>
3.1	Basics of scattering theory . . . . .	15
3.2	Pair correlation function . . . . .	19
3.3	Diffractionmetry . . . . .	20
3.4	Powder diffractionmetry analysis . . . . .	22
3.5	Reflectometry . . . . .	22
3.6	Parratt formalism . . . . .	25
3.7	Polarized neutron reflectometry . . . . .	25
3.8	Surface scattering . . . . .	27
<b>4</b>	<b>Sample preparation methods</b>	<b>31</b>
4.1	Thin film growth mechanism . . . . .	31
4.2	Oxide Molecular Beam Epitaxy System . . . . .	33
4.2.1	Requirements to the system . . . . .	33
4.2.2	Setup . . . . .	34
4.3	High Pressure Oxygen Sputtering Automat . . . . .	36
4.4	Comparison of MBE and sputtering . . . . .	37

<b>5</b>	<b>Sample characterization techniques</b>	<b>39</b>
5.1	In-situ analysis techniques . . . . .	39
5.1.1	Low-Energy Electron Diffraction . . . . .	39
5.1.2	Reflection High-Energy Electron Diffraction . . . . .	40
5.1.3	Auger Electron Spectroscopy . . . . .	42
5.2	In-house (ex-situ) instruments . . . . .	42
5.2.1	X-ray Reflectometer . . . . .	42
5.2.2	Powder X-ray Diffractometer . . . . .	43
5.2.3	Atomic Force Microscope . . . . .	44
5.2.4	Magnetic Property Measurement System . . . . .	44
5.2.5	Physical Property Measurement System . . . . .	46
5.2.6	Rutherford Backscattering Spectrometer . . . . .	47
5.2.7	Scanning Transmission Electron Microscopy and energy dispersive X-ray Spectroscopy . . . . .	48
5.3	Instruments at large-scale facilities . . . . .	49
5.3.1	High-Resolution X-Ray Powder Diffractometer (11-BM) . . . . .	49
5.3.2	Diffuse Neutron Scattering Spectrometer (DNS) . . . . .	50
5.3.3	High Resolution Powder Diffractometer (BT-1) . . . . .	53
5.3.4	Magnetic Reflectometer with high Incident Angle (MARIA) . . . . .	53
5.3.5	Polarized Beam Reflectometer (PBR) . . . . .	55
<b>6</b>	<b>Ordering phenomena in <math>\text{La}_{1/3}\text{Sr}_{2/3}\text{FeO}_3</math> powder and thin films</b>	<b>57</b>
6.1	$\text{La}_{1/3}\text{Sr}_{2/3}\text{FeO}_3$ and its versatility . . . . .	57
6.2	Powder study . . . . .	61
6.2.1	Sample preparation . . . . .	62
6.2.2	Results . . . . .	65
6.2.3	Conclusion . . . . .	82
6.3	Thin film study . . . . .	83
6.3.1	Determination of growth parameters . . . . .	83
6.3.2	Substrate preparation . . . . .	86
6.3.3	Effect of post-annealing and stoichiometric layer growth . . . . .	86
6.3.4	Magnetization of a single layer . . . . .	92
6.3.5	Resistivity of a single layer . . . . .	95
6.3.6	Conclusion . . . . .	99
<b>7</b>	<b>Magnetism in <math>\text{La}_{2/3}\text{Sr}_{1/3}\text{MnO}_3</math> thin films</b>	<b>101</b>
7.1	Magnetism in $\text{La}_{2/3}\text{Sr}_{1/3}\text{MnO}_3$ . . . . .	101
7.2	Sample preparation and structural analysis . . . . .	102
7.3	Magnetization influenced by strain . . . . .	105
7.4	Conclusion . . . . .	107
<b>8</b>	<b>Interface effects in <math>\text{La}_{1/3}\text{Sr}_{2/3}\text{FeO}_3/\text{La}_{2/3}\text{Sr}_{1/3}\text{MnO}_3</math> heterostructures</b>	<b>109</b>
8.1	Sample preparation and structural analysis . . . . .	109
8.2	Macroscopic magnetization . . . . .	116
8.3	Layer magnetization . . . . .	124



---

8.3.1	Depth-resolved magnetization . . . . .	124
8.3.2	Magnetization reversal mechanism of sample LSMOfinal . . . . .	129
8.4	Conclusion . . . . .	132
8.5	Outlook . . . . .	134
<b>9</b>	<b>A quest for p-electron magnetism</b>	<b>135</b>
9.1	The ideas behind p-electron magnetism . . . . .	135
9.1.1	(Ba/Sr)TiO <sub>3</sub> . . . . .	135
9.1.2	KTaO <sub>3</sub> /SrTiO <sub>3</sub> heterostructures . . . . .	137
9.2	Experimental work . . . . .	138
9.2.1	BaTiO <sub>3</sub> . . . . .	139
9.2.2	KTaO <sub>3</sub> . . . . .	144
9.3	Discussion . . . . .	150
<b>10</b>	<b>General outlook</b>	<b>153</b>
	<b>Acknowledgments</b>	<b>155</b>
	<b>Bibliography</b>	<b>157</b>
<b>A</b>	<b>Acronyms</b>	<b>169</b>
<b>B</b>	<b>Physical quantities</b>	<b>171</b>
<b>C</b>	<b>Physical constants</b>	<b>173</b>
<b>D</b>	<b>Supplementary information</b>	<b>175</b>
D.1	Definition of fitting parameters . . . . .	175
D.2	LSFO powder sample . . . . .	176
D.3	LSMOfinal . . . . .	179
D.4	LSFOfinal . . . . .	183
	<b>List of Figures</b>	<b>192</b>
	<b>List of Tables</b>	<b>204</b>



# 1 Introduction

Nowadays the requirements on devices in information technology are rapidly increasing, which makes it necessary to find new routes to create highly efficient devices. Transition metal oxides are promising candidates to fulfill these requirements [3]. The physical properties of such materials are determined by their highly correlated electron system, which leads to a multiplicity of fascinating phenomena like superconductivity [4], colossal magnetoresistance (CMR) effect [5], or multiferroic behavior [6, 7], to name just a few interesting examples, which show the high potential of this material class.

The ground state of these materials is determined by a delicate equilibrium of different degrees of freedom like spin order, charge order, or crystal lattice distortions, respectively. This enables one to tune or change the physical properties by external influences. These influences can, e.g. be lattice strain, magnetic or electric fields.

Besides the bulk materials, heterostructures of transition metal oxides expand the possibilities of designing new artificial material systems. Heterostructures are thin film systems of different materials which grow epitaxially on each other. Sample preparation with state-of-the-art growth techniques such as oxide molecular beam epitaxy or high oxygen pressure sputtering enables the growth of thin film systems with atomically sharp interfaces in between two different layers. These interfaces can show completely new properties which cannot be found in the parent bulk materials or single layers. One example is the combination of the two dielectric perovskite oxides  $\text{LaAlO}_3$  and  $\text{SrTiO}_3$  leading to superconductivity which is confined to a thin sheet at the interface [8]. An induced magnetism at the interface of these two non-magnetic materials [9] could also be found. Some further examples are the combination of the two antiferromagnetic materials  $\text{LaMnO}_3$  and  $\text{SrMnO}_3$ , which show a strong ferromagnetic interface magnetization [10]. Besides these interesting phenomena coupling via the interface of two materials can be achieved through influencing lattice strain, magnetic, or electronic degrees of freedom. One example are multiferroic materials, which are rare in nature, because normally ferromagnetic and ferroelectric behavior is contradicting. The reason is that ferroelectric behavior requires empty electron d-shells, whereas for ferromagnetism these electrons are essential [11]. The combination of a ferromagnetic and ferroelectric material as a heterostructure provides a new approach to artificial multiferroic materials. Achieving a coupling between these layers via lattice strain, for instance, enables a new kind of a highly efficient storage material [12], which uses electric fields to write the magnetically stored data.

The interface coupling of two different systems is the central point in this work. A crucial part of this thesis is dedicated to the growth of high quality heterostructures, which is in general not trivial, especially for transition metal oxides. The rather complex

structure, which is often a (distorted) perovskite structure, makes high demands on the growth processes like high growth temperatures, and slow growth rates, which supports interdiffusion between two layers and affects the interface properties significantly.

The first system is the heterostructure  $\text{La}_{1/3}\text{Sr}_{2/3}\text{FeO}_3/\text{La}_{2/3}\text{Sr}_{1/3}\text{MnO}_3$ , which has been chosen as an ideal model system to study the influence of charge carrier doping on the interfacial magnetization of a transition metal oxide, where ferromagnetism and conductivity are present.  $\text{La}_{1/3}\text{Sr}_{2/3}\text{FeO}_3$  acts as a charge carrier reservoir for the ferromagnetic  $\text{La}_{2/3}\text{Sr}_{1/3}\text{MnO}_3$  layer. Charge carrier doping at the interface can be drastically changed by a significant change in resistivity of the  $\text{La}_{1/3}\text{Sr}_{2/3}\text{FeO}_3$  layer, which undergoes a Verwey-like transition at 200 K. Further properties of  $\text{La}_{1/3}\text{Sr}_{2/3}\text{FeO}_3$  are antiferromagnetism and charge ordering, which occurs at the same temperature. The chosen stoichiometry of  $\text{La}_{2/3}\text{Sr}_{1/3}\text{MnO}_3$  is deep in the ferromagnetic dome [13] and any changes of the interfacial magnetism with temperature must be caused by changes in the electronic structure of the  $\text{La}_{1/3}\text{Sr}_{2/3}\text{FeO}_3$  as we pass through the Verwey transition at 200 K. As  $\text{La}_{1/3}\text{Sr}_{2/3}\text{FeO}_3$  resistivity changes by eight orders of magnitude between 300 K and 10 K, a continuous tuning of the proximity effect is possible. A further point of interest is the magnetic coupling mechanism of the antiferromagnet  $\text{La}_{1/3}\text{Sr}_{2/3}\text{FeO}_3$  and the ferromagnetic  $\text{La}_{2/3}\text{Sr}_{1/3}\text{MnO}_3$ , which has been investigated with regard to an exchange bias effect and the mechanism of magnetization reversal. These heterostructures have been grown with a combination of Oxide Molecular Beam Epitaxy (OMBE) system and High Oxygen Pressure Sputtering Automat (HOPSA). Prior to the work on thin films a study of polycrystalline  $\text{La}_{1/3}\text{Sr}_{2/3}\text{FeO}_3$  has been inserted in order to investigate the atomic and magnetic structure of the bulk material. In a second part of the thesis, a novel approach to create functional magnetic materials for information technologies was attempted. In common magnetic materials, magnetism originates from unfilled transition metal d or f shells. An exciting recent idea is to try to achieve magnetism within the p-electron system. This opens potentially new routes towards multifunctional materials.

One system is a heterostructure build from  $\text{KTaO}_3$  and  $\text{SrTiO}_3$ , which does not contain a typical magnetic ion and the magnetism originates from polarized oxygen *p* orbitals within a charge imbalanced interface as reported by Oja et al. [2]. Exchanging  $\text{SrTiO}_3$  with  $\text{BaTiO}_3$ , which is a ferroelectric material, could lead to a multiferroic compound. In this thesis the focus lies on the growth of  $\text{KTaO}_3$ . A further study was done on  $\text{BaTiO}_3$  powder, where a theoretical work published by Gruber et al. [1] predicts a magnetic ground state due to doping with boron, carbon, or nitrogen, which is an effect of the spin polarization of the dopant's p orbitals. Next to the artificial heterostructure approach to achieve multiferroicity, this kind of material can be used as a magnetically doped ferroelectric material, where coupling of both degrees of freedom can be achieved through lattice strain effects.

### Outline of this thesis

This thesis starts with this introduction into the fascinating world of transition metal oxides followed by the basic theory which introduces the perovskite structure, the crystal field, and the magnetic interactions in the underlying system, for instance. As scattering is frequently used in this work, the scattering theory is introduced in detail in **Chapter 3**.

---

The basics of thin film growth and the used thin film preparation techniques are described in **Chapter 4** in detail, because lots of efforts were necessary to achieve high quality thin films. **Chapter 5** introduces the used characterization techniques and instruments. The following chapters are divided as follows:

**Chapter 6** gives an introduction into  $\text{La}_{1/3}\text{Sr}_{2/3}\text{FeO}_3$  and summarizes the work on this compound, which includes the polycrystalline powder preparation and analysis as well as single layer growth and characterization. Additionally, this chapter focuses on synchrotron X-ray and neutron powder diffractometry data, which helps to reveal the atomic and magnetic structure of the polycrystalline powder.

**Chapter 7** introduces the  $\text{La}_{2/3}\text{Sr}_{1/3}\text{MnO}_3$  single layer, which includes an overview about its versatile properties, sample preparation and the characterization of the grown layers.

**Chapter 8** contains the detailed discussion about the combination of  $\text{La}_{1/3}\text{Sr}_{2/3}\text{FeO}_3$  and  $\text{La}_{2/3}\text{Sr}_{1/3}\text{MnO}_3$  to a multifunctional bilayer system. A crucial part of this work is the magnetization and neutron data in order to understand the reversal mechanism of magnetization and the influence of the charge carrier density changes due to the resistivity changes of  $\text{La}_{1/3}\text{Sr}_{2/3}\text{FeO}_3$ . This also includes polarized neutron reflectometry measurements.

**Chapter 9** describes the work on  $\text{BaTiO}_3$  powder doping and single layer  $\text{KTaO}_3$ . Here, the main focus lies on the development of  $\text{KTaO}_3$  growth procedures.

Each chapter is concluded separately and also an detailed outlook is given there. However, a short outlook with respect of the complete thesis is given in **Chapter 10**.

**Appendix A, B, and C** provide a list of all used acronyms, physical quantities and constants. **Appendix D** contains supplementary information as refinement parameters, detailed growth procedures, and additional measurements.



## 2 Basics

This chapter introduces the perovskite structure and related properties. Furthermore it will focus on  $\text{SrTiO}_3$  (STO), which has been used as the substrate material for all thin films grown throughout this work.

An introduction into crystal field theory and magnetic interaction arising in the treated systems will also be given.

### 2.1 Perovskite structure

The original perovskite  $\text{CaTiO}_3$  was discovered by Gustav Rose in 1839 and is named after the Russian mineralogist Lew Alexejewitsch Perowski. Materials which show the same or similar structure are described as perovskite structure. All discussed materials in this thesis exhibit perovskite structures. The main characteristic for materials with perovskite structure are two types of atoms on different sites of a cubic lattice, the A-site and B-site. The B-site atom is surrounded by six nearest oxygen atoms which build an octahedron. This octahedron is the structural building block. The A-site and B-site ions must fit into the voids. The oxygen atoms are located at the centers of the cube faces,

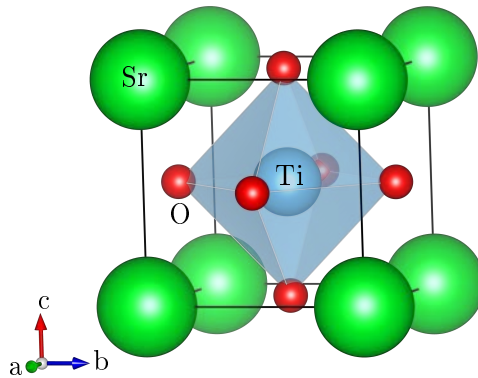


**Figure 2.1:** Cubic perovskite structure of STO. The A-site is occupied by Sr atoms, the B-site by Ti atoms. The blue marked octahedron specifies the oxygen environment, which is characteristic for the perovskite structure. The dedicated space group is  $\text{Pm}\bar{3}\text{m}$ . The figure was made with VESTA [14].

which are created by eight A-site atoms at the edges of a cubic unit cell. Figure 2.1 shows the room temperature cubic perovskite structure of the commonly used substrate STO.

In this case the transition metal titanium occupies the B-site and strontium occupies the A-Site as depicted.

Not all materials crystallize in a cubic configuration, even the eponym  $\text{CaTiO}_3$  (CTO) does not crystallize in a cubic structure. As the ionic radii play a key role for the crystal space group, the quite small Ca ions lead to an orthorhombic distortion [15]. The theory of the influence of the ion size on the structure was described by Goldschmidt in 1926 [16]. He defined the so-called tolerance factor  $\tau$ , which can be written for the chemical formula  $\text{ABX}_3$  as

$$\tau = \frac{r_A + r_X}{\sqrt{2}(r_B + r_X)},$$

with the ionic radii  $r_i$  for the different atoms in the compound. The calculated tolerance factor  $\tau$  for the example STO is 0.94. After comparing the calculated value with Table 2.1 one can expect a cubic perovskite structure, which was confirmed by several groups [17]. However, below 105K STO undergoes an antiferrodistortive phase transition [18, 19], which is shown in Fig. 2.2. It is characterized by a transition from a cubic to a tetragonal structure by rotation of the oxygen octahedron around a cubic axis with a rotation angle  $\phi$ . Adjacent oxygen octahedra rotate oppositely. This is a transition from space group

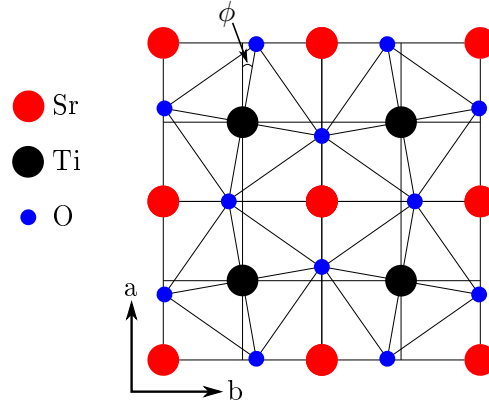


**Figure 2.2:** Antiferrodistortive transition at 105 K of STO. The oxygen octahedron rotates around the cubic  $c$ -axis with the rotation angle  $\phi$  which leads to a transition from cubic to tetragonal. The rotation of the octahedra in two adjacent cells is opposite. Adapted from [18].

$\text{Pm}\bar{3}\text{m}$  to  $\text{I4}/\text{mcm}$ , where the unit cells of the cubic and tetragonal phases are connected by  $a_{\text{tet}} \approx \sqrt{2}a_{\text{cub}}$  and  $c_{\text{tet}} \approx 2c_{\text{cub}}$  [20]. This means that the primitive unit cell is four times larger than in the cubic phase. In the course of this thesis the influence on magnetic layers grown on STO is discussed, especially in proximity to  $\text{La}_{2/3}\text{Sr}_{1/3}\text{MnO}_3$  (LSMO), which will be discussed in detail later on (Chapter 7).

The difference of the ionic radii in the compound  $\text{La}_{1/3}\text{Sr}_{2/3}\text{FeO}_3$  (LSFO) leads to a slightly distorted perovskite structure, namely a hexagonal unit cell with space group  $\text{R}\bar{3}\text{c}$ . It has six chemical formula units per unit cell and is shown on the left hand side of Fig. 2.3. One can also easily construct the rhombohedral (pseudo cubic) unit cell. This cell has small distortions compared to a perfect cubic structure which means a small deviation of about  $0.01^\circ$  from the right angle. LSMO also crystallizes in space group  $\text{R}\bar{3}\text{c}$ . The deviation



from the rectangular shape is  $0.26^\circ$ . In the pseudo cubic cell the space diagonal  $[111]$  is equivalent to the hexagonal  $c$ -axis.

**Table 2.1:** Values of tolerance factor for different perovskite coordinations.

tolerance factor $\tau$	type of structure
$> 1$	hexagonal
$0.9 - 1$	cubic
$0.7 - 0.9$	orthorhombic/rhombohedral

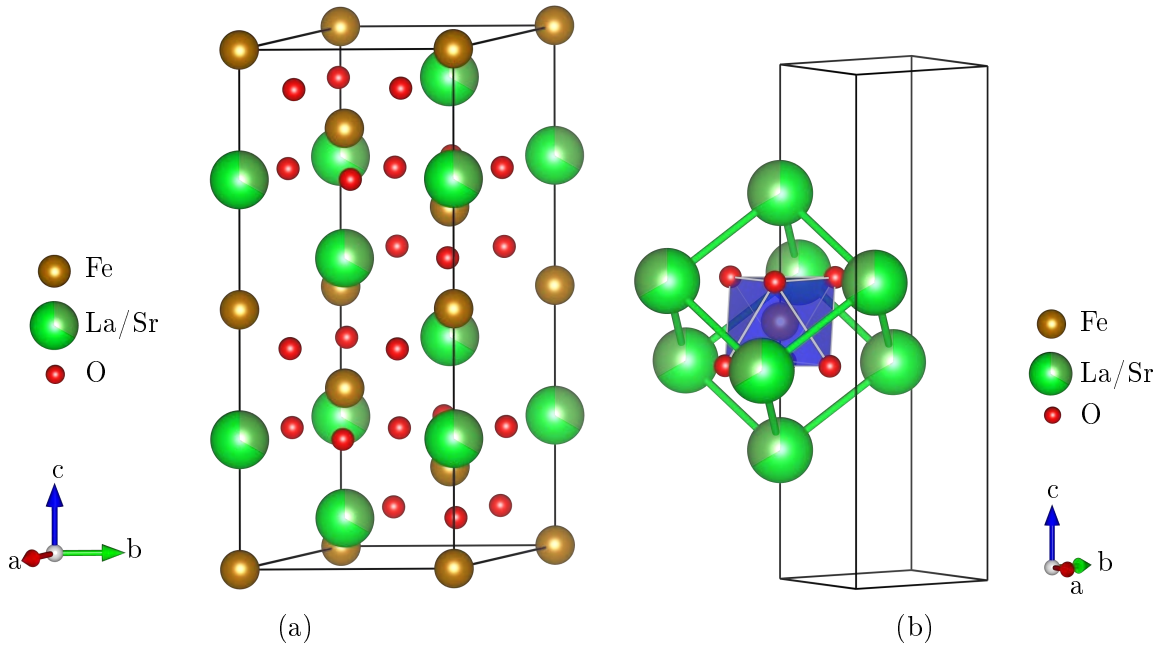


**Figure 2.3:** (a) Hexagonal unit cell of LSFO with space group  $R\bar{3}c$ , which contains six chemical formula units. The A-site is occupied statistically with 33 % Lanthanum and 67 % Strontium which is indicated by two different green tones. (b) Rhombohedral (pseudo cubic) unit cell, which is a slightly distorted cubic perovskite structure. The blue polyhedron indicates the octahedral oxygen environment. One can easily see that the  $[111]$  direction of the pseudo cubic structure is equivalent to the  $c$ -axis of the hexagonal unit cell. Both figures were created with VESTA [14].

The interface between two layers in a heterostructure usually exhibit strain. The strain is induced by different lattice constants which lead to either compressive or tensile strain. For the growth of LSFO and LSMO the substrate STO is a perfect candidate, because LSFO and LSMO have a lattice parameter difference of only 0.1%, so that the strain is kept at a minimum level. The lattice parameter of all materials are listed in Tab. 2.2. In spite of the fairly small strain in such an interface, the properties within the interface can be changed. For instance, the strain can distort the so-called crystal field, which can have an influence on the magnetic ordering. The next section introduces the crystal field briefly to mediate the key ideas of the crystal field theory.

**Table 2.2:** Room-temperature lattice parameter and their relative deviations of cubic STO [21] and pseudocubic LSMO [22] as well as pseudocubic LSFO [23].

	$a$ [Å]	$\Delta a/a_{\text{STO}}$ [%]
SrTiO <sub>3</sub>	3.901(1)	0
La <sub>2/3</sub> Sr <sub>1/3</sub> MnO <sub>3</sub>	3.8750(3)	0.67
La <sub>1/3</sub> Sr <sub>2/3</sub> FeO <sub>3</sub>	3.8718(3)	0.75

## 2.2 Crystal field

The crystal field theory plays a crucial role within the class of transition metal oxides and can explain many interesting physical properties of them. In this chapter the crystal field of a central transition metal ion surrounded by six oxygen ions in a octahedral arrangement as seen in the perovskite structure (section 2.1) is described.

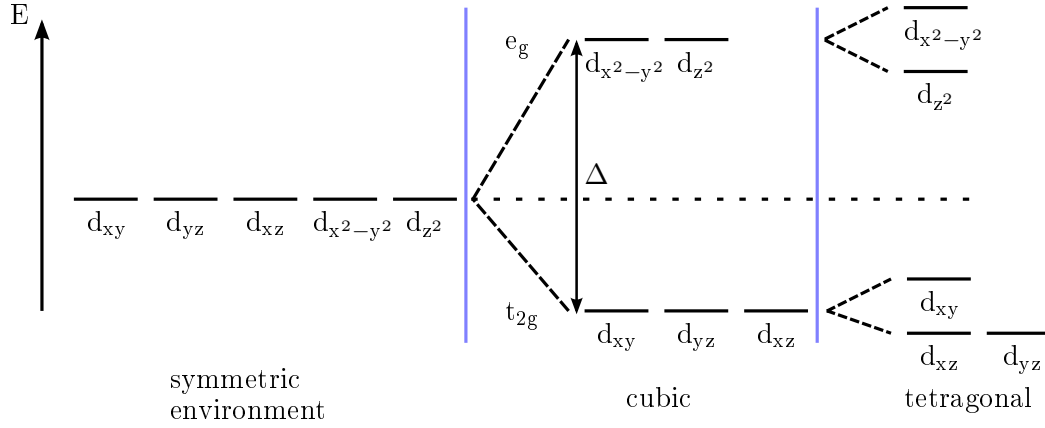
As discussed in [24], the crystal field theory relies on the assumptions that the oxygen ions (ligands) surrounding the transition metal atom are considered to be structureless (point-like), but the detailed electronic structure of the transition metal ion has to be taken into account. The Hamiltonian for the system can be written as

$$\mathcal{H} = \mathcal{H}_0 + V + W. \quad (2.1)$$

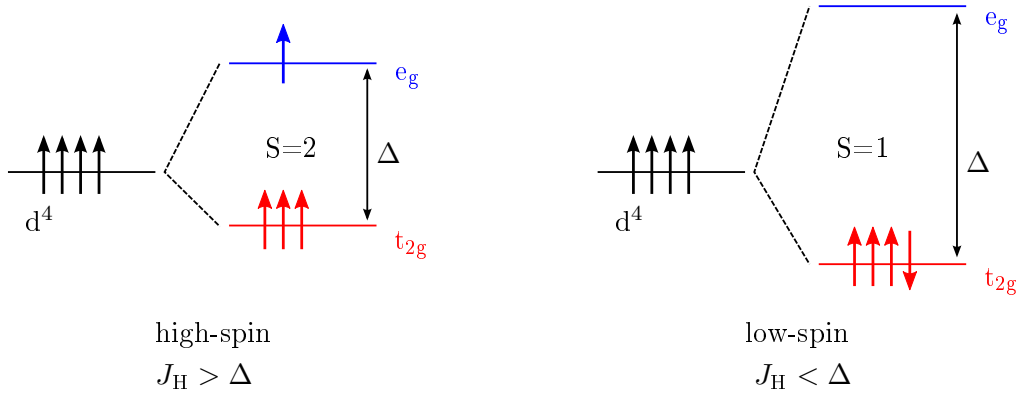
$\mathcal{H}_0$  describes the kinetic energy of the electrons of the transition metal atom and their interaction with its nucleus.  $V$  is the interaction potential of the point-like ligands with the electrons of the central atom, whereas  $W$  is the interaction between the ligands and the charged nucleus of the central atom.

Fig. 2.4 depicts the energy levels of the discussed central atom. In a symmetric ligand environment the energy ground state is fivefold degenerate and lifted in energy compared to a free ion. In contrast, a cubic environment of ligands as existing in an ideal perovskite structure shows an energy splitting, which is known as crystal field splitting  $\Delta$ , and it is geometry specific. The former fivefold degenerate energy level splits into a  $t_{2g}$  and a  $e_g$  level with threefold and twofold degeneracy, respectively. The  $d_{xy}$ ,  $d_{yz}$ , and the  $d_{xz}$  lie on the lower  $t_{2g}$  level, whereas the upper  $e_g$  level is twofold degenerate with the  $d_{x^2-y^2}$  and  $d_{z^2}$ . A change of the value of the crystal field splitting can lead to different spin states as shown in Fig. 2.5. Regarding the first Hund's rule the system prefers a parallel spin alignment. This appears if Hund's exchange energy  $J_H$  is larger than the crystal field splitting  $\Delta$  and from there a high-spin state follows. If  $\Delta$  exceeds  $J_H$  a parallel spin alignment is no more favorable and a low-spin state sets in. The crystal field thus significantly influences the magnetic moment of the transition metal atom. The transition metal oxides are known to exist in the high spin state.

The degeneracy of the cubic environment can be lifted by the Jahn-Teller effect [25]. It describes the reduction of symmetry while reducing the degeneracy of the system. The twofold  $e_g$  splits into two different orbitals, and the  $t_{2g}$  splits also into two different energy levels, but the lower one is still degenerate. A sketch of the splitting is shown on the right in Fig. 2.4. This splitting can also be caused by strain. Especially, the growth of a thin



**Figure 2.4:** Crystal field splitting of a transition metal ion with different oxygen environments. The crystal field splitting energy  $\Delta$  separates the  $e_g$  and  $t_{2g}$  energy level.



**Figure 2.5:** Two different spin configurations for the four electrons of  $\text{Fe}^{4+}$  in a cubic oxygen environment, which is depicted in Fig. 2.1, for instance.

film on a substrate, whose lattice parameters do not match perfectly, leads to strain, either compressive or tensile, within the interface in between. The strain at the interface can then influence the magnetic or orbital ordering. Tuning the crystal field by applying strain, for instance, helps one to develop new material systems that can exhibit magnetic properties, which cannot be found in their bulk state. Especially thin film systems provide the opportunity to design new systems. The advantages of combining materials as a thin film system will become clear during this thesis.

## 2.3 Charge ordering

Verwey was first to discover the effect of charge ordering, namely in magnetite  $\text{Fe}_3\text{O}_4$  [26], where he tried to explain the abrupt change in resistivity below a certain temperature. This temperature is named Verwey temperature  $T_V$ .

Besides magnetite the effect can be found in other materials with mixed valences. Above  $T_{CO}$  the charges are equally distributed over the whole crystal, but below  $T_{CO}$  the charges

start to localize and form a periodically ordered super-lattice, which can lead to symmetry lowering. Charge ordering sets in due to a strong interaction between electrons. The ordering is mostly driven by interatomic Coulomb interactions. One approach to describe the charge ordering can be done with the Hubbard model [27]. The ordering in magnetite [28] is a consequence of the ratio  $U/w$  of the Hubbard bandwidth  $w$ , which includes the kinetic energy of the electrons, and the interatomic Coulomb energy  $U$ . For large values, which means, that the electrons are fairly localized, the charge ordered state is stable. Besides electrostatic interaction the charge ordering can also be driven by magnetic exchange, as treated in Sec. 6.1 for LSFO, for instance.

## 2.4 Magnetic interactions

In transition metal oxides the 3d electrons are responsible for magnetic ordering. However, the 3d electrons are fairly localized due to the oxygen atoms in between of two magnetic transition metal atoms, thus, direct exchange cannot explain magnetic ordering in these systems [29]. The interaction between the magnetic atoms is mediated by the oxygen atoms, which leads either to superexchange or double-exchange. These two interactions dominate the magnetic ordering in LSFO and LSMO and will be introduced briefly in the next sections.

### 2.4.1 Superexchange interaction

Superexchange is a consequence of the overlap of the cation d-orbitals and the oxygen p-orbitals which lie in between of the cations. The  $\text{Fe}^{3+}$ , for instance, has half occupied d orbitals which overlap with the oxygen p-orbitals.

The superexchange can be described by a virtual hopping process from second-order perturbation theory in the Hubbard model [30,31], so called kinetic exchange. The virtual hopping process reduces the total energy of electrons. A real hopping process would lead to an increased Coulomb energy, which cannot be compensated by a gain in kinetic energy. Depending on the orbital occupations and the angles between the magnetic ions the interaction can be either ferromagnetic or antiferromagnetic. This is described with the Goodenough-Kanamori rules [32–34]:

1.  $180^\circ$  exchange between filled or empty cation orbitals leads to an antiferromagnetic coupling
2.  $180^\circ$  exchange between filled and empty cation orbitals leads to a ferromagnetic coupling
3.  $90^\circ$  change between filled cation orbitals leads to a ferromagnetic coupling

### 2.4.2 Double-exchange interaction

The double exchange interaction is a magnetic interaction between magnetic ions with different valences. Compared to the superexchange mechanism the double exchange is a

real hopping process of electrons within the  $e_g$  orbital of the metal cations. The involved cations, here manganese for instance, have to exist in different oxidation states, where the electrons can lower their kinetic energy due to delocalization. Fig. 2.6 depicts a hopping process between a  $\text{Mn}^{3+}$  and  $\text{Mn}^{4+}$  ion. Black indicates the original state, whereas red is the state after the hopping process took place. The real hopping of electrons is a consequence of the energetically degenerated states, and thus, the double exchange leads to a (half-) metallic behavior. According to [35] the real electron hopping process is accompanied by

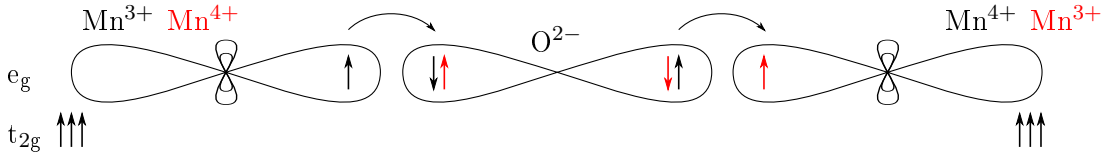


**Figure 2.6:** Illustration of the double-exchange mechanism between two manganese atoms with different valences. Black indicates the state before the electron hopping occurs, whereas red is the end state. As double exchange is a real hopping process the valence of the manganese atom changes.

ferromagnetic alignment of the metal atoms, which follows directly from Hund's rules. Both the superexchange and the double exchange determine the magnetic and electronic properties in  $\text{La}_{1-x}\text{Sr}_x\text{MnO}_3$ , which leads to a rich phase diagram with respect to structure, magnetic properties, and electronic properties, while changing the stoichiometry with  $x$ . A detailed overview about this system is adjoined to Chapter 7.

### 2.4.3 Exchange bias effect

In the course of this thesis a ferromagnetic thin film is combined with an antiferromagnetic one. This can lead to the exchange bias effect. According to [36] exchange bias is an effect which is related to the exchange anisotropy created at the interface of an antiferromagnetic and ferromagnetic material and is not restricted to thin film systems. First observations of an exchange anisotropy was done by Meiklejohn and Bean in 1956, when they were working on Co particles which were embedded in their native antiferromagnetic oxide. A review of the exchange anisotropy is given in [37]. Nevertheless thin film systems are favored for investigating exchange bias effects, because the interface between thin films can be controlled perfectly and engineered with respect to user requirements.

The exchange bias effect usually appears in systems where  $T_N < T_C$ , but this is not required in general.  $T_N$  is the Néel temperature of the antiferromagnet and  $T_C$  is the Curie temperature of the ferromagnet. A simple visualization of the effect is shown in Fig. 2.7. First the sample is cooled below  $T_C$  and then a magnetic field  $\mu_0 H$  is applied to magnetize the ferromagnet. Due to  $T > T_N$  the second layer remains paramagnetic. While field cooling the sample below  $T_N$  the magnetic moments in the second layer order antiferromagnetically (1). In the example, the interlayer coupling between the antiferromagnetic and ferromagnetic layers is assumed to be ferromagnetic depicted by the red arrows on Fig. 2.7. In first approximation, the antiferromagnetic order is not influenced by the external field. The interface coupling prevents the ferromagnet from switching in field direction<sup>3</sup> until the field overcomes this coupling and the layer can follow the applied

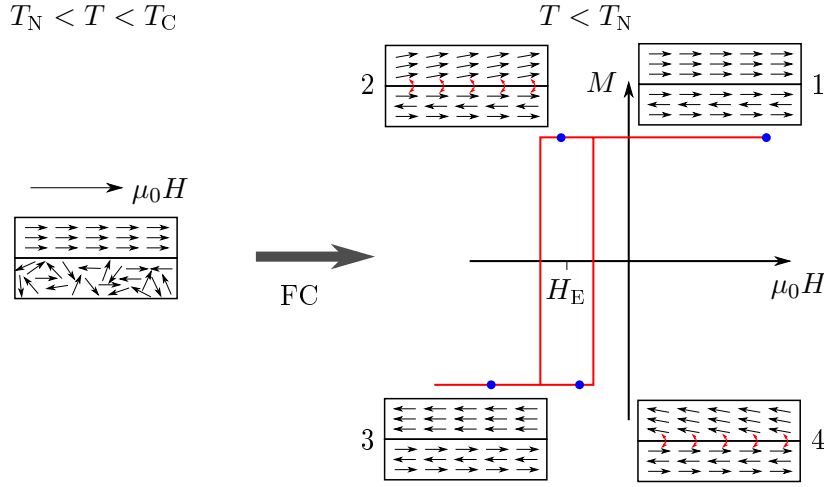


**Figure 2.7:** A simplified illustration of the exchange coupling between a ferromagnetic and an antiferromagnetic thin film. Adapted from [36].

field (2). Coming from the negative field (3) the ferromagnet switches earlier (4), because of the ferromagnetic coupling. As one can see in Fig. 2.7 the field-dependent hysteresis is shifted towards a negative field. This shift is called exchange bias field  $H_E$ .

Besides this simplified picture, lots of different parameters influence a real system, such as anisotropy, roughness, spin configuration or magnetic domains. A clear microscopic understanding of the exchange bias effect is not yet reached [36].

## 2.5 Magnetic anisotropy

Magnetic anisotropy describes the alignment of a ferromagnetic or an antiferromagnetic axis in a sample [38]. The energy which is necessary to align the magnetization into a direction that is not parallel to the ferromagnetic or antiferromagnetic axis is described by

$$E_a = K \sin^2 \theta,$$

with  $\theta$  the angle between  $M$ , the magnetization, and the anisotropy axis. In general anisotropy is temperature dependent and must tend to zero at  $T_C$  if a magnetic field is not applied.

For the description of the magnetic anisotropy of magnetic thin films, different contributions have to be considered. The main contributions for thin films are the magnetocrystalline, shape, surface, and strain anisotropy.

### 2.5.1 Magnetocrystalline anisotropy

The magnetocrystalline anisotropy is caused by spin-orbit interaction of the electrons. The alignment of electron orbitals is strictly coupled to the crystal structure, and thus the electron spin is also directly coupled to the crystal structure. Usually the spins prefer

the alignment along crystallographic axes, which leads to a magnetic anisotropy. Easy and hard magnetic axes develop in the crystal lattice [38]. Besides the magnetocrystalline anisotropy shape, surface, and strain influence the anisotropy of the thin film system. In addition, the latter named anisotropy tend to dominate and thus they mainly determine the magnetic anisotropies of thin films.

### 2.5.2 Shape anisotropy

The shape anisotropy is a contribution with is linked to the shape of the sample. The magnetization of the sample causes a stray field (or demagnetization field within the sample), which is described by the second Maxwell equation

$$\nabla \cdot \vec{B} = \mu_0 \nabla \cdot (\vec{H}_s + \vec{M}) = 0,$$

where  $H_s$  is the stray field. The stray field is dependent on the relation

$$H_{s,i} = -N_{ij} \cdot M_j; \quad i, j = x, y, z$$

in which  $N$  is called demagnetization factor and is strongly dependent on the shape of the sample. For thin films one gets  $(N_x, N_y, N_z) = (0, 0, 1)$  and one can follow that the stray field (or demagnetizing field) is minimized by a alignment of the spins perpendicular to the surface normal [38]. However, roughening of the thin film surface influences the stray field itself, which leads to a change of the magnetic anisotropy, which cannot be predicted easily.

### 2.5.3 Surface anisotropy

Surface anisotropy describes the magnetic anisotropy which originates from the anisotropic surrounding of surface atoms. It was first discussed by Néel in 1956. Mostly it comes from the surface monolayers which exhibit broken symmetry, but it extends to the first few monolayers due to structural relaxation [38]. The total anisotropy is described by

$$E_a = K_{\text{eff}} \sin^2 \theta.$$

$K_{\text{eff}}$  is expressed by

$$K_{\text{eff}} = K_v + K_s/d,$$

where  $d$  is the thin film thickness, and  $K_v$  and  $K_s$  the anisotropy constants corresponding to volume and surface, respectively. Thus, for thin films with low thickness,  $K_s$  can dominate the system and result in a spin alignment parallel to the surface normal.

### 2.5.4 Strain anisotropy

Another contribution to the anisotropy is strain. The anisotropy energy is expressed by

$$E_a = K_{\sigma_N} \sin^2 \theta = \frac{3}{2} \lambda_s \sigma_N \sin^2 \theta,$$

where  $\lambda_s$  is the saturation magnetostriction and  $\sigma_N$  describes the uniaxial stress which is dependent on the elastic modulus of the underlying material. As epitaxial strain can persist for many monolayers, it is possible that the strain anisotropy overcompensates the surface anisotropy and forces the magnetization to align differently.

The description of anisotropy in thin films is fairly complicated as one has to consider many different contributions, which can be influenced by the growth process of the thin films itself. Especially strain at surfaces or interfaces as well as roughness or crystalline imperfections can change the anisotropy and is often temperature dependent. The magnetic anisotropy in the system is a result of a complicated interplay of all anisotropic contributions. Thus, a precise prediction of anisotropy in thin films is complicated and cannot be done within this thesis, but plays a crucial role in understanding of the magnetization data as shown later on.

## 2.6 Small polaron conduction

In many transition metal oxides the interaction between electrons and optical phonons is strong [39]. This strong interaction leads to the formation of so-called polarons. A polaron is a quasiparticle consisting of a phonon and an electron and can be classified as large or small polaron considering the coupling of the phonon and electron. A large polaron is moving like an electron in a band, but due to the interaction with the lattice the effective mass of the quasiparticle is increased compared to the electron mass in a metallic conductor. In contrast, a small polaron is formed under a strong interaction, when an electron is trapped by an ion. This means that the electron is located at the ion site and this limits the size of the polaron, and thus, it is called small polaron. Such a polaron has usually a finite lifetime, which can range from ps to ms. Absorbing thermodynamic energy from its environment, the small polaron is able to hop from one ion to another. The mobility  $\mu$  of a small polaron can be described by

$$\mu = \mu_0 \exp(-W_H/k_B T). \quad (2.2)$$

$W_H$  is the activation energy, which is necessary to initiate hopping processes [39].  $T$  is the temperature, and  $k_B$  is the Boltzmann constant. Thus, the exponential function in eq. 2.2 is proportional to the probability per time for an electron jumping from one site to another.

According to Devlin et al. [40] the underlying conduction mechanism in LSFO is non-adiabatic, where the polaron binding energy can then be written as  $W_p = 2W_H$ . The non-adiabatic case exhibits a low tunneling probability of the electron through the crystal lattice during a lifetime period of the small polaron. For calculating the resistivity and specific conductivity eq. 2.2 has been used to get

$$\sigma_s = \frac{1}{\rho_r} = \sigma_{s0} T^{-3/2} \exp\left(-\frac{W_H}{k_B T}\right).$$

This equation has been used in order to confirm the conduction mechanism in both, the polycrystalline and thin film samples. More details are given in the dedicated sections later on.



## 3 Scattering theory

Scattering techniques are widely used to study materials in a non-destructive way. As probing particles X-ray photons, neutrons, and electrons have been used to investigate the nuclear and magnetic structure of the systems under investigation. This chapter introduces scattering in general and then focuses on the different methods like reflectometry or diffractometry. Finally some important characteristics of neutrons will be introduced. The scattering theory sections follow [41] and [42].

### 3.1 Basics of scattering theory

In 1924 Louis-Victor de Broglie postulated the matter wave. Besides photons, classic particles like neutrons and electrons exhibit a wave-particle dualism. The wavelength of the particle wave depends on the momentum of the particle and can be calculated by

$$\lambda = \frac{h}{p},$$

where  $\lambda$  is the wavelength of the particle,  $h$  Planck's constant, and  $p$  the absolute value of the particle momentum. Those particles can thus be used as scattering particles and the theory of waves can be used for it. Furthermore within this chapter we only consider the first Born approximation, where multiple scattering is neglected. In contrast, electrons exhibit strong interactions while penetrating matter and the first Born approximation cannot be used strictly for the case of electron scattering.

Fig. 3.1 shows a typical elastic scattering experiment within the Fraunhofer approximation. This far field approximation assumes that the sample is considerably smaller than the distance source-sample and sample-detector. In this approximation the incident and scattered waves can be considered as plane waves. The assumption is valid for all cases discussed in this thesis. In addition a monochromatic source is necessary, which only emits one selected wavelength.

The wave vector of the incident beam in Fig. 3.1 is described by  $\vec{k}$ , whereas  $\vec{k}'$  is the wave vector of the scattered beam. For elastic scattering, which we assume here,  $k$  is defined as

$$k = |\vec{k}| = |\vec{k}'| = k' = \frac{2\pi}{\lambda}.$$

$\lambda$  is again the wavelength of the incident and scattered beam. Now one can define the scattering vector  $\vec{Q}$  as

$$\vec{Q} = \vec{k}' - \vec{k}. \tag{3.1}$$

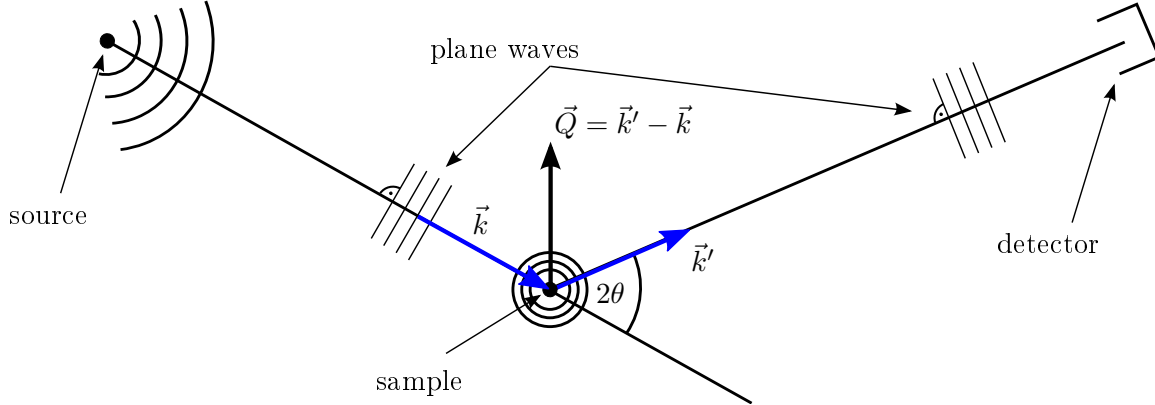


**Figure 3.1:** Scattering experiment within the Fraunhofer approximation. An incident plane wave is scattered towards a detector. Adapted from [41].

According to de Broglie, the momentum of a particle corresponding to the wave with the wave vector  $\vec{k}$  is given by  $\vec{p} = \hbar\vec{k}$ . The momentum transferred during the scattering is thus  $\hbar\vec{Q}$  with the scattering vector  $\vec{Q}$ . The absolute value of the scattering vector in dependence of the wavelength  $\lambda$  and the scattering angle  $2\theta$  can be represented with eq. 3.1 by

$$Q = |\vec{Q}| = |\vec{k}' - \vec{k}| = \sqrt{k^2 + k'^2 - 2kk' \cos 2\theta}.$$

With the addition theorem

$$\cos 2\theta = 1 - 2 \sin^2 \theta$$

one gets for  $Q$

$$Q = \frac{4\pi}{\lambda} \sin \theta. \quad (3.2)$$

In a scattering experiment the scattering cross-section is important. The scattered intensity is detected by a detector which covers the solid angle

$$d\Omega = \frac{dS}{r^2},$$

where  $dS$  is the active detector area and  $r$  the distance between the scattering event and the detector. The definition of the cross-section is shown in Fig. 3.2. The measured intensity by the detector is proportional to the cross-section, which is in principle the probability for an interaction between the incident particle and the sample matter. The differential cross-section

$$\frac{d\sigma}{d\Omega} = \frac{dn}{Jd\Omega} \quad (3.3)$$

is proportional to the probability that a particle is scattered into the solid angle  $\Omega$  after an interaction with the sample.  $dn$  is the number of detected particles and  $J$  is the incident

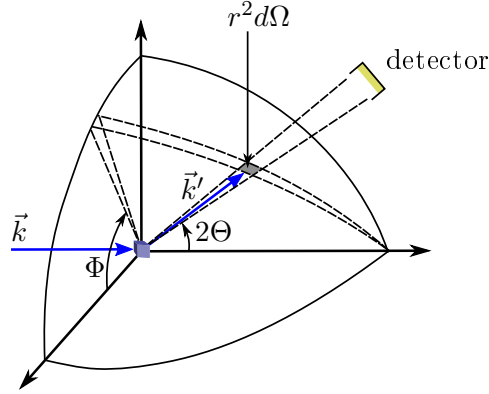


**Figure 3.2:** Definition of the scattering cross-section. The scattered intensity is proportional to the cross-section. Adapted from [41].

beam flux, which is used as a normalization for Eq. 3.3. The total cross-section can be calculated by integration to

$$\sigma = \int_0^{4\pi} \frac{d\sigma(\Theta, \Phi)}{d\Omega} d\Omega.$$

A microscopic calculation of the differential cross-section makes a quantum mechanical description necessary. For neutrons the interaction can be described by Schrödinger's equation

$$\mathcal{H} = \left( -\frac{\hbar}{2m_n} \Delta + V(\vec{r}) \right) \psi = i\hbar \frac{\partial}{\partial t} \psi, \quad (3.4)$$

where  $\psi$  is the probability density,  $V(\vec{r})$  the interaction potential, and  $m_n$  the rest mass of a neutron. The square of the absolute value of the probability density  $|\psi|^2$  of the scattered wave is proportional to the differential cross-section. The solutions of Schrödinger's equation are the possible states of the system. Within the elastic scattering regime it is possible to describe the time evolution of the system within the wave function by the factor  $e^{-i\frac{(E-V)t}{\hbar}}$ . With this Ansatz one can deduce a wave function for the spatial part of  $\psi$  from Eq. 3.4, which can be written as

$$(\Delta + k^2(\vec{r})) \psi = \frac{2m_n}{\hbar} V\psi, \quad (3.5)$$

where  $k^2(\vec{r})$  is expressed by

$$k^2(\vec{r}) = \frac{2m_n}{\hbar^2} (E - V(\vec{r})). \quad (3.6)$$

An analog approach for electromagnetic radiation is based on Maxwell's equations [43]. A solution for Eq. 3.5 for the case of  $V \equiv 0$  (propagation in vacuum), under consideration of the Fraunhofer approximation, is a plane wave. Thus  $\psi_0$  is the solution of the homogeneous wave function and can be written as

$$\psi_0 = \psi_A e^{i(\vec{k}\vec{r} - \frac{E}{\hbar}t)}. \quad (3.7)$$

The inhomogeneous solution ( $V \neq 0$ ) of Eq. 3.5 can be achieved by using the Green function to get the solution [41, 42]. This expansion of the wave function is called Born series. For the case of a weak interaction as expected for neutrons, for instance, only the first order term of the series has to be considered. For electrons which exhibit a stronger interaction with matter, higher orders of the series are necessary. Now we get

$$\psi(\vec{r}) \approx e^{i\vec{k}\vec{r}} - \frac{m_n}{2\pi\hbar^2} \frac{e^{ikr}}{r} \int V(\vec{r}') e^{-iQ\vec{r}'} d^3r'. \quad (3.8)$$

The principle applied in Eq. 3.8 is the well-known Huygens principle. It is easy to identify the scattering amplitude  $f(\vec{Q})$  as

$$f(\vec{Q}) = \frac{m_n}{2\pi\hbar^2} \int V(\vec{r}') e^{-\vec{Q}\vec{r}'} d^3r'. \quad (3.9)$$

It is a measure for the amplitude after the scattering process dependent on the scattering vector  $\vec{Q} = \vec{k}' - \vec{k}$ . Eq. 3.9 is the Fourier transform of the scattering potential. The square of the absolute value of the wave function is proportional to the differential cross-section,

$$\frac{d\sigma}{d\Omega} = |f(\vec{Q})|^2 = \frac{m^2}{4\pi^2\hbar^4} \left| \int V(\vec{r}') e^{-\vec{Q}\vec{r}'} d^3r' \right|^2.$$

It is not possible to do the back transformation due to the so called phase problem. As mentioned the intensity is the square of the absolute value of the scattered amplitude and in real scattering experiments only the intensity in the so-called reciprocal space can be measured. Thus the phase information is lost, which makes a back transformation to the real-space impossible. To solve this issue it is necessary to find suitable models to simulate the experiment. Then the model has to be changed iteratively under consideration of the measured data until matching between simulation and experiment has been found.

X-ray scattering predominantly takes place at the electrons of the sample. This means that the amplitude of the scattered wave is proportional to the Fourier transform of the electron density  $\rho_s$  of the sample. Thus one gets

$$f(\vec{Q}) = \int \rho_s e^{i\vec{Q}\vec{r}'} d^3r'. \quad (3.10)$$

After replacing  $\rho_s$  in Eq. 3.10 with its Fourier components [44] one can easily get

$$F(\vec{Q}) = \sum_{\vec{G}} \int n_{\vec{G}} e^{i(\vec{G}-\vec{Q})\vec{r}'} d^3r', \quad (3.11)$$

where  $\vec{G}$  is the reciprocal lattice vector, and  $n_{\vec{G}}$  the Fourier coefficients.  $F$  is the sum taken over the reciprocal lattice vectors. Eq. 3.11 is invariant under lattice translation. The introduction of the reciprocal lattice can be found in detail in [41, 44], for instance. However, a short introduction is given later on.

By setting  $\vec{Q} = \vec{G}$  in Eq. 3.11 it follows that the argument of the exponential function is zero, which maximizes the sum of the amplitude.  $\vec{Q} = \vec{G}$  is also known as the Laue

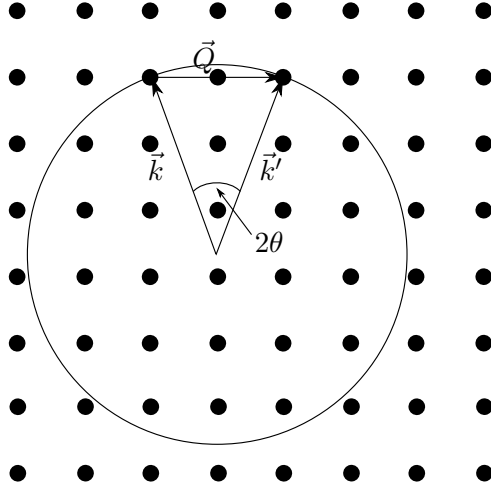


**Figure 3.3:** Ewald construction to visualize the Laue condition. The scattering condition is only fulfilled for lattice points which lie on the Ewald sphere (or Ewald circle in the 2D projection).

condition. Fig. 3.3 shows a visualization of the Laue condition. The radius of the Ewald sphere is  $k = |k| = |k'|$  (condition for elastic scattering). Only if two lattice points lie on the Ewald sphere a scattering reflection can be observed. Under the assumption of an ideal experiment and a perfectly periodic crystal lattice the lattice points are described by  $\delta$ -functions and the border of the Ewald sphere is infinitesimal. A real scattering experiment leads to a broadening of both the lattice points and the border of the Ewald sphere, which makes it easier to fulfill the scattering condition.

It is obvious that one can derive Bragg's equation,

$$2d_{\text{hkl}} \sin \theta = n\lambda,$$

with  $d_{\text{hkl}}$  the distance between lattice planes, and  $\lambda = \frac{2\pi}{k}$  the wavelength, from the Ewald construction. Thus, the equivalence between Laue condition and the well-known Bragg equation can be easily shown.

The next section treats the pair correlation function shortly, which makes clear which information one gets from an intensity distribution from a scattering experiment.

## 3.2 Pair correlation function

The sections above show the conditions for observing coherent scattering. Following [41] it is possible to show, which information is provided or accessible from the intensity distribution. As mentioned the relation between intensity and scattering amplitude is given by

$$I(\vec{Q}) \sim |f(\vec{Q})|^2.$$

Together with Eq. 3.10 and the variable substitution  $\vec{R} = \vec{r}' - \vec{r}$  we obtain

$$I(\vec{Q}) \sim \int P(\vec{R}) e^{i\vec{Q}\vec{R}} d^3R,$$

which means that the Fourier transform of the intensity is proportional to the Fourier transform of the function  $P(\vec{R})$ . This function is usually called pair correlation function, which can be written as

$$P(\vec{R}) = \int \rho_s^*(\vec{r})\rho_s(\vec{r} + \vec{R})d^3r.$$

A periodic arrangement of an atom pair leads to an extremum of the pair correlation function. Following the steps above one can interpret the pair correlation function as a function which reproduces all the vectors connecting one atom with another one, but only in a periodic arrangement.

Additionally one can say that a scattering experiment measures the pair correlation functions. Only the distance between atom pairs is relevant, but not the absolute position.

### 3.3 Diffractometry

Now it is natural to apply the basics shown above in order to determine the crystal metrics. Since the used X-ray and neutron beams have a wavelength in the range of  $10^{-10}$  m (This is called one Ångström (Å) = 0.1 nm, which will be used during the thesis.) corresponding to the typical distance between atoms, they are suitable to investigate crystal structures thoroughly. Here only a brief introduction into diffraction is given, for a detailed introduction the reader is referred to Ref. 41,42,44,45, for instance.

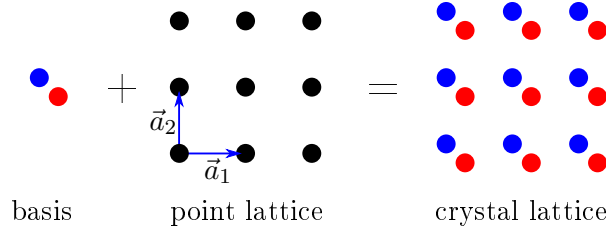


**Figure 3.4:** Construction of 2D projection of a crystal lattice. The crystal lattice is a convolution of a basis consisting of atoms and a mathematical point lattice.

Fig. 3.4 shows the construction of a crystal lattice. It is a convolution of a mathematical point lattice and a basis which includes the base atoms. The position of these atoms cannot be described with the mathematical point lattice, and thus, they are necessary to build the crystal lattice completely. The lattice itself is described by the lattice vectors  $\vec{a}_1$ ,  $\vec{a}_2$ , and  $\vec{a}_3$ . All lattice points can be addressed by using the linear combination  $\vec{a}$

$$\vec{a} = u\vec{a}_1 + v\vec{a}_2 + w\vec{a}_3,$$

where  $u, v, w \in \mathbb{Z}$ . On the other hand the basis is given by a vector  $\vec{r}_i$ , where  $i$  is an atom within the basis.  $\vec{r}_i$  is described by using the lattice vectors,

$$\vec{r}_i = r_{1,i}\vec{a}_1 + r_{2,i}\vec{a}_2 + r_{3,i}\vec{a}_3,$$

but  $0 < r_{j,i} < 1$ . Hence,  $r_{j,i}$  describes the position of the base atoms within one single unit cell.

In the case of an ideal crystal and an infinite mathematical lattice with the lattice vectors from above, a diffracted intensity can only be found for  $I(\vec{Q})$ .

$$\vec{G}_{hkl} = h\vec{g}_1 + k\vec{g}_2 + l\vec{g}_3$$

is the reciprocal lattice vector and  $h$ ,  $k$ , and  $l$  are the Miller indices. The relation between  $\vec{a}_i$  and  $\vec{g}_j$  can be written as

$$\vec{a}_i \cdot \vec{g}_j = 2\pi\delta_{ij},$$

with the Kronecker symbol  $\delta_{ij}$ . The reciprocal lattice is the Fourier transform of the crystal lattice. It is obvious that the  $\vec{G}$  introduced in Sec. 3.1 is the reciprocal lattice vector  $\vec{G}_{hkl}$ , with  $\vec{Q} = \vec{G}_{hkl}$  according to the Laue condition. After introducing the basics of crystal lattices, it is necessary to include the structure factor to describe the intensity of the scattered beam. The Born approximation introduced in section 3.1 is also used here. As mentioned the intensity is proportional to the squared absolute value of the structure factor

$$I(\vec{Q}) \approx |F(\vec{Q})|^2.$$

The structure factor is defined as

$$F(\vec{Q}) = \sum_i f_i(\vec{Q})e^{i\vec{Q}\vec{r}_i},$$

where  $f(\vec{Q})$  is the atomic form factor. A diffraction experiment normally measures only relative intensities [46]. Therefore it is necessary to introduce a scale factor  $I_0$ , where all constant parameters of the instrument are concluded. In addition non-constant corrections have to be considered, which are usually dependent on the scattering angle. For a nuclear diffraction from single crystals the intensity is given by

$$I(\vec{Q}) = I_0 \cdot L \cdot A \cdot E \cdot |F(\vec{Q})|^2. \quad (3.12)$$

$L$  is the instrument specific Lorentz factor.  $A$  describes the absorption of the sample, which is dependent on the geometry and the linear absorption coefficient of the sample. The remaining parameter  $E$  is the extinction coefficient, which describes the deviation from the assumed kinematic approximation (Born approximation).

One part of this thesis is about powder diffraction experiments, which have been used extensively to optimize the powder preparation method and to analyze the structure in detail. Therefore X-ray and neutron experiments were performed at a synchrotron X-ray source and at a neutron reactor. This will be discussed later on.

Powder is consisting of small crystallites with sizes of a few micrometer, which are usually randomly oriented. This means that all scattering vectors are observed at the same time, which leads to the so-called Debye-Scherrer rings. The reflections with the same magnitude of the scattering vector are not necessarily equivalent, they can origin from different scattering planes.

In a powder diffraction experiment one has to consider that one averages over all equivalent crystal directions. This leads to a dimensionality reduction of intensity information [46].

Thus, two additional corrections have to be introduced, namely  $M$  and  $P$ .  $M$  is the multiplicity which takes into account all equivalent crystal directions.  $P$  is the preferred orientation parameter, which is used for the correction of deviations from the assumed random orientation of the crystallites in the powder.

The following section shows how to treat the data gained from a powder diffractometry experiment. As already mentioned it is not possible to calculate the structure from the scattering intensity, because of the lost phase information. Thus, structure models are necessary to analyze the data.

### 3.4 Powder diffractometry analysis

The two methods for data analysis of X-ray and neutron data from powder experiments are the Le Bail and the Rietveld refinement [47, 48]. Both refinement techniques are implemented in Jana2006 [49], which has been used for data analysis.

The key difference between a Le Bail and a Rietveld refinement is how they consider the intensities. The Le Bail refinement uses intensities which are obtained from the previous fitting cycle. The starting values of the intensity are arbitrarily set to identical quantities. The Le Bail routine can be perfectly used, if one is interested in the lattice metrics and the instrument parameters. All the in-house powder diffractometry data is analyzed with the Le Bail refinement technique.

On the other hand the Rietveld refinement calculates the intensities from the structure factor. Due to its consideration the refinement with the Rietveld technique is more complex and more difficult compared to the Le Bail refinement, but it allows a structure solution.

Two different figures of merit are usually used to characterize the quality of the refinement [48]. The reliability factor  $R_p$ , which can be defined as

$$R_p = \frac{\sum_{i=1}^n |Y_i^{\text{exp}} - Y_i^{\text{calc}}|}{\sum_{i=1}^n Y_i^{\text{exp}}},$$

with the observed and calculated intensities,  $Y_i^{\text{exp}}$  and  $Y_i^{\text{calc}}$  summed over all measured points  $n$ . The second used figure of merit is weighted profile residual  $R_{\text{wp}}$  whose definition is

$$R_{\text{wp}} = \left[ \frac{\sum_{i=1}^n w_i (Y_i^{\text{exp}} - Y_i^{\text{calc}})^2}{\sum_{i=1}^n (Y_i^{\text{exp}})^2} \right]^{\frac{1}{2}},$$

with the weight  $w_i$  of the dedicated data point. All figures of merit are calculated automatically while using the data analysis software Jana2006 [49].

### 3.5 Reflectometry

Besides diffractometry, which provides information about the crystal structure, reflectometry is an important tool to get information about the stacking and roughness of thin film



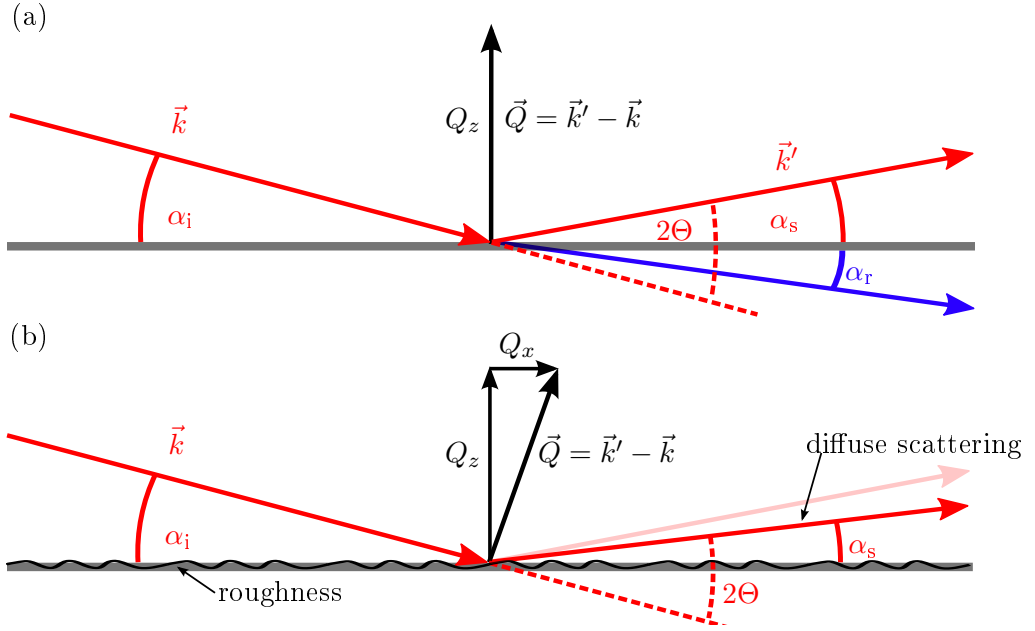


**Figure 3.5:** Scattering geometry of a typical reflectometry experiment. In the case of specular scattering (a), where  $\alpha_i$  and  $\alpha_s$  are equal,  $\vec{Q}$  is perpendicular to the sample's surface and thus only  $Q_z \neq 0$ . The blue arrow is the refracted beam with the angle  $\alpha_r$ . In case of  $\alpha_i \neq \alpha_s$  the off-specular scattering or diffuse scattering occurs and lateral structures can be probed (b). The scattering vector  $\vec{Q}$  has a non-vanishing lateral component.

systems. However, compared to diffractometry multiple scattering has to be considered and the first order Born Approximation is not longer valid [50]. The typical scattering geometry is given in Fig. 3.5. For specular scattering (a), which means  $\alpha_i = \alpha_s$ , only  $Q_z$  is nonzero. As the scattering vector is perpendicular to the sample surface, reflectometry probes the Scattering Length Density (SLD) in  $z$ -direction. According to Bragg's law one can easily see that small scattering angles (low values of  $Q_z$ ) lead to larger structures (nanometer range), if one uses the same wavelength as in the diffractometry case. For diffuse scattering (b), which is the off-specular case with  $\alpha_i \neq \alpha_s$ , also  $Q_x$  or  $Q_y$  have to be considered.

Specular reflectivity provides information about structures in out-of-plane direction such as thickness or roughness, while averaging laterally. Diffuse scattering contains information about the lateral structure of the interface or surface. Lateral structures with high correlation length lead to sharp reflections. For a more detailed view on the theory, Ref. 41 and 45 are recommended.

The incident beam is not only reflected at the surface but also refracted into the sample. In Fig. 3.5 the incident beam under  $\alpha_i$  is reflected with the angle  $\alpha_s$  and refracted into the sample with  $\alpha_r$ . If a further layer is existing, the refracted beam is also scattered at this interface, with a reflected and a refracted part of the beam. The reflected beams from each interface in the sample can interfere constructively or destructively, so that one observes minimums and maximums.

To calculate the reflectivity and transmittance of the incoming beam, the geometrical

optics can be used. As one knows from visible light, Snell's law

$$n_a \cos \alpha_i = n_l \cos \alpha_r \quad (3.13)$$

describes the behavior of a X-ray beam in matter, where  $n_a$  is the index of refraction in air and  $n_l$  is the index of the layer. The index of refraction  $n = 1 - \delta + i\beta$  has a real part, called dispersion, and an imaginary part, which describes absorption. Especially for X-rays close to absorption edges, the absorption becomes significantly high. For neutrons, the real part is given by

$$\delta = \frac{\lambda^2}{2\pi} \sum_j b_j \rho_j,$$

where  $b_j$  is the coherent scattering length and  $\rho_j$  the number density of the different elements. For X-rays  $\delta$  can be determined as

$$\delta = \frac{\lambda^2 r_0}{2\pi} \sum_j \rho_j (Z_j + f'_j),$$

$r_0$  is the classical electron radius,  $Z$  the number of electrons of the atom and  $f'$  is a correction for dispersion close to resonance energies.  $f'$  can be neglected far from absorption edges. As  $\delta$  is usually larger than 1, in the order of  $10^{-6}$ ,  $n_s$  becomes smaller than 1 for neutron and X-ray beams and the beam is refracted towards the interface. With Eq. 3.13 the angle of total refraction can be calculated [41]. One can easily see that total reflection appears below a critical angle  $\alpha_t \approx \sqrt{2\delta}$ .

According to classical optics, Fresnel's formulas describe the reflectivity and transmittance at a flat surface. One can derive the reflectivity as

$$R = \left| \frac{\theta - n_1 \theta_1}{\theta + n_1 \theta_1} \right|^2,$$

and the transmittance as

$$T = \left| \frac{2\theta}{\theta + n_1 \theta_1} \right|^2,$$

where  $\theta = \alpha_i = \alpha_s$ ,  $\theta_1 = \alpha_r$ , and  $n_1$  the index of refraction within the first layer. The resulting reflectivity  $R$  and transmittance  $T$  are shown in Fig. 3.6. For angles below  $\theta_t$  the incoming intensity is reflected completely. Only an evanescent wave with a propagation vector parallel to the surface exists and no propagating wave along the  $z$ -direction of the sample can be found. Angles higher than  $\theta_t$  lead to a partial penetration of the incoming wave. The reflectivity decreases with higher transmittance. The transmissivity reaches its maximum at  $\theta_t$ , because the incident and the reflected wave interfere constructively and build a standing wave. Due to the interference the amplitude is doubled, which leads to  $T = 4$ .

For a system with several interfaces one has to calculate  $R$  and  $T$  recursively for each interface, which is known as the Parratt formalism and introduced now.

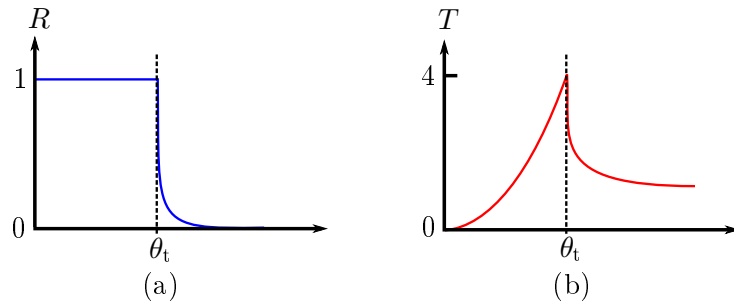


**Figure 3.6:** The reflectivity  $R$  (a) and the transmittance  $T$  (b) for the case of vanishing absorption. In both  $\theta_t$  is the key angle. For  $R$  below  $\theta_t$  total reflection takes place.  $T$  shows a different behavior. At  $\theta_t$  the incident and scattered wave interfere constructively, which means that the amplitudes can be added. From a doubled amplitude  $T = 4$  follows, because it is the square value of the amplitude. Adapted from [41].

### 3.6 Parratt formalism

For a system with  $n$  layers a recursive usage of the Fresnel equations is necessary. This algorithm was developed by L. G. Parratt in 1954 [51]. For this thesis, the fitting of the reflectivity data is done with the software GenX [52]. GenX uses the differential evolution algorithm for fitting X-ray and neutron data and has the Parratt recursion formalism implemented. It also allows the user to create sample models and to define parameter dependencies easily and completely free by supporting python scripts. This variety makes GenX an essential part of this work with regard to evaluation of the collected X-ray and neutron reflectivity data.

The used figure of merit (FOM), which describes the quality of the fit, compares the measurement and the fitted data on a logarithmic scale. It is defined as

$$FOM = \frac{1}{N-1} \cdot \sum_i^N |\log M_i - \log S_i|,$$

where  $M_i$  is the measured and  $S_i$  the simulated intensity related to each  $Q_i$  value, and  $N$  the number of data points. The errors of the fitted values are determined by varying the simulation until the FOM changes reach 5%. It leads to asymmetric errorbars, because this procedure is done for both directions ( $\pm$ ) separately.

In the systems used during this work, magnetic properties play a crucial role. To get access to the microscopic magnetization, Polarized Neutron Reflectometry (PNR) has been used in order to determine the microscopic magnetic properties of the samples.

### 3.7 Polarized neutron reflectometry

Due to the dipole-dipole-interaction of the neutron's magnetic moment with the magnetic induction inside the sample, it is necessary to add a magnetic part to the scattering

potential, so that one gets

$$V(\vec{r}) = \frac{2\pi\hbar^2}{m}b\rho_N - \gamma_n\mu_N\vec{B}\hat{\vec{\sigma}}. \quad (3.14)$$

As mentioned before in the nuclear part of the scattering potential  $b$  is the scattering length and  $\rho_N$  is nuclear number density. The subtrahend of Eq. 3.14 is the magnetic part of the scattering potential with the constants  $\gamma_n$ , the gyromagnetic factor for neutrons, and  $\mu_N$ , the nuclear magneton. Furthermore  $\hat{\vec{\sigma}} = \{\hat{\sigma}_x, \hat{\sigma}_y, \hat{\sigma}_z\}$  is the spin operator which consists of Pauli-matrices.  $\vec{B}$  denotes the magnetic induction field. With the magnetic part of the potential the differential magnetic cross section can be derived, as shown in Ref. 53, and written as

$$\frac{d\sigma}{d\Omega} = (\gamma_n r_0)^2 \left| \frac{1}{2\mu_B} \langle \hat{\sigma}'_y | \hat{\vec{\sigma}} \vec{M}_\perp(\vec{Q}) | \hat{\sigma}_y \rangle \right|^2.$$

Only  $\hat{\sigma}_y$ , the spin state before, and  $\hat{\sigma}'_y$ , the spin state after the scattering plays a role here, which means that the spin direction of the neutrons is the  $y$ -direction to be consistent with the definition  $x, y, z$  in this thesis. Here, the quantization axis is defined by the applied magnetic field. In addition only the magnetization perpendicular to the scattering vector contributes to the differential magnetic cross-section. The magnetization of the sample in this direction can be accessed by PNR.

The neutron spin is aligned either parallel (up,  $\uparrow$ ) or antiparallel (down,  $\downarrow$ ) to the  $y$ -direction, so it can be expressed with the neutron wave function as spinor

$$\psi(\vec{r}) \rightarrow \begin{pmatrix} \psi_\uparrow(\vec{r}) \\ \psi_\downarrow(\vec{r}) \end{pmatrix}.$$

After inserting Eq. 3.14 into Schrödinger's equation one obtains a coupled system of differential equations, which can be written as

$$\psi_\uparrow''(\vec{r}) + \left[ k^2 - 4\pi b\rho_N + \frac{2m\gamma_n\mu_n}{\hbar^2}B_\parallel \right] \psi_\uparrow(\vec{r}) + \frac{2m\gamma_n\mu_n}{\hbar^2}B_\perp\psi_\downarrow(\vec{r}) = 0 \quad (3.15)$$

$$\psi_\downarrow''(\vec{r}) + \left[ k^2 - 4\pi b\rho_N - \frac{2m\gamma_n\mu_n}{\hbar^2}B_\parallel \right] \psi_\downarrow(\vec{r}) + \frac{2m\gamma_n\mu_n}{\hbar^2}B_\perp\psi_\uparrow(\vec{r}) = 0. \quad (3.16)$$

$B_\parallel$  is the sample's magnetic field along the neutron guide field, whereas  $B_\perp$  is perpendicular to it, but both are perpendicular to the scattering vector  $\vec{Q}$ . Fig. 3.7 depicts the scattering geometry for an PNR experiment measured at a magnetic single domain sample. As mentioned above the  $y$ -direction is parallel to the applied magnetic field  $\vec{H}$ . If the sample's magnetic field is parallel to  $y$ , only  $B_\parallel$  contributes and the system of differential equations is decoupled. This leads to scattering intensity only in the non-spin-flip channels, the spin of the neutron is conserved. These reflectivity channels are called  $R_{++}$  and  $R_{--}$ .  $R_{++}$  is a result of the sum of the nuclear and the magnetic SLD, whereas  $R_{--}$  is the difference of both contributions.

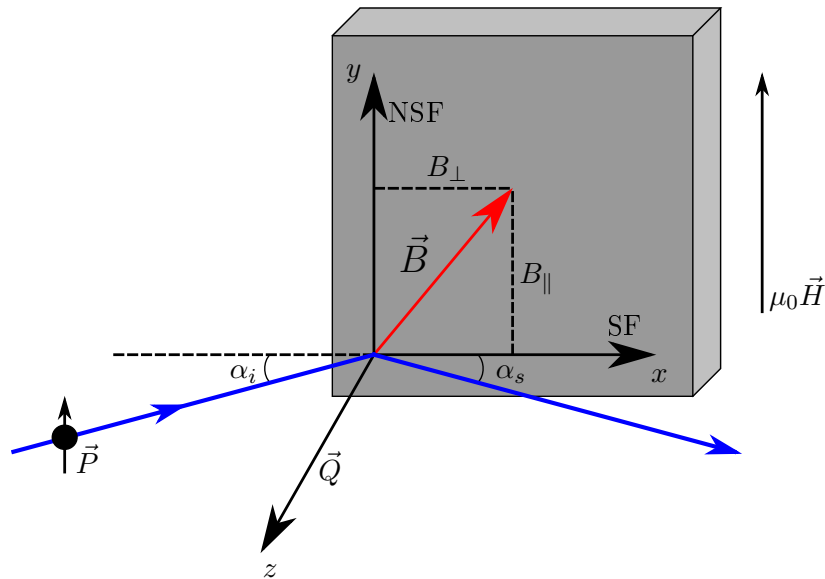


**Figure 3.7:** Sketch of the scattering geometry for PNR. The incident neutrons have a polarization  $\vec{P}$  parallel to the  $y$ -direction. Dependent on the magnetic field within the sample  $\vec{B}$  non-spin-flip (NSF) and spin-flip (SF) processes can be observed. The sample is assumed to be single domain. Adapted from [54].

If  $B_{\perp} > 0$  equations 3.15 and 3.16 are not decoupled, and spin-flip events occur. This corresponds to a rotation of the sample's magnetic field in the  $x$ - $y$ -plane. Those channels,  $R_{+-}$  and  $R_{-+}$ , only contain magnetic information. PNR is consequently the method of choice in order to investigate the magnetic structure of thin film samples. This method has been heavily used to get access to the magnetization depth profile perpendicular to the surface (out-of-plane) and also to study the mechanism of the in-plane reversal of the magnetization.

For samples with multiple magnetic domains the picture shown above is not easily applicable anymore and magnetic diffuse scattering has to be also taken into account. It can be used in order to investigate the domain structure of the sample [55].

## 3.8 Surface scattering

Surface sensitive techniques are important to investigate the surface crystallinity and quality. To achieve surface sensitivity low energy electrons are perfectly suitable since they have mean free paths of only few atomic layers in solid materials [56]. Additionally the wavelength of the electrons must fit to the crystalline dimensions, which are in the region of an Å. According to de Broglie the wavelength of an electron is given by

$$\lambda = \sqrt{\frac{150.4}{E}}, \quad (3.17)$$

with the electron energy  $E$  in eV and the wavelength  $\lambda$  in Å. As low electron energies are used, Eq. 3.17 is derived from non-relativistic physics. The used electron energies of

50 to 300 eV have wavelength in the range of an atomic unit cell. Furthermore energies below 300 eV are well-suitable, because the mean free path in solids is short enough to provide a good surface sensitivity. However, especially for low energy electrons, which interact strongly with the electrons in the sample, simple scattering description according to the Born approximation does not hold anymore. The strong interactions of electrons with matter make it necessary to consider multiple scattering. Nevertheless, the surface unit cell can be obtained with the diffraction conditions derived from kinematic scattering theory, while this theory does not predict the correct scattering intensities [57].

As discussed in Sec. 3.1 only an infinite periodical crystal lattice leads to lattice points. The finite penetration depth of electrons restricts the dimension of the crystal lattice and the lattice points become lattice rods. This can be understood by using the Laue equations,

$$\vec{Q} \cdot \vec{a}_1 = 2\pi h, \quad \vec{Q} \cdot \vec{a}_2 = 2\pi k, \quad \vec{Q} \cdot \vec{a}_3 = 2\pi l. \quad (3.18)$$

Scattering at a surface reduces Eq. 3.18 to only lateral components (parallel to the surface) of the scattering vector. Here  $h, k, l$  are the Miller indices. It means that the third Laue equation in Eq. 3.18 no longer exists. The Fourier transform of a  $\delta$ -function along  $z$  leads to a constant in reciprocal space [57] as shown by

$$f(Q_z) = \int \delta(z) e^{izQ_z} dz = 1.$$

Fig. 3.8 shows the Ewald construction of two-dimensional scattering on a cut along  $k_x$ . The shown lattice rods always intersect with the Ewald sphere and the Laue condition

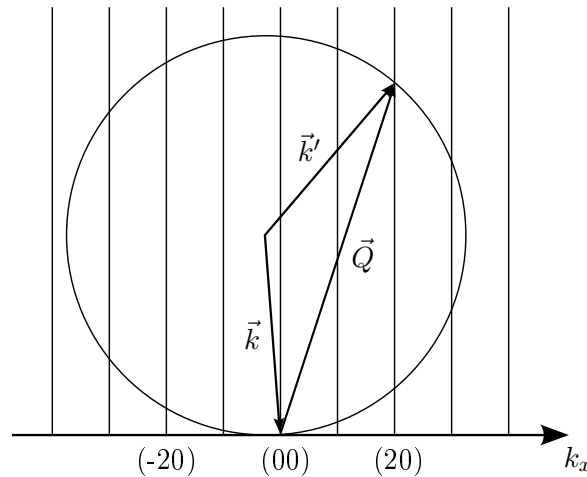


**Figure 3.8:** Ewald construction for two-dimensional surface scattering on a cut along  $k_x$ . Lattice rods appear instead of lattice points. These lattice points always intersect with the Ewald sphere and thus the Laue condition is fulfilled easily for an incoming beam with the wavevector  $\vec{k}$  and the scattered wavevector  $\vec{k}'$ . This sketch is adapted from [57].

is fulfilled for every electron energy and scattering geometry and a scattering pattern is visible.

In a real experiment the electron's penetration depth is not restricted to the first atomic layers. The component perpendicular to the surface needs to be considered and the third Laue equation cannot be neglected completely. As a consequence of an influence of the third Laue equation due to the loss of the strict two-dimensionality, the intensities of the corresponding Bragg spots are modulated, because of the modulation of the lattice rod's intensities. For a more detailed overview in electron scattering Ref. 57 is recommendable, for instance.

Another way to achieve a high surface sensitivity is scattering under grazing incidence, even if the electron energy is high. Small incidence angles ( $2^\circ$ -  $5^\circ$ ) lead to a mean-free path through the sample with only a small penetration depth perpendicular to the surface due to total reflection. This also leads to a vanishing third Laue equation.

Both methods have been used extensively during the thesis. The first method is used in a Low Energy Electron Diffraction (LEED), the second in a Reflection High Energy Electron Diffraction (RHEED) experiment, which will be introduced in section 5.1.

X-rays can also be used for surface sensitive studies. For angles smaller than the angle of total reflection  $\alpha_t$  (see 3.5) the penetration of X-rays perpendicular to the surface is very small, usually in the order of a few atomic layers. X-rays are thus also usable for analyzing the surface, but have not been used during this thesis.





## 4 Sample preparation methods

A lot of powerful thin film growth techniques were developed in recent years, especially for the application of oxide thin films. The approaches of growing thin films are partially different, but all used methods are belonging to physical vapor deposition techniques. Growing samples is a complicated interplay of thermodynamic parameters as temperature and growth speed. The first section will handle the basics of the theory, which is important for growing good thin films. During this thesis the oxide molecular beam epitaxy system (OMBE) and high oxygen pressure sputtering automat (HOPSA) were used for the deposition of thin films. Both preparation methods will be introduced in this chapter. The LSFO layers were prepared with OMBE, whereas the LSMO and  $\text{KTaO}_3$  (KTO) layers were grown with the HOPSA.

### 4.1 Thin film growth mechanism

A multitude of thermodynamic mechanisms has to be considered to understand the thin film growth. These are shown in the upper part of Fig. 4.1. The most important parameters are the kinetic energy of the condensed atom, the surface energy of the substrate and film, the elastic energy caused by strain in heterostructures, and the binding energies between the surface atoms among themselves and between them and the substrate atoms. Heteroepitaxy is the growth of an epitaxial thin film on a substrate, which is made of another material, for instance. These parameters can either be influenced by the used instrument or by the selection of substrate material. The growth technique itself influences the kinetic energy of incoming particles. Typical energies for thermal evaporation techniques like OMBE are 1 eV, whereas the kinetic energy for sputtering is usually slightly higher, but close to 1 eV, because thermalization takes place. Furthermore the substrate temperature is a crucial parameter. It determines the kinetic energies of the particle on the substrate surface. Low temperatures and thus low kinetic energies lead to the formation of particle clusters instead of building flat films. The reason is that the insufficient energy of the particles leads to a movement to rather local energy minima than global minima of the surface. A high particle flux will also prevent the atoms from finding their global energy minima [58, 59].

Besides the instrument related parameters, the selection of the substrate material and parameters is also important and one has to find a suitable substrate for the growth application. Firstly, the sticking coefficient of the substrate is important. It describes the ratio between adsorption and desorption and describes in principle the binding conditions between substrate and film atoms. This coefficient is mostly temperature dependent, and

usually the probability for desorption increases with increasing temperature. Additionally, a high substrate temperature also leads to higher surface energies, and a change of the grain boundaries of the grown film becomes feasible. Secondly, the lattice parameters and the modulus of elasticity play a role, because they determine the strain energy. As the strain energy is high, the formation of clusters, and thus island growth is most likely [60,61]. To achieve a good thin film growth these parameters have to be found empirically from experiments, because a prediction is practically impossible.

Under consideration of the introduced thermodynamic parameters, three different growth mechanisms can occur, as shown in the lower part of Fig. 4.1. If condensation and following surface diffusion is the predominant mechanism, a thin film formation can start [62]. If a substrate with a good lattice match was chosen, the layer-by-layer growth, also called Frank-van der Merve (Fig. 4.1a), and the island growth, called Volmer-Weber (Fig. 4.1b) growth mode, are possible, which mode is realized depends on the surface energy [59]. As long as

$$\gamma_{\text{layer}} + \gamma_{\text{layer/substrate}} \leq \gamma_{\text{substrate}},$$

one could observe a layer-by-layer growth. For the opposite case, one expects an island growth. In the equation above,  $\gamma_{\text{layer,substrate}}$  is the surface energy of the layer or substrate, and  $\gamma_{\text{layer/substrate}}$  is the surface energy of the interface in between substrate and layer. The third growth mode, the Stranski-Krastanov growth mode is shown in Fig. 4.1c. It is

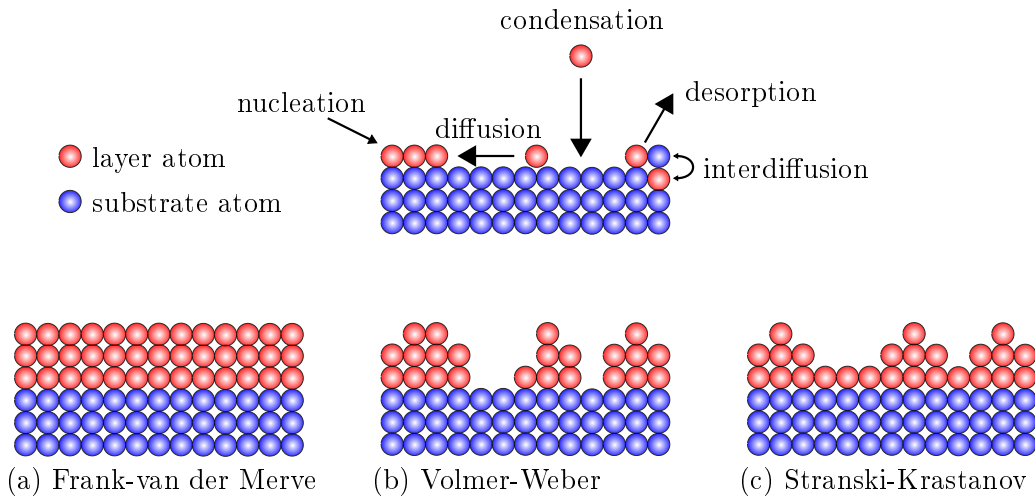


**Figure 4.1:** The upper sketch explains the different mechanism that occur during thin film growth. The bottom figure shows the different heteroepitaxial growth modes, which are caused by the surface thermodynamics. For a smooth layer it is necessary to achieve the Frank-van der Merve growth mode (a), which indicates a perfect layer-by-layer growth.

characterized by a layer-by-layer growth, which is followed by an island growth. A lattice mismatch between substrate and layer is the reason for it. The driving energy is the strain energy of the growing film. With increasing thickness this strain energy will raise and an island formation will become more and more favorable [59].

For thin film growth applications the Frank-van der Merwe growth mode is the desired one to achieve homogeneous and smooth thin film layers. All thermodynamic variables

have to be optimized during the development of the growth procedures for each system used in this thesis. As one can imagine the optimization of a thin film growth process is difficult as so many parameters play a crucial role, especially for the growth of complex oxides, where a perovskite structure with four different atoms is required.

## 4.2 Oxide Molecular Beam Epitaxy System

### 4.2.1 Requirements to the system

For a successful growth of thin films several requirements to the system have to be fulfilled. The main requirement is a vacuum chamber which provides a Ultra High Vacuum (UHV). The reason for using a UHV chamber can be described as follows [59]. On the one hand one has to ensure that the atoms exiting the effusion cells can move to the substrate without any collision with other atoms. The free mean path length  $\lambda_m$  in a vacuum system is given by

$$\lambda_m = \frac{k_B T}{\sqrt{2\pi} p_i d_m^2}, \quad (4.1)$$

where  $d_m$  is the molecular diameter,  $T$  the temperature,  $p_i$  the pressure, and  $k_B$  the well-known Boltzmann constant. For a base pressure of  $10^{-8}$  Pa and an approximated diameter of  $1 \text{ \AA}$ , one gets a free mean path length of  $10^8$  m, which is obviously high enough for the used systems that the atoms cannot interact with each other, because the probability for collisions is almost zero. Nevertheless the second critical point is the number of residual gas atoms. These atoms limit the purity of the thin films, because they can become incorporated during the growth. Thus, it is necessary to increase the time, which is necessary to get one monolayer of impurity atoms. According to Ref. 58 the remaining number of molecules (or atoms) of the gas species  $i$ , which stick to the unit area of substrate surface in unit time can be described by

$$w_i = p_i \sqrt{\frac{N_A}{2\pi k_B M_i T}}. \quad (4.2)$$

$p_i$  is the partial pressure in Pascal (Pa) of the residual gas species  $i$ ,  $M_i$  its molecular weight,  $T$  the temperature, and  $N_A$  the Avogadro constant. With the assumption that the residual gas consists of nitrogen molecules and the temperature is room temperature (300 K) one can easily simplify Eq. 4.2 to

$$w_{N_2} = 2.87 \cdot 10^{22} \cdot p_i [\text{m}^{-2}\text{s}^{-1}].$$

$w_{N_2}$  is the number of nitrogen atoms impinging on the surface. A typical number of atoms on a square meter is  $10^{19}$ . Then it is easy to calculate the time for the formation of one monolayer of impurity atoms on the surface as

$$t_{ML} = \frac{10^{19}}{w_{N_2}}. \quad (4.3)$$

A reasonable growth rate for oxide is about 60 s for a monolayer<sup>1</sup>. For the examined oxide materials the lattice parameter is ca. 4 Å, which gives a growth rate of 4 Å per minute. The grown systems have got an overall thickness of roughly 1000 Å. For that a growth duration of 4 h is necessary. To get a minimum of contamination one should not exceed one monolayer of impurity atoms during the growth [58]. The pressure requirement for the OMBE system is  $\approx 10^{-8}$  Pa ( $10^{-10}$  Torr), which is the base pressure by chance of the used OMBE system as follows later on. One has to admit that this calculation is just a rough estimation. The contamination during the growth process depends on a lot of thermodynamic variables, such as the substrate temperature, the sticking coefficient, and so forth, but has not been further specified.

### 4.2.2 Setup

The used OMBE system was manufactured by DCA Instruments Finland and is commercially available. It is build of three main parts, the load lock, the buffer line, and the main chamber. A sketch of the instrument is shown in Figure 4.2a. The desired UHV is achieved with different pumping techniques.

The load lock is pumped with a turbopump with a scroll backing pump. The buffer line and the connected Auger Electron Spectroscopy (AES) chamber are pumped by two different pumps, a turbopump with backing pump and an ion getter pump. The main chamber is equipped with a turbopump connected to a backing scroll pump. The second pump which is used is a cryopump. The mechanism of a cryopump is quite simple. It is based on condensation of atoms and molecules on a very cold surface. A helium closed cycle cryostat is used to maintain the temperature of about 10 K of the cold surface. Most atoms and molecules within the main chamber simply stick at the cold surface without any probability to escape. A residual gas analyzer, which is in principle a mass spectrometer, is installed to quantify the UHV conditions during operation.

As shown in fig. 4.2a a LEED and a AES are mounted for in-situ analysis of the sample before and after the growth. These instruments will be introduced in 5.1 later on. The growth of the samples takes place in the main chamber. Six effusion cells and two electron beam evaporators are installed and can be used simultaneously. A precise Proportional-Integral-Derivative (PID) controller regulates the source's temperatures to maintain stable fluxes. As molecular oxygen is not highly reactive an atomic oxygen source is installed and directed towards the sample to improve oxidization of the growing layers. Thereby a oxygen plasma is used to provide atomic oxygen, which is produced by inductively coupled 13.6 MHz high-frequency alternating current. This is crucial in order to ensure oxygen saturation of the growing samples, because molecular oxygen is less reactive than atomic oxygen. The desired oxygen is directed towards the sample and its flux is controlled by a mass flow controller. Fig. 4.2b shows a horizontal cross section of the main chamber. The sample is mounted upside-down in the middle, whereas the effusion sources are mounted at the lower part of the chamber to keep the distance between source and sample large. This is necessary to ensure a homogeneous material flux for a homogeneous layer growth on the substrate. To avoid contamination and to cool the growth environment, the upper

---

<sup>1</sup>The following chapters will make clear, why it is necessary to grow thin films slowly.

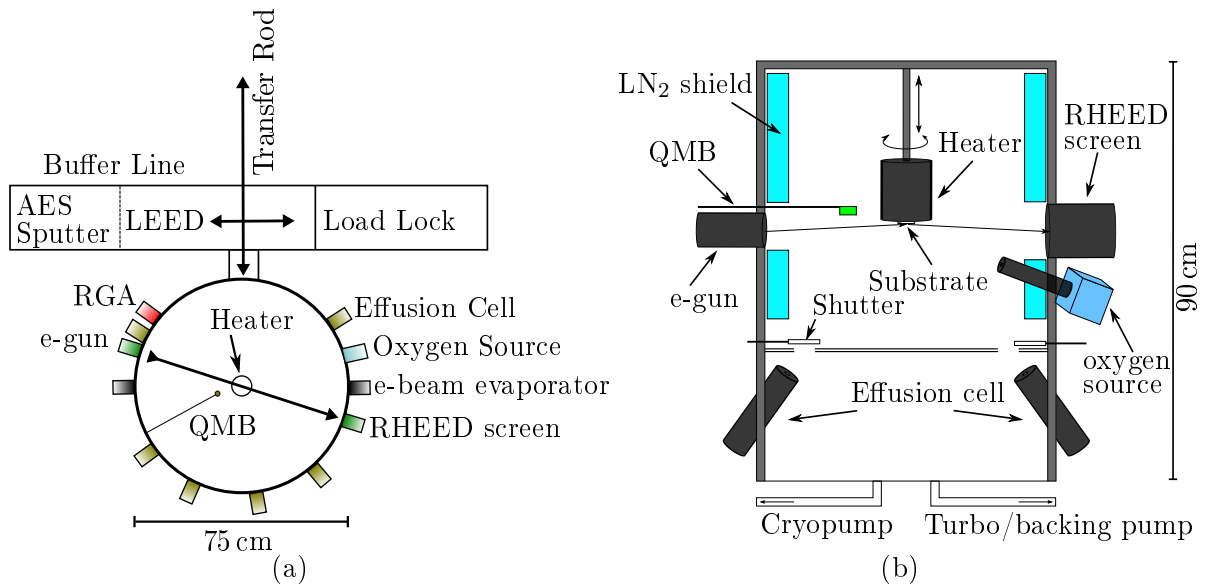


**Figure 4.2:** (a) Bird's eye view of the used system. The system is divided into three sections. The load lock, the buffer line, and the main chamber. A transfer system allows one to move the sample within the system. The main chamber, or growth chamber, is equipped with two electron beam evaporators and six effusion cells. In total up to eight elements can be evaporated simultaneously. (b) depicts a cross section of the main chamber to see the arrangement of the equipment that is necessary for sample growth. The substrate is mounted upside-down on a heater. The oxygen source and the evaporators can be closed with shutters. Both sketches are not true to scale. AES: Auger electron spectroscopy, QMB: quartz microbalance, LEED: low energy electron diffraction, RHEED: reflection high energy electron diffraction, RGA: residual gas analyzer.

half of the chamber is equipped with a liquid nitrogen cryo shield, which catches atoms that have not hit the substrate to avoid uncontrolled backscattering. Furthermore the cryo shield is necessary to prevent the chamber from heat radiation, which is caused by high temperatures of the effusion cells. For a rate calibration a Quartz Microbalance (QMB) is used. A deposited mass on a piezoelectric quartz crystal reduces the resonant frequency thereof, which is known as the Sauerbrey effect [63]. The change of the resonant frequency can be used to determine the current rate for the calibration. To measure the rate, the microbalance is moved to the sample position. During the actual sample growth the microbalance has to be removed from this position, otherwise it would screen the sample from the incoming molecular beam. A rate measurement during thin film growth is thus not possible. This fact is a disadvantage of the system design. To compensate this, a high flux stability has to be ensured, so that monitoring and regulating the effusion cells during the growth is not necessary. The procedure of rate calibration is explained in detail in Sec. 6.2. RHEED has been used to analyze the sample surface prior, during, and after the growth process. The RHEED technique is introduced in Sec. 5.1.

The deposition procedures used during this thesis were done in codeposition mode. Codeposition uses all effusion cells parallel in contrast to shuttered growth, where a sequential mono layer growth is pursued.

### 4.3 High Pressure Oxygen Sputtering Automat

A high oxygen pressure sputtering automat (HOPSA) has also been used for thin film growth. A sketch of the used sputtering machine is shown in Fig. 4.3. The high pressure oxygen sputtering technique is based on radio frequency (RF) sputtering, where a high-frequency electric field (13.6 MHz) is used to ignite a oxygen plasma between target and substrate electrode. The oxygen partial pressure used during the sputtering process lies between 100 and 300 Pa, it prevents the layer from getting oxygen deficiencies. The ionized atoms from the process gas bombard the target, where target atoms are ejected then. Those atoms are almost always neutral, so that they can move to the substrate without any influences of the applied rf electric field. As a target a commercially available one with the desired stoichiometry has been used and is bonded to a magnetron sputter target holder. Magnetron sputtering has been used to increase the sputter efficiency with additional magnetic fields applied by permanent magnets behind the target. Due to the Lorentz force the electrons have to move on spiral paths, which lead to electrons captured near the target surface. Due to an enhancement of collisions more ions are created and thus an increase of the sputtering rate can be observed. Furthermore due to the accumulation of electrons near to the target the plasma is limited to the target region which reduces the backsputtering effect, when the substrate also gets sputtered [64]. The achievable sputtering rate lies in the region of  $1 \text{ \AA}/30 \text{ s}$ .

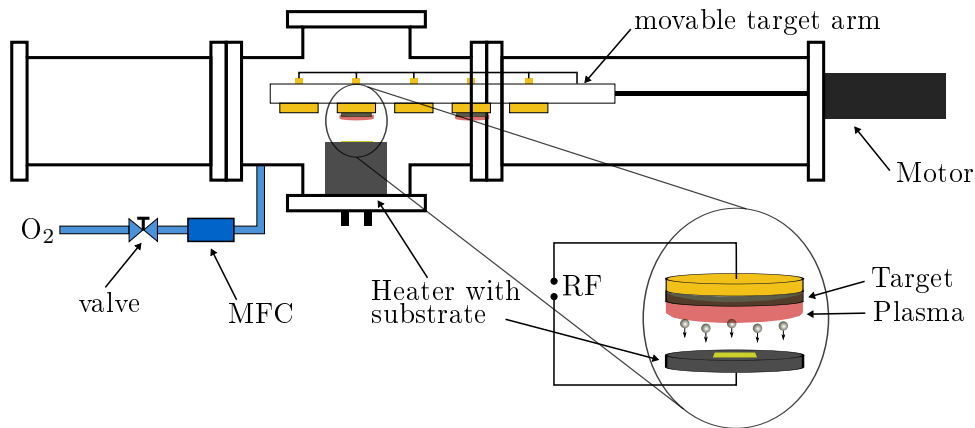


**Figure 4.3:** Sketch of the used high oxygen pressure sputtering automat. Two targets can be used simultaneously to grow multilayer systems and the movable target arm is necessary to start and stop the growth as well as switching between two targets. The target size is ca 5 cm, the distance between substrate and target can vary within a few centimeters. The zoom shows a detailed view on the target, heater, and substrate.

To avoid impurity atoms a base pressure of  $10^{-4}$  Pa has to be reached with a turbopump and backing pump before starting the sputtering process. After reaching the base pressure, the process gas is regulated by a mass flow controller (MFC). Therefore the pumping cross-section of the turbopump has to be reduced, because usually a turbopump is designed to work at significantly lower pressures. A substrate heater enables one to heat the sample up to 1300 K. A movable target arm has been used to initiate and stop the sputtering by moving the target to the substrate position and away. A plasma generator with automatic

tuning ignites the oxygen plasma and keeps it stable. A direct measurement method of the current sputter rate is not included. The rate calibration has to be done ex-situ with X-Ray Reflectometry (XRR) which is introduced in 5.2.1. Furthermore, other in-situ methods are also not installed.

## 4.4 Comparison of MBE and sputtering

Samples grown with different growth methods like OMBE and sputtering cannot be considered as equal. At first the instruments used for the epitaxy and sputtering are different. The OMBE base pressure is UHV, whereas sputtering base pressure is only High Vacuum (HV), which is a difference of at least four orders of magnitude in pressure. According to Sec. 4.2.1, this influences the amount of impurity atoms which are incorporated into the growing thin film. This fact can influence the quality and thus the physical properties of the thin film. Sometimes, as discussed later, the OMBE system is not suitable or not working for some films. Technical problems during this work made it necessary to grow the LSMO layers with the sputtering technique, although OMBE would have been the better choice. Secondly, as mentioned, the kinetic energies of the particles are also slightly different for both techniques, namely  $\approx 1$  eV for thermal evaporation and  $> 1$  eV for sputtering. This fact also influences the physical properties of thin films, in spite of working close to the thermal equilibrium.

Vila-Fungueiriño et al. investigated the influence of different growth conditions on the magnetic anisotropy of  $\text{La}_{0.7}\text{Sr}_{0.3}\text{MnO}_3$  [65]. For thin film preparation they used pulsed laser deposition, which is far from thermodynamic equilibrium, and slow chemical solution deposition method under quasi-equilibrium conditions. They found out that magnetic anisotropy is determined by the growth method and thus by the proximity to the thermodynamic condition during the thin film growth. As a result they stated that the nature and magnitude of the magnetic anisotropy can be influenced by tuning the thermodynamic parameters within a thin film growth process. The used growth methods are not the same, and this effect can influence the sample properties under the use of OMBE and sputtering. However, this has not been investigated during this thesis.





## 5 Sample characterization techniques

### 5.1 In-situ analysis techniques

Three instruments are installed in the OMBE chamber for in-situ surface analysis, two for structural and one for surface stoichiometry analysis. In-situ methods exhibit the main advantage that they can be performed without breaking the UHV during growth or directly after. This fact prevents the surface from getting contaminated by adatoms, so that the surface structure and composition can be analyzed undisturbed. However, these in-situ methods have also been used to analyze the surface of the sputtered samples ex-situ.

#### 5.1.1 Low-Energy Electron Diffraction

Low-Energy Electron Diffraction (LEED) is a method to investigate the crystalline structure of the sample surface. As mentioned in Sec. 3.8, low energy electrons with a wavelength in the range of typical atom distances ( $\approx 1 \text{ \AA}$ ) are perfect as probes for surface sensitive measurements. A common LEED setup is shown in Fig. 5.1.

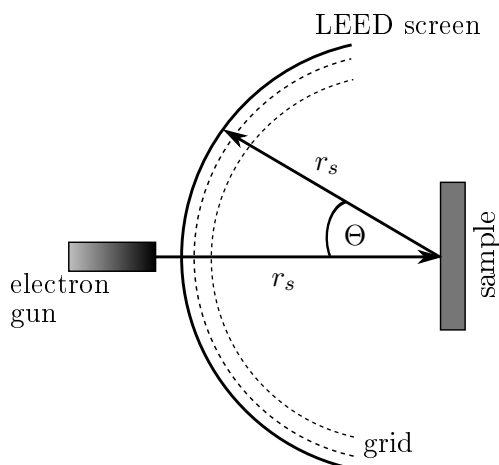


**Figure 5.1:** Sketch of a LEED system. The electrons are accelerated towards the sample and impinge perpendicular to the sample surface and are then diffracted in direction of the LEED screen. Inelastically scattered electrons are filtered by an energy filter. The grid is used to further accelerate the elastically scattered electrons to trigger fluorescence on the screen.

In order to avoid interaction of the electrons with residual gas atoms a large mean free path length is necessary. This is a further reason for using an UHV environment besides

keeping the surface clean. The electron gun (source) produces electrons by thermionic emission from a hot filament. The electrons are then accelerated by a Wehnelt cylinder perpendicular to the sample surface and collimated with an electrostatic lens system. The accelerating voltage and thus the associated electron energy is variable and has been used between 50 eV and 300 eV. After getting backscattered from the sample the electrons have to pass a retarding grid, which acts as an energy filter to remove inelastic scattered electrons from the spectrum. Since the electron energy is very low and not sufficient to trigger fluorescence on the screen, the electrons are accelerated to  $\approx 6$  keV in order to achieve fluorescence.

As briefly mentioned above, the finite penetration depth of the electrons into the surface and the dynamic scattering theory make the LEED a powerful, but demanding tool for surface analysis. In this work the LEED has only been used qualitatively to evaluate the crystalline quality of the substrate surface and of the grown thin films. A good crystallinity is indicated by sharp reflections on the screen. For a deeper insight into LEED Ref. 57 and 66 are recommendable.

### 5.1.2 Reflection High-Energy Electron Diffraction

The Reflection High-Energy Electron Diffraction (RHEED) system is the second surface sensitive instrument which is installed in the main chamber. Due to the grazing incidence angle scattering geometry an in-situ measurement during the growth is possible, and thus a growth monitoring is in principle possible. Fig. 5.2 depicts the principle of the RHEED

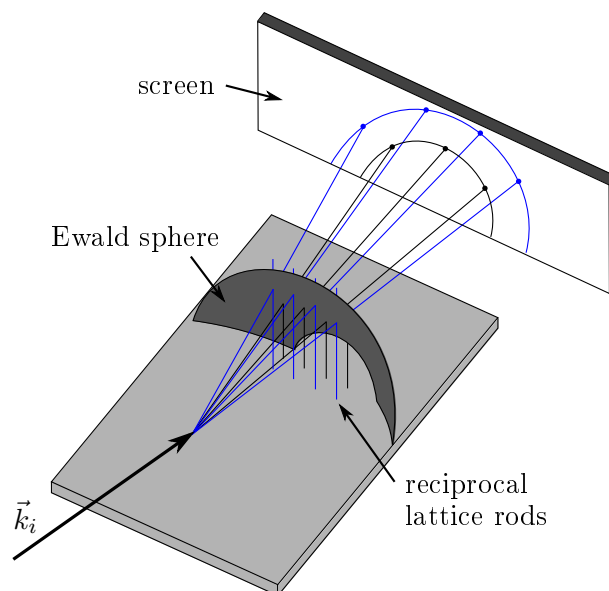


**Figure 5.2:** RHEED scattering geometry. The grazing incidence electron beam is only scattered from the 2D surface, which leads to lattice rods instead of lattice points (see. 3.8). The scattered electrons become visible after impinging on a fluorescence screen and are detected by a video camera.

technique. A collimated high energy electron beam is produced by an electron gun and

directed to the sample under an angle of smaller than approximately  $2^\circ$ . The grazing angle leads to a very low penetration of electrons perpendicular to the sample surface due to total reflection. As explained in Sec. 3.8, the third Laue condition is not valid any more for this case and reciprocal lattice points become lattice rods, consequently. Fig. 5.2 also shows the Ewald sphere and the reciprocal lattice rods as an example. The lattice rods always intersect with the Ewald sphere, which leads to a diffraction pattern for every scattering vector  $Q$ . After being scattered from the sample the electrons trigger a signal on a fluorescence screen which is observed by a video camera. RHEED has also been

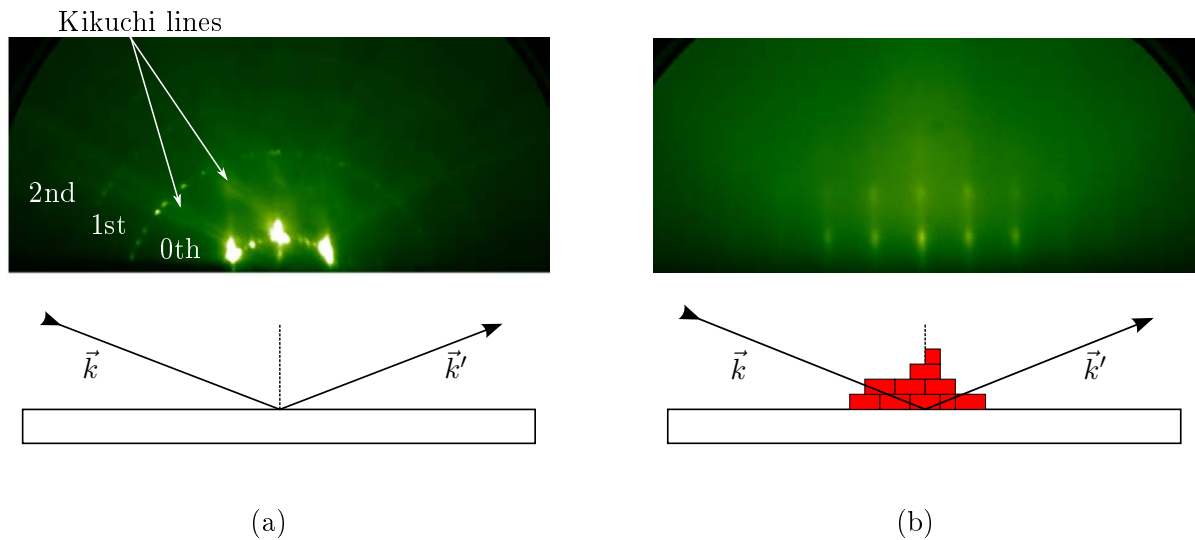


**Figure 5.3:** (a) is a RHEED pattern of a cleaned silicon substrate. Point-like reflections on higher Laue ring indicate a very smooth surface. Kikuchi lines are an indication of a perfectly shaped surface. In contrast (b) depicts an obviously island growth of manganate on STO, where a 3D diffraction pattern overlies.

used as a qualitative experiment during growth. Fig. 5.3 shows two different RHEED patterns of samples with different qualities. Fig. 5.3a depicts a smooth silicon substrate. Higher Laue orders are clearly visible. Additionally diagonal lines with the origin in the zeroth order reflection appear. They are called Kikuchi lines and are independent of the elastic scattering. The primary scattering process is inelastic scattering, which involves phonons and plasmons. They are sharp for crystals with high bulk and surface order, and thus they depend strongly on the surface morphology [67, 68]. Terraces and steps on the surface cause a significant broadening of the Kikuchi lines.

In contrast a rough surface of a manganate thin film on a STO substrate with island growth is shown in Fig. 5.3b. The electrons are not only reflected from the 2D surface, but they also penetrate the island, which leads to a bulk-like scattering pattern of the cubic structure. Additionally, the Kikuchi lines vanished, which corresponds to the assumption that the surface is dominated by island growth. For a rough surface without the emergence of clear islands, the RHEED pattern smears simply out. Thus, RHEED is an ideal probe to get in-situ information about the surface quality, even during growth.

### 5.1.3 Auger Electron Spectroscopy

Auger Electron Spectroscopy (AES) can be used for analyzing the surface's chemical composition. Therefore, element specific secondary electrons, so called Auger-electrons, can be analyzed. Incoming electrons, produced and accelerated by an electron gun, with an energy of 3 keV transfer their energy to electrons in low energy levels. The gain in energy of those electrons is high so that they can leave the atom. Since this state with unoccupied energy levels is energetically unfavorable, an electron from a higher energy level (outer shell) moves to this free energy level. The energy difference between the high and low state is transferred to another outer electron. This electron leaves the atom due to the gain of energy. The energy of this electron is element specific and a sensitive detection of the electron energy gives information about the composition of the sample surface. Due to technical problems the AES device could not be used during this thesis, but is mentioned for the sake of completeness.

## 5.2 In-house (ex-situ) instruments

All instruments used on-site are called in-house instruments including experiments performed at PGI-9 and at the Ernst Ruska-Centre for Microscopy and Spectroscopy with Electrons.

### 5.2.1 X-ray Reflectometer

The Bruker AXS D8 Advanced has been used for structural characterization of the prepared thin films either in reflectometry or in diffractometry mode. A sketch is depicted in Fig. 5.4. Due to its geometry only the crystalline out-of-plane components can be accessed. The system uses a copper X-ray source, where the  $\text{Cu K}_{\alpha_1}$  radiation with

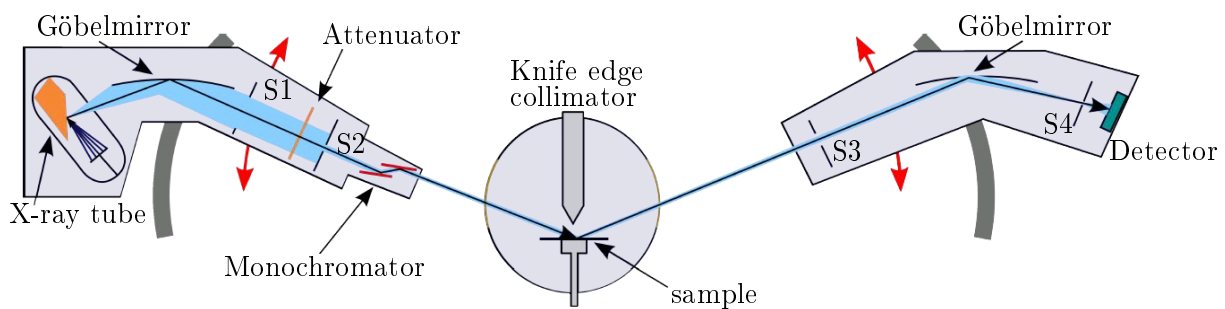


**Figure 5.4:** Sketch of the Bruker D8 Advanced X-ray reflectometer. This instrument has been used for the structural characterization of the thin films. Only the tube and the detector can be moved. Thus only out-of-plane information is provided by specular scattering. However, off-specular scattering gives informations on lateral correlations. Sketch taken from [69].

$1.54055 \text{ \AA}$  is collimated and selected with a Göbel mirror and a slit system as well as a following channel cut monochromator. It is used to get rid of the background (mainly the bremsstrahlung) and other characteristic transitions, which exhibit different wavelengths. These beam improvements are highly necessary for the different measurements.

The reflectivity measurements, which are performed under small angles (up to  $\theta = 10^\circ$ ), require a good collimation of the beam in order to measure long range correlations. On the other hand wide angle scattering requires a highly monochromatic beam to achieve atomic resolution. To overcome the high intensity differences, especially for reflectivity measurements, an automatic rotary absorber is installed to prevent the detector from oversaturation and radiation damages. To achieve the best resolution a slit system and a Göbel mirror is also installed on the side of the one dimensional detector. The available  $2\theta$  range is  $0^\circ$  to  $110^\circ$ . This makes it possible to measure reflectometry under low and diffractometry under high incident angles.

### 5.2.2 Powder X-ray Diffractometer

The in-house powder diffractometer Huber Guinier G670 has been used for a precise analysis of unit cell metric of powder systems. Especially, it has been extensively used to assist the optimization of powder preparation procedures in order to get a single phase powder.

A sketch of the powder diffractometer is shown in Fig. 5.5. A copper X-ray source is used with a monochromator and collimator. The monochromatic beam has a wavelength of  $1.54055 \text{ \AA}$ , which is the selected  $\text{Cu K}_{\alpha_1}$  transition.

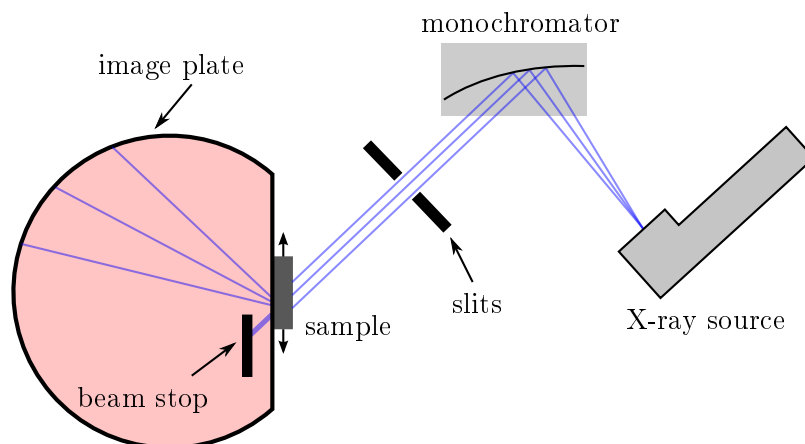


**Figure 5.5:** Sketch of the in-house powder diffractometer Huber Guinier G670. A monochromatized and collimated X-ray beam is scattered by a powder sample. The primary beam is blocked with a beam stop. An image plate detects the scattered intensity. This geometry is called Guinier technique and is commonly used.

As seen in the sketch, the measurement is done in transmission mode. Therefore a thin powder film is used between two very thin Mylar<sup>®</sup> foils. It is necessary to keep the amount of powder as small as possible to prevent high absorption of X-rays. The typical mass of powder is less than 1 mg. To improve the statistics the sample is moved through the X-ray beam permanently, thus the exposed sample area becomes increased. The direct beam is blocked by a suitable beam stop, while the scattered intensity is detected with an image plate detector. An image plate gets exposed during the measurement and can be read out after the measurement is finished. The image plate covers a  $2\theta$  range between  $0$  and  $100^\circ$  with a resolution of  $0.005^\circ$ .

### 5.2.3 Atomic Force Microscope

For surface analysis an Agilent Technologies 5400 Atomic Force Microscopy (AFM) has been used. The AFM technique is a versatile technique for probing the topological properties of the sample surface, which is probed in position space [70] within a subnanometer scale. The sample surface is directly mapped and, compared to scattering methods, a complex simulation of the sample is not necessary. The AFM technique is based on the interaction between the sample surface and a measuring tip. The approximation of the interaction between a pair of neutral atoms is given by the Lennard-Jones potential [71].

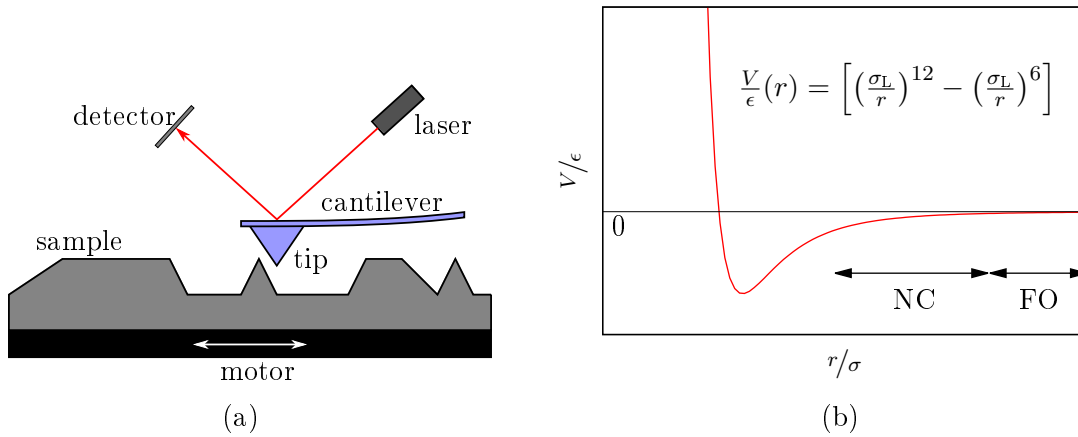


**Figure 5.6:** (a) shows the AFM measurement technique which is based on the interaction between sample and tip. The tip is oscillating near its resonant frequency and the amplitude is measured with a laser and a detector. (b) depicts the underlying Lennard-Jones potential, which is a good approximation to describe the interaction between surface atoms and tip atoms.  $V$  and  $r$  are normalized to constants  $\epsilon$  and  $\sigma_L$ , respectively. The AFM has been used in non-contact (NC) mode. FO is the range, where the tip can freely oscillate.

The AFM measuring method is depicted in Fig. 5.6. It has been used in the non-contact mode. The cantilever and tip are driven at their resonant frequency. The amplitude is measured from a deflection of a laser beam which is detected by a 4-quadrant detector. The change of the amplitude caused by the interaction between sample and tip is compensated by a height correction of the sample with a high-precision piezoelectric scanner. The correction done by the scanner is the topological height profile. This height profile is used to analyze the sample surface in order to get information about roughness within an area of a few  $\mu\text{m}^2$ . The interaction of the tip with the sample can be described with the Lennard-Jones potential in good approximation, as shown in Fig. 5.6b.

### 5.2.4 Magnetic Property Measurement System

A Quantum Design Magnetic Property Measurement System (MPMS) has been used to characterize the macroscopic magnetic properties of the samples. As depicted in Fig. 5.7 the MPMS main parts are a superconducting magnet to generate a magnetic field up to 7 T, a superconducting pick-up coil which couples inductively to the sample, and a rf

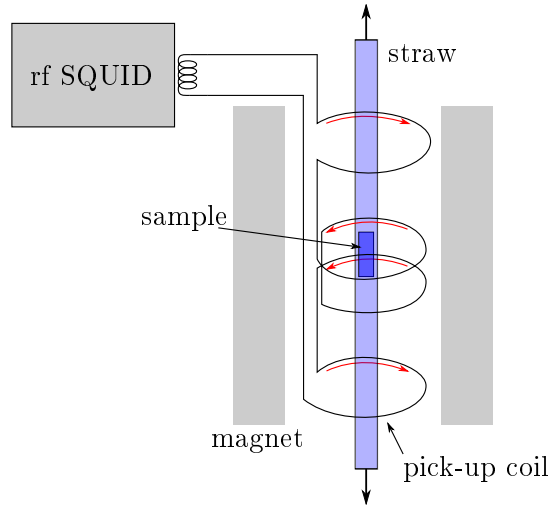


**Figure 5.7:** Measurement technique of the used Quantum Design MPMS. The sample is mounted in a straw and is moved through a second order gradiometer. The gradiometer is thus coupled inductively to the sample. The pick-up system is then coupled to a rf SQUID.

SQUID. The SQUID itself is a device which consists of a superconducting ring which is interrupted by usually two very thin Josephson contacts [72]. From quantum mechanics one knows that the magnetic flux within a superconducting ring has to be quantized with the magnetic flux quantum  $\Phi_0 = 2.07 \cdot 10^{-15}$  Vs. A change of the external magnetic flux leads to a change of the magnetic flux in the ring with a multiple of the magnetic flux quantum. This makes a precise determination of the external magnetic flux possible.

The pick-up coil is built as a second order gradiometer, which is wound in a set of three coils. As indicated by red arrows in Fig. 5.7 the upper coil is a single turn wound clockwise, the center coil are two turns counter-clockwise, and the bottom coil is also a single turn wound clockwise. This configuration is used to reduce noise in the detection circuit caused by the surrounding magnet [73]. The pick-up coil is then connected to the rf SQUID [74], which measures the induced voltage from the moving sample precisely. From the resulting response function of a magnetic dipole moving through the pick-up coil the corresponding magnetic moment of the sample can be derived, which is done by the instrument software automatically.

The whole setup is installed in a dewar and constantly held under liquid helium to maintain the superconducting behavior of the superconducting coils. The sample temperature can be chosen between 1.9 K and 400 K. The sample is mounted in a drinking straw whose length is larger than the extension of the pick-up coils. A signal originating from the drinking straw is avoided, because the drinking straw as a homogeneous medium is thus not inducing a signal to the pick-up coil (no magnetic flux change).

The MPMS achieves a sensitivity of approximately  $10^{-12}$  Am<sup>2</sup>. The drinking straw itself provides a very low background, which is necessary while observing very tiny magnetic moments. The disadvantage is its heat sensitivity, which limits the maximum temperature to 350 K.

Both, the temperature dependency and the field dependency of the powder and thin film samples were measured with the MPMS, because of its high sensitivity.

### 5.2.5 Physical Property Measurement System

A Quantum Design Physical Property Measurement System (PPMS) is a multifunctional measurement device which can be used to measure a large variety of physical properties. The basis of the system is a liquid helium dewar, wherein a sample chamber and a superconducting magnet is installed. Temperatures between 1.9 K and 400 K are easily accessible and also a magnetic field up to 9 T can be applied. During this work the PPMS was used with the “Resistivity Option” and the “Heat Capacity Option”. The former was used to measure the temperature dependency of the resistivity up to ca. 10 M $\Omega$  with a four-point or two-point method, respectively. Therefore samples have been contacted with platinum wires which have been fixed on the sample surface with silver paste.

The latter was used to measure the heat capacity under constant pressure, which is defined as

$$C_p = \left( \frac{\partial Q}{\partial T} \right)_p,$$

where  $\partial Q$  is the heat, which is necessary to cause a temperature change  $\partial T$ . For solid materials the thermal expansion is mostly negligible and thus one can assume  $C_p \approx C_v$ . A

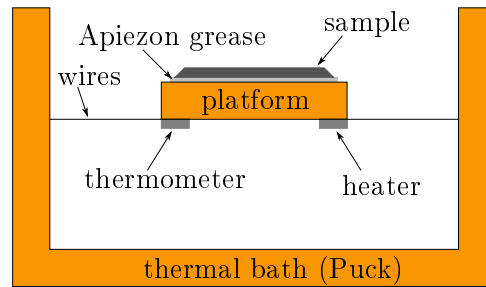


**Figure 5.8:** Heat capacity measurement option of the PPMS. The puck will be connected to the PPMS dewar. Adapted from [75].

sketch of the sample platform is shown in Fig. 5.8. The sample platform is connected to the PPMS sample puck, which serves as a thermal bath. A small sample is attached to the sample platform with Apiezon grease to ensure good thermal contact. The typical sample mass is a few mg. The sample platform is equipped with a heater and thermometer and is suspended by contact wires from the puck. It is necessary to ensure that the thermal conductance is dominated by the wires of the sample platform. During the measurement a known amount of heat is applied at constant power for a fixed time. This heating is followed by a cooling of the same duration. Afterwards the relaxation time of the system can be determined and the heat capacity can be calculated [75].

Under the circumstance that the internal diffusion time, which is necessary to reach a thermal equilibrium state within the sample, is larger than the relaxation time, the value of the measured heat capacity is too small. This also happens for a poor thermal contact between sample and platform. Especially the unshaped pieces from a sintered pellet, or the powder sample, have only poor thermal contact. Thus the measurement is rather qualitative, and can only be used to find phase transitions without determining the absolute value of the heat capacity as described later on.



### 5.2.6 Rutherford Backscattering Spectrometer

Rutherford Backscattering Spectrometry (RBS) is a technique to analyze the stoichiometry of the grown thin films. It is a very important instrument for developing thin film growth procedures with the objective of perfect stoichiometry. RBS uses a backscattering geometry as depicted in Fig. 5.9. An ion source provides light helium ions which are accelerated with a particle accelerator towards the sample and then backscattered under the scattering angle  $\theta$ . The measurements were carried out at the PGI-9 (Forschungszentrum Jülich GmbH)<sup>1</sup> and at the Ion Beam Center (Helmholtz Zentrum Dresden Rossendorf)<sup>2</sup> with helium energies of 1.4 MeV.

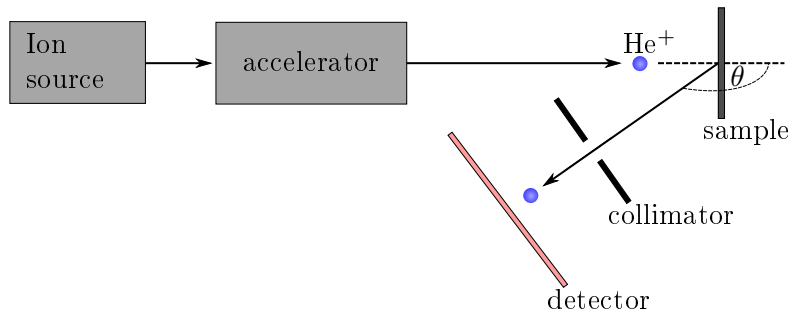


**Figure 5.9:** Sketch of a RBS experiment. An ion source provides helium ions that are accelerated towards the sample and then backscattered under the scattering angle  $\theta$ . The backscattered ions are detected with an energy sensitive detector.

In a first approximation RBS can be described within the kinematic scattering theory. The energy of the backscattered helium ions depends on the masses of the involved particles in the sample. The energy of the backscattered particle is element specific and can be used for analysis of the stoichiometry. As described in Ref. 57, the energy  $E_1$  of the helium ion after the scattering process can be written as

$$E_1 = \kappa^2 \cdot E_0.$$

$E_0$  is the initial energy and  $\kappa$  is the kinematic factor, which is

$$\kappa = \frac{\cos(\theta) + \sqrt{\frac{m_t^2}{m_{\text{He}}^2} - \sin^2(\theta)}}{1 + \frac{m_t}{m_{\text{He}}}}.$$

$m_t$  and  $m_{\text{He}}$  are the masses of the target atom and the helium ion, whereas  $\theta$  is the scattering angle as shown in Fig. 5.9. In a real experiment the incident ions penetrate the sample and lose energy gradually due to Coulomb interaction with atoms in the sample. This is known as the stopping power, which cannot be predicted reliably for light atoms like oxygen. This makes a simulation much more complicated. An empirical model is used under consideration of the thickness and the density of the sample and is implemented in the software package RUMP [76]. This program has been used to analyze the data

<sup>1</sup>Dr. Jürgen Schubert, Dr. Bernd Holländer, and Willi Zander.

<sup>2</sup>Dr. René Heller.

obtained from the PGI-9 experiment. For the samples measured at HZDR the data was analyzed by René Heller.

The error of the measurement lies within a few percent and depends on the species of the scattering atoms. Basically, RBS is based on an accurate calculation of the stopping power, and as mentioned, this calculation is not reliable for light elements.

### 5.2.7 Scanning Transmission Electron Microscopy and energy dispersive X-ray Spectroscopy

In contrast to the introduced X-ray and neutron scattering methods Scanning Transmission Electron Microscopy (STEM) is a method to probe the sample microscopically in position space. The measurement was performed with the great support of the Ernst Ruska-Centre for Microscopy and Spectroscopy with Electrons.

STEM uses a focused electron beam which impinges on a very thin sample which has to be prepared beforehand as explained later on, and the transmitted electrons are detected. The complete STEM image is formed by scanning the focused beam over the sample. Besides this information, the setup provides element specific information via Energy Dispersive X-ray Spectroscopy (EDX). Element characteristic radiation is emitted when outer-shell electrons move to the vacancies in the inner shell of a atom generated by an incident electron beam. These emitted X-rays are detected with an energy sensitive detector.

As the electron beam scans the sample this information is also space-resolved and the element distribution within the sample can be measured. For instance, a detailed introduction is given by Williams and Carter [77].

The following steps, the sample preparation and measurement as shown below, were done under the responsibility of Dr. Juri Barthel, ER-C.

#### Sample preparation

For transmission electron microscopy a thin lamella, usually several 100 nm, has to be cut from the sample with focused ion beam milling. Beforehand a 40 nm thick gold layer is deposited via sputtering to prevent charging during the ion milling process. Then a thin cross-section lamella was cut by focussed ion beam milling either with an FEI Helios Nanobeam 400S [78] or with an FEI Helios Nanobeam 460F1 [79]. Further thinning was achieved by using a gentle argon beam of 900 eV and final surface cleaning was done with a 500 eV argon ion beam with a Fischione Model 1040 Nanomill. An overview TEM measurement of a prepared sample is shown in Fig. 5.10. Besides the substrate and two layers, the conductive Au layer and a protective Pt layer is visible.

#### Measurement

STEM was performed with a FEI Titan G2 80-200 [80] operated at 200 kV. The instrument is used with a CEOS DCOR probe CS-corrector which provides a spatial resolution of 1 Å. This detector is placed in the high-resolution annular dark field regime. EDX was done with a high-efficiency Super-X 4-SDD windowless detection system [81].

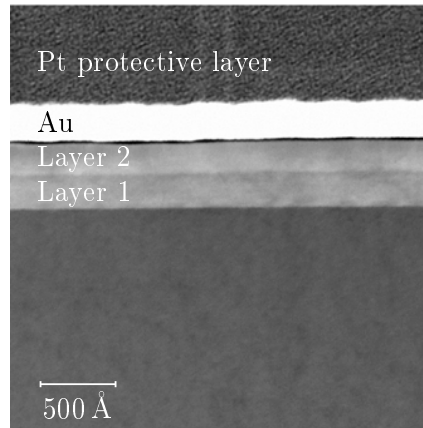


**Figure 5.10:** Overview of a TEM measurement of a sample after preparation.

The electron probe was tuned with 1 nA current to generate a sufficient signal. This is necessary to achieve spatially resolved EDX mappings of the layer interface.

## 5.3 Instruments at large-scale facilities

Highly precise investigation of nuclear and magnetic structures requires instruments at large-scale facilities. These kind of instruments are located at synchrotron radiation and neutron sources. During this thesis several instruments have been used. For the powder experiments the high-resolution X-ray powder diffractometer (11-BM)<sup>3</sup> has been used. The powder sample has been measured at the diffuse neutron scattering spectrometer (DNS)<sup>4</sup> and at the high resolution neutron powder diffractometer (BT-1)<sup>5</sup>. The investigations of the magnetization profile of thin films have been done at the Polarized Beam Reflectometer (PBR)<sup>5</sup> and at the Magnetic Reflectometer with high incident angle (MARIA)<sup>4</sup>.

### 5.3.1 High-Resolution X-Ray Powder Diffractometer (11-BM)

High-resolution X-ray Powder Diffractometry at the Advanced Photon Source of the Argonne National Laboratory (APS) was performed at 11-BM at APS via Mail-In Proposal to analyze LSFO powder in order to determine structural changes accompanying the magnetic and electronic phase transitions. The expected changes are very small. Those small structural changes make it necessary to use highly monochromatic radiation with a very high photon flux in order to see small splittings of reflections and even reflections with very low intensity. Due to the small wavelength the accessible  $Q$  range is large and higher order reflections can be analyzed.

An overview of the experiment is given in [82]. As the experiment is a Mail-In experiment the usable temperature range was limited to temperatures between 100 and 300 K. The

<sup>3</sup>Advanced Photon Source at the Argonne National Laboratory, Argonne (USA)

<sup>4</sup>Heinz Maier-Leibnitz Zentrum at the FRMII, Garching (D)

<sup>5</sup>NIST Centre for Neutron Research, Gaithersburg (USA)

fully linear polarized beam with a size of  $0.5 \times 1$  mm has a wavelength of  $0.41418(1)$  Å. The detector covers an angle range from  $0.5$  to  $50^\circ$ , and a maximum available  $Q$  value of  $12.8 \text{ \AA}^{-1}$  follows.

### 5.3.2 Diffuse Neutron Scattering Spectrometer (DNS)

The cold neutron time-of-flight Diffuse Neutron Scattering Spectrometer (DNS) at the Heinz Maier-Leibnitz Zentrum (MLZ) (Fig. 5.11) is a versatile instrument which can be used for powder analysis in order to separate nuclear coherent, nuclear spin incoherent, and magnetic scattering contributions. DNS is a high intensity instrument with medium resolution, which has been used at a wavelength of  $3.3$  Å and  $4.5$  Å, respectively. With relatively large wavelength a  $Q$  value up to  $3.5 \text{ \AA}^{-1}$  was achievable which is optimized for measuring the large magnetic unit cells of LSFO, for instance.

The incoming neutron beam is monochromatized by a double-focusing monochromator and polarized by supermirror-based polarizer. The spins can then be manipulated by a flipper followed by a set of orthogonal  $xyz$ -coils. The spin can thus be set in any direction. The wide-angle polarization analysis is achieved by using 24 units of polarization analyzers simultaneously [83,84]. A closed-cycle cryostat was used to cool the sample between  $5$  K and  $300$  K.

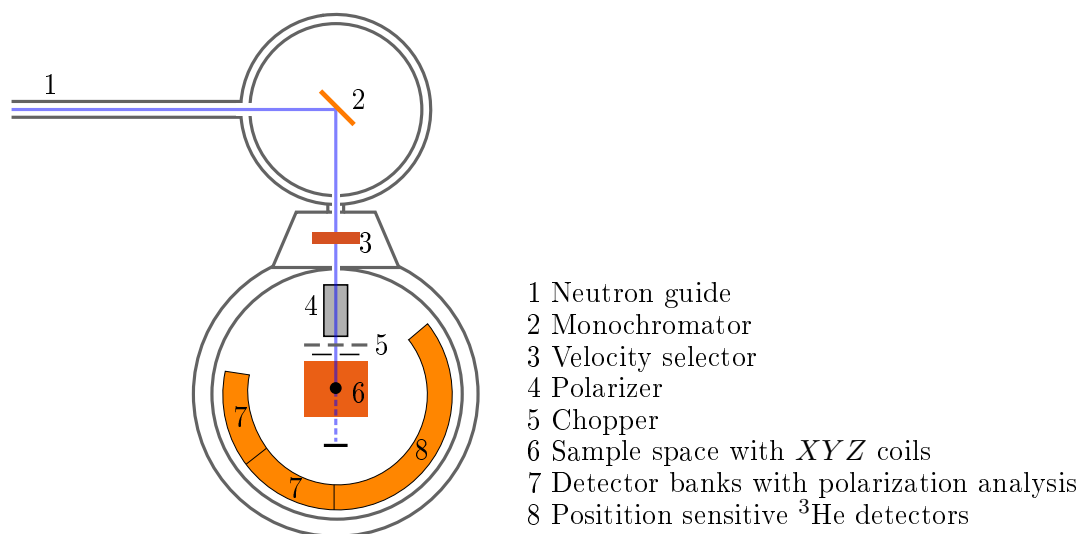


**Figure 5.11:** Schematic drawing of the DNS. Adapted from [83].

### Separation of coherent, spin incoherent, and magnetic scattering

The DNS supports  $xyz$ -polarization analysis which enables one to separate coherent, spin incoherent, and magnetic scattering cross sections. Polarization analysis is necessary to separate magnetic and nuclear reflections if they overlap or to separate nuclear and magnetic diffuse scattering over a large  $Q$  range, for instance. This section introduces the idea and theory of the  $xyz$ -separation briefly.

A common method for polarization analysis is the  $\parallel - \perp$  method [85]. For this method the polarization has to be aligned parallel and perpendicular to the scattering vector. Taking the difference of the different contributions under consideration of non-spin-flip and spin-flip scattering, one separates the magnetic scattering from the other contributions like nuclear coherent or spin incoherent scattering. But this method is based on the measurement with a single detector. The need to rotate the polarization into these two directions makes an application together with an area detector impossible. For such a detector the angle between polarization and scattering changes in dependence on the position of the detector within the multidetector.

In [86] a generalization to the  $xyz$ -difference method is shown. In Fig. 5.12 the scattering geometry of the DNS experiment is depicted. The principle of this generalization is to

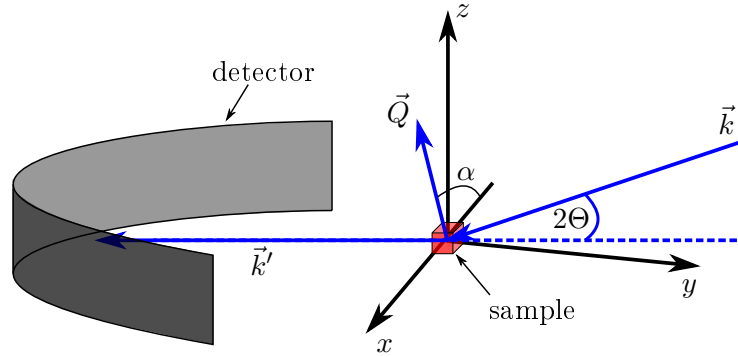


**Figure 5.12:** DNS scattering geometry.  $\vec{Q}$  lies in the  $x$ - $y$ -plane and  $\alpha$  is the angle between the  $x$ -axis and  $\vec{Q}$ .

consider the neutron polarization in  $x$ ,  $y$ , and  $z$  direction and to measure the non-spin-flip and spin-flip intensities of each polarization state. With the unit vectors  $\vec{e}_x$ ,  $\vec{e}_y$ , and  $\vec{e}_z$  along  $x$ ,  $y$ , and  $z$ , respectively, the polarization of the neutron can be written as

$$\vec{P} = P_x \vec{e}_x + P_y \vec{e}_y + P_z \vec{e}_z.$$

For a powder with collinear magnetization the magnetic cross section becomes simpler, because the correlation functions are

$$\langle\langle M_x M_x \rangle\rangle = \langle\langle M_y M_y \rangle\rangle = \langle\langle M_z M_z \rangle\rangle,$$

whereas the mixed ones

$$\langle\langle M_x M_z \rangle\rangle, \langle\langle M_x M_y \rangle\rangle, \langle\langle M_z M_y \rangle\rangle$$

are zero [86]. One gets six equations, which include all kinds of scattering, and includes nuclear coherent, nuclear incoherent, nuclear spin incoherent, and magnetic scattering cross-sections. The spin-flip cases can be written as

$$\frac{\partial \sigma_{\uparrow\downarrow}^x}{\partial \Omega \partial \omega} = \frac{1}{2} \frac{\partial^2 \sigma_{\text{mag}}}{\partial \Omega \partial \omega} (\cos^2 \alpha + 1) + \frac{2}{3} \frac{\partial^2 \sigma_{\text{inc}}^{\text{spin}}}{\partial \Omega \partial \omega}, \quad (5.1)$$

$$\frac{\partial \sigma_{\uparrow\downarrow}^y}{\partial \Omega \partial \omega} = \frac{1}{2} \frac{\partial^2 \sigma_{\text{mag}}}{\partial \Omega \partial \omega} (\sin^2 \alpha + 1) + \frac{2}{3} \frac{\partial^2 \sigma_{\text{inc}}^{\text{spin}}}{\partial \Omega \partial \omega}, \quad (5.2)$$

$$\frac{\partial \sigma_{\uparrow\downarrow}^z}{\partial \Omega \partial \omega} = \frac{1}{2} \frac{\partial^2 \sigma_{\text{mag}}}{\partial \Omega \partial \omega} + \frac{2}{3} \frac{\partial^2 \sigma_{\text{inc}}^{\text{spin}}}{\partial \Omega \partial \omega}, \quad (5.3)$$

whereas the non-spin-flip contributions are expressed as

$$\frac{\partial \sigma_{\uparrow\uparrow}^x}{\partial \Omega \partial \omega} = \frac{1}{2} \frac{\partial^2 \sigma_{\text{mag}}}{\partial \Omega \partial \omega} \sin^2 \alpha + \frac{1}{3} \frac{\partial^2 \sigma_{\text{inc}}^{\text{spin}}}{\partial \Omega \partial \omega} + \frac{\partial^2 \sigma_{\text{coh}}}{\partial \Omega \partial \omega} + \frac{\partial^2 \sigma_{\text{inc}}^{\text{nuc}}}{\partial \Omega \partial \omega}, \quad (5.4)$$

$$\frac{\partial \sigma_{\uparrow\uparrow}^y}{\partial \Omega \partial \omega} = \frac{1}{2} \frac{\partial^2 \sigma_{\text{mag}}}{\partial \Omega \partial \omega} \cos^2 \alpha + \frac{1}{3} \frac{\partial^2 \sigma_{\text{inc}}^{\text{spin}}}{\partial \Omega \partial \omega} + \frac{\partial^2 \sigma_{\text{coh}}}{\partial \Omega \partial \omega} + \frac{\partial^2 \sigma_{\text{inc}}^{\text{nuc}}}{\partial \Omega \partial \omega}, \quad (5.5)$$

$$\frac{\partial \sigma_{\uparrow\uparrow}^z}{\partial \Omega \partial \omega} = \frac{1}{2} \frac{\partial^2 \sigma_{\text{mag}}}{\partial \Omega \partial \omega} + \frac{1}{3} \frac{\partial^2 \sigma_{\text{inc}}^{\text{spin}}}{\partial \Omega \partial \omega} + \frac{\partial^2 \sigma_{\text{coh}}}{\partial \Omega \partial \omega} + \frac{\partial^2 \sigma_{\text{inc}}^{\text{nuc}}}{\partial \Omega \partial \omega}. \quad (5.6)$$

Six channels are necessary to measure the separation of nuclear, nuclear spin incoherent, and magnetic contributions. Now it is possible to calculate and separate all scattering contributions, but the isotropic nuclear incoherent part cannot be separated from the nuclear coherent part with this method. Therefore eq. 5.1 to eq. 5.6 can be solved to

$$\begin{aligned} \frac{1}{2} \frac{\partial^2 \sigma_{\text{mag}}}{\partial \Omega \partial \omega} &= 2 \left( \frac{\partial \sigma_{\uparrow\downarrow}^x}{\partial \Omega \partial \omega} + \frac{\partial \sigma_{\uparrow\downarrow}^y}{\partial \Omega \partial \omega} - 2 \frac{\partial \sigma_{\uparrow\downarrow}^z}{\partial \Omega \partial \omega} \right) \\ &= 2 \left( -\frac{\partial \sigma_{\uparrow\uparrow}^x}{\partial \Omega \partial \omega} - \frac{\partial \sigma_{\uparrow\uparrow}^y}{\partial \Omega \partial \omega} + 2 \frac{\partial \sigma_{\uparrow\uparrow}^z}{\partial \Omega \partial \omega} \right) \end{aligned}$$

$$\frac{\partial^2 \sigma_{\text{inc}}^{\text{spin}}}{\partial \Omega \partial \omega} = \frac{3}{2} \left( -\frac{\partial \sigma_{\uparrow\downarrow}^x}{\partial \Omega \partial \omega} - \frac{\partial \sigma_{\uparrow\downarrow}^y}{\partial \Omega \partial \omega} + 3 \frac{\partial \sigma_{\uparrow\downarrow}^z}{\partial \Omega \partial \omega} \right).$$

However, one cannot distinguish between isotope incoherent and coherent scattering, and the combination can be written as

$$\frac{\partial^2 \sigma_{\text{coh}}}{\partial \Omega \partial \omega} + \frac{\partial^2 \sigma_{\text{inc}}^{\text{isotope}}}{\partial \Omega \partial \omega} = \frac{\partial \sigma_{\uparrow\uparrow}^z}{\partial \Omega \partial \omega} - \frac{1}{2} \frac{\partial^2 \sigma_{\text{mag}}}{\partial \Omega \partial \omega} - \frac{1}{3} \frac{\partial^2 \sigma_{\text{inc}}^{\text{spin}}}{\partial \Omega \partial \omega}.$$

In this work this method was used to investigate magnetic diffuse scattering, which arises from states with shorter correlation length and is expected to appear close to phase transitions.

Firstly, without this method it would not be possible to distinguish between nuclear and magnetic diffuse scattering. Secondly, a separation of magnetic from nuclear diffraction peaks has also been done.

DNS is very helpful to separate different scattering contributions, but has only limited achievable  $Q$  range. In order to investigate the crystal and magnetic structure thoroughly, especially for large  $\vec{Q}$  values, high-resolution powder diffractometry is necessary. This measurement has been performed on the BT-1 diffractometer at NIST Centre for Neutron Research (NCNR).

### 5.3.3 High Resolution Powder Diffractometer (BT-1)

The High Resolution Powder Diffractometer BT-1 at NCNR has been used for powder analysis in order to measure also a probably subtle lowering of the symmetry, which could be expected for the low temperature phase of LSFO as discussed later. This requires the separation of reflections for high scattering angles. Neutrons in contrast to X-rays have a constant form factor for nuclear scattering, which provides the advantage of being able to measure also high-order reflections. Additionally, neutron powder diffraction can be used to measure magnetic properties of the powder. Both were used in order to get detailed information about the LSFO powder.

For the purpose of observing high order reflections a Ge (733) monochromator is used which provides neutrons with a wavelength of  $1.197 \text{ \AA}$  and the highest resolution for the high  $Q$  range. The instrument uses 32 detectors which cover a  $2\theta$  range of  $0^\circ$  to  $167^\circ$ , and thus  $Q_{\text{max}}$  is  $10.4 \text{ \AA}^{-1}$ . A closed-cycle refrigerator provides the possibility to reach temperatures between room temperature and 10 K. A detailed description of the instrument can be found in [87].

The experiment was provided through the Mail-In sample service. The executive scientist for measurements and data acquisition was Hui Wu from NCNR.

### 5.3.4 Magnetic Reflectometer with high Incident Angle (MARIA)

The magnetic reflectometer with high incident angle (MARIA) at MLZ was used for the analysis of the magnetization profile of the thin film samples. It is an instrument which is optimized for probing magnetic interface effects and magnetic layers down to subnanometer scale and is thus perfectly suitable for the intended investigations. A sketch of the experiment is given in Fig. 5.13 (a). The wavelength selection is done with a velocity selector that provides a wavelength within the range  $4.5 \text{ \AA} < \lambda < 14 \text{ \AA}$ . The width of the wavelength distribution is  $\frac{\Delta\lambda}{\lambda} = 0.1$ . MARIA also provides polarization of the neutrons for the investigation of magnetism as treated in Sec. 3.7. Polarization analysis is enabled by a wide angle  $^3\text{He}$  cell to distinguish between different scattering channels (non-spin-flip and spin-flip) in order to get information about the alignment of the in-plane magnetization. The detector is a position-sensitive two-dimensional  $^3\text{He}$  detector, which also allows the measurement of the diffuse scattering. Diffuse scattering contains information about the correlation length within the sample in either lateral or vertical direction. Several slits are used to collimate the beam [88].

The versatile sample environment provides sample cooling from 300 K to 5 K and magnetic fields up to 1.2 T.

Basically, MARIA has been used to measure the in-plane reversal of magnetization at 110 K, which is depicted in Fig. 5.14. As one has to consider the guide field direction, which ensures the neutron's polarization, only fields along the guide field can be applied, otherwise one loses the polarization of the neutrons. In general, it is not strictly true. It also depends on the sample properties, and one can have a non-adiabatic spin flip. Anyhow, it reduces the measurement to the part shown by the solid line in Fig. 5.14. Before the measurement the sample was saturated in positive field direction to  $M_s$ . A small and reversed field has been applied then. To probe the solid line part the field was

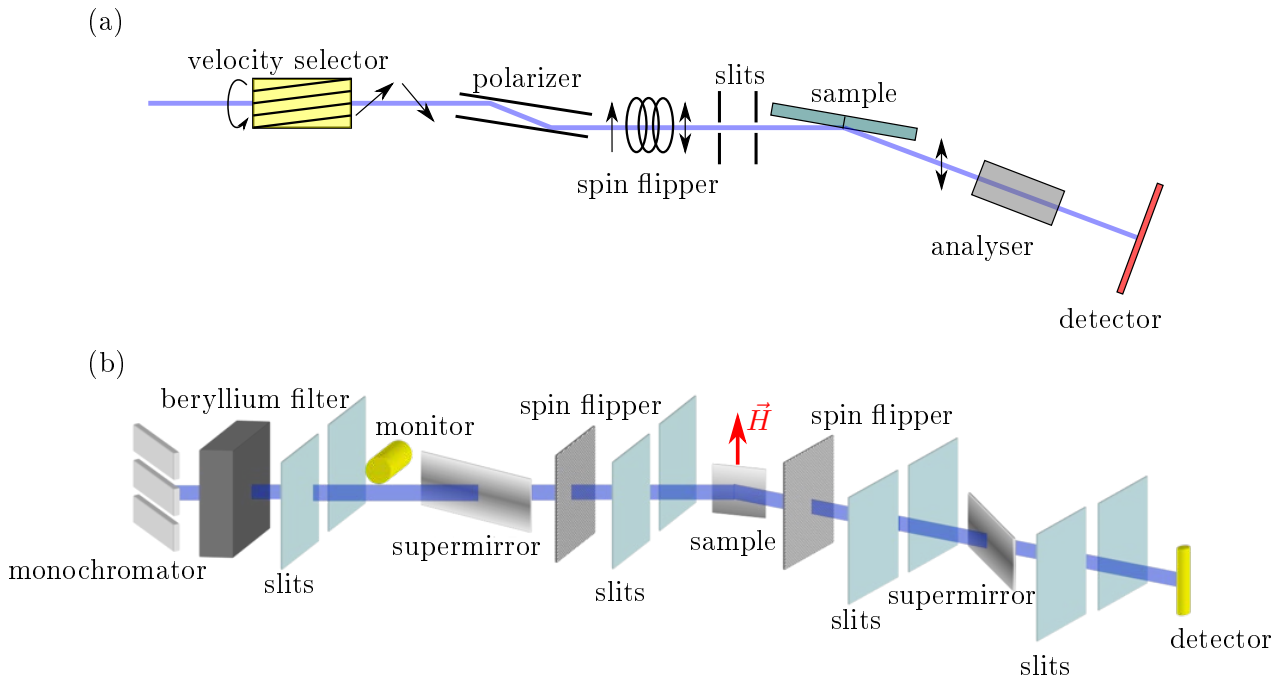


**Figure 5.13:** (a) Sketch of the MARIA reflectometer. The velocity selector determines the wavelength of the neutrons. Slits collimate the neutron beam before scattering from the sample. Polarization of the neutrons occurs in a polarizer, whereas the analyser is used for polarization analysis after the scattering event. A cryostat for cooling applications and a magnet are available. Adapted from [88]. (b) A drawing of the PBR experiment. The neutron beam is monochromatized and then polarized by a supermirror. A spin flipper allows one to flip the spin direction. After being scattered from the sample the neutrons are detected with a  $^3\text{He}$  detector. A supermirror is used for analyzing the polarization of the neutron beam. Taken from [89].

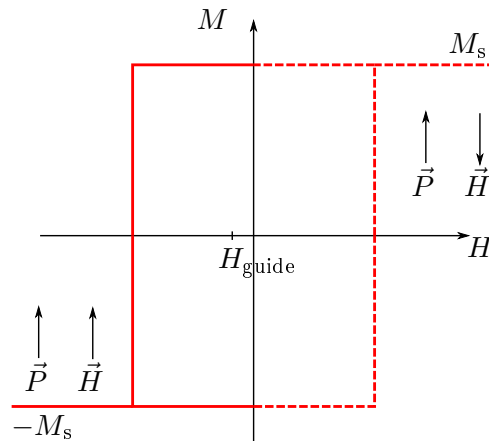


**Figure 5.14:** Half-hysteresis measurement performed with MARIA. To maintain the neutron polarization only the part shown by the solid line is accessible.

changed and the reflectivity for a fixed  $Q_z$  value was measured with polarization analysis in order to measure both the non-spin-flip and spin-flip channels.



### 5.3.5 Polarized Beam Reflectometer (PBR)

The second PNR instrument which was used was the Polarized Beam Reflectometer (PBR) at NCNR. A sketch of the instrument is depicted in Fig. 5.13 (b). PBR uses a pyrolytic graphite focusing monochromator followed by a beryllium filter, which suppresses the  $\lambda/2$  contamination. The used wavelength was  $4.75 \text{ \AA}$  with  $\frac{\Delta\lambda}{\lambda} = 0.03$ . Slit systems are used to collimate the beam. A supermirror polarizes the beam and a spin flipper is available to flip the neutron spin. The sample environment can be equipped with a closed cycle cryostat which enables measuring from 330 K to 10 K as well as magnetic fields parallel to the sample surface up to 0.75 T. For polarization analysis a second flipper and supermirror is installed. The detection of the scattered neutrons is done with a one dimensional  $^3\text{He}$  detector [89].

The PBR was mainly used to measure the temperature dependence of the reflectivity from 10 K to room temperature with polarized neutrons in order to determine the magnetic depth profile of the samples. As one uses a line detector, only the specular reflectivity can be measured. Information from diffuse scattering cannot be gained. The data reduction was done with beamline software which includes polarization correction and background subtraction.



## 6 Ordering phenomena in $\text{La}_{1/3}\text{Sr}_{2/3}\text{FeO}_3$ powder and thin films

The following chapter starts with an introduction of bulk and thin film LSFO, which includes an overview about the state of research.

The second part of this chapter deals with the work on LSFO powder samples, which includes sample preparation as well as characterization. The last part is about thin film growth and characterization. Developing thin film growth processes was a crucial part of this thesis. All work on developing thin film growth procedures of LSFO will then be transferred to the aforementioned heterostructures consisting of LSFO and LSMO.

### 6.1 $\text{La}_{1/3}\text{Sr}_{2/3}\text{FeO}_3$ and its versatility

LSFO with the chemical formula



is a versatile material which exhibits lots of interesting phenomena. It crystallizes in space group  $R\bar{3}c$  (see Fig. 2.3a) with the room temperature lattice parameters listed in Tab. 6.1. In a purely ionic picture of the valences, in Eq. 6.1, the Fe ion features a non-

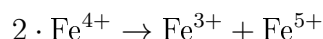
**Table 6.1:** Lattice parameters of LSFO with space group  $R\bar{3}c$  at room temperature from [23].

$a, b$ [Å]	$c$ [Å]	$V$ [Å <sup>3</sup> ]	$\alpha = \beta$ [°]	$\gamma$ [°]
5.4751(4)	13.415(2)	58.04(7)	90	120

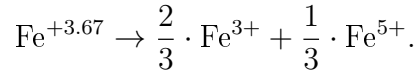
integer valence states, which means that LSFO must have two different iron valences, namely  $\text{Fe}^{3+}$  and  $\text{Fe}^{4+}$ .  $\text{Fe}^{+3.67}$  can then be written as

$$\text{Fe}^{+3.67} \rightarrow \frac{2}{3} \cdot \text{Fe}^{4+} + \frac{1}{3} \cdot \text{Fe}^{3+}.$$

This purely ionic model is reported by Battle et al. [90], for instance, and thus is assumed. Below a temperature of 200 K, the nominal  $\text{Fe}^{4+}$  disproportionates and the content of  $\text{Fe}^{4+}$  vanishes gradually. The disproportionation



occurs, which leads to



Mössbauer spectroscopy measurements at room temperature [90–92] and photoemission spectroscopy measurements [93] confirm the disproportionation of  $\text{Fe}^{4+}$ . In addition, the measurement was repeated with an in-house Mössbauer setup as a diploma thesis project<sup>1</sup>, and also showed that charge disproportionation takes place below 200 K. The  $\text{Fe}^{5+}$  size is small compared to  $\text{Fe}^{3+}$  and only appears under strongly oxidizing conditions [92]. Below 200 K charge ordering of the disproportionated charges sets in, which is shown in

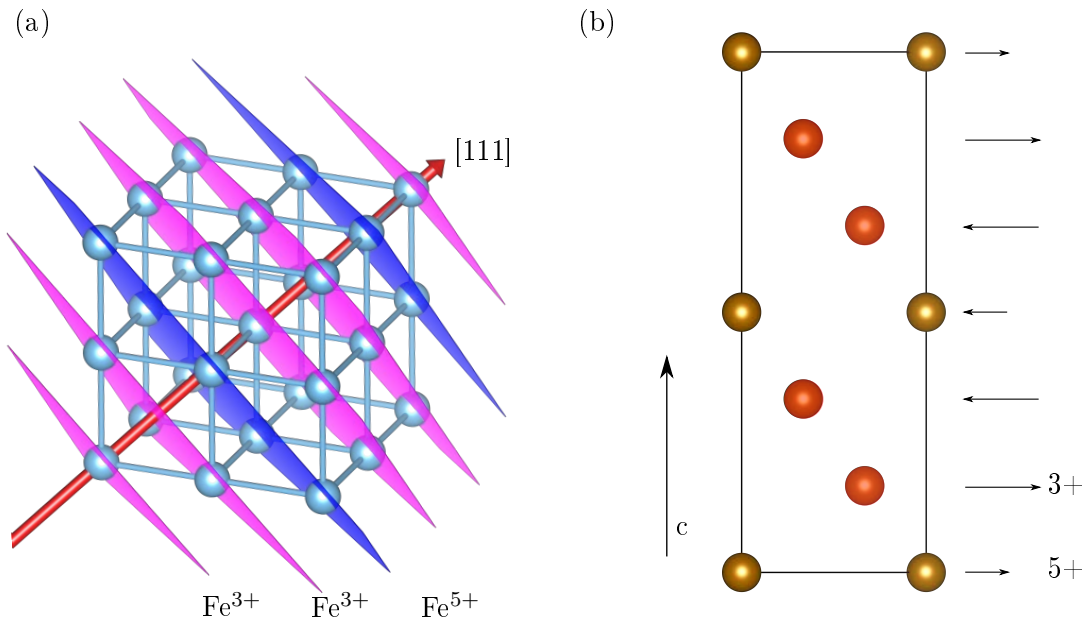


**Figure 6.1:** (a) Charge ordering of LSFO along the [111]-direction (red arrow) of the pseudo cubic unit cell. The ordering vector for the charge ordered phase is  $\vec{q}_{\text{CO}} = (1/3, 1/3, 1/3)$ . The colored planes perpendicular to the [111]-direction indicate the position of the  $\text{Fe}^{3+}$  and  $\text{Fe}^{5+}$ , respectively. (b) depicts the charge and magnetic ordering in space group  $R\bar{3}c$  projected onto the (010) plane. The arrows show the different spin states of  $\text{Fe}^{3+}$  and  $\text{Fe}^{5+}$ . Adapted from [94]. Sketches are generated with VESTA [14].

Fig. 6.1. Upon further cooling the charge ordering gradually develops [91] in the [111]-direction of the pseudo-cubic unit cell (a) or  $c$  direction of the parent space group  $R\bar{3}c$  (b). The sequence  $\dots\text{Fe}^{3+}\text{Fe}^{3+}\text{Fe}^{5+}\text{Fe}^{3+}\text{Fe}^{3+}\text{Fe}^{5+}\dots$  sets in, and thus the ordering vector is  $\vec{q}_{\text{CO}} = (1/3, 1/3, 1/3)$  written in terms of the pseudo cubic unit cell [95]. The charge ordering is accompanied by a Verwey Transition [95–97] which is a transition from a semiconducting to an insulating state, and is originally known from  $\text{Fe}_3\text{O}_4$  [26]. Fig. 6.2 shows a typical resistivity measurement of polycrystalline LSFO during cooling the sample from room temperature to 10 K. It shows a resistivity change of eight orders of magnitude from

<sup>1</sup>The measurement was part of Thomas Breuer’s diploma thesis from 2012. Measurement and data evaluation was done by Dr. Benedikt Klobes.

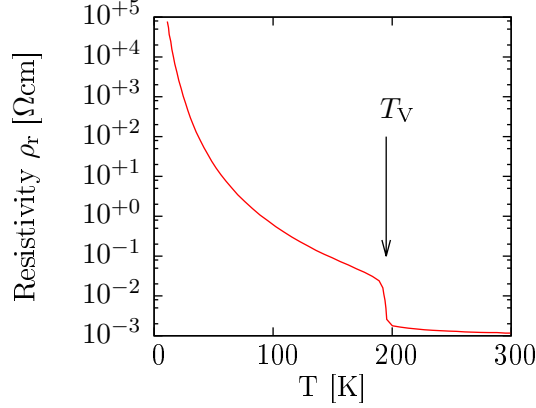


**Figure 6.2:** Resistivity measurement of polycrystalline LSFO. The measurement was performed while cooling the sample from room temperature to 10 K. Data taken from [96].

a semi-conducting to an insulating state with a significant jump at  $T_V$ . This transition point is called Verwey temperature.

Furthermore, at 200 K antiferromagnetic ordering sets in, whose transition temperature is known as Néel temperature  $T_N$ . According to Section 2.4, the coupling between different iron ions is mediated by an oxygen ion (superexchange or double exchange) in between and is either antiferromagnetic or ferromagnetic [98]. The superexchange leads to an antiferromagnetic interaction between homovalent iron ions, whereas the interaction for the heterovalent case is dominated by the double exchange and is ferromagnetic.

The antiferromagnetic order is developed in the pseudo cubic [111] - direction as the charge ordering and the ordering vector of it is  $\vec{q}_{AF} = (1/6, 1/6, 1/6)$  [94,95]. The spin order sequence is ...  $\uparrow\downarrow\downarrow\uparrow\uparrow$  ... and can be easily explained by considering the different magnetic interactions between the iron ions.

Under a cubic environment in crystal field theory (Sec. 2.2) the fivefold degenerate  $d$ -orbitals split into a twofold degenerate  $e_g$  and a threefold degenerate  $t_{2g}$  orbital. As the Hund's exchange energy is still dominating compared to the crystal field splitting,  $\text{Fe}^{3+}$  has the configuration  $t_{2g}^3 e_g^2$  and  $\text{Fe}^{5+}$  has  $t_{2g}^3$ . Besides the high-spin state,  $\text{Fe}^{3+}$  can also exhibit a low-spin configuration  $t_{2g}^5$ , which sets in for high crystal field splitting energies. In LSFO  $\text{Fe}^{3+}$  is in the high-spin state [92].

Mostly, charge ordering is caused by a competition between the Coulomb energy of localized electrons and the kinetic energy of them as described by Mott and Friedman [99] for  $\text{Ti}_3\text{O}_4$ , for instance. Mizokawa et al. [100] and McQueeney et al. [98] proposed that the magnetic interactions in the LSFO system drive the charge ordering transition. Inelastic neutron scattering on powder was performed by McQueeney et al. in order to determine the ferromagnetic exchange coupling constant ( $J_F$ ) between  $\text{Fe}^{3+}$ - $\text{Fe}^{5+}$  pairs and the antiferromagnetic exchange ( $J_{AF}$ ) between  $\text{Fe}^{3+}$ - $\text{Fe}^{3+}$  pairs. They found that the system fulfills the criterion

$$\left| \frac{J_F}{J_{AF}} \right| = 1.5 > 1$$

for charge ordering driven by magnetic interactions. They explain this behavior with

an appreciable hole density on the oxygen sites, which screens the intersite Coulomb interaction significantly and only the magnetic exchange is stabilizing the charge ordering. Powder measurements have the disadvantage that reflections with same scattering angle are overlain, which makes a distinction impossible. Further detailed investigations require large single crystals for inelastic neutron scattering, which are not yet available. The only single crystals which are available in very good quality are thin films, which are single crystals stabilized by the substrate, but they are not suitable for inelastic neutron scattering, because of the small expected signal due to its low mass.

In this work LSFO is further investigated in order to get information about the magnetic diffuse scattering close to  $T_N$ . Magnetic diffuse scattering is expected while going from the disordered paramagnetic to the ordered antiferromagnetic state. For this purpose diffuse neutron scattering with  $xyz$  polarization analysis has been performed in order to separate nuclear, magnetic, and spin incoherent scattering contributions, because magnetic diffuse scattering is weak and coexists with the usually stronger nuclear diffuse scattering and spin incoherent scattering.

According to Woodward et al. [101] it is likely that the oxygen environment of the small-sized  $\text{Fe}^{5+}$  is distorted leading to a reduction of symmetry in the charge disproportionated state, which is in contrast to the behavior explained in literature, where no structural phase transition is reported. Woodward et al. focused on  $\text{CaFeO}_3$ , which also undergoes a charge disproportionation at 290 K. The effect of  $\text{Fe}^{5+}$  is expected to be very small and high-resolution neutron or X-ray diffraction is necessary in order to see very small distortions. Nevertheless they were able to confirm a small distortion of the  $\text{Fe}^{5+}$  environment by X-ray scattering. A lowering of the space group symmetry from orthorhombic (space group Pbnm) to monoclinic (space group  $\text{P}2_1/\text{n}$ ) takes place. The observed changes in structure are marginal, which makes a measurement extremely difficult. Woodward et al. spent a long beamtime at a synchrotron source to confirm their assumption of a lowered symmetry.

The same behavior is also expected for LSFO and leads to a systematical synchrotron X-ray and neutron diffraction study to determine the structural influences of the charge disproportionation.

Especially in recent years an increased interest in LSFO **thin films** could be observed in literature. Sichel-Tissot et al. [102] showed that the charge ordering remains stable in [111] direction of the pseudo-cubic unit cell for thin films grown on STO via MBE technique. Synchrotron radiation has been used by them in order to measure the  $(\frac{4}{3} \frac{4}{3} \frac{4}{3})$  charge ordering reflection of two thin films with different thickness and oxygen content. The expected reflection appears below  $T_{\text{CO}}$ , and increases in intensity while further cooling. Both thin films show the same ordering direction in spite of their different oxygen saturation levels. From this the authors followed that the charge ordering is very stable and cannot be influenced easily.

A Verwey transition and a magnetoresistance effect are also measurable in LSFO thin films [40, 97]. The influence of thickness [103] and stoichiometry [104] on the Verwey transition has been systematically investigated recently by Minohara et al. and Xie, respectively. Fig. 6.3 (a) shows the temperature dependence of the Verwey transition of LSFO grown on a STO substrate with varying thickness. Above the critical thickness of 200 Å a Verwey transition can be observed, but thicker layers exhibit a more pronounced

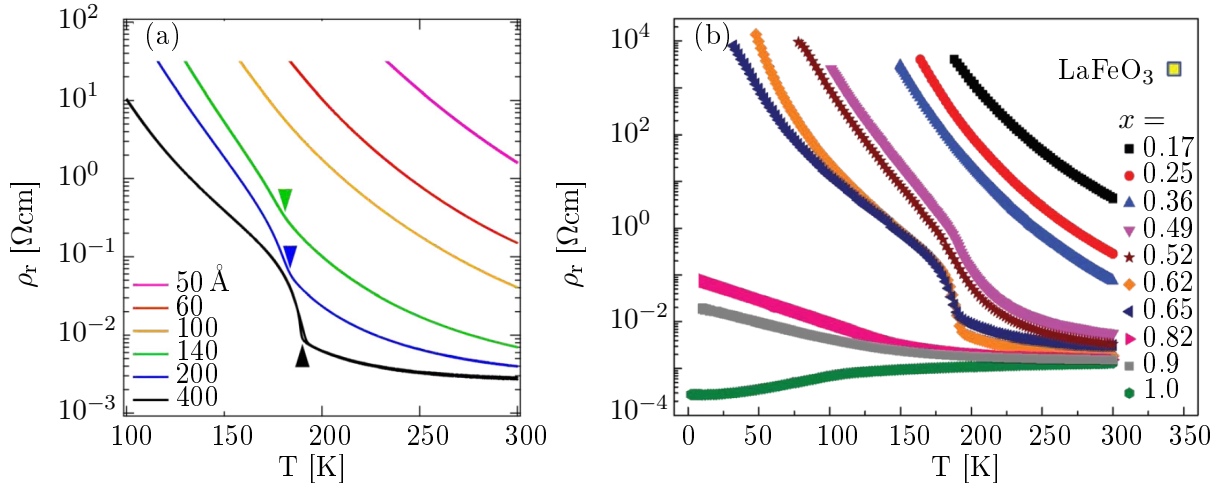


**Figure 6.3:** (a) depicts the thickness dependence of the resistivity measured on a LSFO thin film grown on STO. Reprinted from [103], with the permission of AIP publishing. Above the critical thickness of 200 Å a transition can be observed. In contrast (b) shows resistivity measurements of  $\text{La}_{1-x}\text{Sr}_x\text{FeO}_3$  grown on STO. Reprinted figure with permission from [104]. Copyright (2014) by the American Physical Society. A clear effect of the stoichiometry is visible, already a small deviation from  $x = 0.65$  leads to a smearing of the Verwey transition.

transition. This means that the jump at  $T_V$  is significantly larger. Furthermore, thin films with low thickness are always insulating and do not show a Verwey transition.

In Fig. 6.3 (b) the influence of stoichiometry on the resistivity is depicted. The strontium content  $x$  has also a strong influence on the behavior of the system regarding the semiconductor to insulator transition. Small deviations from  $x = 0.65$  influence the transition itself and the Verwey temperature  $T_V$ , which is shifted to lower temperatures for the case of an excess of strontium. Within the range  $0.62 < x < 0.90$  a clear Verwey transition can be observed. For high strontium contents the thin film stays metallic or semiconducting, whereas low  $x$  leads to insulating behavior over the measured temperature range.

It will be shown that getting the proper stoichiometry and good quality during developing growth procedures of thin films is a challenge. The layers are sensitive to their growth parameters especially regarding the correct stoichiometry and thickness. This has to be taken into account seriously and is further discussed at a later time.

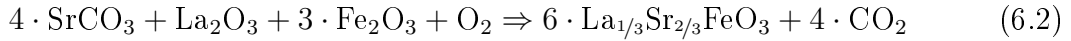
## 6.2 Powder study

A prerequisite, and treated initially, was the preparation of single phase LSFO powder, but the main focus lies on the investigation of the crystalline structure, as well as the magnetic properties. The size of a  $\text{Fe}^{5+}$  ion is small compared to the  $\text{Fe}^{3+}$  ions, and an influence on the crystalline symmetry according to Woodward et al. [101], who found a symmetry lowering due to  $\text{Fe}^{5+}$  ions in  $\text{CaFeO}_3$ , is assumed. To prove the crystal symmetry X-ray synchrotron and neutron powder measurements were performed at 11-BM@APS and BT-1@NCNR via Mail-In sample measurement service. Diffuse magnetic scattering was investigated at DNS@MLZ.

### 6.2.1 Sample preparation

The powder preparation process used for sample preparation is mainly adopted from Park et al. [105] and from Thomas Breuer<sup>2</sup>. The aim of the optimization is to achieve a stoichiometric and structurally single-phase powder.

To achieve this, the following solid state reaction



has been used. The process shown in Fig. 6.4 has been used to prepare single-phase powder. Firstly, it is necessary

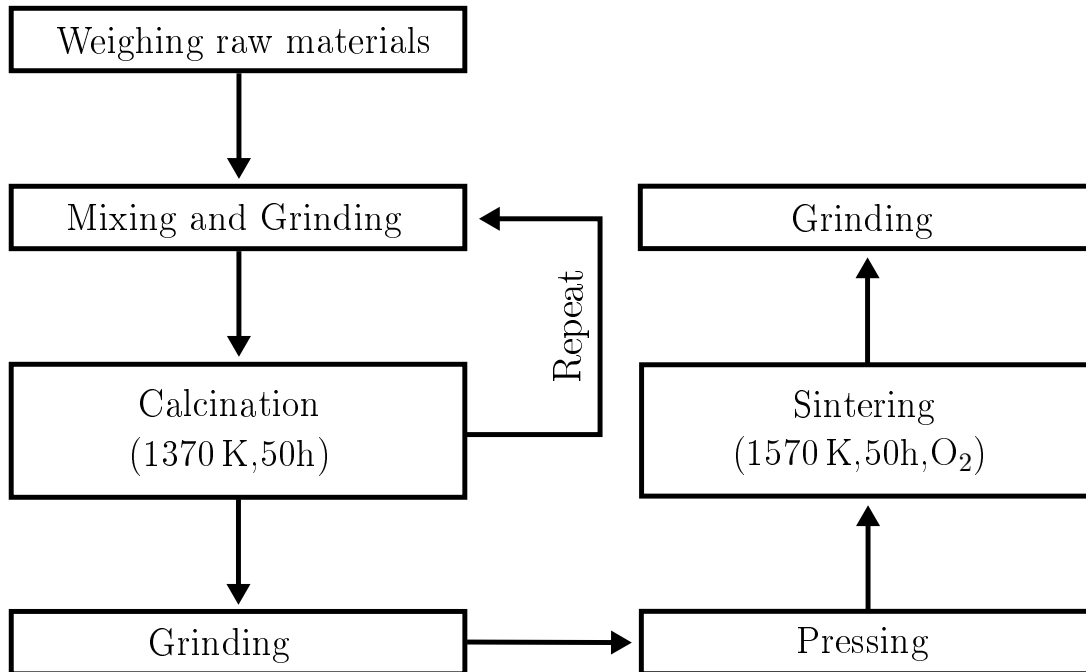


**Figure 6.4:** Process steps for powder preparation. To prepare high quality powder several calcination and sintering steps are necessary. The calcination took place under ambient pressure, whereas the sintering was done under a continuous oxygen flow.

to calculate the desired weight percent, which are listed in Tab. 6.2.

**Table 6.2:** Calculated molar masses and weight percent of the required starting materials.

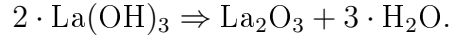
Compound	molar mass [u]	mass [weight-%]
$\text{La}_2\text{O}_3$	325.809	23.35
$\text{SrCO}_3$	147.629	42.32
$\text{Fe}_2\text{O}_3$	159.688	32.33

Before mixing the starting materials in a proper ratio it is necessary to dry the starting materials to ensure the correct weight percent. Especially,  $\text{La}_2\text{O}_3$  hydrogenates easily

<sup>2</sup>diploma thesis, 2011



under air and has to be heated to 1170 K under ambient conditions to initiate the chemical reaction



To prevent the  $\text{La}_2\text{O}_3$  from re-hydrogenation the weighing process has to be done at 470 K. All other compounds have been dried at 400 K.

After weighing the starting materials precisely with regard to Tab. 6.2, the resulting powder has to be mixed and ground for two hours in a ball mill. A subsequent 50 h calcination process at 1370 K in air at atmospheric pressure in an alumina crucible initiate the solid state reaction 6.2. To ensure that the solid state reaction runs completely it

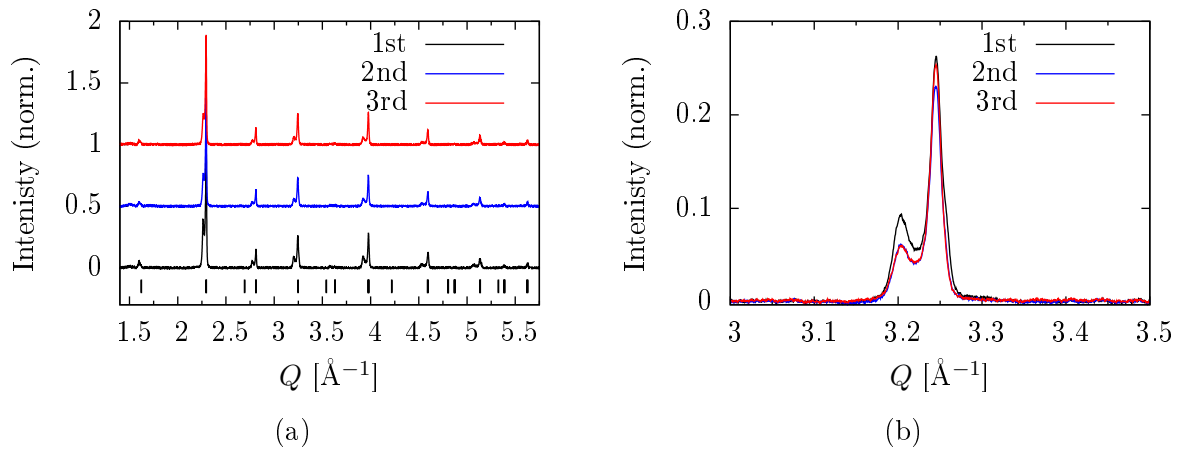


**Figure 6.5:** (a) Measured X-ray powder data after each calcination step. For a better visibility the data sets are shifted along the  $y$ -axis. The vertical markers indicate the theoretically calculated peak positions of the expected space group  $R\bar{3}c$ . (b) A zoom on the (2-24) reflection in order to see the changes of each calcination step in detail.

is necessary to repeat the grinding and calcination process several times until further treatment cannot improve the result. The diffractometry data after each calcination steps is shown in Fig. 6.5a. A zoom on a selected reflection is shown in Fig. 6.5b. The double reflection means, that the powder after the calcination steps is not single phase, and the structure does not fit to the expected symmetry. It was not possible to identify the additional phase, but after the sintering the sample is single phase and no need for further analysis was seen.

A significant change between the first and second calcination step is present, which means that the additional phase slowly vanishes. A further calcination step cannot improve the result compared to the second step. Thus, two calcination steps are sufficient, but a third step is recommended to ensure that the calcination was already completed.

A sintering step was done in order to get a single phase powder. It requires that the powder is pressed to pellets to increase the density of the material, which supports the solid state reaction, as diffusion between grains is significantly more likely. The sintering process was performed at 1570 K for 50 h in a tube furnace while a continuous oxygen flow ensures oxygen saturation of the material.

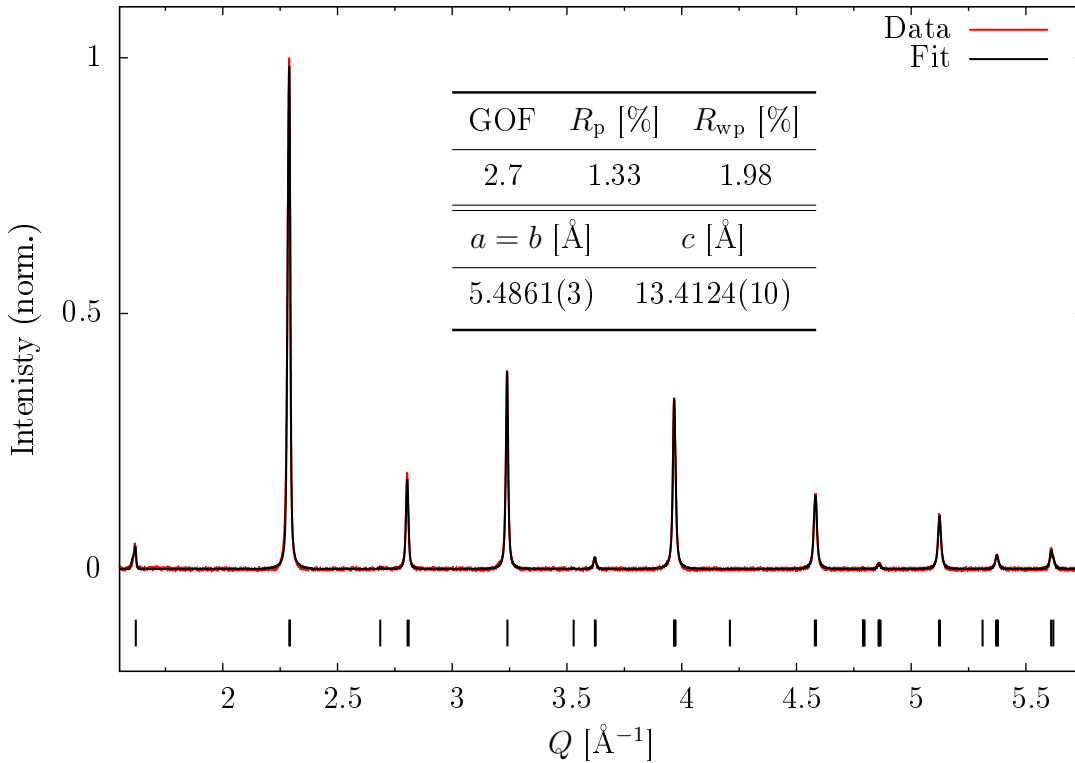


**Figure 6.6:** Powder XRD measurement at room temperature and the Le Bail fit (see section 3.4) after sintering. The preparation process leads to a single phase crystalline powder with the expected space group  $R\bar{3}c$ . The parameters obtained from the fit are listed in the table. They confirm the goodness of the fit. The lattice parameters are also shown.

The sintered pellets were then pestled and grinded to get a homogeneous powder. The room temperature measurement and the Le Bail fit done with Jana2006 [49] is shown in Fig. 6.6. A single phase powder with the expected space group  $R\bar{3}c$  was successfully prepared. The goodness of fit and the  $R$  values, shown in the table in Fig. 6.6, are in region of a few percent and the profile function fits well to the measurement data.

In spite of confirming the expected crystalline structure with its single phase a stoichiometry analysis of the prepared powder was done. Two different methods were used in order to determine the amount of both, the metal or the oxygen atoms. The first has been done with atomic emission spectroscopy (ICP-OES), the latter one with infrared absorption spectroscopy (IAS). The chemical analysis was performed by ZEA-3:Analytics<sup>3</sup>. The relative error on the measurement is 20% for weight percent values lower 0.1%, and 3% for values above 1%, whereas values between 0.1% and 3% exhibit an error of 10%.

Tab. 6.3 shows the results of the stoichiometry analysis. The stoichiometry can be confirmed considering the measurement errors. Furthermore a tiny contamination is visible, which probably arises from the powder preparation itself. The contamination sources are the mortar, the ball mill, and the used crucible, for instance. But those contaminations are very small, and influences are not expected to be significant.

<sup>3</sup>Head of ZEA-3:Analytics and responsible person is Dr. Stephan Küppers.

**Table 6.3:** The weight percent results are listed in (a). The measurement was performed by ZCH-3:Analytics. Pt and Zr could be found as impurities which obviously arise from the preparation process, but are small enough to be neglected. (b) shows the result calculated for one chemical formula unit normalized to Fe.

(a)			(b)	
Element	weight-%	Method	Element	Content
Fe	26.2(8)	ICP-OES	Fe	1
La	21.7(7)	ICP-OES	La	0.333(10)
Sr	27.3(8)	ICP-OES	Sr	0.664(30)
O	22.8(1)	IAS	O	3.040(10)
Pt	0.16(2)	ICP-OES	Pt	0.0018(3)
Zr	0.05(1)	ICP-OES	Zr	0.0011(1)

## 6.2.2 Results

### Specific Heat

Measuring the specific heat of the powder is important for the further characterization of the powder. Phase transitions are accompanied by a change of the specific heat and this helps to characterize the transitions properly or to find further phase transitions. First one can introduce the heat capacity  $C$ , which is given by

$$C = \frac{\partial Q}{\partial T},$$

where  $\partial Q$  is the heat change of the sample,  $dT$  the temperature change caused by the heat change. Actually the sample environment plays a crucial role and one has to distinguish between  $C_p$  and  $C_V$ .  $C_p$  is the heat capacity under constant pressure, whereas  $C_V$  is measured under constant volume. For solid state materials one measures in principle  $C_p$ , because of the thermal expansion of the sample. But the volume change is rather small, and one can assume

$$C_p \approx C_V$$

in good approximation. Thus, the intrinsic energy of the system is

$$dU = \delta Q + \delta W = \delta Q,$$

with  $dV = 0 \rightarrow \partial W = 0$ . Expressed with the free energy one gets

$$C_p = \left. \frac{\partial Q}{\partial T} \right|_p = \frac{dU}{dT} = -T \frac{d^2 G}{dT^2}.$$

A first order transition, which is expected for the underlying system, exhibits a discontinuous first-order change of the free energy  $G$ . This means that the second-order derivative,

the heat capacity, shows a pole. Thus, a significant peak nearby the phase transition is expected and is connected to latent heat. From the measured heat capacity one can calculate the specific heat by normalizing to the sample mass.

The PPMS instrument has been used, whose introduction is given in section 5.2.5. A reliable sample measurement requires a perfect heat contact to the measurement platform. Here a fragment of a sintered pellet and powder were used, where only a poor heat contact could be achieved. Thus, the measurement data is damped, and the peak is not as pronounced as expected. The purpose of the specific heat characterization was to measure the whole temperature range from 5 to 300 K to ensure that there are no further than the expected magnetic and electronic phase transitions.

Both, powder or fragment, were fixed on the sample platform with Apiezon<sup>®</sup> N grease. Quantum design recommends using the N grease for temperatures below 200 K, because for temperatures above 215 K the grease starts to melt which gives an additional signal. With a pure grease measurement before adding the sample one tries to eliminate this contribution. A small signal always remains in the measurement data, and thus this range is not as reliable as desired. The H grease, which is usually recommended for temperatures above 200 K could not be used, because it was not possible to fix the sample tightly, especially for low temperatures, where the grease becomes hard and inflexible.

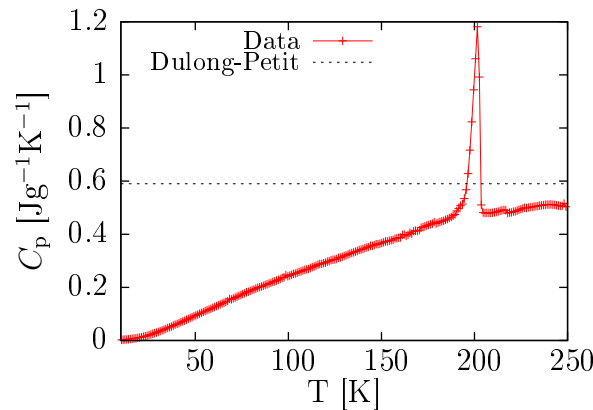


**Figure 6.7:** Specific heat of 1 mg LSFO. For temperatures above 215 K, the used Apiezon<sup>®</sup> N grease influenced the measurement. At 201.7(1) K a clear peak is visible, which is typical for a first order phase transition.

Fig. 6.7 shows a specific heat measurement of 1 mg LSFO powder. At 201.7(1) K a pole can be seen, which is characteristic for a first order phase transition. Between 215 K and 250 K the contribution of the used N grease is visible as mentioned. The measurement shows that no further peaks are visible leading to the conclusion that no further transitions like structural transitions appear between 10 K and 250 K. The dotted line in Fig. 6.7 is the value of the Dulong-Petit law  $c = 3R \cdot \frac{M_i}{N_i}$ , where  $R$  is the gas constant,  $M_i$  the molar mass, and  $N_i$  the number of atoms within one crystallographic unit cell. It is an upper limit for the phononic specific heat contribution, but does not consider the electron contributions like magnetization or conduction. One can see that the specific heat tends to approach the Dulong-Petit-law except in the peak region, and the difference between measurement and Dulong-Petit limit at high temperature is attributed to the incorrect determination of

the mass and the effects of the used grease. Furthermore the heat transport, especially in the pellet, is bad due to the grainy structure. As a consequence a quantitative evaluation is not meaningful, but also not necessary for the required purpose.

It could be shown that the LSFO powder shows a clear first order phase transition at 201.7(1) K. According to Battle et al. [90] oxygen deficiencies lead to a decrease of the transition temperature, and the transition temperature for a saturated sample is  $\approx 200$  K. However, this is in agreement with the characterized samples, and oxygen saturation has been reached. There are no hints for further phase transition between 10 K and 200 K in the specific heat data.

## Resistivity

The Verwey transition in LSFO has been measured with the PPMS system using the resistivity option with a 4-wire method. A sketch of the measurement principle is depicted in Fig. 6.8. As the determination of the resistivity cannot be performed on powder, a box shaped piece of sintered powder pellet was used. The dimensions of the sample are  $2.5 \times 4.5 \times 1.5 \text{ mm}^3$ . The derivatives  $\frac{d \log \rho_r}{dT}$  and  $\frac{d^2 \log \rho_r}{dT^2}$  were used in order to determine the transition temperatures, because on a log scale the transition is more clearly.

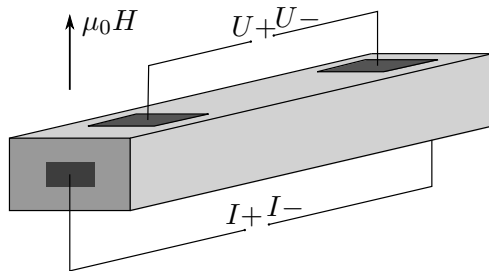


**Figure 6.8:** 4-wire measurement principle for determination of the resistivity of the sample. The measurement has been performed with the PPMS. The dimension of the measured sample is  $2.5 \times 4.5 \times 1.5 \text{ mm}^3$ .

Fig. 6.9a shows a resistivity measurement taken during cooling and warming of the sample. As common for first order phase transitions a thermal hysteresis is expected as confirmed for LSFO thin films by Ueno et al. [97]. It can be clearly seen that the transition temperature for both measurements varies significantly. The transition temperatures can be determined as 197(1) K and 203(1) K for cooling and warming, respectively. The thermal hysteresis is normal for first order transition, but possibly the measurement error on the transition temperature is large. As the sample mass (74 mg) and dimensions are rather large, an equilibrium state could be missed and the sample temperature did not correlate to the measured temperature due to poor thermal contact and poor heat transport between the

grains inside the sample. The chosen sample was the smallest possible with respect to placing electrical contacts properly.

As a sintered sample was used for the resistivity characterization intergranular effects influence the measurements, because hopping processes between micrograins in the sintered and disordered powder might increase the resistivity significantly [106]. Furthermore water, which can be diffused into the sample, influences the sample measurement. It freezes upon cooling and can change the grain distances and orientations, which would explain the slightly increased resistivity in the warming curve. This was measured after the cooling curve. Both transitions are not as abrupt as shown in Fig. 6.2 [96]. The jump reported by Ma [96] is ten times larger than observed here and the room temperature resistivity is two orders of magnitude lower. This could also be attributed to the porous and grainy

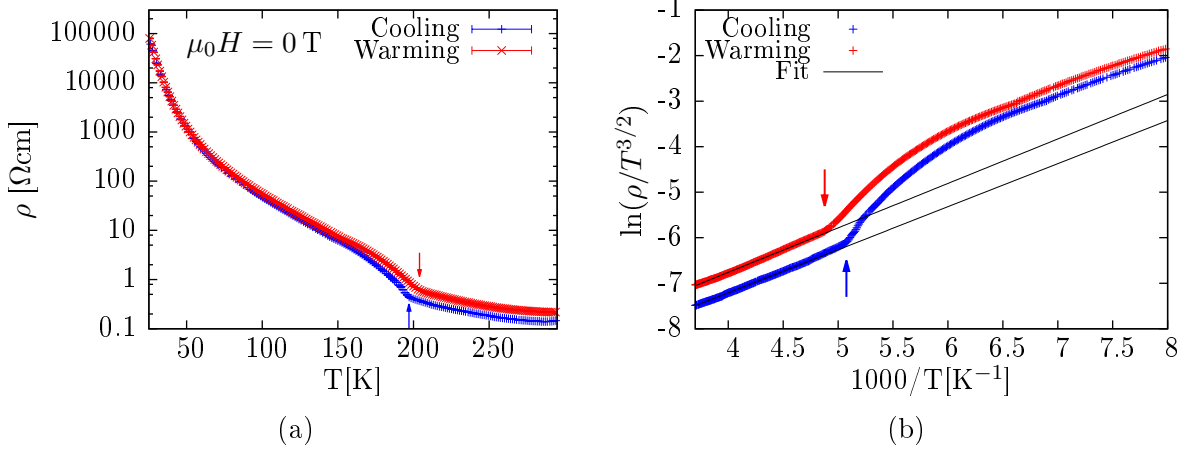


**Figure 6.9:** (a) shows two resistivity measurements. The red is measured during cooling, whereas the blue was measured during warming (b) depicts the fit to the measured data of the non-adiabatic polaron model for  $T > T_V$ . The colored arrows point to the determined transition temperatures.

structure of the sintered powder with the same reason as mentioned above. Nevertheless the transition temperature while warming corresponds to the transition temperature determined with the specific heat measurement.

It has been shown earlier that the desired stoichiometry, as well as the structure, could be confirmed. These reasons for changing the shape of the transition can be excluded. Nevertheless the measurement shown by Ma [96] shows the same resistivity change over 6.5 orders of magnitude within 300 K and 20 K. This encourages the assumption that micrograins in the porous material influence the resistivity measurement, which leads to a reduced change at the transition, and an increased absolute resistivity value. However, the relative change in resistivity stays the same.

The mechanism of conduction is attributed to a non-adiabatic small polaron model (Sec. 2.6) in which the temperature dependence of the resistivity has the form

$$\rho_r = \rho_{r0} T^{3/2} \exp\left(\frac{W_H}{k_B T}\right),$$

where  $W_H$  is the activation energy of the small polaron, and  $T$  the temperature.  $k_B$  is the Boltzmann constant. A variable-range hopping conductivity model in granular media was faulted after consideration of the thin film results, which show the same resistivity behavior, but for single crystalline samples. Fig. 6.9b shows the cooling and warming measurement data in a  $\ln(\rho_r/T^{3/2})$ - $1000/T$  plot with the fit for determination of the activation energy of the small polaron. For both, cooling and warming, the activation energy  $W_H$  can be calculated as 0.082(1) eV and 0.084(1) eV from the fitting parameter. At the transition temperature, marked with colored arrows, the conduction mechanism changes to a different behavior. This will be discussed in detail in section 6.3, where the conductivity behavior of films is discussed. The change in the underlying conductivity mechanism could be addressed to the set in of the charge and antiferromagnetic ordering, which reduces the hopping probability for electrons and leads to a highly insulating state.

## Magnetic properties

For the purpose of the magnetic characterization with the MPMS, the powder was filled into a small plastic capsule, which was then fixed in a drinking straw. Fig. 6.10a shows a magnetization measurement during warming and cooling in an applied field of 7 mT. The measurement data shows a significant thermal hysteresis, which is common for first order transitions. The transition temperatures are 197.8(5) K and 204.7(5) K for cooling and warming, respectively. This is in good agreement with the resistivity determined in the last part.

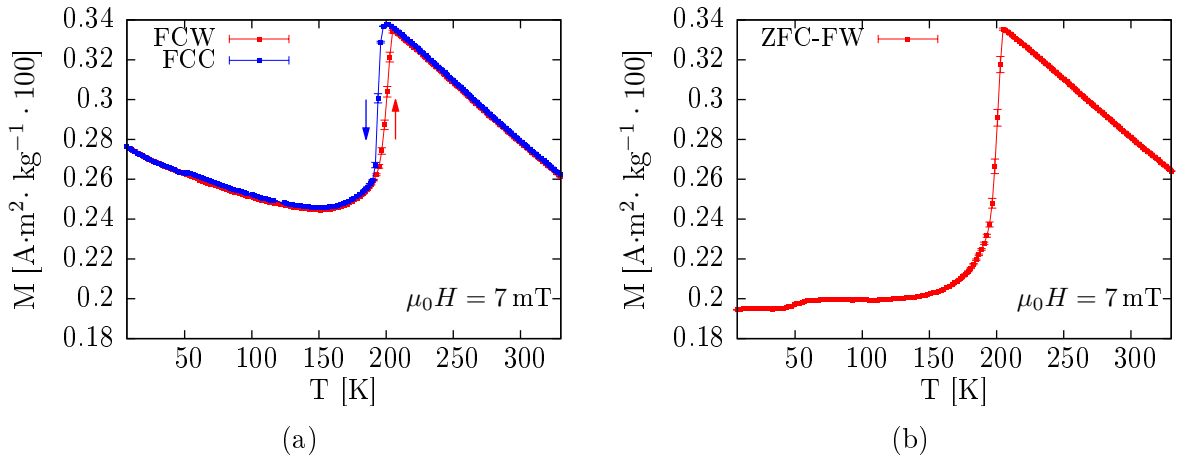


**Figure 6.10:** (a) shows a set of magnetization measurements. The blue curve has been measured during field-cooling (FCC) in 7 mT. After field-cooling in 7 mT the red curve was measured during field-warming (FCW) in the same field. A thermal hysteresis is present with transition temperature 197.8(5) K and 204.7(5) K, respectively. (b) is measured with an applied field while warming after zero-field cooling (ZFC-FW).

Below 150 K an increase of the magnetization can be observed, which is an indication of a structure with a ferromagnetic component or spin canting. Potentially, the charge order is not completely developed yet, which leads to a metallic behavior with double exchange interaction in parts of the sample. Thus, the ferromagnetic ordering is stabilized as a consequence of the applied external magnetic field. The measurement during warming after zero-field cooling does not show this behavior (Fig. 6.10b). Without an applied field the spins are mostly aligned antiferromagnetically and are frozen, and cannot be influenced by the magnetic field easily.

At 50 K the magnetization shows an additional step, but an additional phase transition can be excluded according to the specific heat measurements. It does not show any further transitions between 10 K and 200 K. Supposably, the spins are canted due to the distorted perovskite structure. Below 50 K the canting becomes reduced and a decreasing magnetization can be observed. The FCW measurement does not show this behavior, which is a consequence of frozen spins, which cannot be influenced by an applied field. Close to the phase transition both the FCC and FCW measurements become equal.

A Curie-Weiß behavior

$$\chi = \frac{C}{T + T_N},$$

with Curie constant  $C$ , and the Néel temperature  $T_N$ , cannot be seen above the phase transition within the measured temperature range. This means that the magnetization is not purely paramagnetic and short range correlation are still present, even at temperatures far above  $T_N$ . To reach the Curie-Weiß behavior it is necessary to measure at higher temperatures. Firstly, the MPMS does not allow higher temperatures. Secondly, and more crucial, heating of the powder leads to a loss of oxygen. Oxygen deficiencies highly influence the magnetic and electronic properties which was proposed in [91], for instance. In addition, an oxygen loss was evidenced by Thomas Breuer with thermogravimetry during a former diploma thesis project. The change of the magnetic properties changes the state of the system during the measurement and the result is not meaningful any more.

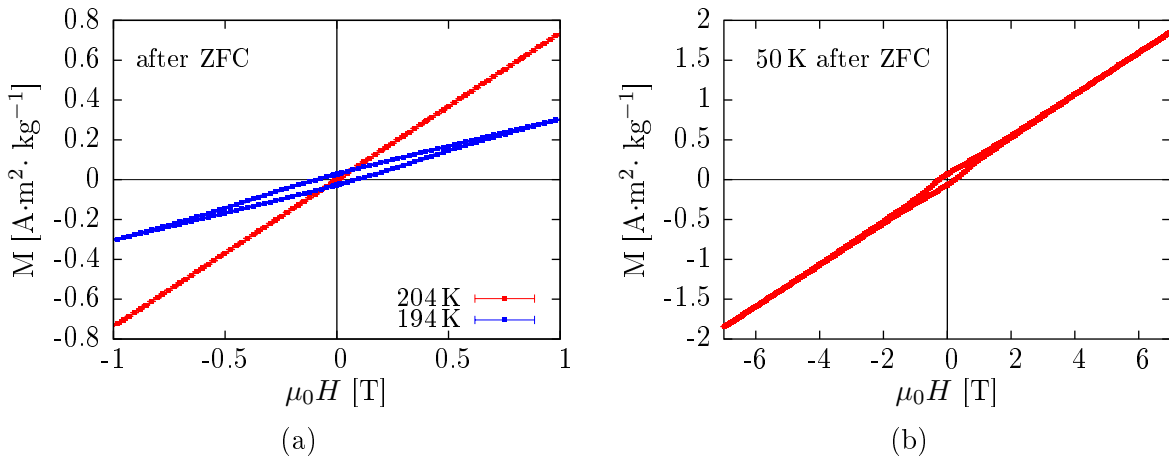


**Figure 6.11:**  $M - H$ -measurements at different temperatures after zero-field cooling. **(a)** shows a measurement right above (204 K) and below (194 K) the phase transition. **(b)** shows a measurement at 50 K for high magnetic fields, but saturation of the magnetization cannot be reached.

Fig. 6.11 shows  $M - H$ -measurements at different temperatures. Fig. 6.11a compares a measurement below and above the transition temperature. The measurement below the phase transition shows a significant hysteretic behavior. As discussed, the sample is not a simple antiferromagnet. It either exhibits a weakly canted antiferromagnetic ordering or a second magnetic phase with e.g. metallic double-exchange behavior or both. The coercive field is  $\mu_0 H_c = 0.2524$  T and the remanence is  $M = 0.068$   $\text{A}\cdot\text{m}^2\cdot\text{kg}^{-1}$ . The low remanence shows that the possible canting is likely unstable, but dominates the measurement under an applied field. At the transition temperature the measurement shows an almost closed loop and a purely paramagnetic behavior sets in as expected. The  $M - H$ -measurements correlate with the phase transition, which verifies that the additional magnetization is part of the antiferromagnetic phase and probably caused by spin canting. A parasitic



ferromagnetic phase was reported by Park et al. [105]. They attributed the spontaneous magnetization to oxygen deficiencies.

Fig. 6.11b shows a further measurement covering the maximum magnetic field range. The magnetic field of 7 T, which is the maximum field provided by the MPMS, is not sufficient to saturate the sample. This shows that the antiferromagnetic ordering is very stable, and a very high magnetic field is necessary to align all spins in field direction.

Whereas MPMS measurements provide the magnetization averaged over the whole sample, measurements with neutrons give access to the microscopic magnetic structure. An experiment at DNS at MLZ [83] has been done in order to determine the temperature dependent magnetic properties. The main advantage of this instrument is the  $xyz$ -polarization analysis, which enables one to separate the nuclear coherent, the magnetic, and the nuclear spin incoherent contributions from the scattering signal as introduced in Section 5.3.2. This separation is necessary to analyze pure magnetic diffuse scattering and the temperature dependency of the sublattice magnetization.

The separation has been performed with “dnsplot” which is part of the program “plotscript” [107]. The program considers standard measurements to do a flipping ratio correction and background subtraction as well as corrections of the detector efficiency. The standard samples are a NiCr alloy which is an isotope incoherent scatterer. It is suitable for the flipping ratio correction by comparing spin-flip and non-spin-flip channels, whose ratio is known. However, for a wavelength of  $3.3\text{\AA}$  NiCr is no more a purely incoherent scatterer, which influences the corrections as discussed later on. Vanadium as a spin incoherent scatterer produces isotropic scattering and is used to do a detector efficiency correction. These necessary standard measurements were done before introducing the sample to the sample environment.

In order to calculate the differential cross section from the scattering data the method of self-normalization with the sample’s spin incoherent scattering contribution has been used. With the incoherent scattering cross sections of each element taken from [108], the total incoherent cross section for one LSFO formula unit can be calculated to  $\sigma_{\text{LSFO}}^{\text{inc}} = 0.8167$  barn. The differential cross section is then determined by

$$\frac{d\sigma}{d\Omega_{\text{mag}}} = \frac{I_{\text{mag}}}{I_{\text{inc}}} \cdot \frac{\sigma_{\text{LSFO}}^{\text{inc}}}{4\pi}, \quad (6.3)$$

where  $I_{\text{mag}}$  is the separated magnetic intensity and  $I_{\text{inc}}$  the spin incoherent scattering intensity [53]. The self-normalization is very useful, because it additionally cancels out the sample mass and the related number of unit cells, respectively. Furthermore it is independent on the irradiated sample area, and it cancels out the influences of a varying incoming neutron beam flux which impinges on the sample. Eq. 6.3 can also be written with  $I_{\text{nuc}}$  instead of  $I_{\text{mag}}$  in order to get the differential cross section for the nuclear coherent scattering.

Fig. 6.12 depicts a 5 K measurements with separated spin incoherent, nuclear coherent, and magnetic contribution. The measurement was performed with a neutron wavelength of  $3.3\text{\AA}$ . According to Kirill Nemkovskiy (personal communication) not all appearing reflections are reliable. For  $Q$  values below  $0.5\text{\AA}^{-1}$  the measured intensity is strongly influenced by a shadowing effect from the beamstop, which affects the shape and intensity

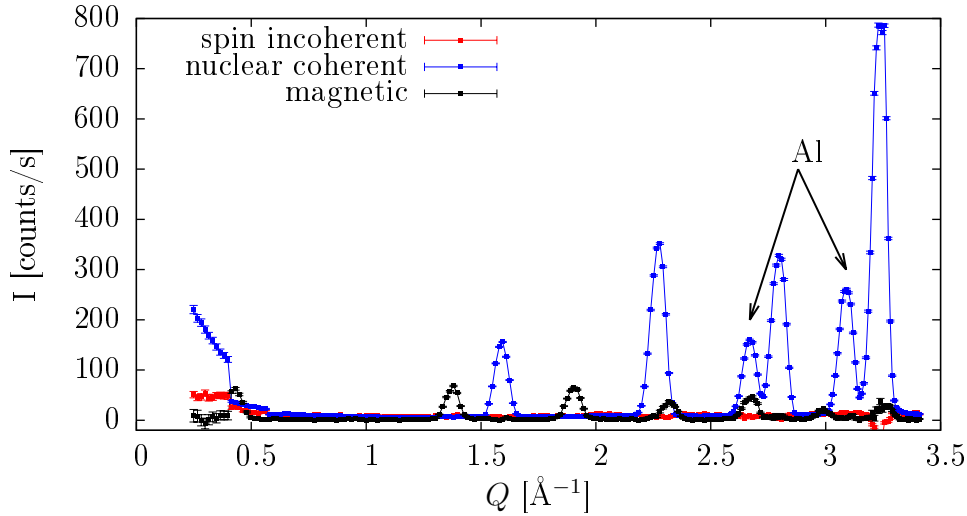


**Figure 6.12:** DNS measurement performed at 5 K without self-normalization. Separation of the different contributions has been done with `dnsplot`. Additionally, the two labeled reflections are Al (111) and (200). Aluminium has been used as sample holder and sample environment.

of the reflection significantly. Furthermore at around  $3.25 \text{ \AA}^{-1}$  a deep in the spin incoherent contribution indicates a problem with the separation analysis. This reflection was then also omitted for the refinement. For a wavelength of  $3.3 \text{ \AA}$ , which enables the investigation of a large  $Q$  range, the NiCr reference sample is no longer a purely incoherent scatterer and produces an additional reflection at  $3.05 \text{ \AA}^{-1}$ . Under consideration of the mentioned limitations of reliability only the range  $0.5 < Q < 2.5 \text{ \AA}^{-1}$  was used for the refinement of the data. This also limits the reliability of the Rietveld refinement as will be seen later. However, the DNS experiment was planned in order to investigate diffuse scattering, and to measure the sublattice magnetization over a large temperature range.

Except of the deep at around  $3.25 \text{ \AA}^{-1}$  the spin incoherent scattering is constant over the whole  $Q$  range, and can be easily used in order to get absolute values with eq. 6.3. The arrows in Fig. 6.12 point to reflections, which are caused by the aluminium sample holder, and can be identified as (111) and (200), respectively.

A zoom on the magnetic reflections with their temperature dependency is depicted in Fig. 6.13. With an intensity integration for each reflection within  $1.27 < Q < 2.42 \text{ \AA}^{-1}$  one gets the sublattice magnetization as shown in Fig. 6.14. The transition temperature  $T_N$  can be determined as  $203(1) \text{ K}$ , which is in agreement with the transition temperature measured with the MPMS. In consideration of the specific heat data, which shows a significant peak at the transition temperature, the magnetic transition can be identified as a first order transition. It is also supported by the macroscopic magnetization, which shows a thermal hysteresis for heating and cooling, and an abrupt change of the magnetic order parameter at  $T_N$ , which is also characteristic for first order transitions. However, from the sublattice magnetization shown in Fig. 6.14 it is not clear. Due to problems with the scaling factor of the magnetic data with regard to the nuclear one, as discussed later, the sublattice magnetization is normalized and not given in absolute values. Additional temperature steps, especially below  $T_N$ , would be necessary to distinguish between first order

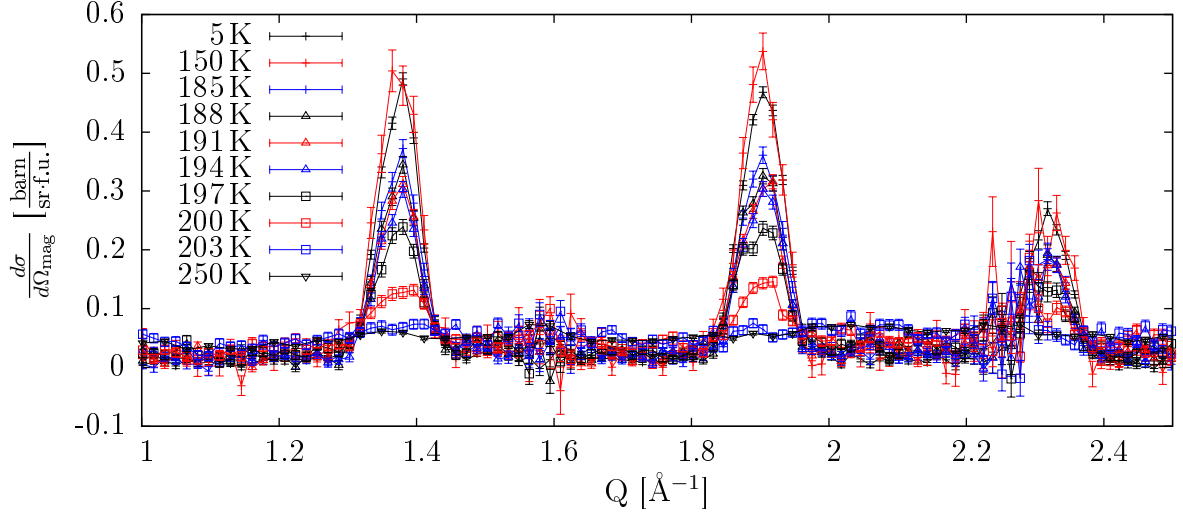


**Figure 6.13:** Temperature dependency of the differential magnetic cross section. The higher order reflections are not shown for a better clarity. The measurement was performed upon warming after cooling to 5 K.

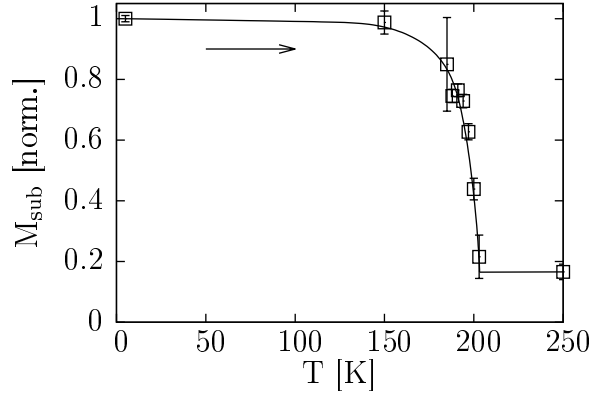


**Figure 6.14:** The temperature dependency of the sublattice magnetization, which is defined as the square root of the magnetic scattering cross section, is given. It has been determined by intensity integration of the reflections within  $1.27 < Q < 2.42 \text{ \AA}^{-1}$ . For the integration a background subtraction was done. The measurement was performed while warming from 5 K to 250 K. A smoothed curve is shown as a guide to the eye.

or second order transition in this case. In addition, it can be seen that the intensity does not drop to zero above the transition. Short range correlations which persist above  $T_N$ , can be a reason for the non-vanishing scattering intensity. To prove this, measurements at higher temperatures have to be performed.

Reaching  $T_N$  the antiferromagnetic long-range ordering (LRO) breaks down abruptly for a first order transition and the magnetic correlation length is then infinitesimal. For  $T < T_N$  one sees the fluctuations accompanying LRO, which is not in saturation. For  $T > T_N$  one sees regions of short range ordering (SRO) building up as a precursor of the LRO state. Besides the fluctuations, the SRO with a reduced magnetic correlation length

also gives rise to magnetic diffuse scattering. Thus, these reasons lead to a broadening of the reflections close to the phase transition, but can also persist for temperature far away from the transition as seen in Fig. 6.14.

Considering the 203 K measurement, which is the phase transition temperature, no peak broadening can be found, but an increased constant background. It is supposed that the broadening of the reflections is large, and the intensity is equally distributed over the whole  $Q$  range. The diffuse scattering, indicated by an increase of the intensity over the whole  $Q$  range persists at least up to 250 K. The MPMS data clearly showed a transition around 200 K. However, even at 250 K a behavior according to the Curie-Weiss law is not measurable (measurement shown in Fig. 6.10). This indicates that the magnetic behavior is not purely paramagnetic and short range correlations still exist. That a clear peak broadening cannot be quantified can be related to the instrument itself. The polarization analysers have a diminishing transition (sensitivity) for higher energies. Therefore it is likely that one does not integrate over the relevant fluctuation spectrum. Thus, only a small part of the diffuse scattering becomes visible. This is broad in  $Q, E$ -space for the underlying first order transition, where the susceptibility  $\chi$  does not diverge.

LSFO crystallizes in space group  $R\bar{3}c$ . The antiferromagnetic unit cell has a reduced symmetry. Under consideration of the expected magnetic ordering propagation vector along the  $c$ -axis and the magnetic moments aligned in the  $a - b$  - plane, the magnetic subgroup can be determined as  $P\bar{1}$  [109, 110]. The refinement takes the nuclear unit cell parameter into account and reduces the symmetry to accommodate the magnetic moments following that the magnetic space group exhibits only one inversion center, which is centered in the unit cell. The magnetic data of the 5 K measurement was used in order to determine the magnetic structure. Fig. 6.15 shows the magnetic data and the Rietveld refinement done with Jana2006 [49]. The refinement only considers  $0.5 < Q < 2.5 \text{ \AA}^{-1}$  as discussed above, but the whole  $Q$  range is shown for the sake of completeness. The refinement of the magnetic data uses the profile scale factor gained from the refinement of the nuclear data and was kept constant during refinement of the magnetic data (all refinement parameters are listed in Appendix D.2). The unit cell parameters could be determined as  $a = b = 5.4911(86) \text{ \AA}$  and  $c = 13.5068(152) \text{ \AA}$ , which is in agreement with the nuclear structure parameters. The refinement ended up with  $R_w = 0.08 \%$  and  $R_{w,\text{profile}} = 7.92 \%$ . From this refinement the magnetic ordering parallel or antiparallel to the  $a$  or  $b$  direction can be seen. However, the refinement converged for magnetic moments, which are lower than expected from literature ( $\text{Fe}^{5+}$ :  $2.72(6)\mu_B$ ;  $\text{Fe}^{3+}$ :  $3.61(3)\mu_B$  [94]), and from the BT-1 measurements as shown in the next section. Each  $\text{Fe}^{5+}$  ion carries a magnetic moment of  $M_1 = 1.732(34)\mu_B$ , and each  $\text{Fe}^{3+}$  ion  $M_2 = 1.344(23)\mu_B$ . During data refinement it could be seen, that the profile scale factor does not hold for nuclear and magnetic data, but the problem is not related to the separation analysis. This was checked by creating and analyzing an unpolarized data set by building a sum of all spin-flip and non-spin-flip channels. An obvious discrepancy was evident. In consideration of the problem with NiCr and the short wavelength of  $3.3 \text{ \AA}$ , which influences the flipping ratio correction, a  $4.5 \text{ \AA}$  measurement was also analyzed, but was limited to 5 K and large angle increments. The data and refinement are shown in Fig. D.1 in the appendix, where all refinement parameters can be found. From this Rietveld refinement  $a = b = 5.402(29) \text{ \AA}$

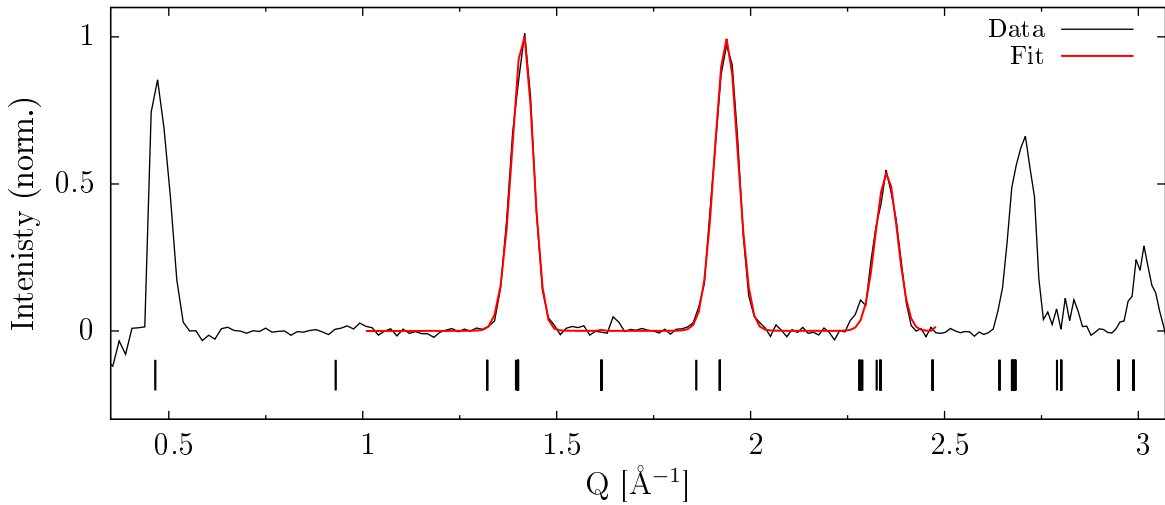


**Figure 6.15:** Neutron powder diffraction and Rietveld refinement measured at 5 K. The intensity and peak shape of the first reflection at  $0.5 \text{ \AA}^{-1}$  is influenced by the beam block and thus not considered during refinement. Additionally, the reflections above  $2.5 \text{ \AA}^{-1}$  are also not reliable, as discussed, and were not considered for the refinement as well. The used magnetic space group is  $P\bar{1}$ . The vertical lines indicate the position of calculated peaks, but for some of them the modeled intensity is zero.

and  $c = 13.194(102) \text{ \AA}$  followed. The longer wavelength shortened the available  $Q$  space and less nuclear and magnetic reflections are observable. Nevertheless the refinement gave  $M_1 = 3.12(43)\mu_B$  and  $M_2 = 4.26(22)\mu_B$ . Anyhow, the values are higher than expected, but exhibit large errorbars caused by the large increments of the measurements, which limits the peak shape determination. That the  $4.5 \text{ \AA}$  measurement is close to the expected values, there is obviously a problem with the short wavelength of  $3.3 \text{ \AA}$ , which could not be identified. To locate the problem, measurements with longer wavelength have to be performed over the whole accessible temperature range.

### High-resolution atomic and magnetic structure determination

The DNS experiment with its advantage of a  $xyz$  polarization analysis has a rather long wavelength and only covers a small  $Q$  range, whereas the following experiments exhibit very high resolution and cover a large  $Q$  range simultaneously. This is necessary, because the assumed small deviations from the room-temperature space group  $R\bar{3}c$  appear at high  $Q$  values. X-ray synchrotron radiation has also been used in order to get evidence of the charge ordering in the system. Based on the parent space group  $R\bar{3}c$ , the subgroups  $R\bar{3}$  and  $P\bar{1}$  are a possibility as both space groups can accommodate two different iron sites, each with a different symmetry.

The synchrotron X-ray measurement was performed at the 11-BM beamline at APS via Mail-In sample service. This service provides fast access to a synchrotron powder diffraction experiment, but the sample environment options like cryostat or magnet are limited. Thus, the lowest accessible temperature is 100 K. Additionally, the measure-

ment time is limited to one hour per temperature step. The accessible temperature range

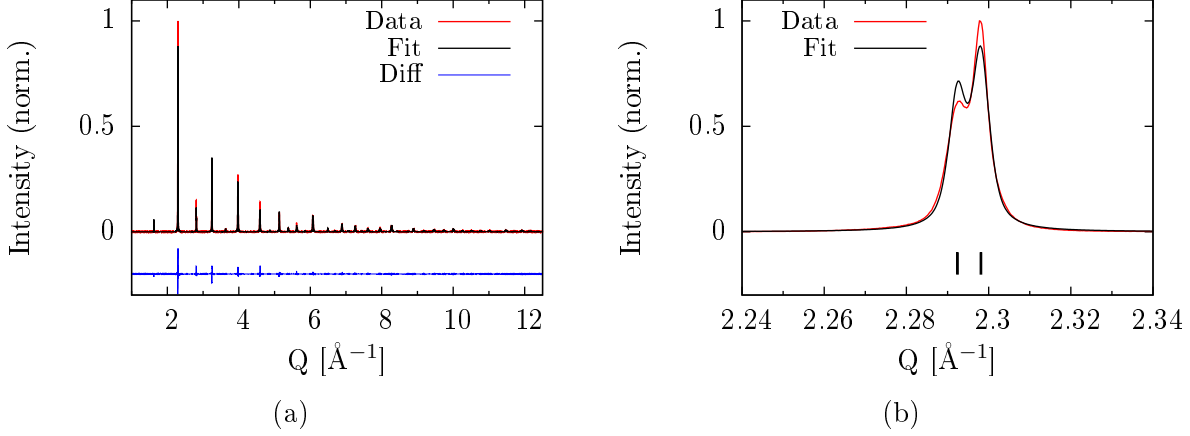


**Figure 6.16:** 100 K powder X-ray diffractometry measurement performed on 11-BM @ APS. (a) gives an overview and includes the Rietveld refinement data. The difference of data and simulation is also depicted, but shifted by -0.3. The symmetry space group is  $R\bar{3}c$ . (b) is a zoom in on the region around the  $(2\bar{1}0)$  and  $(104)$  reflection. Refinement parameters are listed in Appendix D.2.

was between 100 K and room temperature in steps of 20 K, which did not allow probing the phase transition at 200 K thoroughly. The used wavelength was  $0.41418(1) \text{ \AA}$ , which allows one to measure a large  $Q$  range up to  $13 \text{ \AA}^{-1}$ . The powder was measured in a Kapton<sup>®</sup> tube with an inner diameter of 0.8 mm, which is necessary to keep the absorption of the beam as low as possible. Fig. 6.16a shows a measurement performed at 100 K including the Rietveld refinement and the difference between measurement and refined profile. The parameters of the figure of merit are shown in Tab 6.4. The weighted  $R$  value of the profile function is 13.40%, which means, that the agreement between profile function and the measured data is poor. Fig. 6.16b, which depicts a detailed view on the  $(2\bar{1}0)$  and  $(104)$  reflections, respectively, shows a deviation in detail. The intensity of both reflections is not modeled correctly, whereas the peak positions fit to the calculated ones. Several approaches were used to describe the data and to get rid of the differences.

**Table 6.4:** Model and profile  $R$  values from refinement. Explanation of these values is given in section 3.4. Further refinement parameters are listed in Appendix D.2.

	$R$ [%]	$R_w$ [%]
Model	3.37	5.32
Profile	10.61	13.40

A Pseudo-Voigt function was used, which includes the broadening of reflections, and the resolution of the experiment as well.

The flanks of the reflection appear broadened in the measured data and an anisotropic strain broadening  $[111]$  was considered, but could not improve the profile function's  $R$  value.

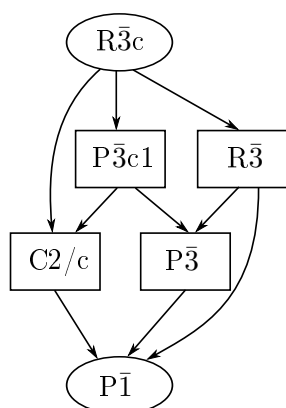


**Figure 6.17:** Subgroup graph under the assumption, that the number of chemical formula units per unit cell stays constant. Data taken from [109].

The broadened flanks can also be caused by additional reflections, which are not described with the assumed model. Reducing the crystal symmetry leads to an increased number of reflections in the diffractometry pattern, which are not present in the originally assumed high symmetry space group  $R\bar{3}c$ , and can possibly change the profile to fit to the measurement. Under assumption of a constant number of chemical formula units per unit cell one has to consider several subgroups as shown in Fig. 6.17. This subgroup graph was created with [109] and describes the successive reduction of symmetry from the highest symmetry space group  $R\bar{3}c$  to the lowest considered symmetry  $P\bar{1}$ , which only contains an inversion centre. Removing the  $c$  glide plane leads to  $R\bar{3}$ , and a further loss of the 3-fold rotoinversion axis ends in the lowest symmetry  $P\bar{1}$ . Both space groups exhibit two distinct iron sites, and are candidates for the refinement. Other assumed symmetry changes concern the Bravais type, which can change from a rhombohedral to a primitive or  $C$  centered lattice. To test the shown space groups Jana2006 [49] has been used and it was found that a lower symmetry is not obvious in the data. The additional reflections for the lower symmetry case appeared in regions, where no intensity was measured and did not help to improve the profile matching.

Changing the atomic displacement parameter from isotropic to anisotropic does not improve the profile function as well. The vibrational movements of the atoms are not restricted to distinct crystal directions and seem to be isotropic.

A preferred orientation of the crystallites in the Kapton<sup>®</sup> tube, which was used for the measurement as explained, was found to be most likely the reason for the problems with the profile function. It is known that crystals break along preferred orientations during pestling, for instance. The very small Kapton<sup>®</sup> tube helps to orient these crystallites in a non-randomized way, because of its small inner diameter and long length of several centimeters. The refinement considers a preferred orientation along the  $(2\bar{1}0)$  reflections and all equivalent ones, for instance. It seems that a preferred orientation of the crystallites causes a disagreement of the profile function. Introducing such preferred orientation to the refinement leads to better result, but is still not in good agreement with the experimental data. It was not possible to determine the proper orientation, and in all likelihood, more than one preferred orientation has to be considered. The problem of the profile function is still not identified. The 11-BM measurement can confirm the assumed space group  $R\bar{3}c$ , but cannot give any new results concerning a distortion caused by the small-sized  $Fe^{5+}$  ions. The expected results are very small, because the distortion of the oxygen environment is only hardly measurable with X-rays and the beamtime was not long enough with respect to Woodward et al. [101]. In order to see the influences of the  $Fe^{5+}$  on the oxygen octahedron, which would lead to a symmetry reduction, a long synchrotron measurement should be planned. Furthermore the problem of the preferred orientation of crystallites has to be avoided somehow.

Apart from the profile function problems, the 11-BM measurement provides a precise determination of the temperature dependent lattice parameters gained from Le Bail profile matching shown in Fig. 6.18. The lattice parameters  $a, b$  and  $c$  shrink during cooling.

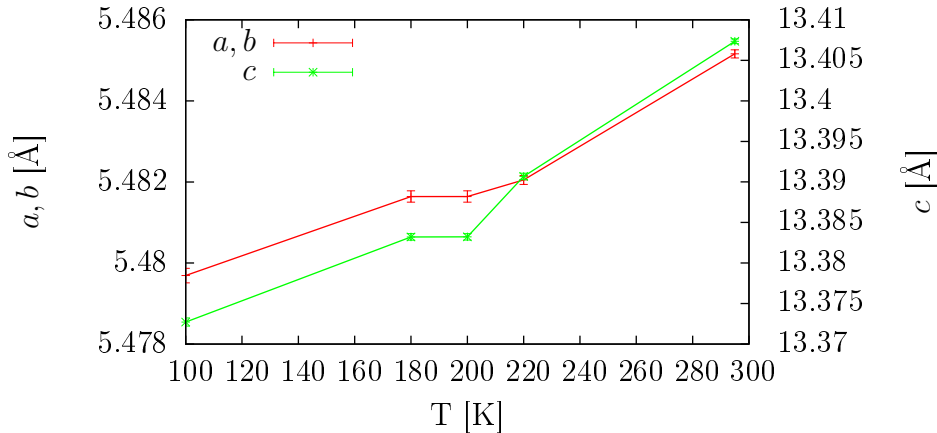


**Figure 6.18:** Temperature dependence of the lattice parameter measured with 11-BM.

Around the phase transition temperature the lattice parameters remain constant as expected, because energy is used to develop the charge and magnetic ordering. More precise measurements with smaller temperature steps and larger temperature range are necessary to probe the temperature dependence around the transition in detail. However, it cannot be provided by the Mail-In sample service.

LSFO undergoes a charge ordering transition which is created by a  $\text{Fe}^{3+}$  and  $\text{Fe}^{5+}$  ordering along the pseudo-cubic [111] direction. The contrast between both ions in a X-ray experiment is only caused by two electrons, and thus rather weak, but can be measured with a high resolution synchrotron diffraction experiment. The charge ordering is  $\text{Fe}^{3+}\text{Fe}^{3+}\text{Fe}^{5+}$ , which corresponds to a triplication of the nuclear pseudo-cubic unit cell and leads to reflection with the notation  $(\frac{n}{3}\frac{n}{3}\frac{n}{3})$  with respect to the nuclear unit cell.

Fig. 6.19 shows the charge ordering  $(\frac{2}{3}\frac{2}{3}\frac{2}{3})$  reflection. The signal obtained during the experiment is very weak, but a clear temperature dependence can be seen. For temperatures below the transition temperature, an increased intensity can be observed, which is attributed to the occurrence of charge ordering. The 100 K temperature shows the most pronounced change in intensity, which is in agreement with the statement that the charge ordering develops gradually while cooling. This leads to decreased FWHM of the reflection. On the other expected positions with  $n = 1, 4$  this weak behavior can also be found. At  $n = 3$  the charge ordering reflections coincides with the nuclear reflection, which is much stronger. The signal is quite small compared to the structural reflections. It is only about 0.01% of the  $(2\bar{1}0)$  reflection, and lies marginally above the background. Thus a consideration of the charge ordering in the refinement program was not possible. Nevertheless, the charge ordering is visible in the data, although very weak and it fits to the expected calculated positions within the measurement errors. To improve the data one has to perform a longer measurement in order to achieve more statistics around the charge ordering reflections to clearly separate the reflections from the background. Secondly, a measurement at lower temperatures is helpful, because the charge ordering is



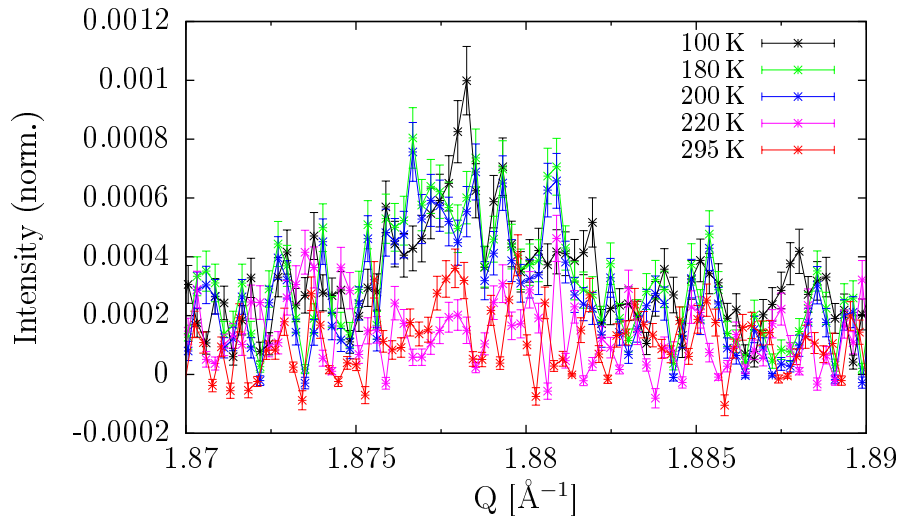


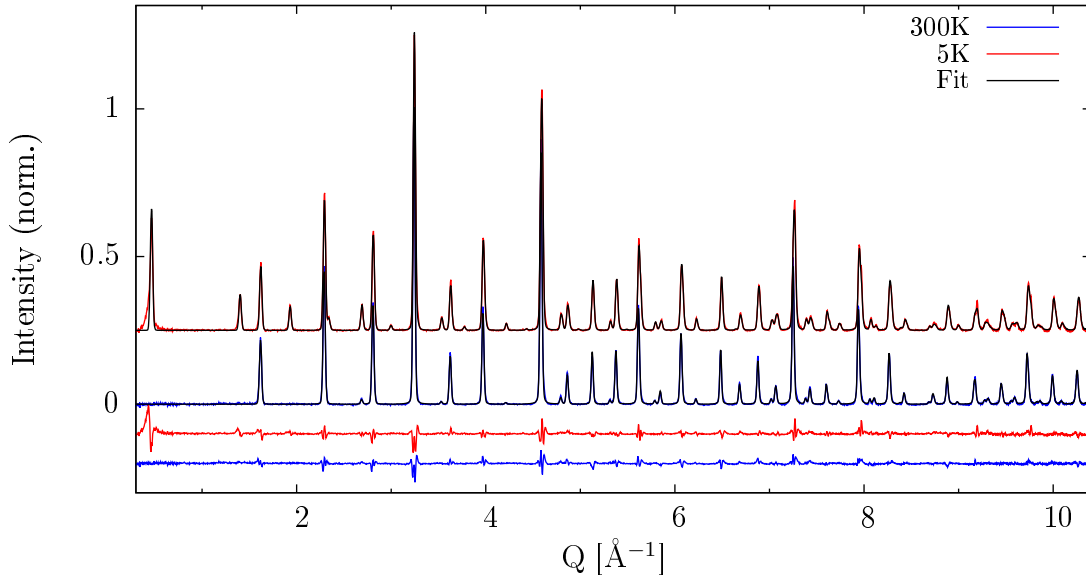
**Figure 6.19:**  $(\frac{2}{3}\frac{2}{3}\frac{2}{3})$  charge ordering reflection. A clear difference can be seen for the measurement above compared to below the charge ordering transition.

then completely developed and thermal influences are minimized.

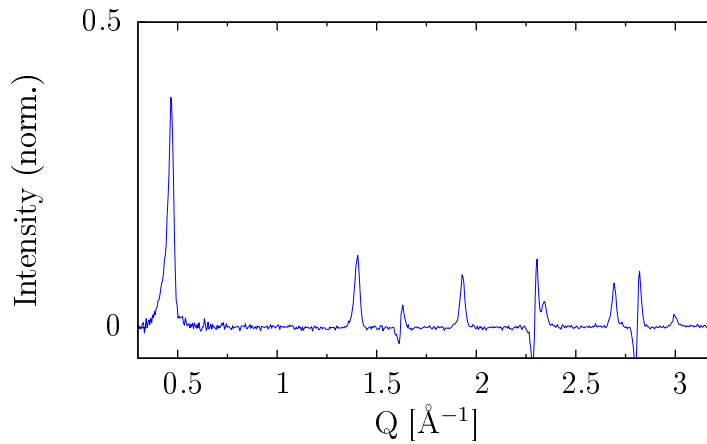
High-resolution neutron powder diffractometry performed at BT-1 at NCNR via Mail-In sample service was used in order to achieve a precise nuclear structure determination and to confirm the magnetic structure with regard to the DNS measurement shown earlier. The experiment used a Ge (733) monochromator, which provides a wavelength of 1.197 Å. This kind of monochromator enables a higher resolution for higher  $Q$  values, but reduces the number of incoming neutrons by a factor of 10 and the resolution for low scattering angles. The increased resolution was thought to be helpful in order to see small distortions of the oxygen octahedron, which become visible at high scattering angles. The formfactor for neutrons scattered at the nuclei is constant over the whole  $Q$  range, whereas the magnetic formfactor is strongly dependent on  $Q$  and decreases rapidly. Thus, the low  $Q$  range data contains both the magnetic and the nuclear reflections, the high  $Q$  data contains only structural information.

Fig. 6.20 shows a measurement at 300 K, which is well above the transition temperature at about 200 K, and a measurement at 5 K. The latter temperature is far away from the transition temperature, and it can be assumed that the charge disproportionation as well as the antiferromagnetic ordering is fully developed. The figure has also included the profile functions from the refinement done with Jana2006 [49]. The plots below zero correspond to the difference between profile function and measured data. The  $R$  values are listed in Tab. 6.5, and confirm the crystal structure with space group  $R\bar{3}c$  of the 300 K measurement.

The low temperature measurement at 5 K exhibit additional reflections, which can be attributed to the antiferromagnetic ordering. A difference plot of the 300 K and 5 K measurement within a small  $Q$  range is depicted in Fig. 6.21 to show the most significant magnetic reflections. As the form factor for magnetic scattering decays with increasing  $Q$  the magnetic reflections become invisible for high  $Q$ . Assuming a magnetic propagation



**Figure 6.20:** Neutron powder diffractometry measurements and Rietveld refinements at 300 K and 5 K. The 5 K measurement is shifted by 0.25 along the intensity axis. At -0.2 and -0.1 the difference between measurement and refinement is plotted. At 5 K clear additional reflections can be observed and are attributed to the magnetic scattering. The  $R$  values of the refinements can be seen in Tab. 6.5, further refinement parameters are listed in Appendix D.2.



**Figure 6.21:** The difference between 300 K and 5 K measurement. The peaks with negative intensity are uncompensated nuclear reflections due to a shrinking of the crystal lattice upon cooling.

vector parallel to the  $[001]$  - direction of the hexagonal unit cell (or  $[111]$  - direction of the pseudo cubic unit cell) and an alignment of the magnetic spins in the  $a - b$  - plane, a refinement in the magnetic space group  $P\bar{1}$  provides the lowest  $R$  values and the best agreement between measurement and refinement has also been shown in the DNS part. The lattice parameter for the magnetic phase at 5 K can be then given as  $a = b = 5.4762(7) \text{ \AA}$  and  $c = 13.3598(26) \text{ \AA}$  and is in agreement with results gained from

the DNS experiment.

As introduced earlier the antiferromagnetic ordering is ...  $\uparrow\uparrow\downarrow\downarrow\uparrow$  ..., which corresponds to  $\text{Fe}^{5+}\text{Fe}^{3+}\text{Fe}^{3+}\text{Fe}^{5+}\text{Fe}^{3+}\text{Fe}^{3+}$ . The refinement gives the magnetic moments for  $\text{Fe}^{5+}$  and  $\text{Fe}^{3+}$  as  $2.51(36)\mu_{\text{B}}$  and  $3.53(23)\mu_{\text{B}}$  per unit cell, respectively, which is in agreement with the magnetic moments obtained from Battle et al. [94]. However, one has to mention, that this solution is not unambiguous, because the refinement also converged for equal magnetic moments for both iron ions with a slightly higher  $R$  value. A clear sign for different iron ions and ordering of these cannot be confirmed reliably from this neutron data.

**Table 6.5:** 300 K and 5 K model and profile  $R$  values from refinement done with Jana2006 [49].

300 K	$R$ [%]	$R_w$ [%]	5 K	$R$ [%]	$R_w$ [%]
Model	2.50	3.83	Model	3.87	6.22
Profile	4.91	6.28	Profile	6.60	7.92

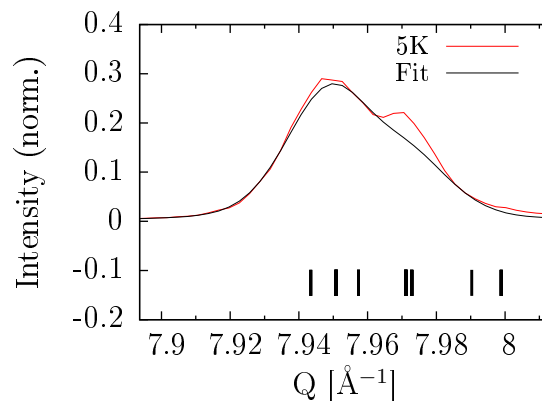


**Figure 6.22:** Zoom on a small  $Q$ -range to illustrate problems of the calculated profile function. The vertical lines show the positions of calculated reflections.

Fig. 6.22 shows a zoom on a selected peak as an example, that both the refinement and the data show a difference in intensity. Especially, the shape of the reflections is not modeled properly, but peak positions are calculated correctly. The two reflections appearing in the flank of the shown reflection cannot describe the measured intensity. A systematic that reflections of a certain type deviate could not be identified. However, over the whole diffractometry measurement range no additional reflections appear which could not be indexed. Neither a lowering of the symmetry nor introducing an additional impurity phase could improve the profile function significantly. Further efforts are necessary to investigate the structure thoroughly and to identify the reasons for the features found during both, synchrotron and neutron analysis.

Apart from discussion explained above, the resolution of the experiment can also play a role, because it is not constant over the whole  $Q$  range and is probably overestimated for the low  $Q$  region and underestimated for the high  $Q$  region.

### 6.2.3 Conclusion

Stoichiometric single phase LSCO powder was prepared successfully via a solid state reaction. In-house experiments confirm the Verwey transition and paramagnetic to antiferromagnetic transition. The specific heat measurement could be used to exclude additional structural transitions while cooling to the low temperature phase.

The DNS measurement showed the temperature dependence of the sublattice magnetization, whose transition temperature is in good agreement with the in-house magnetometry measurements. The magnetic transition is identified as a first order transition. Originally, the DNS experiment was intended to measure the magnetic diffuse scattering while passing the magnetic phase transition temperature. The measurements do not show large contributions of diffuse scattering except close to and above the phase transition, where an overall increase of the background was found. The broad or vanishing diffuse scattering contribution can be most likely related to the experiment itself. The integral measurement of DNS can only be evaluated properly in the so-called quasistatic approximation. This is only justified, if integration of the entire fluctuation spectrum can be achieved. On one side of the energy spectrum this is limited by the Bose-factor, whereas on the other side it is limited by the initial neutron energy. However, experimental factors like analyser transmission and energy dependent detector efficiency also play a crucial role.

One objective of this thesis was the high-resolution determination of the atomic and magnetic structure, where both synchrotron X-ray and neutron scattering was used. The synchrotron experiment exhibits an effect of preferred orientations, which makes a interpretation of the data almost impossible, because the direction of the preferred orientation is unknown. However, low intensity charge order superlattice reflections along the pseudo cubic [111] direction have been observed, which exhibit a significant temperature dependency. To consider this small signal with the Rietveld refinement a precise measurement at those positions has to be performed and was not possible during the time limited Mail-In sample service measurement.

With neutron powder diffractometry it was successful to identify the magnetic space group as  $\text{P}\bar{1}$ . The symmetry lowering is a consequence of the magnetic moments, which are found to be clearly aligned in the  $a - b$ -plane. The refinement cannot confirm a distortion of the oxygen octahedron. However, there are still features in the data, especially in the peak shape. Further efforts are necessary to clear this conflict, but a solution is not yet found. Additionally, a charge ordering along [111] is evidenced in the synchrotron data. However, a clear sign for iron ion ordering from the neutron data cannot be seen.

Summing up all informations achieved from different measurement the powder sample shows the expected properties. A change in symmetry cannot be found, but can also not be excluded. As both synchrotron and neutron powder experiments were done as Mail-In samples, the sample environment options like cryostat and, especially, the measurement times, were limited and have to be increased in order to finally exclude or confirm a distortion caused by the small  $\text{Fe}^{5+}$  ions in the structure.

## 6.3 Thin film study

After the powder experiments discussed in the last section, the LSFO thin films preparation with the molecular beam epitaxy technique will be introduced in order to prepare the growth of multifunctional heterostructures. One of the main advantages of the OMBE system is the possibility to control the thin film growth in many ways as described in chapter 4. However, this flexibility makes the development of good samples laborious, because lots of preparation parameters have to be considered. These include the growth temperature, the molecular flux from the evaporation sources, and the oxygen partial pressure, for instance. The central issue is to find appropriate parameters, which have to be found empirically using experience with a subsequent optimization of these.

### 6.3.1 Determination of growth parameters

The following sections describe the development of LSFO thin film from the first try to a stoichiometric, crystalline, and smooth thin film. To achieve this goal the parameters have to be optimized iteratively as shown in Fig. 6.23. Using starting parameters from experience, first thin films were grown followed by structural analysis with LEED, RHEED, XRR, and XRD, as well as stoichiometry analysis with RBS (A list of all used acronyms can be found in Appendix A). The results have been used to optimize the growth parameters accordingly as described later on.

The rate or frequency change of each material has to be determined in order to reach roughly the desired stoichiometry. Therefore one has to find the ratio of rates between all involved effusion cells, iron, strontium, and lanthanum, respectively. The rate of each cell is measured with a quartz microbalance. The resonant frequency of the quartz changes with a deposition of mass on its surface and is measured. To achieve the ratio  $1 \cdot \text{La} : 2 \cdot \text{Sr} : 3 \cdot \text{Fe}$  one can calculate, in first good approximation, the necessary frequency changes considering their molecular mass with the relation

$$\Delta f_{\text{La}} = c_{\text{La}} \cdot \frac{M_{\text{La}}}{M_{\text{Fe}}} \cdot \Delta f_{\text{Fe}}, \quad (6.4)$$

and

$$\Delta f_{\text{Sr}} = c_{\text{Sr}} \cdot \frac{M_{\text{Sr}}}{M_{\text{Fe}}} \cdot \Delta f_{\text{Fe}}, \quad (6.5)$$

where the factor  $c_{\text{La}} = 1/3$  and  $c_{\text{Sr}} = 2/3$  takes the stoichiometric fraction in LSFO into account. The frequency change  $\Delta f_{\text{Fe}}$  has been used as the reference, whose starting value considers a slow growth rate of  $\approx 90 \text{ s/unit cell}$ . Following Eq. 6.4 and Eq. 6.5 the desired frequency changes are  $\Delta f_{\text{La}} = 0.829 \cdot \Delta f_{\text{Fe}}$  and  $\Delta f_{\text{Sr}} = 1.046 \cdot \Delta f_{\text{Fe}}$ , respectively. These formulas are only a first approximation, and do not consider substrate sticking coefficients, different oxidation states under oxygen atmosphere, but are usually good enough as starting values.

If one considers oxidation, it is necessary to assume that  $\text{La}_2\text{O}_3$ ,  $\text{SrO}$ , and  $\text{FeO}_2$  is deposited on the quartz during rate calibration and one has to correct the values  $c_{\text{La}}$  and

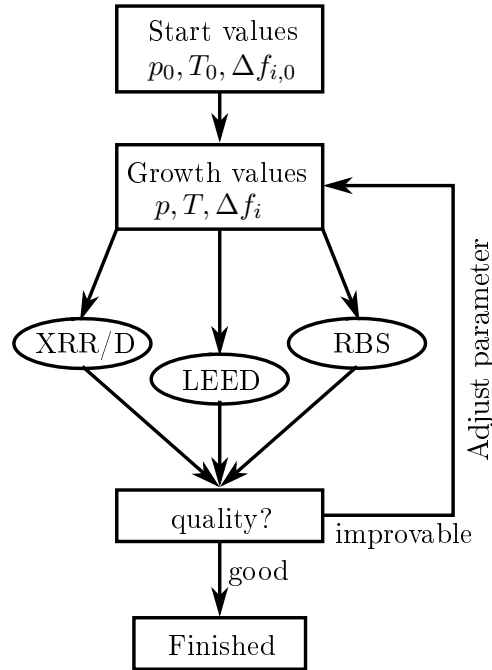


**Figure 6.23:** Sketch of the OMBE thin film growth process optimization. The frequency changes can be roughly calculated as shown in Eq. 6.4 and 6.5. The start values are empirical experiment values. After the growth of the first layer the structure was analyzed with LEED, RHEED, XRR and XRD, and RBS. If, with regard to surface morphology, crystalline structure, and stoichiometry, a good sample has been reached, the growth process optimization is completed. If not, the growth parameter have to be adjusted until a good quality sample has been achieved.

$c_{\text{Sr}}$  to 0.22 and 0.62, respectively. As Fe has several valence states, which cannot be predicted reliably, the values are only better approximations. Fig. 6.24 shows the relation between the assumed  $c_{\text{La}}$  and the ratio between the La and Fe stoichiometry. The samples

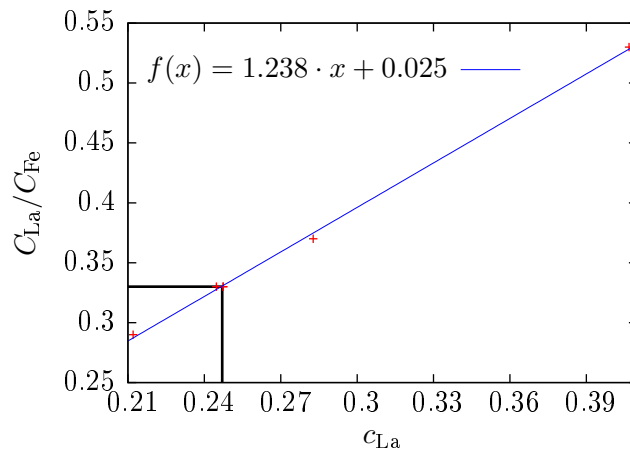


**Figure 6.24:** Evaluation of Eq. 6.4 with  $c_{\text{La}}$ .  $C_{\text{La}}/C_{\text{Fe}}$  is the ratio between La and Fe from RBS measurements. All thin films were grown under comparable growth conditions.

summarized here are grown at comparable growth conditions with growth temperatures

between 1220 K and 1240 K, but the slightly different growth temperatures fit all together and a linear dependence can be found. Thus, a large influence of the growth temperature within the used temperature range on the stoichiometry is not present. The variation is only about 2%. From the RBS measurement one gets  $c_{\text{La}} = 0.247$ , which is slightly above the calculated value of 0.22. This is in good agreement, because the simple model does not consider the different sticking coefficient of STO and the used quartz surface, for instance.

The exact growth rate has to be determined ex-situ with X-ray reflectometry measurements. The quartz microbalance is not suitable for measuring the growth rate of complex structures, because the surface properties are different compared to those of the used substrate. Thus, a rather incomparable layer is expected. Furthermore one has to consider that the growth temperature plays a crucial role to achieve a smooth and crystalline layer. However, the quartz is cooled to achieve a precise rate measurement, and thus the surface thermodynamics of the quartz are completely different compared to the growth conditions used. This usually avoids getting crystalline structures. The quartz microbalance has been used to achieve a reproducibility, but ex-situ calibration measurements are required, especially measurements for the determination of the stoichiometry with RBS. To measure the rate of each effusion cell for the thin film growth accurately, it is necessary to place the quartz microbalance at the position of the substrate, which excludes rate monitoring during the actual growth process. Thus, for the actual growth the rate must

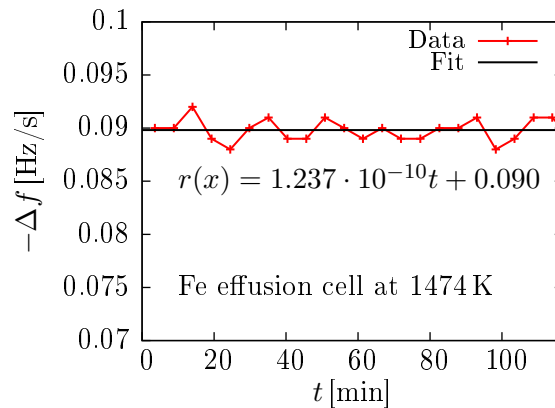


**Figure 6.25:** Frequency change observation caused by deposited Fe prior growth over 120 min with each data point averaged over 5 min. The frequency change is  $0.090(2) \frac{\text{Hz}}{\text{s}}$  and is stable within the measurement error.

be stabilized over the whole growth period and this takes time. Using oxygen during a growth process will also influence the effusion cells themselves by oxidization, and thus the rate calibration has to be done under oxygen atmosphere. Afterwards it is necessary to wait until a thermodynamical equilibrium state has been reached. To ensure stability, the rates are monitored and adjusted during two days at minimum, and, if possible, checked after the growth process. Fig. 6.25 shows a frequency change observation caused by the iron flux over 120 min, which corresponds to a usual growth duration. One can see that the effusion cell is stable within the measurement errors during this time. Usually a rate variation of maximum 5% over one day was found for all effusion cells, which is

also approximately the measurement uncertainty of the quartz microbalance and of the RBS stoichiometry determination. In addition, a growth rate control by a measurement of RHEED oscillations was intended, but a realization was not achieved due to technical problems. The measurement could significantly contribute to improving the quality of a thin film as discussed earlier, because it enables real time monitoring during sample growth.

### 6.3.2 Substrate preparation

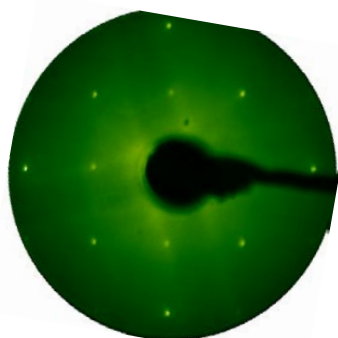


**Figure 6.26:** LEED image of a STO substrate taken at 100 eV after annealing. Clear and sharp reflections indicate a crystalline and clean surface.

Two different substrate materials were used in order to develop an optimized growth procedure. The first samples were grown on MgO which exhibits a face-centered cubic lattice with  $a = 4.217 \text{ \AA}$ . Due to the large lattice mismatch it is not the ideal candidate, but contains no strontium, which makes it easier to distinguish between the LSFO layer and substrate with RBS. Thus it is used for approaching the proper stoichiometry.

For an epitaxial thin film growth STO is an ideal substrate as introduced in chapter 2. During this thesis commercially available STO substrates from Crystek GmbH [112] were used. These substrates exhibit a good crystallinity and smooth surface as also confirmed by Schmitz and Zakalek [69, 113], for instance. The substrates were cleaned in an ultra sonic bath for 3 min in acetone followed by 3 min in ethanol and

then directly transferred to the load lock of the OMBE system.

To get rid of any residuals remaining on the surface and to achieve a smooth surface, annealing steps are necessary. Therefore the substrates have been heated to 770 K overnight followed by an one hour annealing step above growth temperature, usually at 1270 K or 1320 K. Fig. 6.26 depicts a LEED image taken at 100 eV after the annealing procedure. Sharp and bright reflections indicate a clean and crystalline substrate surface after annealing and provide a good basis for epitaxial thin film growth applications.

### 6.3.3 Effect of post-annealing and stoichiometric layer growth

Besides the stoichiometry, the substrate temperature during thin film growth is an important parameter, which heavily influences the roughness parameter and crystalline quality. These are coupled to the growth thermodynamics as explained earlier. As rough starting values, temperatures taken from Xie et al. [104] were used. However, the temperature measurement is highly dependent on the used system, because the position and type of the temperature sensor influence the value of the measurement. Usually all systems exhibit large temperature offsets and a direct transfer of parameters from one to another system is difficult. Several growth attempts reveal that the literature values are too low, because they do not lead to a crystalline structure. The best result was reached at a



growth temperature of 1240 K with regard to surface and layer morphology. However, improvements were still necessary to further reduce roughness of the layer.

Xie et al. [104] suggested to add annealing steps after the thin film growth. As mentioned in chapter 4, annealing steps can significantly increase the quality of the thin films with respect to layer crystallinity and surface quality. High annealing times can favor interdiffusion between substrate and thin film within the interface region. During development of the growth procedure, an annealing time of 5400 s at growth temperature and a second annealing step at 470 K provides the best results for the single layer growth. As an example that post-growth annealing enhances the thin film quality, two samples with otherwise identical parameters (Tab. 6.6, plasma power 300 W,  $p_{\text{O}_2} = 4 \cdot 10^{-7}$  mbar) were grown via codeposition with and without annealing. The sample without annealing (LSFO<sub>na</sub>) was cooled to room temperature with 5 K/min in oxygen, whereas the other sample was annealed (LSFO<sub>a</sub>). Both samples exhibit the same stoichiometry of  $\text{La}_{0.33}\text{Sr}_{0.74}\text{FeO}_{3-\delta}$ , which was measured and analyzed by R. Heller from Helmholtz Zentrum Dresden-Rossendorf (HZDR). The  $\delta$  values are 0.3 and -0.14, respectively. RBS cannot measure light atoms precisely, and the error of both values is quite large, but cannot be estimated reliably. Measuring the oxygen content in thin films is still a large problem in research. As shown by Zakalek [113] the used oxygen partial pressure is sufficient to saturate the sample with oxygen. The author used a XRD technique to analyze the state of oxygen saturation. The saturation is closely related to the lattice spacing of (00l) planes and changes with the oxygen content reproducibly.

The effect of annealing is apparent from the comparison of RHEED images shown in Fig. 6.27. Without annealing, the pattern is slightly smeared. This indicates a higher surface roughness and also the correlation length of the lateral 2D crystal structure is lower. Furthermore, higher Laue orders with sharp reflections can be found after sample annealing, whereas sample LSFO<sub>na</sub> shows lots of diffuse scattering. High surface roughness increases the contribution of diffuse scattering to the pattern. As described in section 5.1.2, the significant Kikuchi lines after annealing are also characteristic for a high surface quality. Fig. 6.28a shows the reflectivity measurements of both samples. To simulate both

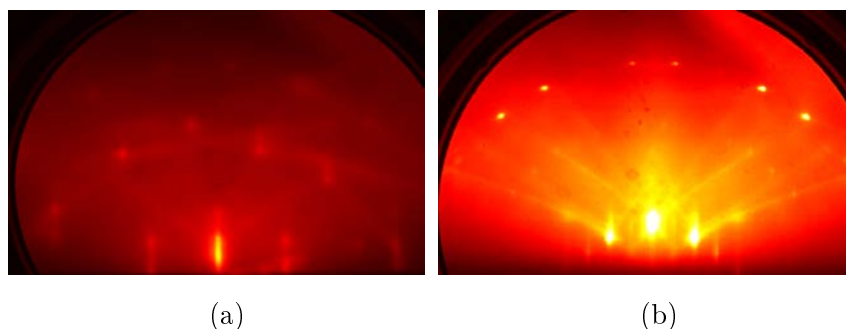


**Figure 6.27:** (a) A RHEED image of sample LSFO<sub>na</sub>. (b) An image of sample LSFO<sub>a</sub>. Both measurements are done at room temperature.

samples an additional top layer with a density reduced by 10% is necessary. Fig. 6.28b depicts the SLD of the annealed sample, and additionally, it contains a calculated layer of the same thickness, which exhibits the theoretical SLD, but no top layer. The resulting

**Table 6.6:** Summary of different growth parameters used for growth process optimization. Post-growth sample annealing analysis was done with samples which exhibit a slightly increased strontium content. The final sample was grown with an adjusted strontium rate, which further improved the sample quality.

	$-\Delta f_{\text{Fe}}$ [Hz] [s]	$-\Delta f_{\text{Sr}}$ [Hz] [s]	$-\Delta f_{\text{La}}$ [Hz] [s]	Substrate annealing [K]	$T_{\text{growth}}$ [K]	$t_{\text{growth}}$ [s]	rate [Å] [s]	post annealing and cooling [K]	composition
$\text{LSFO}_{\text{na}}$	0.091	0.083	0.056	1270 (60 min) 1220 (10 min)	1220	7000	0.055	5 $\frac{\text{K}}{\text{min}}$ to 270 no annealing	$\text{La}_{0.33}\text{Sr}_{0.74}\text{FeO}_{3-\delta}$
$\text{LSFO}_a$	0.091	0.083	0.056	1320 (60 min) 1240 (10 min)	1240	7000	0.049	1240 (90 min) 2 $\frac{\text{K}}{\text{min}}$ to 470 470 (30 min) 2 $\frac{\text{K}}{\text{min}}$ to 270	$\text{La}_{0.33}\text{Sr}_{0.74}\text{FeO}_{3-\delta}$
$\text{LSFO}_{\text{final}}$	0.092	0.077	0.056	1320 (60 min) 1240 (10 min)	1240	7000	0.047	1240 (90 min) 2 $\frac{\text{K}}{\text{min}}$ to 470 470 (30 min) 2 $\frac{\text{K}}{\text{min}}$ to 270	$\text{La}_{0.33}\text{Sr}_{0.67}\text{Fe}_{1.03}\text{O}_{3-\delta}$

**Table 6.7:** Parameters from simulation shown in Fig. 6.28 and Fig. 6.31a, respectively, in order to compare samples with different growth parameters (Tab. 6.6). The final sample (LSFO<sub>final</sub>) is a further optimized layer, with respect to stoichiometry, after the investigation of the annealing influences.

	LSFO <sub>na</sub>	LSFO <sub>a</sub>	LSFO <sub>final</sub>
$d_{\text{LSFO}}$ [Å]	$363.94^{+0.96}_{-2.27}$	$330.10^{+1.38}_{-1.19}$	$309.25^{+0.47}_{-0.52}$
$\sigma_{\text{LSFO}}$ [Å]	$8.59^{+0.77}_{-0.01}$	$8.73^{+0.99}_{-0.84}$	$7.61^{+0.03}_{-0.79}$
$\sigma_{\text{substrate}}$ [Å]	$5.43^{+0.40}_{-0.01}$	$5.17^{+0.07}_{-0.55}$	$4.92^{+0.02}_{-0.02}$
$d_{\text{top}}$ [Å]	$19.50^{+0.82}_{-0.36}$	$13.59^{+0.45}_{-1.78}$	$19.93^{+0.03}_{-0.79}$
$\sigma_{\text{top}}$ [Å]	$6.54^{+0.11}_{-0.11}$	$6.10^{+0.10}_{-0.13}$	$7.50^{+0.01}_{-0.01}$

parameters are summarized in Tab. 6.7.

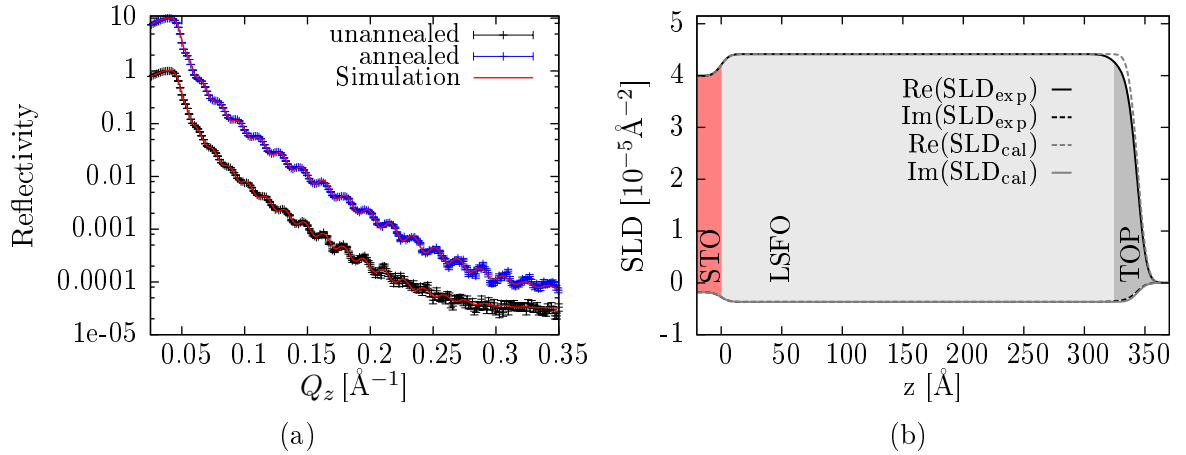


**Figure 6.28:** (a) Reflectivity and dedicated simulations. The curve for LSFO<sub>a</sub> is shifted by a factor of 10. All simulation parameters can be found in Tab. 6.7. (b) The SLD for sample LSFO<sub>a</sub> and of a calculated layer.

The layers do not show a significant difference. In addition, the atomic density is  $0.0162 \text{ \AA}^{-3}$  and  $0.0164 \text{ \AA}^{-3}$  for sample LSFO<sub>na</sub> and LSFO<sub>a</sub>, respectively. Besides the marginal differences between the not annealed and the annealed sample found with XRR, XRD revealed a large influence of the annealing step on the crystallinity.

Fig. 6.29 shows the (002) reflection of the sample LSFO<sub>na</sub> (a) and sample LSFO<sub>a</sub> (b). Besides the substrate (002) reflection, which has been used as reference, both samples show a clear LSFO layer reflection. The out-of-plane lattice parameters of the LSFO layer are shown in Table 6.8. Due to the lattice mismatch of 1% between LSFO layer and STO substrate, the layers exhibit tensile strain. A direct measurement of the in-plane lattice parameters is on the agenda, but a good approximation is to assume that the unit cell volume always stays constant, the layer is fully strained, and epitaxy is present. In principle, the in-plane lattice parameters relax with increasing the distance from the substrate. With reservations, it is possible to evaluate the in-plane lattice parameters using

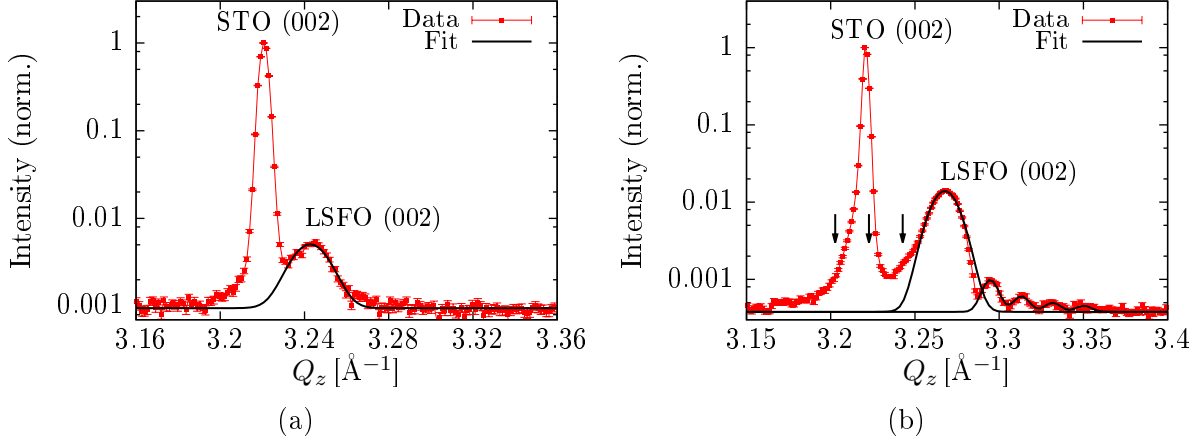


**Figure 6.29:** (a) The (002) reflection of sample  $\text{LSFO}_{\text{na}}$ . (b) is the same reflection for the annealed sample  $\text{LSFO}_{\text{a}}$ . The measurement was performed at room temperature. The arrows in (b) point to the position of thickness oscillations, which are overlain by the substrate reflection. The position of the thickness oscillations has been determined with a sum of Gaussians.

**Table 6.8:** Measured out-of-plane lattice parameter  $c$  and calculated in-plane values  $a$ . The substrate was used as a reference (\*) (Sec. 9.2.2) to correct the scattering angle  $\theta$ .

	$\text{LSFO}_{\text{na}}$	$\text{LSFO}_{\text{a}}$	$\text{LSFO}_{\text{final}}$	substrate
$c$ [Å]	3.8753(2)	3.8453(1)	3.8482(2)	3.9017(1)*
$a$ [Å]	3.8777(6)	3.8927(5)	3.8913(7)	3.9017(1)*

the calculated pseudo-cubic cell volume  $V = 58.27(1) \text{ \AA}^3$  from LSFO powder (Sec. 6.2). The in-plane lattice parameters are listed in Tab. 6.8. The pseudo-cubic unit cell of  $\text{LSFO}_{\text{na}}$  is smaller than of the  $\text{LSFO}_{\text{a}}$ , which leads to higher in-plane strain. The determined full width at half maximum for the not annealed sample is  $0.0203(4) \text{ \AA}^{-1}$ . It is proportional to the thickness of the layers or, more precisely, to the correlation length in  $c$ -direction. The thickness can then be calculated to  $310(7) \text{ \AA}$ . Compared to the thickness determined by XRR, the layer is not fully correlated. The differences can be attributed to lattice imperfection in the case of sample  $\text{LSFO}_{\text{na}}$ , which is also confirmed by a slightly increased  $c$  value and reduced atomic density. Maybe an amorphous layer exists in between substrate and layer without annealing, because the in-plane and out-of-plane lattice parameters do not indicate strain induced by the substrate. Those imperfections can also explain the increased thickness of the layer, while keeping the growth parameters compared to the annealed sample.

Smooth samples with a good crystalline quality show so-called thickness oscillations, which are an interference phenomenon between crystal lattice and surface.  $\text{LSFO}_{\text{na}}$  does not show any thickness oscillations, which also indicate that the not annealed sample shows a poor quality with respect to structure and surface morphology. Additionally the normalized intensity of the thin film reflection is about three times lower compared to the annealed sample.

The annealing process improves the crystalline quality of the layer significantly. The XRD measurement shows clear oscillations on the right of the layer reflection. These oscillations correspond to a thin film thickness of  $339(5) \text{ \AA}$ , which is in good agreement with the thickness obtained from the XRR experiment. Consequently, the layer is completely crystalline. The black arrows in Fig. 6.29b point to the thickness oscillations, which are overlain by the substrate reflection. On the left of the substrate peaks, thickness oscillations are somehow extinct. As shown in Tab. 6.6 the Sr content is slightly too high and has to be adjusted as shown in the following part. In summary it is possible to increase the surface and, especially, the crystalline quality after adding an annealing step after growth.

Now, the single layers have further been optimized in order to reach a proper stoichiometry. Besides the annealing, the stoichiometry also influences the structure of the layers as expected. A non-stoichiometric sample exhibits defects in the crystal structure to compensate the absence or excess of atoms and ions, respectively. It has been found that adjusting the Sr rate, while keeping all parameters including the annealing, leads to a sample which shows an ideal surface morphology and crystalline structure. Fig. 6.30a

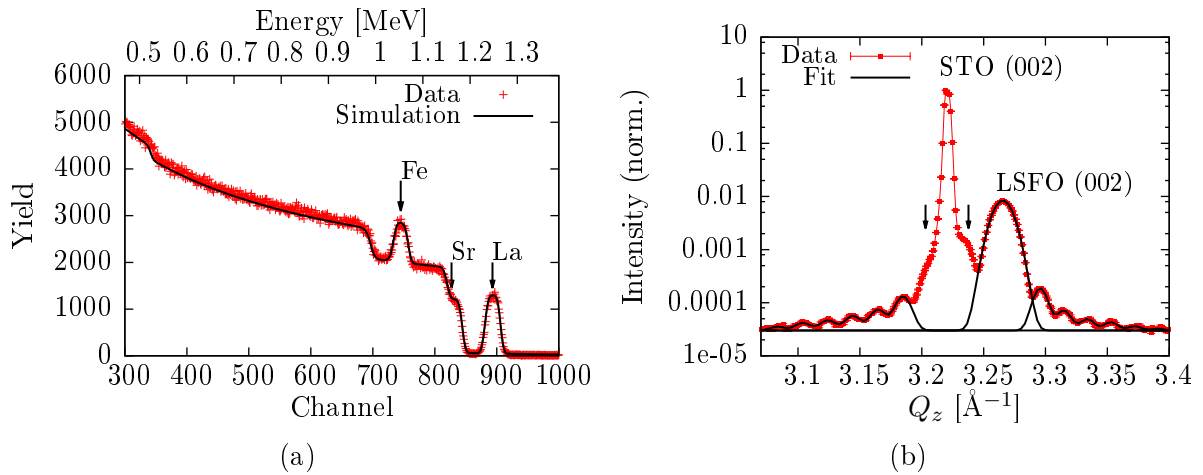


**Figure 6.30:** (a) RBS data and simulation. The measured sample exhibits the composition  $\text{La}_{0.33}\text{Sr}_{0.66}\text{Fe}_{1.03}\text{O}_{3-\delta}$ . (b) Measurement of the (002) reflection. The black line is the fit for each oscillation. The thickness oscillations are clearly visible up to high orders, which also confirms the smoothness and crystallinity of the layer.

shows a RBS measurement of such an optimized layer, which is named  $\text{LSFO}_{\text{final}}$  in the corresponding tables. The composition can be determined as  $\text{La}_{0.33}\text{Sr}_{0.66}\text{Fe}_{1.03}\text{O}_{3-\delta}$ . The determined iron content seems slightly increased from the stoichiometric value of 1, but is within about one  $\sigma$  of the nominal value. The ratio between lanthanum and strontium fits the expected ratio. Thus, the stoichiometry is confirmed within the measurement error (4%). Nevertheless, one has to mention, that the error on the strontium content might be higher due to the substrate's strontium content. As one sees, the contrast between layer and substrate makes it difficult to determine the strontium stoichiometry with high precision. Fig. 6.30b shows the (002) reflection of substrate and layer. The calculated lattice parameter for substrate and layer are listed in Tab. 6.8. The measurement shows clear thickness oscillations on the left and right of the layer reflection which indicate a smooth

surface and good crystallinity as well. From the oscillations the thickness of the layer can be determined as  $330(1) \text{ \AA}$ . This value is in excellent agreement with the thickness parameter obtained from the XRR measurement ( $329.2(7) \text{ \AA}$ ). The surface quality has also been confirmed with LEED, and XRR as depicted in Fig. 6.31. The parameter from the XRR simulation can be found in Tab. 6.7. The optimized sample exhibits a smooth surface

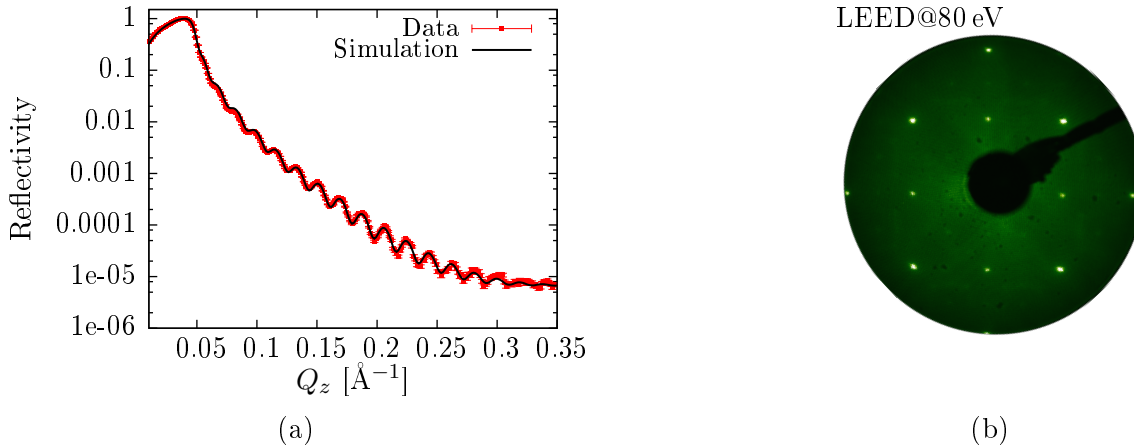


**Figure 6.31:** (a) XRR data and simulation. The parameters are shown in Tab. 6.7. (b) LEED image taken at 80 eV. Very sharp reflections confirm the good surface morphology of the sample.

with a roughness of approximately two unit cells, but still a top layer has to be assumed to simulate the data properly. All samples that have been analyzed need such a surface layer. It is attributed to aging effects or hydrogenation as mentioned. The reflectometry measurement is an ex-situ method, and it is possible that a surface contamination with adsorbed atoms or oxygen loss makes it necessary to assume an additional top layer. In contrast LEED (Fig. 6.31b), which is an in-situ method, does not show any indication of an unusual surface morphology. Contrariwise it shows very clear and sharp reflections, which are attributed to a perfect surface structure.

In conclusion, a sample growth process was developed successfully, which leads to a smooth surface and good out-of-plane crystalline structure. Post-growth annealing steps and reaching the proper stoichiometry are quite important to achieve a good layer. The next parts show the magnetic and electronic characterization of the sample  $\text{LSFO}_{\text{final}}$ .

### 6.3.4 Magnetization of a single layer

As known from powder experiments a paramagnetic to antiferromagnetic transition at around 200 K is expected. Measuring antiferromagnetic thin films is accompanied by lots of problems. From the powder magnetization measurements it is possible to estimate the expected magnetization in the paramagnetic phase right before the transition. The layer mass can be calculated by considering the substrate size and the measured layer thickness as  $3.5 \mu\text{g}$  which leads to an expected signal of  $2 \cdot 10^{-11} \text{ Am}^2$ . This is close to the sensitivity limit of the MPMS [73]. However, as one can see later on, the measured magnetization is

about two orders of magnitude higher. This is most likely attributed to a ferromagnetic phase which could be identified.

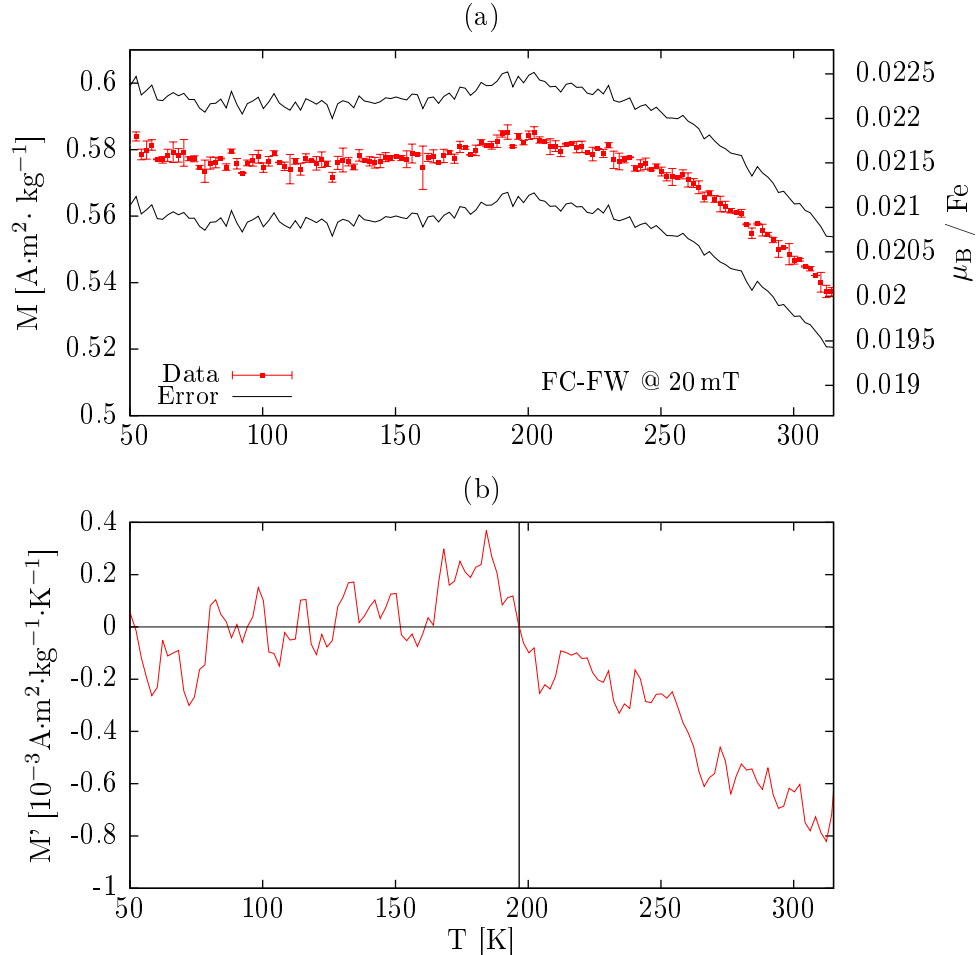


**Figure 6.32:** (a) Magnetization measurement of a LSFO single layer. The measurement has been taken during field-warming after field-cooling in 20 mT along [100]. The red error bars describe the error of the MPMS, whereas the black lines are the maximum and minimum error, which follows from the imprecise determination of the mass of the thin layer, but has the same magnitude for all measurement points. (b) First derivative of the data. The zero of the derivative, which corresponds to a maximum in the data, is at 196(10) K.

In general, it seems to be quite tough to prove the antiferromagnetic properties of the thin film samples with the MPMS. The measurement has been performed between 50 K and 320 K after field-cooling at 20 mT with a magnetic field applied along [100]. Fig. 6.32 (a) shows the measurement data. The red error bars indicate the error resulting from the measurement. The black lines label the maximum error of the value, which comes from the uncertainty of the determination of the sample mass. In spite of the uncertainty the normalization has been used in order to compare different samples and measurements due to the need to cut samples before measurements. From determination of the sample surface size and measuring the layer thickness it is easy to calculate the volume or mass of the samples, respectively.

The measurement shows that there is a broad transition at  $196(10)$  K, which was determined calculating the first derivative of the magnetization data depicted in Fig. 6.32 (b). Different origins are found to cause the broad transition. Fig. 6.33 shows the schematic temperature dependency of the susceptibility of an antiferromagnet.  $\chi_{\perp}$  is the case of the magnetization perpendicular, whereas  $\chi_{\parallel}$  is the case parallel to the applied field. The magnetic field is aligned parallel to the  $[100]$  or  $[010]$  direction of the substrate. One expects an antiferromagnetic alignment along  $[111]$  direction of the pseudocubic unit cell,

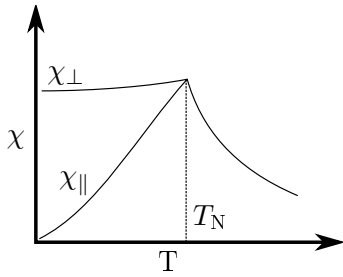


**Figure 6.33:** Schematic explanation of the temperature dependence of the susceptibility of an antiferromagnet.

which is neither parallel nor perpendicular to the applied field. Thus a mixture of both components was measured. Besides the broad antiferromagnetic transition, a ferromagnetic contribution can be identified. If one distributes the measured magnetic moment to the number of Fe atoms, which can be calculated from the mass, the magnetic moment per Fe atom can be determined as  $\approx 0.0215\mu_{\text{B}}/\text{Fe}$ . The origin of this additional component is unclear. Either there are uncompensated spin contributions from the antiferromagnetic arrangement, or the sample contains a pure ferromagnetic phase. For thin films the coupling and canting of the spins can be different, and probably small distortions can cause an alignment in

field direction. Further validation for a ferromagnetic component is shown in Fig. 6.34, which shows a  $M-H$ -measurement at 110 K after the sample has been cooled from 320 K in an applied field of 20 mT along  $[100]$  direction of the substrate. The measurement has been corrected for the diamagnetic background originating from the substrate by using a straight line fitted to the high-field range of a  $M-H$ -measurement.

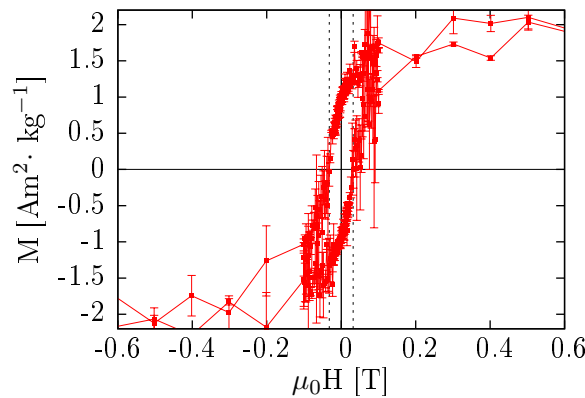


**Figure 6.34:** A  $M-H$ -curve measured at 110 K after field-cooling in 20 mT along  $[100]$ . The dotted lines are describing the coercive field  $H_C$ . The opening of the hysteresis hints a ferromagnetic component.

The saturation is reached at 0.4 T with a magnetic moment of  $0.073(5)\mu_{\text{B}}$  per Fe ion. The squareness, defined as the quotient of remanence and saturation magnetization, can be calculated as  $m_{\text{R}}/m_{\text{S}} = 0.5$ , which indicates an anisotropy in the system. The anisotropy



in the layer has not been further investigated due to sensitivity problems while using the sample rotator option.

As the magnetization data is not convincing, it is difficult to confirm the antiferromagnetic behavior. Obviously, there is a transition at 196(10) K, but an overlaying ferromagnetism from uncompensated magnetic moments in the antiferromagnetic alignment (e.g. spin canting) or an additional ferromagnetic phase is present. An additional phase can originate from the interface between layer and substrate or from the top layer, which exhibits a different stoichiometry and oxygen saturation as shown. If one assumes a purely ferromagnetic layer with Fe moments as expected from an ionic model, the measured magnetization can be caused by a layer with a thickness of only 4 to 8 Å.

Additionally, the confined dimensionality to a thin layer can also influence the magnetic behavior compared to bulk LSFO [114]. Further efforts are necessary in order to investigate the magnetic properties thoroughly. To increase the signal arising from the sample, thicker samples are highly necessary. A direct measurement of the antiferromagnetic ordering with neutrons should be planned, but there the thickness of the layer is a crucial point and a very sensitive instrument has to be chosen.

That LSFO thin films exhibit an antiferromagnetic behavior below  $T_V = T_N$  could be shown with 707 eV soft X-ray resonant scattering by Okomoto et al. [115]. They could confirm at a 1000 Å thick layer grown with Pulsed Laser Deposition (PLD), that the ordering is maintained in the pseudo-cubic [111] direction.

### 6.3.5 Resistivity of a single layer

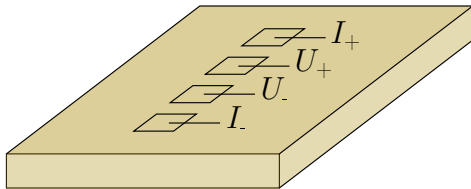


**Figure 6.35:** Four-wire contacting for resistivity measurement. Optionally magnetic fields are applied perpendicular to the sample surface.

The resistivity  $\rho$  of the thin film has been measured with the resistivity option of the PPMS and Dyna-Cool PPMS using both a four-point and a two-point method. To contact the samples to the system platinum wires and silver paste have been used. The arrangement of contacts for a four-point measurement on the sample surface and the corresponding voltage and current contact positions are shown in Fig. 6.35. The measurements are compared qualitatively due to the sample size and the contact size, which are varying between the measurements of the different samples. Initially, we are highly interested

to see the transition clearly, which is undoubtedly measurable. As the surface of the single layer is smooth the contacts made with silver paste are the problem. They can get loose while cooling or heating and thus the measurement is highly influenced by the quality of the contacts. Further efforts have to be done in order to improve the contact quality. For example, depositing of gold electrodes can improve contact quality, but is not part of this thesis.

A limitation is caused by the instrument itself. As described in Section 6.1 the expected change in resistivity is about eight orders of magnitude. The used PPMS system has its measurement limit at 10 MΩ. The absolute value of the resistance of a single conducting layer is in the range of kΩ. Thus, with PPMS it is only possible to measure a part of the

whole temperature range. For a larger resistance the PPMS DynaCool can be used, which provides a 2-point measurement option, and allows to measure up to  $5\text{ G}\Omega$ , but the lowest measurable value is  $10\text{ M}\Omega$ . A combined measurement with both instruments has been used in order to cover the largest possible temperature range. Resistivity measurements of two different samples are presented in Fig. 6.36a and Fig 6.36b. The first sample was grown without post-growth annealing, whereas the latter one was heat treated after the growth process. Both samples show a significant increase in resistivity while cooling. The

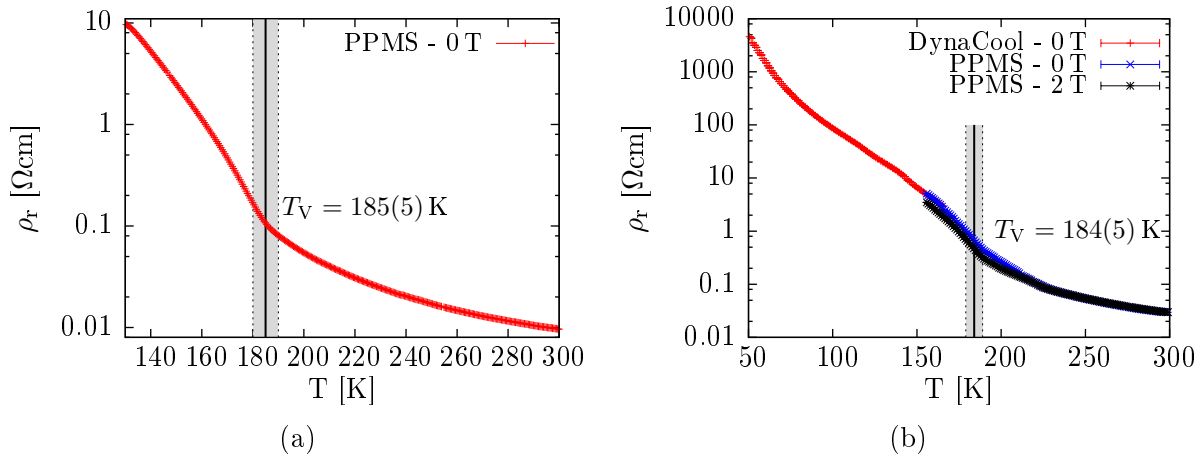


**Figure 6.36:** (a) Resistivity measurement of a sample during cooling prepared without post-growth annealing. In contrast (b) shows a resistivity measurement of a LSFO single layer prepared with post-growth annealing with and without an applied field. To extend the measurement range, a PPMS-DynaCool instrument with a 2-point measurement technique has been used for low temperatures. Both layers exhibit the desired stoichiometry and a layer thickness of  $309\text{ \AA}$ . The first derivative of this measurement is shown in Fig. 6.37.

resistivity increases slightly upon cooling from  $300\text{ K}$  by one order of magnitude, until the transition temperature  $T_V$  is reached. This behavior is similar to a semiconductor. At  $T_V$  a transition from a weak to a high insulating state takes place.

Both samples show a transition at  $T_V = 185(5)\text{ K}$  and  $T_V = 184(5)\text{ K}$ , respectively. The high uncertainty of the measurement due to the technique of fixing the electric contacts does not allow one to measure the absolute value of the resistivity reliably. Especially, the size of the contacts cannot be maintained the same for each sample. The transition itself is smeared for both samples, and a precise determination of the transition temperature is difficult and was done by calculating the first derivative. This is shown in Fig. 6.37. The reversal point, which one finds at the minima, is assumed as the transition temperature. The first derivative clearly shows an minimum at  $184(5)\text{ K}$ . The less pronounced minima at higher temperatures are attributed to measurement artifacts.

There are two different reasons found in literature, which can explain this. Firstly, Xie et al. [104] showed that the stoichiometry of the layers has a significant influence on the transition temperature and shape, which is depicted in Fig. 6.3b in section 6.1. As mentioned the Sr content has a larger error due to the missing contrast between substrate and layer. Nevertheless the magnitude of this effect is small and within the error of the measurement. This means that an possibly improper stoichiometry within the RBS

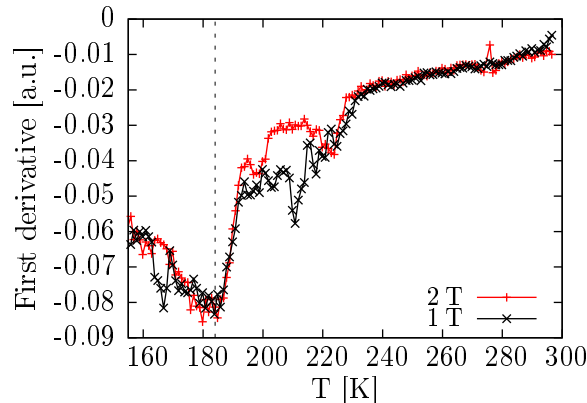


**Figure 6.37:** First derivative of measurement shown in Fig. 6.36b. The minimum of the derivative corresponds to the Verwey transition temperature. The less significant minima are measurement artifacts. A moving window derivative has been used.

measurement error cannot explain the transition which is smeared and shifted to lower transition temperatures. Secondly, Minohara et al. [103] found, that a critical thickness has to be reached for a clear transition as shown in Fig. 6.3a. Unfortunately, these results have been published recently and could not be considered during the sample preparation. The samples used here exhibit a thickness of 309 Å which lies below the critical thickness of 400 Å for a (001)-oriented substrate. This causes an unclear transition with a lower transition temperature, because charge ordering is lost gradually with layer thickness. The underlying physics is still unclear, but Minohara et al. attribute the effect to the isotropic nature of the  $3d$  orbital in the high-spin electronic configurations. They suggest that the charge-ordered state could also be isotropic. If the domain size of the charge-ordered states becomes larger than the thickness of the layer, the charge-ordered state becomes unstable. Then the Verwey transition, which is connected to the charge-ordering transition, disappears. In addition, they report that this effect is irrespective of the crystallographic orientation, which strengthens the assumption, that the isotropic character of the Fe ions plays a crucial role.

One can see that the thickness-dependency related influence is much higher than the effect arising from the stoichiometry variations. Thus, the small layer thickness of the underlying sample is the obvious reason for a smeared transition.

In spite of the not fully developed transition the relative resistivity change between 300 K and 50 K is about five orders of magnitude, which is in good agreement with literature values.

Devlin et al. [40] proposed that the transition indicates a change in the underlying conduction mechanism which is in agreement with the powder characterization results. They could confirm a non-adiabatic small polaron model [116] for temperature above  $T_V$ , which can be described by

$$\rho_r = \rho_{r0} T^{3/2} \exp\left(\frac{W_H}{k_B T}\right), \quad (6.6)$$

where  $W_H$  is the activation energy of the small polaron,  $k_B$  the well-known Boltzmann

constant, and  $T$  the absolute temperature. A short introduction into small polarons is given in Sec. 2.6. Such a small polaron has an extent size of less than one unit cell. Fig. 6.38a shows the non-adiabatic model fit to the measured resistivity. The activation energy  $W_{\text{H}}$  can be calculated as 0.118 eV, which is higher compared to Xie et al., but as expected the clear transition vanishes below  $T_{\text{V}}$  [103].

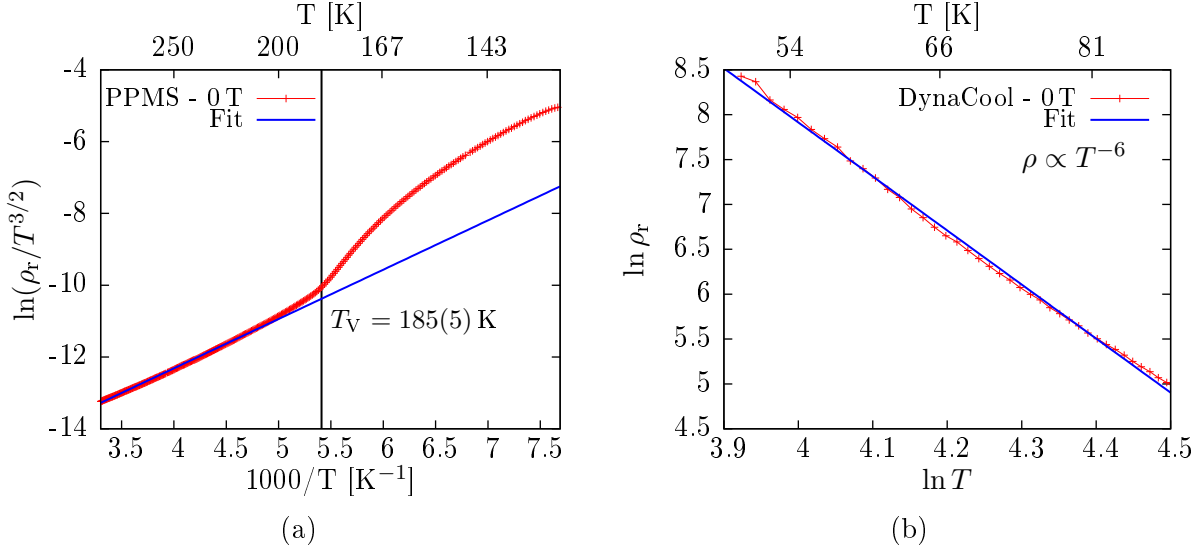


**Figure 6.38:** (a) Replot of the data in order to fit the non-adiabatic small polaron model. The vertical line indicates the position of the transition temperature  $T_{\text{V}}$ . (b) Double ln plot to determine the power law eq. 6.7 according to [40]. The used temperature range was selected to be far below the transition temperature.

It is obvious that the non-adiabatic small polaron model does not fit for temperatures below the phase transition. This indicates a change in the underlying conduction mechanism, which is clearly visible in Fig. 6.38a. However, further reducing the thickness leads to non-adiabatic polaron behavior over the whole temperature range as reported in [103]. Below  $T_{\text{V}}$  the system cannot be described with the non-adiabatic small polaron model. Devlin et al. [40] found a non-exponential function of transport, namely the power law

$$\rho_r = \rho_{r0} T^p. \quad (6.7)$$

The evaluation of the low temperature data measured with a 2-point method at the DynaCool instrument is shown in a double ln plot in Fig. 6.38b. The low temperature range fits to the suggested power law, and  $p$  can be determined as  $-6$ . This power law behavior of the resistivity is unusual [40], and indicates the presence of a novel or unusual transport mechanism below the transition temperature. The mechanism is not yet understood. However, the authors of Ref. 40 assume, that the complex ordering phenomena, the antiferromagnetic structure and charge ordering, is responsible for their observation. As described, the antiferromagnetic ordering sets in at the temperature  $T_{\text{V}}$ . The charge ordering is accompanied by a Verwey and a paramagnetic to antiferromagnetic transition. It is assumed in the Hubbard model, that the electron spin has to be conserved while hopping from one to another atom. This is due to neglecting any terms in the Hamiltonian, which could change the magnetic quantum number, such as spin-orbit coupling. As

reported in [94], for instance, the antiferromagnetic sequence is ...  $\uparrow\uparrow\downarrow\downarrow\uparrow$  ... within one unit cell. This means that ferromagnetically coupled trilayers are coupled antiferromagnetically. Thus the electrons have to hop at least a distance of  $\sqrt{6}a$  with respect to the pseudo-cubic unit cell. This distance can further be increased by consideration of thermal perturbation, which can cause spin fluctuations. However, the hopping distance is fixed by the magnetic ordering. As this explanation is only a hypothesis, further investigations are necessary in order to get a complete understanding of the conduction mechanism appearing in LSFO.

Furthermore, the behavior found by Devlin et al. is in good agreement with the samples treated in this thesis. Within the interpretation of the data according to Devlin et al., the antiferromagnetic behavior can also be confirmed, and in addition the thin film results are in accordance with our powder experiments, where an antiferromagnetic ordering below  $T_N$  can be seen clearly.

### 6.3.6 Conclusion

LSFO single layers on STO have been successfully grown with the OMBE technique. A smooth surface and crystalline structure have been achieved, which can be seen with RHEED, XRR, and XRD measurements. The roughness parameter of the grown sample is less than two pseudo-cubic unit cells. Post-growth annealing is considered as a crucial part of the sample growth, which shows a significant improvement, especially of the crystalline structure of the thin film.

The stoichiometry is the desired one within the measurement errors. To increase the accuracy of the stoichiometry, controlling RHEED oscillation is required. Haeni et al. [117] showed the RHEED controlled growth for STO, where they could achieve a stoichiometry accuracy lower than 1%. RHEED controlling and monitoring was not possible during this thesis due to technical problems and has to be done in future in order to achieve further improvements of the sample quality.

The characterization of the electronic and magnetic properties is more difficult. The macroscopic magnetization features only a weak antiferromagnetic signature and a clear ferromagnetic signal, which cannot be explained from the powder magnetization measurements.

Neutron diffractometry can be used to determine the antiferromagnetic order directly, but is challenging due to the small layer thickness of thin films. However, reflectometry could reveal a ferromagnetic layer at the substrate to LSFO or LSFO to air interface.

The electronic characterization has revealed the expected behavior and the resistivity changes over five orders of magnitude between 300 K and 50 K. As thin films below the reported critical thickness were investigated, a broad transition from a not fully explained conduction regime in the ordered phase to the small polaron model was found, which can be applied above the Verwey transition. Furthermore, the method of performing the resistivity measurement has to be improved. During the experiments the contacts made with silver paste were a major problem. Deposition of gold electrodes and bonding of thin leads will reduce the contact size significantly and will ensure a proper contact during cooling and heating procedures.



## 7 Magnetism in $\text{La}_{2/3}\text{Sr}_{1/3}\text{MnO}_3$ thin films

This chapter is about the growth and characterization of LSMO single layers as one further step to achieve LSMO/LSFO heterostructures. Firstly an introduction into the system LSMO is given, followed by the development of the growth process. Then, the temperature dependence of the macroscopic magnetization is treated, where the focus lies on the manipulation of magnetism due to structural influences of strain mediated by the STO substrate, for instance.

### 7.1 Magnetism in $\text{La}_{2/3}\text{Sr}_{1/3}\text{MnO}_3$

In recent years  $\text{La}_{1-x}\text{Sr}_x\text{MnO}_3$  has been extensively studied by many groups due to its rich structural, electronic and magnetic phase diagram. This versatility is shown in a bulk phase diagram established by Hemberger et al. and is depicted in Fig. 7.1. The strong coupling of manganites between their electronic, spin, and structural degrees of freedom [118] can be easily influenced by changing the chemical composition  $x$ , for instance. The underlying magnetic exchange mechanisms are super- and double exchange, which have been introduced in chapter 2. In monovalent compounds the superexchange is the predominant exchange mechanism, which leads to antiferromagnetic or ferromagnetic coupling according to the Goodenough-Kanamori rules. As the superexchange mechanism is connected to a virtual hopping process of electrons, it leads to an insulating state. By getting different manganese valences while changing the concentration  $x$  the double exchange mechanism sets in. This mechanism is accompanied by a real electron hopping process and leads to a metallic-like conducting and ferromagnetic phase. Besides these doping effects leading to an influence of magnetic, electronic, and structural properties, strain also influences the LSMO behavior significantly. A choice of interesting works concerning this topic will be shown here.

For LSMO thin films with  $x = 0.3$  Adamo et al. investigated systematically the effect of strain applied by different substrates [119]. Furthermore, Mota et al. [19] showed that the STO substrate, which undergoes an antiferrodistortive transition at 105 K, also affects the magnetization of the system, because it applies an additional biaxial strain to the LSMO layer. As the change in strain applied by the antiferrodistortive transition is rather small, as shown in chapter 2, it proves clearly the high sensitivity of LSMO to strain in general. The superexchange interaction in this system is strongly dependent on the Mn-O and  $\text{MnO}_6$  octahedron tilting as described by Mota et al. [19] and Mochizuki et al. [120]. Furthermore the Mn-O-Mn bond angle, which is also affected by strain, leads to a modification of the electron hopping probability. According to the Hubbard model,

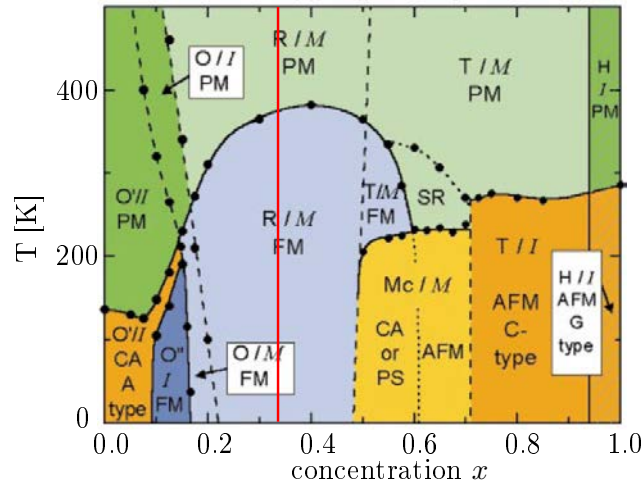


**Figure 7.1:** Structural, magnetic, and electronic phase diagram of  $\text{La}_{1-x}\text{Sr}_x\text{MnO}_3$  from Hemberger et al.. The concentration used here is  $x = \frac{1}{3}$ , which exhibit a rhombohedral crystal structure, and is a metallic-like ferromagnetic material with a bulk  $T_c$  of 370 K. The symbols in the diagram are orthorhombic O, rhombohedral R, tetragonal T, monoclinic Mc, hexagonal H; insulating I, metallic M; ferromagnetic FM, antiferromagnetic AFM, paramagnetic PM. Reprinted from [13], with the permission of AIP publishing.

this leads to change in the exchange interactions as well, which influences the electronic and magnetic behavior of the system [121].

The high sensitivity of LSMO to external parameters motivates a systematical study of the interface in between LSMO and LSFO as the latter provides a large change of the resistivity and enables electronic doping of the LSMO interface region. To investigate the selective manipulation of the interface the LSMO single layers have to be characterized with respect to atomic structure and magnetization first.

## 7.2 Sample preparation and structural analysis

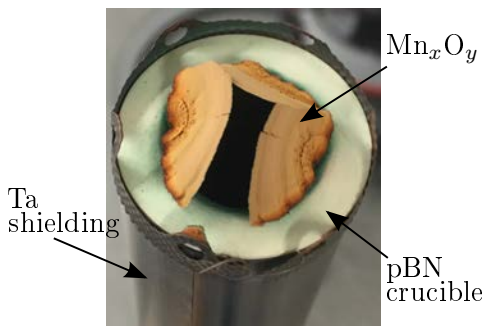


**Figure 7.2:** Image of a closed pBN crucible after two weeks of usage.

The original plan was to grow the LSMO thin films with the OMBE system, because it would lead to very high quality thin films as shown by Zakalek and Schmitz [69,113]. However, the growth processing was overshadowed by technical problems, which made it impossible to grow thin films successfully. The pBN (boron nitrate) crucible, which is the recommended crucible material for the evaporation of manganese, always tended to a complete closure after a few days of operation. The closing process impedes getting stable rates, which are highly necessary in order to grow stoichiometric thin films. Fig. 7.2 shows a closed crucible. The different colors of the closure suggest that at least two different manganese oxides have been formed.

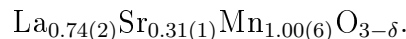


A chemical analysis has not yet been done. Several efforts have been made to overcome this problem. To exclude any contamination of the raw material, manganese pieces from a different manufacturer were used after a HCl cleaning process. Different types of effusion cells with different crucible shapes and filling levels were tested, but did not change the behavior of manganese. A dual filament effusion cell was also bought, which enables the heating of the crucible opening separately and produces a temperature gradient between material and opening. This should make condensation much less likely and should prevent the crucible from a closure, but was also not successful. Furthermore changing the heating and cooling parameters of the cell, as well as the oxygen partial pressure could not solve the problem. Thus, an established method, the high oxygen pressure sputtering technique, has been used in order to achieve high quality thin films. The used HOPSA is introduced in chapter 4.

A commercially (Kurt J. Lesker Company) available stoichiometric target with a diameter of 5 cm has been used to achieve homogeneous and stoichiometric layers. The growth parameters were optimized iteratively under consideration of structural parameters like roughness and crystallinity provided by XRR and XRD measurements. The base pressure of the sputtering chamber is  $3 \cdot 10^{-6}$  mbar(hPa). During the growth process a 120 W plasma has been initiated with an oxygen partial pressure of 2 mbar(hPa). A low growth rate of 90 s per monolayer and a growth temperature of  $T_{\text{growth}} = 1253$  K ensures a good crystalline quality. It is known that complex structures as perovskite structure need time and high temperatures to crystallize with low crystal defects. Besides the oxygen partial pressure low growth rates also ensure oxygen saturation.

Additional annealing steps have been added for quality improvements with respect to surface roughness and crystal quality as shown for LSFO before. For single layers a pre-growth annealing of 5000 s at 1320 K, and post-growth annealing of 1800 s at  $T_{\text{growth}}$  provide the best result. The annealing steps help to heal structural defects of the surface and crystalline structure as shown in detail in chapter 6.3.3.

As the stoichiometry cannot be measured and adjusted during growth, one has to assume that under same growth conditions, the stoichiometry does not change. Thus, reference samples were analyzed with RBS and on occasion the measurement has been repeated to ensure the proper stoichiometry. The stoichiometry for all samples can be given by



The target stoichiometry is not fully maintained during the growth process. This is a consequence of the slow growth process of the sputtering technique in combination with the high vapor pressure of Mn and Sr compared to La. Due to the fixed target stoichiometry a compensation of the loss is not possible. With regard to Fig. 7.1 the LSMO is still in the ferromagnetic and metallic phase. In general the RBS measurement error is not easy to determine, because a lot of effects influence it. Especially the missing contrast between the layer and substrate with respect to strontium makes a precise determination not possible [122]. There is still an uncertainty of the oxygen saturation, and thus  $\delta$  is unknown, because RBS is not sensitive to light atoms. Due to the high oxygen pressure it can be assumed that a saturated state has been reached as shown by Zakalek [113]. Oxygen deficiencies cause a change of the lattice and lead to strain, which was investigated by Dho et al. [123].

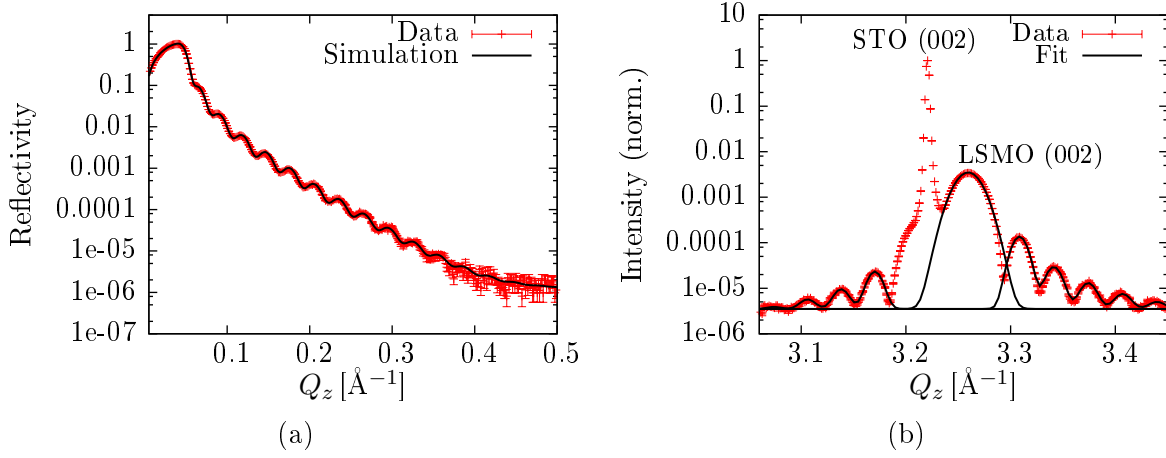


**Figure 7.3:** (a) XRR data and simulation. The corresponding simulation parameters can be found in Tab. 7.1. (b) XRD measurement around the (002)-substrate (STO) reflection. Besides a clear substrate and thin film reflection, thickness oscillations are visible, which indicate a good surface and crystalline quality. The structure parameters are listed in Tab. 7.1.

**Table 7.1:** The left-hand table shows the parameters from simulation shown in Fig. 7.3a. The right-hand table contains the structural parameters as gained from XRD data shown in Fig. 7.3b. The layer's in-plane lattice constant has been calculated from the bulk volume found in [22].

LSMO $d$ [Å]	$192.3^{+1.3}_{-0.1}$		
LSMO $\sigma$ [Å]	$11.7^{+0.9}_{-0.3}$		
LSMO $\rho$ [Å <sup>-3</sup> ]	0.0171	(002)	LSMO substrate
Substrate $\sigma$ [Å]	$5.8^{+0.2}_{-0.2}$	$c$ [Å]	3.8553(3) 3.9027(1)
Top layer $d$ [Å]	$12.2^{+0.1}_{-1.3}$	$a$ [Å]	3.8840(9) 3.9027(1)
Top layer $\sigma$ [Å]	$4.6^{+0.1}_{-0.1}$		
Top layer $\rho$ [Å <sup>-3</sup> ]	0.0140		

XRR and XRD measurements of an optimized thin film shown in Fig. 7.3 confirm the successful sample preparation. The parameters from the simulation of the XRR measurement are shown in Tab. 7.1 on the left. From the LSMO thickness and the growth duration the rate can be calculated to be  $0.043 \text{ \AA/s}$ , approximately 90 s per unit cell. This is necessary to achieve high crystalline quality as mentioned. A low roughness of averaged 2.5 unit cells can also be measured. For a good simulation result a top layer with slightly reduced density has to be considered as described for LSFO in the last chapter. It is most likely an aging effect of the surface caused by the oxygen loss of the surface or hydrogenation, for instance. The interface in bilayer systems is not affected by this effect, and it seems to be reversible under heating in oxygen atmosphere. The thickness of the top layer is only  $12.2 \text{ \AA}$ , but deviates by 20% in density compared to the main layer. It is also imaginable that this is caused by a Mn or Sr depletion of the surface region, which happens due to the used low cooling rates.

The crystal structure is evidenced successfully by measuring out-of-plane reflections. An

experimentally determined substrate out-of-plane lattice parameter (from Ch. 9.2.2) has been used to do a  $\theta_0$  correction. The out-of-plane lattice constant can then be determined as  $3.8553(3) \text{ \AA}$  (Tab. 7.1). This value is averaged over the whole layer thickness and a layer relaxation has not been considered. Maurice et al. [124] reported, that LSMO layers grown with PLD, show a large relaxation length. Layers with a thickness less than  $1000 \text{ \AA}$  do not show a relaxation of the layer lattice parameter to its bulk value. However, PLD is much faster and the results may differ for sputtered samples. As the layer thickness here is less than  $200 \text{ \AA}$ , it can be assumed, that the layer is fully strained. From this assumption and a constant bulk unit cell volume, the in-plane lattice constant can be calculated. However, this is no proof of an in-plane crystallinity. An oriented 2D powder would lead to the same result. Only Bragg reflections with  $h, k \neq 0$  (with in-plane components) can unambiguously prove epitaxial growth. Nevertheless, one gets  $3.8840(9) \text{ \AA}$  under the assumption of epitaxy. As the substrate's in-plane lattice constant is larger, the system is under in-plane tensile strain.

In addition, thickness oscillations are clearly visible, even more clear than in LSFO. They are an interference phenomenon between layer and crystalline structure and only appear for smooth surfaces and are characteristic for a good surface morphology. To determine the distance between the oscillations, the sum of Gaussians has been used. The result for the distance is  $\Delta d = 0.0325(2) \text{ \AA}^{-1}$ , which corresponds to a thickness of  $193(1) \text{ \AA}$ . This thickness is compatible with the main layer thickness determined with XRR, but does not include the top layer within its error. Either the top layer is not crystalline, because the thickness oscillations correspond to the crystalline part of the layer, or the error of thickness determined with the oscillations is larger than expected.

### 7.3 Magnetization influenced by strain

The magnetic characterization has been performed while field-warming after field-cooling (FC-FW) with an applied field parallel to the sample's surface along (100) or (010) with the MPMS. Measurements at different fields are shown in Fig. 7.4. The calculated Curie temperature  $T_C$  is  $330(3) \text{ K}$ , which is smaller than the  $T_C$  expected for bulk LSMO, but it is known that the Curie temperature is reduced for thin films as reported by Boschker et al. [125]. Here the Mermin-Wagner theorem [114] also helps to explain the reduction of  $T_C$ . It describes the destabilization of magnetism while reducing the thickness to a two dimensional layer, which does not show ferromagnetic order.

The measurement at  $70 \text{ mT}$  shows a saturation at  $10 \text{ K}$  with a corresponding averaged magnetic moment of  $3.45 \mu_B$  per Mn atom. A systematic error occurs due to the determination of the sputtered area and thickness, which was used to calculate the magnetic moment per formula unit and magnetization. It is approximately  $1\%$ , but may reach higher values due shadowing effects at the corners and edges. The manganese atoms in the system are  $\text{Mn}^{3+}$  and  $\text{Mn}^{4+}$  with the ratio  $2:1$  under assumption of a stoichiometric sample. Thus, both ions carry different magnetic moments corresponding to  $S = 2$  and  $S = 3/2$ , respectively, which gives an average magnetic moment of  $3.7 \mu_B$ . Under the assumption that the reduction of magnetization is caused by the change in stoichiometry the changed ratio between both Mn ions can be calculated as  $1:1.92$  with the systematic

error mentioned above. Furthermore the oxygen saturation also plays a role, because it influences the crystal structure as reported in [113]. This can cause a damping of the magnetization. And, of course, the destabilization of the magnetization explained by the Mermin-Wagner theorem can play a crucial role, but thicker layers were not analyzed. The measurement at 10 mT shows a significant change in magnetization at 105 K. As men-

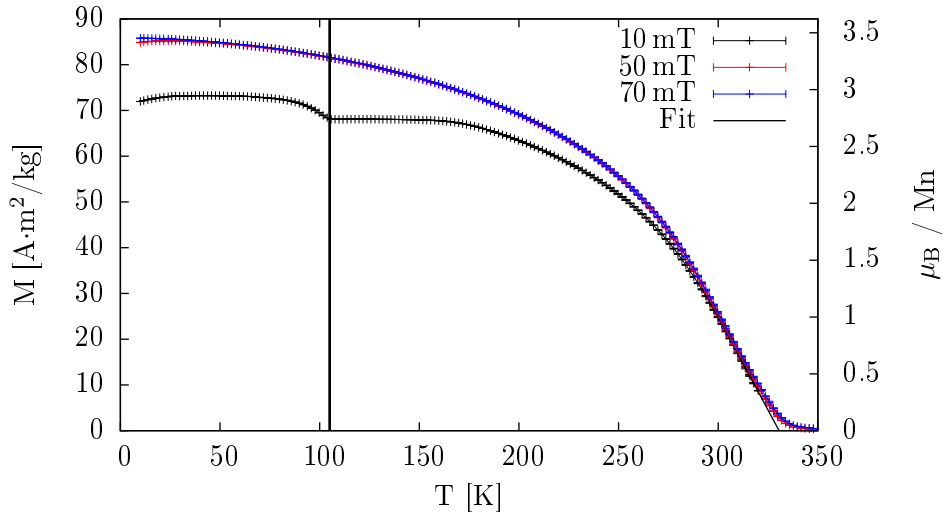


**Figure 7.4:** Field-cooling magnetization measurements at different fields. A linear regression has been used to determine the transition temperature  $T_C = 330(2)$  K for the 10 mT measurement, because the measurement ends at 320 K. The vertical line indicates the substrate's antiferrodistortive transition at 105 K, which significantly influences the magnetization.

tioned in chapter 2, STO undergoes an antiferrodistortive transition at this temperature, where the structure changes from cubic to tetragonal. This temperature is called  $T_{\text{STO}}$ . As the in-plane lattice parameter shrinks at the phase transition, the biaxial in-plane strain also changes. The additional strain does not affect the Mn-O bond length, but changes the Mn-O-Mn bond angle significantly as reported by Miniotas et al. [121] and consequently leads to a change of the superexchange interaction as discussed earlier. In addition, Mochizuki et al. [120] reported a tilting of the  $\text{MnO}_6$  octahedron. Both effects can stabilize the magnetic structure significantly as shown by Moto et al., who reported a significant change in  $M - H$ -measurements. The increase of the coercive field and the remanence has been interpreted by them as a stabilization of the magnetism in the system. This also explains the increase of the magnetization below  $T_{\text{STO}}$ . The effect is large for small fields and vanishes at a field, which is sufficient to magnetically saturate the sample. This is a hint, that 70 mT is sufficient to saturate the measured sample.  $M - H$ -measurements were not done. A further consequence of the structural changes induced by the substrate can be a reconstruction of the magnetic domain pattern as also suggested by Mota et al. [19]. In the case of the 70 mT measurement, where magnetic saturation of the LSMO layer has been reached or nearly reached, the effect is suppressed as a (almost) single domain state is present. In contrast, cooling in a field, which is not sufficient to reach saturation, the picture changes drastically. The unsaturated state, which is not a thermodynamical equilibrium state, can be easily affected by the structural phase transition.

Fig. 7.4 shows a demagnetization effect for the 10 mT and 50 mT at temperatures around 10 K. The decreasing kinetic energy of the system enables an antiferromagnetic-like orientation [126] of the different magnetic domains due to magnetic dipole interaction. The measurement at 50 mT also shows a small demagnetization effect at low temperatures, in contrast to the 70 mT measurement. Above this demagnetization both measurements coincide.

## 7.4 Conclusion

It could be shown that the sputtering process performed with HOPSA is an appropriate method for the growth of nearly stoichiometric LSMO layers. The optimized growth process leads to smooth thin films with high crystalline quality, which make them ideal for growing heterostructures.

The magnetization exhibits a sensitive behavior while changing the substrate structure from cubic to tetragonal, which confirms a high sensitivity to external parameters of LSMO. It shows that LSMO is ideally suited for manipulation of an interface to a material like LSFO, which potentially dopes the LSMO nearby electronically.



## 8 Interface effects in $\text{La}_{1/3}\text{Sr}_{2/3}\text{FeO}_3/\text{La}_{2/3}\text{Sr}_{1/3}\text{MnO}_3$ heterostructures

In chapter 6 and chapter 7 the versatility of LSFO and LSMO single layers is introduced in detail. The following chapter is about heterostructures built of both materials. Furthermore the influence of the stacking, LSFO/LSMO or LSMO/LSFO, was investigated with regard to structural and magnetic properties.

### 8.1 Sample preparation and structural analysis

A successful combination of two well-established growth methods was used in order to achieve high-quality heterostructures regarding the single layer results. Although the two different system are not connected physically to each other high quality samples could be achieved. The combination of two systems was inevitable, because of technical problems with the OMBE system as discussed in chapter 7. Using these two methods means that the vacuum has to be broken for a sample transport under atmospheric pressure to the second growth system which is either the HOPSA or the OMBE system. Possible contaminations during the transport of the samples are cured by performing short annealing steps before the actual growth processes. A LEED measurement at 80 eV, shown in Fig. 8.1, with clear and sharp reflections confirms a high surface quality after transferring a LSMO sample from the HOPSA to the OMBE system even without annealing. However, the different growth methods and the additional heat treatments may influence the interface behavior compared to a sample, whose layers were grown one after another in one single system.

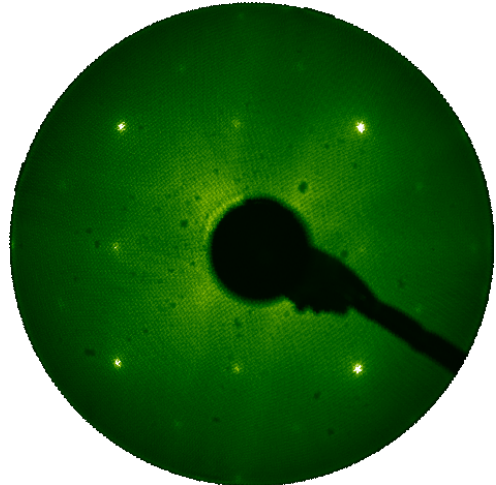


**Figure 8.1:** LEED image measured at 80 eV after transferring sample from HOPSA to the OMBE system. Clear and sharp reflections indicate a good surface morphology.

The kinds of investigated samples and the definition of the sample names are shown in Fig. 8.2. The sample name is chosen according to the last grown layer and is LSFOfinal and LSMOfinal, respectively, for the following chapter.

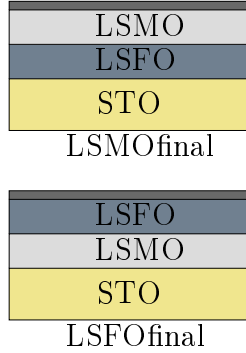


**Figure 8.2:** Different sample stacking and connected sample names.

The used growth processes are adopted from the developed single layer processes including the high growth rate stability which is necessary to avoid a stoichiometry gradient during growth. The rate stability was better than 1% per hour and thus within the measurement error of the quartz microbalance and RBS measurement. The growth duration for each single layer was 4500 s. Anyhow, to avoid re-evaporation of the first grown layer, the pre-growth annealing time and temperature for the second layer was adjusted. To reduce the effect of interdiffusion within the interface region, the post-growth annealing time and temperatures were also reduced. The effect of these changes has been checked using LEED, RHEED, and XRR measurements with respect to the surface and layer quality, and interface roughness.

The final LEED pattern measured at 80 eV for LSFOfinal is shown in the inset of Fig. 8.3c, whereas Fig. 8.3a depicts the LEED image of the LSFO layer before the transfer to the HOPSA chamber. Sharp and high contrast reflections indicate a good surface crystallinity. Additional RHEED and LEED images at different energies are shown in appendices D.3 and D.4. Besides the bright reflections weak sublattice reflections are found for both LSFO layers, clearly visible in the LEED images shown in the appendix (white arrow points to a main reflection; red arrow points to a sublattice reflection). They disappear for higher energies, and thus are only caused by surface atoms. They are caused by a surface reconstruction which appear due to symmetry breaking at the surface where dangling bonds exist and rearrange, for instance.

A summary of all used growth parameters for each layer and sample can be found in the appendix D.3 and D.4, respectively. All measurements performed in the following sections are done with the same two samples.

Fig. 8.3a, and Fig. 8.3c depict the data and simulation of the in-house XRR measurements. The parameters from the simulation are shown in Tab. 8.1, whereas the SLD  $z$  dependence is shown in Fig. 8.3b and Fig. 8.3d. Both layers in both samples exhibit almost the same roughness parameter, which are in the order of one atomic unit cell. As shown throughout the whole thesis, a toplayer is necessary to simulate both samples properly. It is also clear to see that the LSMOfinal exhibits a larger surface roughness compared to LSFOfinal, because the reflectivity of the former decays faster as roughness leads to diffuse scattering which no longer contributes to the specular reflectivity. The increased roughness is most likely attributed to the surface of the toplayer. In particular, the interface in between both layers for both samples is not affected and exhibits a similar roughness. However, one has to mention that X-rays are not suitable to distinguish between iron ions and manganese ions, because the scattering length of both are similar, and no contrast is provided. Interdiffusion of Fe or Mn into their counterpart cannot be probed reliably, and is measured with EDX as presented in the next section.

Another anomaly concerns the SLD of the LSFO layer in both samples. LSFOfinal shows



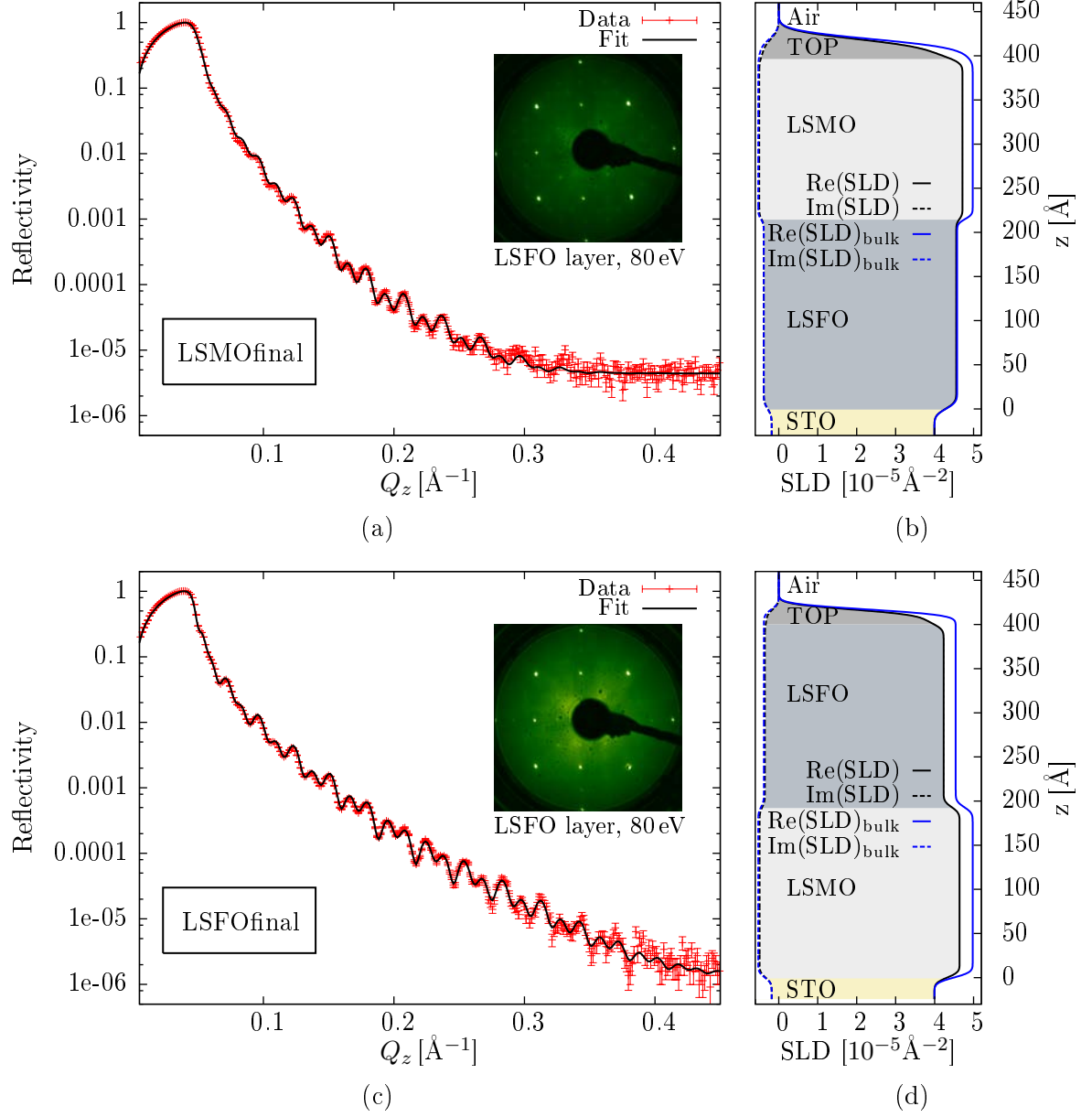


**Figure 8.3:** XRR measurement and simulation of LSMOfinal (a) and LSFOfinal (c), respectively. (b), (d) Corresponding SLD obtained from the simulation. The data analysis was done with GenX [52]. Both samples exhibit neglecting diffuse scattering. Thus, a correction of the specular reflectivity was not done. Insets show a LEED image measured at 80 eV after LSFO deposition, and for LSMOfinal before the deposition of LSMO.

a reduced SLD of the LSFO layer compared to LSMOfinal and to single layers of LSFO. Anyhow, the out-of-plane crystal structure does not show significant differences. The XRD measurement of the (002) reflection is shown in Fig. 8.4 and reveals comparable lattice parameter for both samples which are shown in Tab. 8.2. This result is also as expected from single layer results. However, both layers, LSFO and LSMO, have similar lattice constants, and thus one cannot distinguish and compare both layers within

the same sample. Nevertheless, both layers exhibit a very good crystallinity as shown in

**Table 8.1:** Parameters (thickness  $d$ , roughness  $\sigma$ ) from simulation shown in Fig. 8.3 concerning both samples, LSMOfinal and LSFOfinal, respectively.

	LSMOfinal	LSFOfinal
LSFO $d$ [ $\text{\AA}$ ]	$214.7^{+0.7}_{-0.5}$	$207.3^{+0.5}_{-0.5}$
LSFO $\sigma$ [ $\text{\AA}$ ]	$4.3^{+0.5}_{-0.2}$	$5.2^{+0.2}_{-0.4}$
LSMO $d$ [ $\text{\AA}$ ]	$182.7^{+1.4}_{-0.3}$	$192.9^{+0.9}_{-0.6}$
LSMO $\sigma$ [ $\text{\AA}$ ]	$5.3^{+0.5}_{-0.1}$	$4.0^{+1.0}_{-0.1}$
Substrate $\sigma$ [ $\text{\AA}$ ]	$5.5^{+0.3}_{-0.3}$	$4.8^{+0.5}_{-0.5}$
Top layer $d$ [ $\text{\AA}$ ]	$21.4^{+0.2}_{-0.2}$	$16.7^{+0.2}_{-0.4}$
Top layer $\sigma$ [ $\text{\AA}$ ]	$8.4^{+0.1}_{-0.2}$	$5.2^{+0.1}_{-0.1}$

Fig. 8.4. Thickness oscillations in both samples are a result of a good surface morphology combined with a good crystalline quality and provide information about the total crystalline thickness of the heterostructure. In LSMOfinal, indicated by three arrows in Fig. 8.4a pointing to minima, an additional period is present and can be attributed to the single layer thickness, which is approximately half of the bilayer thickness, and thus twice the oscillation period in  $Q$  space. The interference of both contributions is destructive and leads to a damping of the bilayer oscillations at these positions.

This supports the conclusion that the bilayer system has a very good quality. LSFOfinal only shows a very weak second period which cannot be identified. An evaluation

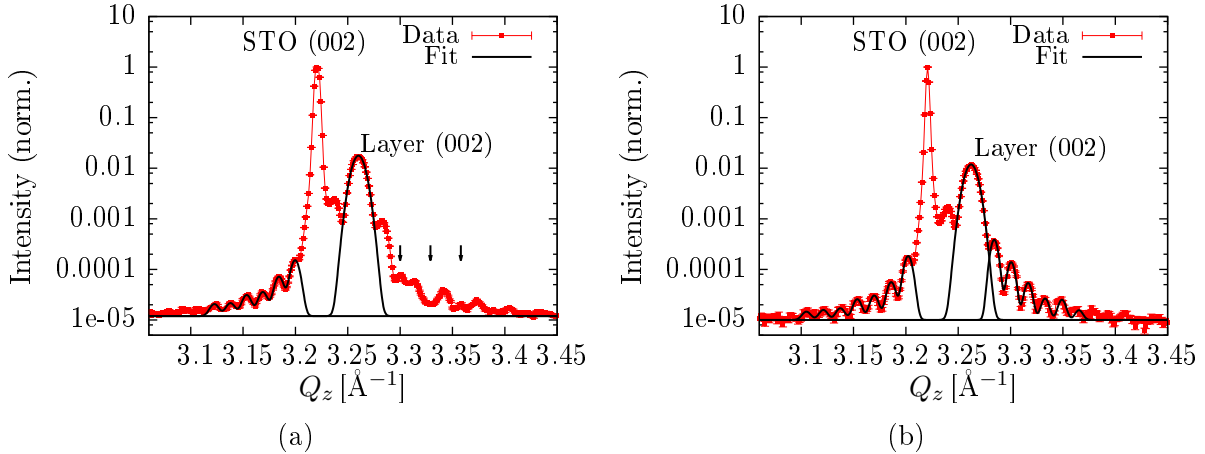


**Figure 8.4:** (002) - measurement of sample LSMOfinal (a) and LSFOfinal (b). A  $\theta_0$  correction was applied. The thickness oscillations were analyzed by applying a sum of Gaussians, which consider the distance between oscillations as a parameter. The thickness oscillations are attributed to the total thickness. However, in (a) a second period was found (see arrows), which is identified as oscillations caused by the single layers. The arrows point to the minima of the second oscillations indicating a destructive interference which extinct the bilayer oscillation significantly.

of the thickness oscillations gives  $407(2) \text{\AA}$  and  $388(2) \text{\AA}$  for LSMOfinal and LSFOfinal,

respectively. For LSMOfinal it is in good agreement with the parameter gained from XRR measurement and confirms crystallinity for the whole bilayer. In contrast, the thickness got from the oscillations for LSFOfinal is slightly reduced. However, except of a small part, the bilayer is crystalline and the surface morphology is good. The small part which does not fit into the interpretation is caused by the toplayer. It shows a different structure as seen from XRR measurements in Fig. 8.3.

**Table 8.2:** Out-of-plane lattice parameter calculated from (002) - reflection of the respective sample is shown.

	LSMOfinal	LSFOfinal
$c$ [Å]	3.8545(1)	3.8520(1)

Fig. 8.5 (a) shows a High-Angle Annular Dark-Field (HAADF)-STEM overview image of sample LSFOfinal. HAADF is an imaging technique which exhibits a Z contrast and enables to do STEM imaging element specific [77]. Details about the sample preparation for the measurement and the measurement itself is shown in Sec. 5.2.7. Both the sample preparation and the measurement was done under the coordination of Juri Barthel, ER-C at Forschungszentrum Jülich.

The measurement shows a pseudo-cubic structure and the A- and B-site of the perovskite structure can be identified as shown in the magnification in Fig. 8.5b. The interface in between LSFO and LSMO is not as sharp as expected. It exhibits a wavy and buckled interface within a few unit cells although the contrast between both layers is low. This is attributed to roughness and was also found for sample LSMOfinal, which is not shown here. Nevertheless, the measured area shows a very well-ordered structure and no structural defects are visible. The spatial resolution of the instrument is about 1 Å, and a precise measurement of lateral strain is not possible, but was also not intended.

Besides the structural information also chemical information was collected through EDX. Therefore, the spatially resolved characteristic X-ray radiation of the specimen was analyzed in order to achieve chemical imaging. For both samples, LSFOfinal and LSMOfinal, the reversal of the approximate 2:1 ratio of Sr and La, and La and Sr, respectively, at the interface could be estimated from the respective line intensity ratios (example is given in appendix D.4.). However, both samples show more or less interdiffusion of Mn and Fe within the interface region. The measurement of Fe and Mn in sample LSMOfinal is depicted in Fig. 8.6. (a) shows the combined HAADF and EDX map, whereas (b) shows an integrated line profile across the interface generated from the map in (a). The approximated interface is indicated by a dashed line in both figures. The maxima of the oscillations correspond to the positions of the Fe and Mn ions, respectively, and are described by the lattice parameter  $c$  which could be determined as 4.0(2) Å. This is in good agreement with the XRD measurements.

LSMOfinal revealed a strong interdiffusion of Fe into the Mn layer, whereas the Mn diffusion is limited to the interface itself and the first following monolayer. The Fe diffusion to the LSMO layer is significant for at least nine monolayers, and cannot be neglected.

Fe and Mn occupy the same positions in the perovskite structure in LSMO (indicated

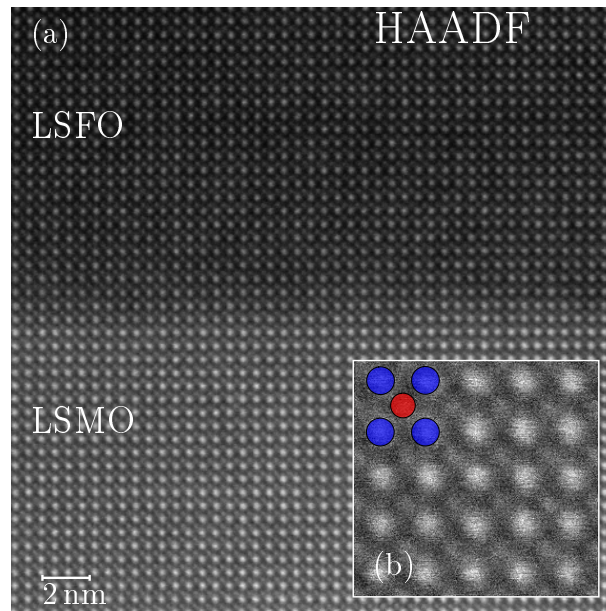


**Figure 8.5:** HAADF-STEM image of the well-ordered interface region of sample LSFOfinal in (a). The interface is not sharp, but is slightly waved and buckled. The inset (b) is a magnification to identify the perovskite structure with its A- and B-sites as indicated by colored spheres.

by red dashed lines in Fig. 8.6b). This fact evidences the interdiffusion of Fe into Mn B-site positions of the perovskite structure near the interface. Most likely the growth temperature of the second layer, which is LSMO, supported the interdiffusion of Fe into the growing LSMO layer. A re-evaporation of Mn during the growth can occur and consequently Fe can easily occupy the former Mn lattice positions.

In spite of overlap of the  $\text{Fe-K}_\alpha$  and  $\text{Mn-K}_\beta$  lines [127], a mixing of both signals cannot explain the large signal of Fe in Mn and it is expected to be real.

In contrast, sample LSFOfinal does not show such strong interdiffusion of Fe into the Mn-rich layer which also supports the idea that the growth mechanism itself caused the observed effects, and that the stacking sequence somehow influences the interdiffusion in the interface region. The corresponding results are depicted in Fig. 8.6, (c) shows the HAADF and EDX combination, (d) the line profile across the interface. Significant intermixing can only be observed at the interface layer. A weak Mn signal is also observed in one further unit cell above the interface. The very weak signal in the following unit cell is attributed to the overlay of the  $\text{La-L}_\gamma$  spectral line which is very close to the analyzed  $\text{Mn-K}_\alpha$  transitions. In addition one has to mention that the EDX signal in general is very weak, because only a few atoms in a layer contribute. This causes relatively large error bars and a quantitative predication with high precision is not possible.

In summary, epitaxial heterostructures of LSMO and LSFO were prepared by a combination of HOPSA and OMBE system. They show low roughness parameter and a good crystalline quality, but also exhibit interdiffusion of Fe and Mn within the interface region. Intriguingly, significant differences in the interdiffusion appear. Whereas LSFOfinal only shows low interdiffusion, LSMOfinal exhibits interdiffusion of Fe in more than one mono-

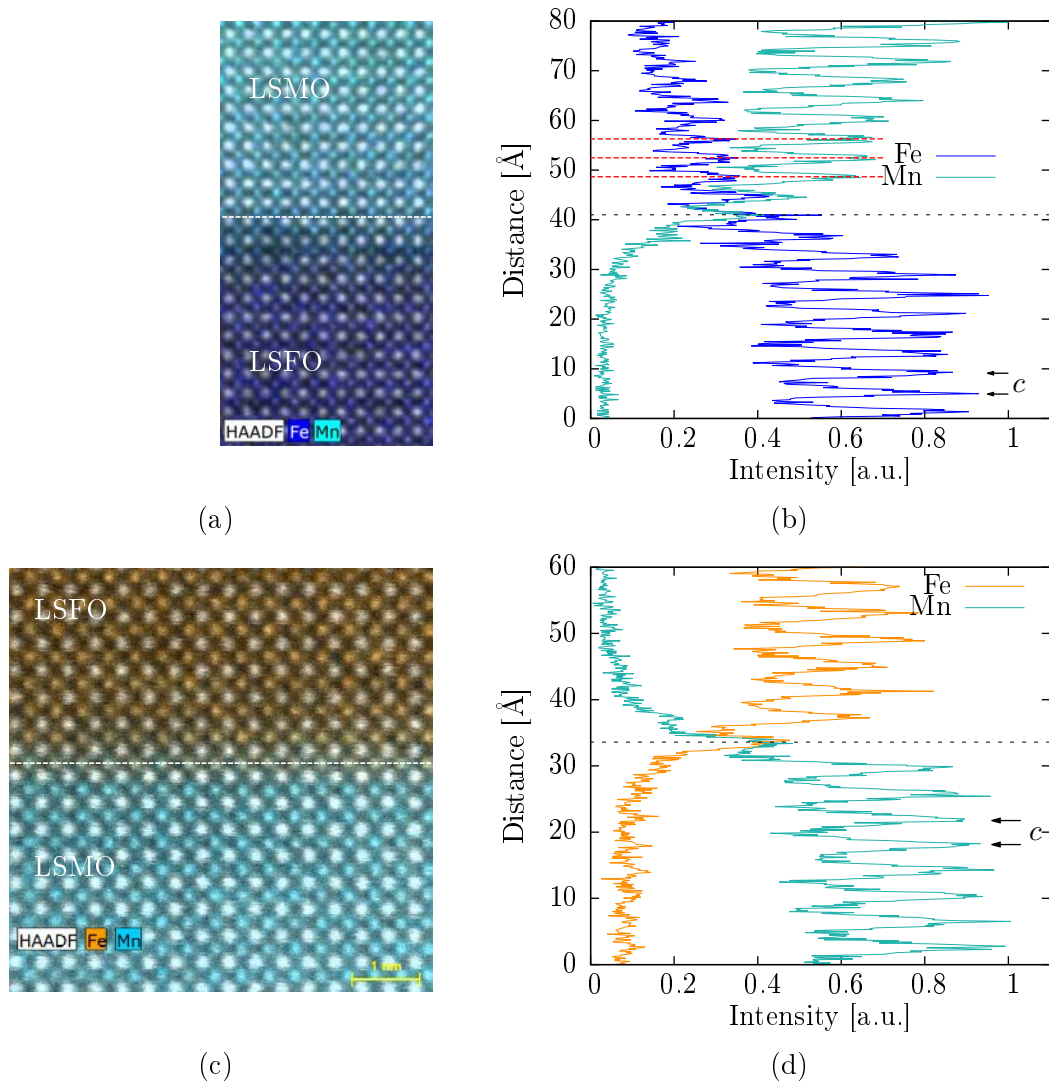


**Figure 8.6:** (a) HAADF-STEM image of sample LSMO<sub>final</sub> including EDX information. Mn ions are colored light blue, Fe ions dark blue. The dashed line estimates the interface between LSMO and LSFO. (b) laterally integrated EDX signal. A clear diffusion of Fe into the LSMO layer is observable. (c) HAADF-STEM image of sample LSFO<sub>final</sub> including EDX information. Mn ions are colored blue, Fe ions orange. The dashed line estimates the interface between LSMO and LSFO. (d) Corresponding EDX signal. Only little interdiffusion nearby the interface can be observed.

layer. It shows interdiffusion into at least nine monolayers from the interface. Obviously, Fe in LSMO<sub>final</sub> is very mobile and diffuses into the LSMO layer easily and equal atomic positions for Mn and Fe evidenced by EDX are found. Thus, the Fe occupies Mn sites, and this could be related to the high Mn vapor pressure, so that Mn re-evaporates from the surface during the growth process.

## 8.2 Macroscopic magnetization

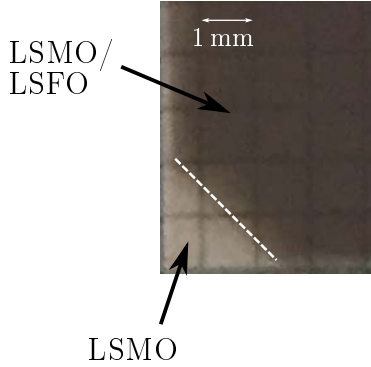


**Figure 8.7:** Sample holder shadowing during LSFO growth.

The magnetization measurements discussed in this section were performed at MPMS unless otherwise specified. For the measurements the sample had to be broken in order to get small sample pieces which are suitable for the MPMS namely approximately 20 to 30 mm<sup>2</sup> (Fig. 8.7). However, STO as an oxide is very hard and it is not easy to cut it. A band saw was not used to prevent the sample from magnetic contaminations. The samples were broken with the help of a glass microscope slide, which mostly did not result in a well-shaped sample piece. The pieces used for the measurement are not similar and for comparison of different sample types a normalization had to be done. The surface area of the samples was determined, and then the quantity of mag-

netic ions and the mass of the grown layers could be calculated under consideration of the XRR thickness values. LSMO is the ferromagnetic compound and thus the magnetization and magnetic moment per magnetic ion of the sample is attributed to this part of the bilayer. Due to the uncertainty of the sample area and thickness as well as the top layer which differs from the original LSMO the systematic error of this measurement might be high and can reach 10%, due to error propagation of several contributions. In contrast, the statistical error is fairly low as depicted by error bars in the corresponding plots. A second problem is illustrated in Fig. 8.7. During LSFO growth with the OMBE system the edges of the samples are somehow shadowed by the sample holder, but during LSMO growth with HOPSA this problem was not present. However, this leads to a contribution of pure LSMO on STO to the signal which is not covered or buffered by the LSFO layer. Thus, all measurements contain a little contribution (up to approximately 15%) of pure LSMO on STO. Additionally, all measurements were corrected for their diamagnetic signal.

In the previous section the structural differences of both samples were discussed in detail. Especially, the interdiffusion within the interface between LSFO and LSMO is significantly different, and thus the assumption that also the magnetic properties are different seems likely.

Curie temperatures  $T_C$  were determined as 345(3) K for LSMOfinal and 333(6) K for LSFOfinal, respectively, as shown in the measurements shown in Fig. 8.8. LSFOfinal exhibits a  $T_C$  which is comparable with the LSMO single layer on STO discussed and determined as  $T_C = 330(2)$  K in chapter 7. However, LSMOfinal exhibits a difference of 12 K which is astonishing and must be related to the growth procedure itself. With regard to the complex phase diagram of LSMO [13] an increase of  $T_C$  could be a consequence of a change in stoichiometry or structure caused by the aforementioned interdiffusion.

Firstly, the LSFO surface beneath exhibits different surface properties compared to STO which can make the change in strain, for instance. That strain influences the magnetic properties which includes  $T_C$  as shown by Adamo et al. [119]. Secondly, to prevent the

system from interdiffusion the post-growth annealing was changed which can influence the stoichiometry as well, because re-evaporation processes are suppressed for lower annealing temperatures. It was decided not to do a systematic study of annealing influences on the layer quality. A verification with RBS was not possible as the characterization of similar layers without significant contrast is quite difficult as mentioned earlier. In addition, EDX could also not answer this question with sufficient accuracy.

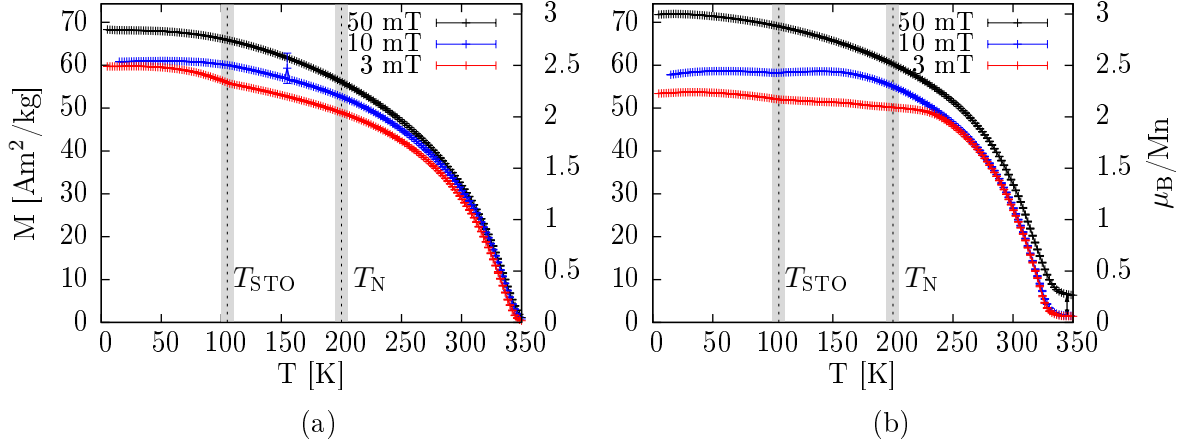


**Figure 8.8:** Magnetization measurement of LSMOfinal (a), which exhibits high Fe interdiffusion to the LSMO layer, and LSFOfinal (b) during field-warming after field-cooling. The field was applied parallel to a [100] direction of STO.

The temperature dependent magnetization measurement shows sample specific differences as shown in Fig. 8.8. The measurement was performed during field-warming after field-cooling (FC-FW) in different magnetic fields applied along the [100] direction of STO. LSMOfinal as shown in (a) shows an significant increase of the magnetization at the structural phase transition of STO for low applied fields (3 mT) as known from single layer LSMO discussed in chapter 7, and is attributed to domain structure changes for unsaturated samples while passing the STO transition temperature due to applied strain. In addition, the 10 mT measurement shows a small demagnetization effect at low temperature which is also caused by the influence of changes in strain reported by Mota et al. [19]. However, LSMO is actually buffered by LSFO which does not show any structural changes near  $T_{\text{STO}}$  and it is not expected that the strain is mediated through 50 unit cells LSFO. This effect is most likely attributed to the shadowing effect during LSFO growth as discussed above and shown in Fig. 8.7. This effect is related to the edges and does not reflect the whole layer. It was not possible to get rid of the shadowed parts of the sample without running the risk of losing the sample.

With regard to the  $M - H$ -measurements presented in Fig. 8.9 for different field-cooling fields, the highest applied field (50 mT) is not sufficient to saturate the samples magnetically. The saturation magnetization gained from the 10 K  $M - H$ -measurements is  $M_{\text{S}} = 3.04(2)\mu_{\text{B}}$  per Mn ion and is lower than the magnetization  $M_{\text{S}} = 3.45\mu_{\text{B}}$  per Mn ion as obtained from the single layer measurement at the same temperature. However, the field for reaching a saturated state is comparable (70 mT). As Fe ions occupy Mn

sites partially, the magnetization nearby the interface may be reduced and explains the reduced saturation magnetization, which is normalized with respect to the whole LSMO layer volume.

Heterostructures with manganite thin films tend to show magnetically dead-layers as reported by Peng et al. [128], for instance. The creation of these layers is not well understood, but most likely doping of the interface by interdiffusion influences the double-exchange interaction, and directly influences the magnetization and conductivity. Additionally, magnetic reconstructions at the interface also influence the creation of a dead-layer as reported by Bruno et al. [129]. Together with the increased  $T_C$  it indicates that the layer properties are different compared to the single layer and LSFO<sub>final</sub> sample.

LSFO<sub>final</sub>, where interdiffusion is not significant, exhibits a magnetization in saturation of  $3.5(1)\mu_B$  per Mn ion. This is in good agreement with the single layer measurement. However, this sample shows differences in the temperature dependency of the magnetization. As expected it shows influences caused by the structural phase transition at  $T_{\text{STO}}$ , but also an additional decrease at around 150 K for the 10 mT measurement, a kink at around 240 K and a slight decrease of magnetization at 150 K for the 3 mT measurement. The demagnetization in both samples is most likely a consequence of an antiferromagnetic interlayer coupling. The demagnetization in an antiferromagnetic coupled superlattice was reported by Ziese et al. [130], for instance. However, this means that the  $T_N$  is significantly lower than expected and is caused by destabilization of the antiferromagnet due to finite size as discussed for charge ordering and the Verwey transition earlier. This effect vanishes at the 50 mT measurement, and thus the interlayer coupling might be weak and can be easily overcome by an applied magnetic field. A further explanation is the influence of the change of the charge carrier concentration caused by the LSFO Verwey transition which would lead to a change in magnetization regarding the LSMO phase diagram by electronic doping. A systematic study with PNR will be discussed in section 8.3, where the depth resolved layer magnetization is a central point of discussion.

A further difference is an additional ferromagnetic phase which can be seen as a shift in  $y$  direction of the 50 mT measurement in Fig. 8.8b with a high  $T_C$ .  $M - H$ -measurements as depicted in Fig. 8.10 for temperatures up to 380 K show a ferromagnetic behavior with a coercive field  $H_C = 20$  mT at 350 K. The measurements were performed with VSM option of the PPMS. 380 K was the highest temperature which could be reached and obviously the transition temperature of the additional phase is higher and could not be determined. As the contribution to the overall magnetic moment is fairly low ( $0.1 - 0.2\mu_B$ ) per Mn ion it is possible that an additional ferromagnetic layer or domain with a different compound has been formed with high  $T_C$  and high  $H_C$ , but cannot be evidenced. Besides the differences of both samples with regard to the FC-FW measurements, the  $M - H$ -measurements at low temperatures show significant differences. Sample LSMO<sub>final</sub> does not show a strong temperature or field-cooling dependence as shown in Fig. 8.9. However, a small change in anisotropy can be found as the squareness  $S$  changes.  $S$  is a measure for anisotropy in the system and defined by  $S = \frac{M_r}{M_s}$ , the quotient of remanence and saturation magnetization. The squareness shows an increase below  $T_{\text{STO}}$  from 0.78 to 0.85. A brief introduction of magnetic anisotropy is given in section 2.5. The anisotropy change is caused by the structural changes in STO as interpreted as strain anisotropy. Furthermore, an exchange bias effect with  $H_E = -1$  mT could be measured, where the field



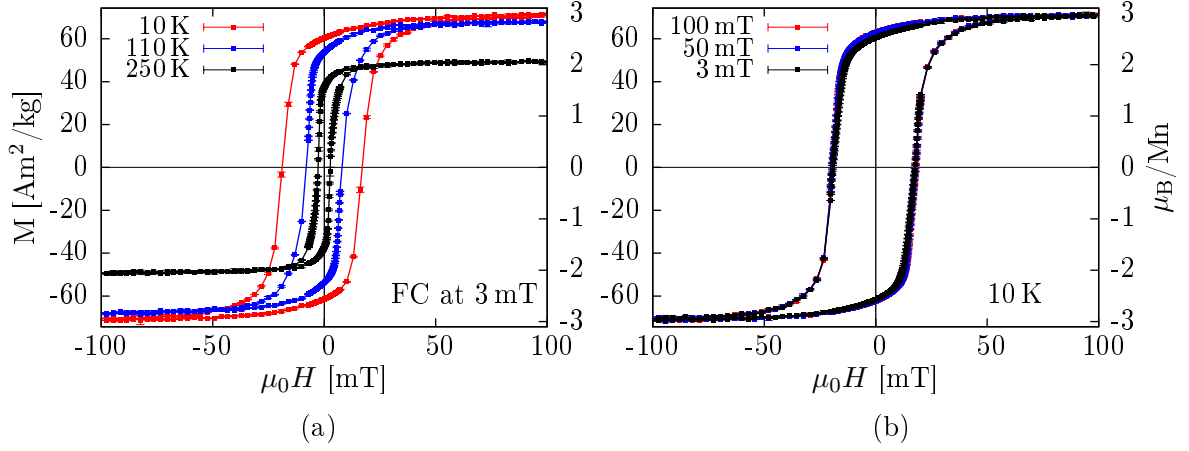


**Figure 8.9:**  $M - H$ - measurements of LSMOfinal. (a) shows hysteresis loops at different temperature after field-cooling at 3 mT. (b) depicts hysteresis loops measured at 10 K after field-cooling in different fields. A slight shift of the loop towards negative fields indicates an exchange bias effect at 10 K. To ensure saturation all measurements were done up to  $\pm 1$  T. The field was applied parallel to a [001] direction of the substrate.

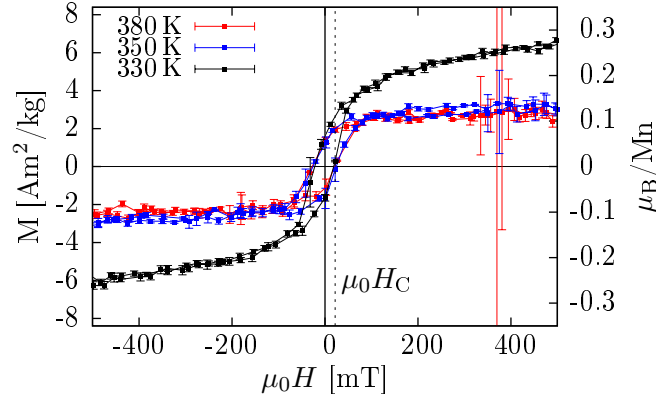


**Figure 8.10:**  $M - H$ - measurement of the high-temperature region of sample LSFOfinal. Even at 380 K a ferromagnetic hysteresis is present which lies well above  $T_C$  of LSMO. This is an indication of an additional ferromagnetic phase with high coercive field  $H_C$  (dashed line) and high  $T_C$ . Measurements were performed at PPMS-VSM.

$H_E$  is known as exchange field. This supports the assumption that a interlayer coupling, although very weak, is present in the system. However, a field-cooling dependency, which can usually be found in exchange bias systems [36], could not be observed. Those measurements after cooling in different fields are shown in Fig. 8.9b. Furthermore the hysteresis loops are symmetric, which suggests an uniform magnetization reversal process for all branches. A PNR measurement (Sec. 8.3) with polarization analysis could show that a magnetization rotation rather than a domain wall motion is present with regard to Fitzsimmons et al. [131] and Paul et al. [132], who investigated the asymmetric reversal of magnetization of exchange biased systems.

In contrast to sample LSMOfinal, LSFOfinal shows a significant temperature dependence

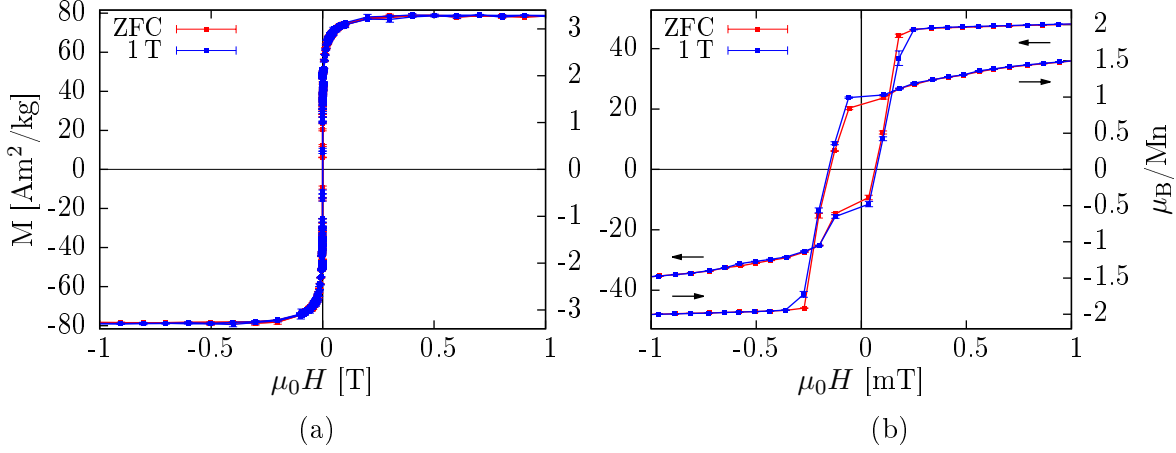


**Figure 8.11:**  $M - H$ - measurements of LSFOfinal after zero-field-cooling and field-cooling in 1 T applied along [001] at 110 K. The measurement was done between  $\pm 1$  T as shown in (a). The closer look depicted in (b) revealed an unusual behavior, known as inversed magnetic hysteresis.

of the hysteresis loops. Fig. 8.11a shows a  $M - H$ - measurement after zero-field and field-cooling at 1 T measured between  $\pm 1$  T and  $\mp 1$  T. At 110 K a FC-FW dependence is not present and both measurements are comparable. The magnetic hysteresis loop shows a magnetic saturation of  $M_S = 3.3(2) \mu_B$  per Mn ion above 300 mT, whereas the coercive field with 0.1 mT is fairly small and also at the resolution limit of the MPMS. The reason for the high magnetic field, which is necessary to reach magnetic saturation, is attributed to one or more anisotropy directions of the sample. It seems most likely that not the easy axis was measured, and thus the principal crystal direction [001] of the substrate, which was aligned parallel to the applied field, is not an easy anisotropy axis in the underlying system. Besides the magnetocrystalline anisotropy, which would prefer an alignment parallel to a high-symmetry axis, shape and surface anisotropy play a crucial role as discussed in section 2.5, especially for thin film systems. The anisotropies cannot be predicted for the underlying system and have to be further investigated as discussed later on.

Fig. 8.11b is a zoom on the region around zero field. It shows an inverted hysteresis. The system switches to a state with opposite magnetization before the field reverses. Both measurements show this behavior, and the measurement is reproducible, which should cancel out any instrument related artifacts. Furthermore the coercive field is very small, 0.1 mT, which indicates that the coupling between both layers is weak and can be influenced by rather small fields.

Whereas the 110 K measurement does not show a significant field-cooling dependence shift of the hysteresis, the 10 K shows this behavior clearly (see Fig. 8.12). For each cooling field the sample was reset by heating it to 350 K which is above  $T_C$  to exclude a training effect. However, one has to remember that LSFOfinal shows an additional ferromagnetic phase (Fig. 8.10) which persists also at 350 K, but higher temperatures could not be reached with the MPMS system due to instrument limitations. The hysteresis was measured from 1 T to -1 T and back directly after the field-cooling procedure and was measured only once. A cycle dependence, which considers a training effect, for instance, was not measured, but

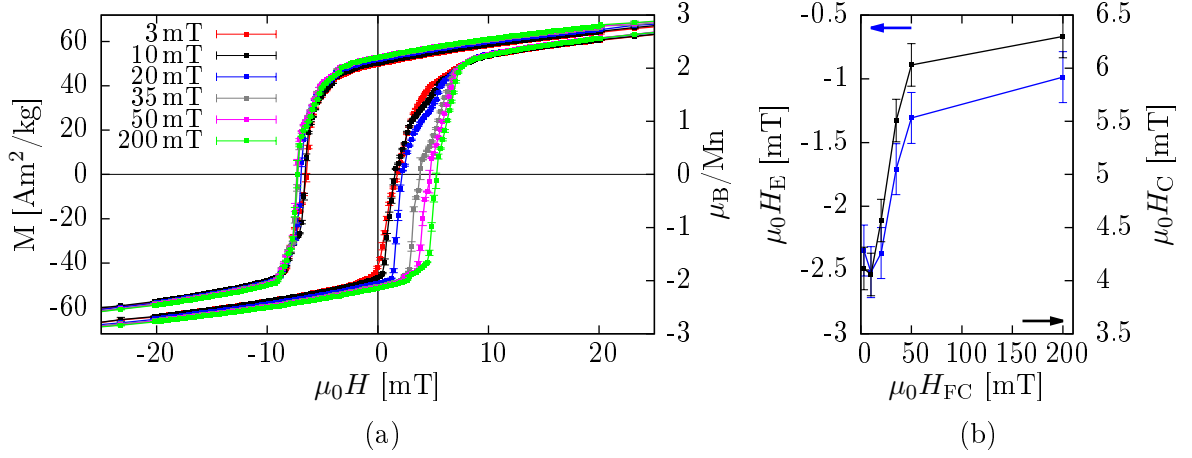


**Figure 8.12:**  $M - H$ - measurements at 10 K of LSFO<sub>final</sub> after field-cooling. The measurement was done from  $\pm 1$  T starting from positive field. A zoom on an interesting region is given in (a). (b) shows field-cooling field dependence in the exchange bias field and coercive field, respectively. The coercive field is defined as  $H_C = (H_{C2} - H_{C1})/2$  and is used to compare the different measurements.

is planned for future experiments.

The hysteresis shift is attributed to an exchange bias effect with an exchange field  $H_E$ . The occurrence hints to a presence of an interlayer coupling either antiferromagnetically or ferromagnetically between LSFO and LSMO. It shows the highest value for the lowest field, and the coercive field changes accordingly (Fig. 8.12b). The antiferromagnet is usually highly dependent on the applied field upon cooling below the Néel temperature  $T_N$  as reported by Nogués et al. [36]. Antiferromagnetic domains develop in principal crystal lattice direction, or distinct anisotropy directions. Anyhow, the stability of the antiferromagnet could be reduced due to the finite thickness of the layer, and thus it can easily be influenced by an applied field. As mentioned earlier, the charge ordering and consequently the Verwey transition is highly dependent on the layer thickness, which gives rise to the assumption that the antiferromagnetic ordering is also influenced and thus destabilized by this (see section 6.3). This could lead to an additional ferromagnetic component within the actual antiferromagnetic LSFO via spin canting. In Fig. 8.12b the field-cooling dependence of  $H_E$  and  $H_C$  suggests that probably higher applied FC fields suppress the exchange bias effect, which has not been measured yet.

Exchange biased systems are known for asymmetric magnetic reversal mechanism which could be shown by Fitzsimmons et al. [131] and Paul et al. [132]. They could show via PNR that magnetization rotation is present for the one, and domain wall motion for the other direction of magnetization. The sample LSFO<sub>final</sub> exhibits a very low coercive field, especially the 110 K measurement,  $H_C$ , and thus a PNR measurement with consideration of four spin channels (spin-flip, non-spin-flip) was not successful, because of the necessary neutron guide field of a few mT, which was sufficient to reverse the magnetization of the sample. To maintain the sample size, the macroscopic magnetization measurements were performed after the neutron measurement and no information about the magnetization behavior could be considered for planning the PNR measurements. Reducing the

neutron's guide field would lead to a depolarization of the neutron beam, and the signal cannot be evaluated correctly with respect to spin- and non-spin-flip contributions. Furthermore, it can be seen that the shape of the hysteresis loop is also cooling field dependent. The aforementioned asymmetric hysteresis loop changes while increasing the applied field. The clearest change of shape is found in the first quadrant of the hysteresis loop coming from negative field to positive field. The lowest field 3 mT shows a soft edge upon increasing of the applied field to reach saturation. For the fields up to 35 mT an additional reversal point is observable. It seems that this reversal point diminishes upon increasing the field, and higher fields lead to a sharpening of the edge, but do not exhibit an additional reversal point. It is intriguing that the largest change appears for a cooling field of 35 mT, the same field for which the enhanced high temperature magnetization is observed as depicted in Fig. 8.10. Probably, this additional ferromagnetic phase is switched and aligned in field direction for higher fields and influences the magnetization process. Another peculiarity is the magnetization in the left upper quadrant. Upon reducing the field from 1 T to -1 T only very small field-cooling dependencies are observable. The connection between the additional magnetization at high temperature and the hysteresis loops at low temperature as well as the shift of the coercive field at 10 K for increasing fields seems quite intriguing.

### Approaches of explanation

The observed effects in LSFO<sub>final</sub> are quite fascinating, and thus possible explanations will be discussed in the following part. However, they are speculative and further measurements have to be considered to find evidences to support or disprove the possible explanations.

An inverted hysteresis as observed at 110 K for LSFO<sub>final</sub> is known in literature and reported by Ziese et al. [130] and Valdivares et al. [133], for instance. The inversion of the hysteresis can have several reasons. One possible mechanism is shown in Fig. 8.13. It contains the assumption that the interlayer coupling of LSFO and LSMO is antiferromagnetic and the stability of the antiferromagnetic ordering in LSFO is reduced at least in the interface region as discussed in chapter 6.3 and expected from the FC-FW measurements. At high applied fields all spins in the ferromagnetic LSMO layer, and a part of the usually antiferromagnetic ordered spins of LSFO, are aligned in field direction.

While reducing the magnetic field the switched antiferromagnetic coupled layers can reorder antiferromagnetically, but the ferromagnetic LSMO is still aligned in field direction due to its low coercive field. Further reducing the field leads to a domination of an antiferromagnetic interlayer coupling while reducing the Zeeman interaction with the external field. This switches the ferromagnetic moments of LSMO, which is fairly soft with a coercive field of  $H_C = 0.8$  mT. Thus, the magnetization is reversed without reversing the applied field. The different shapes of the edges are caused by the antiferromagnetic spins which have to be aligned in field direction against their super-exchange interaction. The backward path is equal. The jump of magnetization in both direction is approximately  $1.5\mu_B$  per Mn ion. It means that about half of the spins flip due to the antiferromagnetic interlayer coupling (see Fig. 8.8b) and a high correlation length is present. However, the averaged magnetic moment carried by an iron ion in LSFO is  $3.7\mu_B$  and consequently the

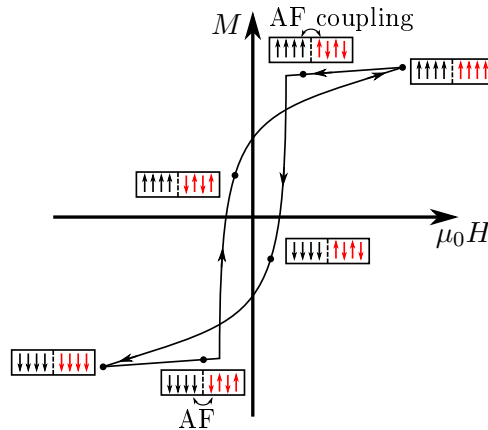


**Figure 8.13:** One possible explanation of the inverted hysteresis in the system, where an antiferromagnetic interlayer coupling is assumed. The interface is indicated by a dashed line. Red arrows are magnetic spins in LSFO, black arrows indicate the spins in LSMO.

magnetization in saturation should be higher except if only a few antiferromagnetic layers contribute to this effect and the antiferromagnetic ordering remains stable in a large part of the overall thickness of the layer.

A second possible mechanism considers at least two different competing anisotropies. As introduced, different anisotropy contributions, namely, the magnetocrystalline anisotropy, shape anisotropy, or exchange anisotropy, for instance, determine the magnetic properties. However, the symmetry for each anisotropy can be different. The interplay between all anisotropies can significantly modify the magnetization reversal processes as reported by Zhang [134]. This means that at 1 T all spins are aligned in field direction and saturation is reached. Reducing the field makes another anisotropy direction preferable, and the spins align into this direction, which leads to a magnetization reversal. Increasing the field to reach the opposite saturation leads to an alignment of spins in field direction, but first it is necessary to overcome the anisotropy energy, which explains the rounded edge of the hysteresis loop. This process is invertible, which thus leads to symmetric inverted hysteresis loops.

That the anisotropy is the driving mechanism is supported by the 10 K measurement shown in Fig. 8.12a, where an inversed hysteresis is not observable. As discussed in chapter 7 the structural phase transition from cubic to tetragonal influences the magnetic properties in LSMO including the strain anisotropy. To fully understand the magnetization a systematic study of the anisotropy, both in-plane and out-of-plane direction is necessary. However, such a study is not part of this thesis.

Besides the macroscopic magnetization one is also interested in the depth resolved temperature dependent magnetization and the determination of the magnetization reversal of the LSMO final sample, which was already mentioned during the interpretation of the underlying hysteresis curve. The layer magnetization characterization was done by PNR with polarization analysis.

## 8.3 Layer magnetization

### 8.3.1 Depth-resolved magnetization

#### Sample modeling for neutron data evaluation

The polarized neutron data evaluation for the depth resolved magnetization was done with GenX [52] which uses an adaptive layer segmentation model. One main advantage of using this model is the separation of the nuclear and the magnetic part of the sample's SLD, which enables one to choose the magnetic layer parameter individually as depicted in Fig. 8.14. Additionally, to reduce the number of free parameters the following connections between nuclear and magnetic layer thickness were used:

$$\begin{aligned}d_{\text{LSFO}} &= d_{\text{ML1}} \\d_{\text{interlayer}} &= d_{\text{ML2}} \\d_{\text{LSMO}} &= d_{\text{ML3}} + d_{\text{ML4}} \\d_{\text{TOP}} &= d_{\text{ML5}}.\end{aligned}$$

The layers ML2 and ML3 are used to describe the transition regions and take into account that the magnetization at the interface can vary from the bulk properties. At the interface region of the LSFO layer (ML2 and ML3) the magnetization might be reduced or even vanish, known as magnetic dead layer behavior. This is reported by Peng et al. [128], for instance. Furthermore, the influences due to electronic doping can also be considered here. The thicknesses of these magnetic layers are varied during fitting and the magnetization was fitted individually for each magnetic layer. However, the shown model was a starting point and is shown for the sake of completeness. It was adjusted with respect to the resulting fit as discussed in the following part. The model for LSMOfinal was chosen likewise and is not shown here.

nuclear	magnetic
TOP	ML5
LSMO	ML4
	ML3
Interlayer	ML2
LSFO	ML1
STO	non-magnetic

**Figure 8.14:** Sample model for LSMOfinal. It is divided into a nuclear and magnetic part. Due to intermixing effects between LSMO and LSFO an interlayer was introduced which considers a Fe loaded LSMO phase as seen from EDX measurements.

Polarized neutron reflectometry quantifies the laterally averaged scattering length density perpendicular to the sample surface. Usually several parameters like thickness, roughness, density, and structure of the chemical unit cell determine the nuclear scattering length density (NSLD), whereas the magnetic scattering length density (MSLD) depends on the magnetization per chemical unit cell and magnetic roughness. Therefore any model needs a large number of parameters, which can be strongly correlated. Hence each refinement must be reviewed carefully. Even if the goodness of fit seems to be satisfactory, the interpretation of PNR can be ambiguous due to parameter correlations. This means that within the used model, for instance, it is not clear whether a high roughness or an interlayer/top layer with reduced or enhanced density determines the SLD as considered. The ambiguousness somehow limits the reliability of the used model, and as far as possible the parameters are linked together to reduce the number of independent parameters.

### Neutron data evaluation

Investigations with polarized neutron scattering of the temperature dependency of the depth-resolved magnetization were done at PBR reflectometer at CNR. A short description of the instrument and the used setup is given in Sec. 5.3.5, and the scattering geometry is explained in Sec. 3.7. As PBR uses a point detector, information about diffuse scattering was not provided, but also not expected considering the good surface morphology revealed from XRR measurements. During the investigation of the magnetization reversal mechanism (section 8.3.2) at MARIA it could be shown that the diffuse scattering can be neglected for temperatures above  $T_{\text{STO}}$ . However, in general one always measures the sum of diffuse scattering and true specular reflectivity.

To maintain the full sample size for neutron scattering, the samples were not characterized prior to the PNR measurements and magnetic values from older samples, which exhibited worse quality, were used in order to optimize the measurement. The used 110 mT magnetic field is not sufficient to saturate the sample as seen in the last section, where the macroscopic measurements are discussed, but was used for the all measurements at PBR. The measurement was started after field-cooling in 110 mT to 10 K. STO undergoes an antiferrodistortive phase transition, whose consequence is an increased roughness (as one can see at the 100 K measurement shown in appendix D.4.4) of the sample. This makes a reliable investigation not possible due to off-specular scattering, which damps and smears the thickness oscillations. Measuring above  $T_{\text{STO}}$  was necessary to investigate the specular reflectivity without doing a correction for diffuse scattering. The limitations of the temperature range limited the accessible resistivity range to approximately four orders of magnitude instead of eight for the whole temperature range (Fig. 6.36b). This limitation may reduce the characteristics of the effect and thus it is difficult to measure in the neutron reflectivity.

Fig. 8.15 shows the normalized reflectivity measurements of sample LSMOfinal and LSFOfinal for three selected temperatures. Additional temperature steps for sample LSFOfinal are shown in Appendix D.4.4. Sample LSMOfinal was measured with a smaller  $Q_z$  range due to beamtime limitations. Additionally, the accessible  $Q_z$  range for a neutron experiment is significantly smaller compared to an X-ray experiment. The reason is the neutron flux and/or a larger penetration depth of neutrons, for instance.

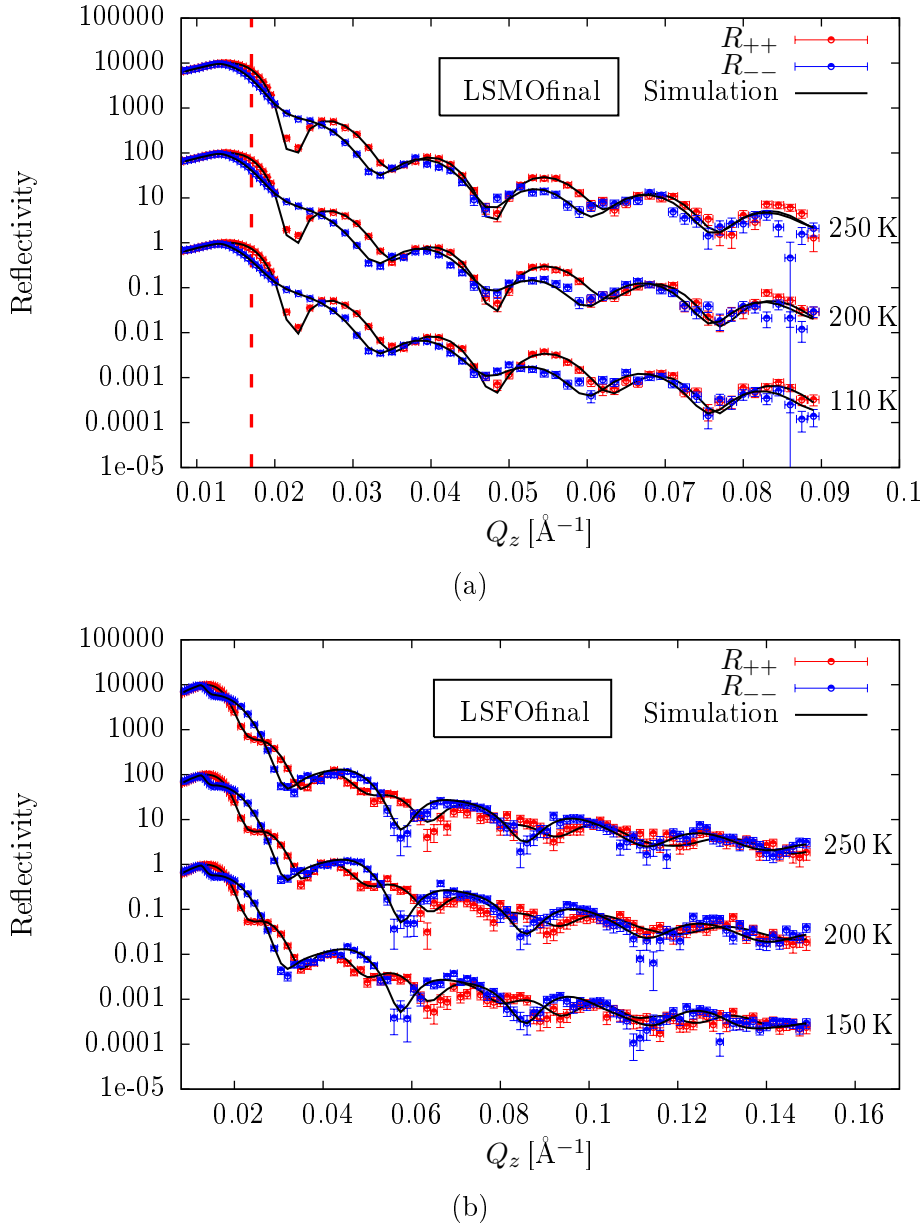


**Figure 8.15:** PNR measurements and simulations of sample LSMOfinal (a) and LSFOfinal (b) at different temperatures for both non-spin-flip channels. The red dotted line indicates the  $Q_z$  position used for the MARIA experiment. The measurements were performed at the PBR instrument after field-cooling in 110 mT. Due to the STO structural phase transition, which causes a significantly increased roughness, the measurement was started above this phase transition. The reflectivity curves are shifted by a factor of 100. The errorbars are scaled with respect to the lowest measurement. All parameters gained from the refinements are listed in appendix D.3.4 and D.4.5. Additional temperatures for LSFOfinal are shown in appendix D.4.4.



Both samples show a difference for both reflectivities  $R_{++}$  and  $R_{--}$ , which evidences an underlying magnetization in the system. The nuclear and magnetic SLDs, named  $SLD_N$  and  $SLD_M$ , are connected as follows:

$$\begin{aligned} SLD_{++} &= SLD_N + SLD_M \\ SLD_{--} &= SLD_N - SLD_M \end{aligned}$$

Here the magnetization is aligned parallel to the polarization of the incoming neutron beam. Sample LSFOfinal shows a shorter oscillation period for the  $R_{++}$  reflectivity compared to the  $R_{--}$  contribution, which cannot be found in sample LSMOfinal. This difference is a consequence of the different interlayer, which exhibits different interdiffusion behavior as described in the prior sections. In sample LSMOfinal, a fairly thick interface region with high iron diffusion could be found, whereas the interdiffusion in sample LSFOfinal is restricted to a maximum of two unit cells. The difference of the  $R_{++}$  channels in both samples is most likely a consequence of the different expansion of the interface, which smeared the oscillations in LSMOfinal. Both samples show more pronounced minima in the  $R_{++}$  reflectivity compared to the  $R_{--}$ , especially the first and third one.

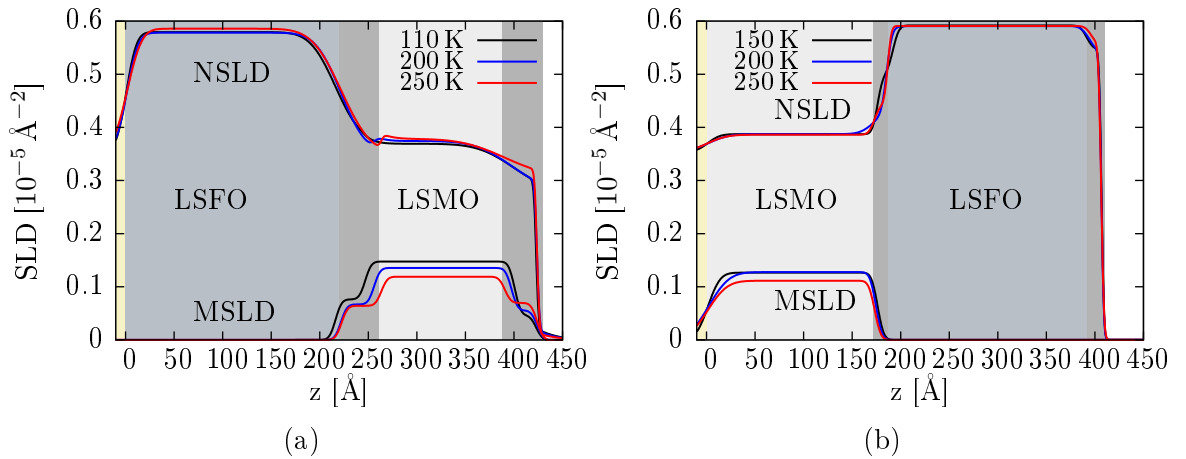


**Figure 8.16:** Real part of nuclear and magnetic scattering length densities (NSLD and MSLD) from simulation of LSMOfinal (a) and LSFOfinal (b) for different temperatures. A height of 0 Å is calibrated to the surface of the substrate. LSMOfinal shows a reduced magnetization in the interface region and top region, whereas LSFOfinal exhibit a homogeneously magnetized LSMO layer. The expansion of the interface region corresponds to the TEM measurements as shown.

The neutron data evaluation was done with the introduced model shown in Fig. 8.14, which was implemented in GenX. It quickly emerged that this model could be simplified, because the refinement of the data converged for a zero thickness of the assumed magnetic layers. For sample LSMOfinal the magnetic layer ML1 was set to zero magnetization. In LSFOfinal only ML1 remained, which corresponds to the complete LSMO layer thickness as discussed later on. The rather complex model was first introduced, because of the completely unknown magnetization profile of the sample.

The refinement of LSMOfinal revealed an inhomogeneous magnetization of the LSMO layer, which is caused by interdiffusion of iron into the LSMO as seen from STEM and

EDX measurements discussed in Sec. 8.1. From the simulation an averaged interlayer thickness of  $35(3) \text{ \AA}$  can be found, which is in good agreement with estimated depth of diffusion from the EDX measurements, which is roughly 9 unit cells ( $35 \text{ \AA}$ ). This interlayer exhibits also a reduced magnetization  $m_{\text{ML}3}$  as shown in the SLD plot. The temperature dependant NSLD and MSLD are shown in Fig. 8.16 and the magnetization values are listed in Tab. 8.3. The very small artefact at around  $260 \text{ \AA}$  in sample LSMOfinal does not have any significance and lies within the error of the simulation. The reduction of the magnetization is most likely a consequence of iron interdiffusion. Chérif et al. [135] reported a reduced  $T_C$  and influences on the magnetic properties for iron doped LSMO. Whereas  $T_C$  depends on the exchange interaction, the reduced moment in the interlayer originates from the additional electron provided by the iron interdiffusion and hence is a single ion effect. As no significant diffuse scattering was found with the MARIA measurement (discussed in the next section), it can be assumed that the interlayer has rather an intrinsically reduced magnetization than a highly increased magnetic roughness with lateral correlations. The latter case would increase the amount of diffuse scattering significantly.

LSFOfinal does not exhibit evidences of a reduced magnetization within the interface and does also not show strong interdiffusion. This supports the assumption that interdiffusion influences the magnetization significantly. Furthermore the top layer magnetization  $m_{\text{ML}5}$  in LSMOfinal is also significantly reduced through approximately 5 – 8 monolayers.  $m_{\text{ML}5}$  is very sensitive to the total reflection angle and is thus not highly correlated to other parameters. Peng et al. [128] investigated magnetically dead layers in LSMO/STO, which are attributed to interfacial doping, and oxygen vacancies, which directly change the double exchange interaction. As XRR and PNR results indicate a reduced density, and oxygen deficiency in the top layer, it is suggested to attribute the reduced magnetization to the top layer as changing  $m_{\text{ML}5}$  would shift the plateau of total reflection as discussed. The density reduction of the toplayer is discussed in the single layer sections in detail. Furthermore table 8.3 shows the averaged magnetization of the magnetic LSMO layer, whereas all other refinement parameters are summarized in appendix D.3.4 and D.4.5. This also includes the interlayer and top layer of sample LSMOfinal, which carry a reduced magnetization. To average the different contributions found in LSMOfinal the equation

$$\bar{\mu} = \frac{\sum_i \mu_i \cdot d_i \cdot \rho_i \cdot z_i}{\sum_i d_i \cdot \rho_i \cdot z_i}$$

can be used, where  $\rho_i$  is the density,  $d_i$  the thickness,  $\mu_i$  the magnetization per unit cell, and  $z_i$  the fraction of magnetic atoms in one unit cell.

The calculated magnetizations are in good agreement with the macroscopic magnetization measurements, whose values are listed in Tab. 8.4. However, no indication, within the errors of the refined parameters, is found that evidences a clear temperature dependency caused by the resistivity change of LSFO. The roughness parameters for LSMOfinal are larger compared to the XRR which can have several reasons. The roughness parameters in the PNR simulation also contain a magnetic roughness parameter. Furthermore X-ray and neutrons as probes are not equally sensitive to the ions in the underlying compound. Whereas the contrast in the XRR measurement is mainly caused by strontium and lanthanum, the contrast in neutron measurements is provided by all ions, especially by iron

**Table 8.3:** Averaged magnetization per unit cell of the LSMO layer in sample LSMOfinal and LSFOfinal for different measured temperatures.

T [K]	LSMOfinal	LSFOfinal
	M [ $\mu_B$ /uc]	M [ $\mu_B$ /uc]
100	-	$3.13^{+0.14}_{-0.20}$
110	$2.88^{+0.12}_{-0.12}$	-
150	-	$2.75^{+0.09}_{-0.12}$
190	-	$2.75^{+0.16}_{-0.13}$
200	$2.76^{+0.09}_{-0.09}$	$2.77^{+0.12}_{-0.09}$
210	-	$2.75^{+0.09}_{-0.19}$
250	$2.23^{+0.13}_{-0.13}$	$2.39^{+0.22}_{-0.20}$

**Table 8.4:** Magnetization in saturation obtained from a  $M-H$ -measurement at 110 K discussed in Sec. 8.2.

LSMOfinal	LSFOfinal
M [ $\mu_B$ /uc]	M [ $\mu_B$ /uc]
3.0(1)	3.3(2)

and manganese. The EDX measurement discussed in the last section shows a clear interdiffusion of iron in the LSMO layer, but no clear deviation of the expected lanthanum to strontium ratios in the LSMO and LSFO layer. Thus, XRR is not sensitive to the interdiffusion, but PNR is. The roughness is assumed to have the extent of several monolayers, but a clear distinction between roughness and the introduced layers with reduced roughness is hardly achievable as discussed in Sec. 8.3.1 briefly. Besides these reasons, the different collimation and penetration of X-rays and neutrons leads to probing different correlations. Especially for the deep interfaces one achieves high sensitivity at high  $Q_z$ . In contrast to sample LSMOfinal, LSFOfinal shows significant differences. The simulation revealed that the LSMO layer is homogeneously magnetized, and no indication for a reduced magnetization could be found. Some reflectivity measurements are depicted in Fig. 8.15. Furthermore, the reliability of the simulation of sample LSMOfinal is smaller compared to sample LSFOfinal, because a smaller  $Q_z$  range was performed and especially effects deep in the sample are not probed thoroughly.

As briefly addressed neutron and X-ray measurements show significant differences, and additionally X-ray measurements were performed always at room temperature. Thus, a simultaneous refinement of X-ray and neutron data was not successful. It was intended to avoid over interpretation of the neutron reflectivity.

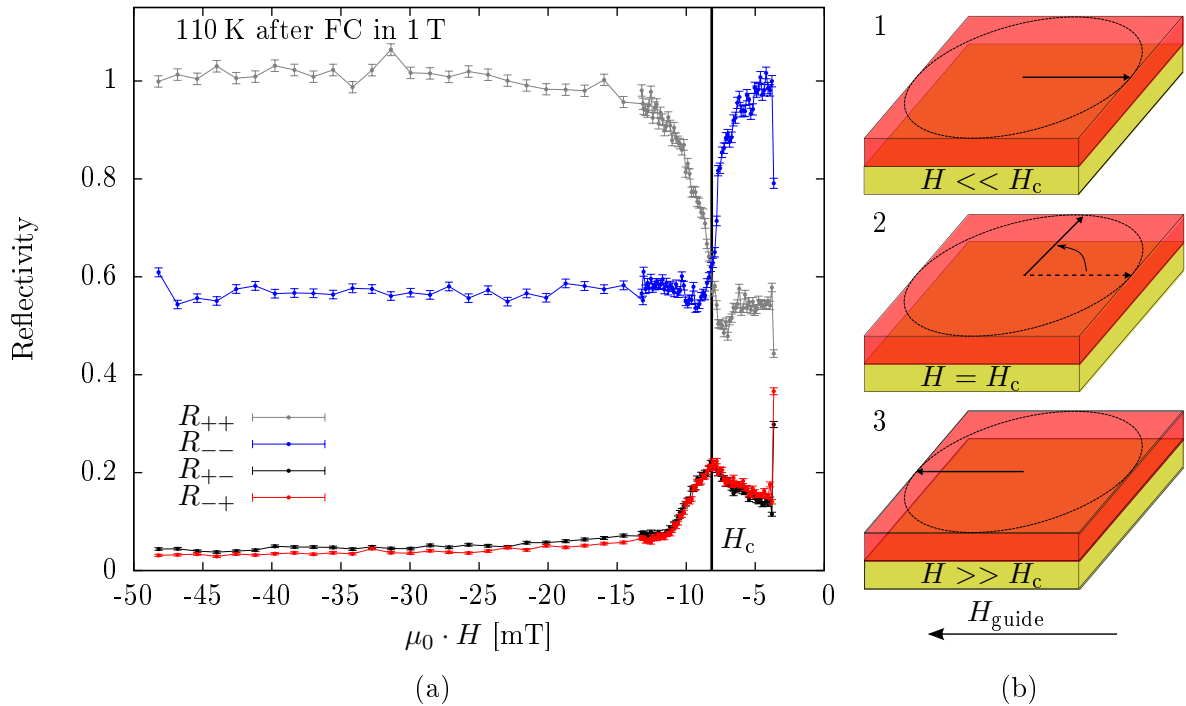
### 8.3.2 Magnetization reversal mechanism of sample LSMOfinal

An investigation of the magnetization reversal process was measured with MARIA at MLZ with polarization analysis in order to measure the non-spin-flip and spin-flip channels.

The significantly increased roughness below  $T_{\text{STO}}$  made it necessary to stay above this temperature. The coercive field of LSFO<sub>final</sub> at 110 K is smaller than 0.1 mT (Fig. 8.11), thus a measurement of the magnetization reversal process is not possible, because the neutron guide field is in the range of a few mT. As mentioned earlier the guide field is necessary to maintain the polarization of the neutrons. Reducing the guide field would lead into a partial depolarization of the neutron beam, which influences the data and analysis, because one does not know whether the neutron flipped prior being scattered from the sample or after. Furthermore controlling such small magnetic fields is also a practical problem, because it is hardly ever controllable. Especially, because a direct measurement of the applied magnetic field at the sample position is not possible.

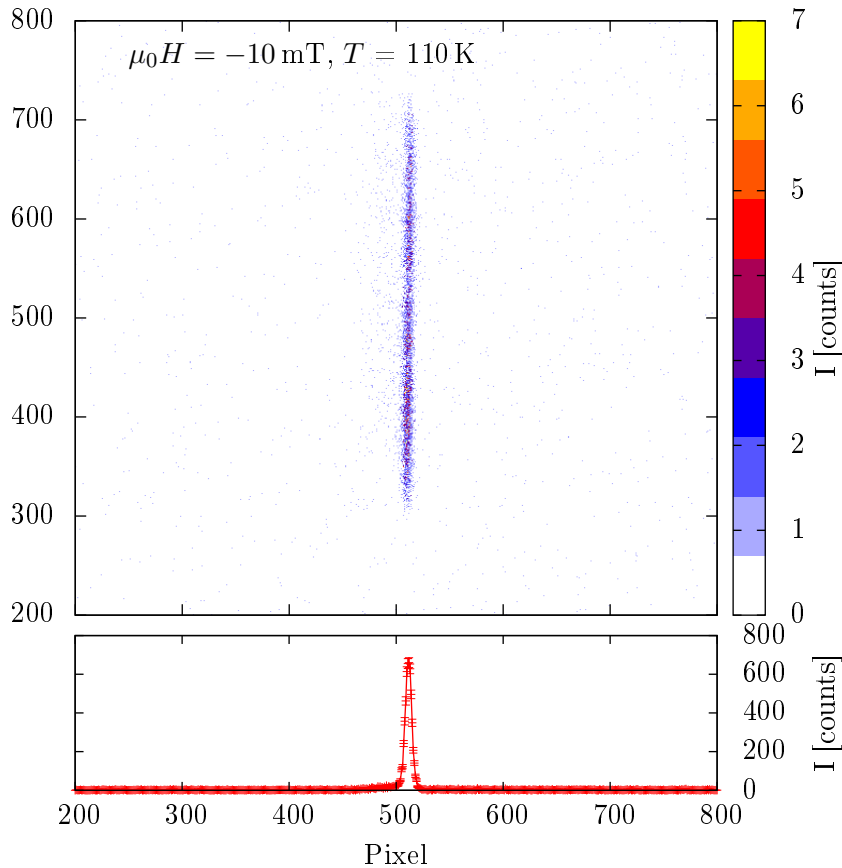
LSMO<sub>final</sub> exhibits a coercive field of 8 mT at 110 K, which is larger than the neutron guide field (Fig. 8.9). The sample was cooled in a field of 1 T, which is aligned parallel to the neutron polarization. After reaching 110 K the sample was saturated in opposite direction with a field of 1 T, then the magnetic field was set to a value comparable to the neutron guide field. An explanation of the measurement of half of a hysteresis loop is depicted in Fig. 5.14. Because of limited beamtime and to probe the magnetization reversal thoroughly only one  $Q_z = 0.017 \text{ \AA}^{-1}$  value was measured. The used position is marked by a red dotted line in Fig. 8.15a. This  $Q_z$  value lies above the critical angle and shows a large difference at magnetic saturation between the non-spin-flip channels as shown in the PNR measurement shown in Sec. 8.3.1.

Fig. 8.17a shows the magnetic field dependence of the reflectivity at the mentioned  $Q_z$  value for the different spin channels. During the measurement the magnetic field was measured not at the sample position, which leads to slightly smaller measured field. Thus, the magnetic field was recalibrated with respect to the MPMS measurements. After field cooling to 110 K in 1 T (antiparallel to the neutron beam polarization) the field was reduced and reversed, which leads also to a magnetization antiparallel to the applied field. This is shown in Fig. 8.17b(1). Data was recorded for fields parallel to the guide field of  $\mu_0 H < -3 \text{ mT}$ . The lowest (negative) field shown in Fig. 8.17a lies below the guide field and as a consequence the neutron polarization is not maintained, which explains the fluctuations here. Increasing the negative field towards the coercive field,  $R_{--}$  drops sharply, and the  $R_{+-}$  and  $R_{-+}$  reflectivities increase significantly. A further increase of the field ( $\mu_0 H < \mu_0 H_c = -8.15 \text{ mT}$ ) leads to a quick raise of the  $R_{++}$  reflectivity, while  $R_{--}$  remains now constant. The intensity in the spin-flip channels  $R_{+-}$  and  $R_{-+}$  decreases and almost reaches zero. However, a flipping ratio correction has not been done. At the coercive field,  $R_{++}$  and  $R_{--}$  are equal, because of a vanishing magnetization contribution parallel to the magnetic field, instead the spin-flip intensity reaches a maximum. This corresponds to the case that the magnetization is rotated perpendicular to the neutron beam polarization (8.17b(2)). The difference between  $R_{++}$  and  $R_{--}$  at saturation (described by 8.17b(3)) is very close to the sum of  $R_{+-}$  and  $R_{-+}$  at the coercive field, which indicates a coherent rotation of the magnetization. The missing diffuse scattering during the magnetization reversal process provides further evidence against a reversal process through domain wall movement. An example detector image of the uu (++) channel is shown in Fig. 8.18. This measurement was taken at -10 mT, which is between the coercive field and the saturation field. The lower figure depicts a



**Figure 8.17:** (a) 110 K PNR hysteresis measurement with polarization analysis of LSMO final. The coercive field was recalibrated with respect to the MPMS measurements. (b) Sketch which describes the reversal process in three steps found in sample LSMO final.

summation of all vertical pixels. The slight asymmetry is caused by a small misalignment of the sample. However, diffuse scattering does not appear during the magnetization reversal of the sample. A field of 1 T was applied to ensure saturation, but not measured, and then measured back from a field of  $-50$  mT. The sketch depicted in Fig. 8.17b shows the process of magnetization reversal for the saturated state antiparallel to the neutron polarization ( $H \ll H_C$ ), the state of perpendicular magnetization ( $H = H_C$ ), and a magnetized state along the neutron polarization which sets in at  $H \gg H_C$ . The backward measurement follows the forward measurement after reaching saturation and is not shown for a better visibility. Anyhow, a reversal of the magnetization on the backward measurement is not expected under consideration of the measured hysteresis loops.



**Figure 8.18:** MARIA detector image of one single measurement of the non-spin-flip uu channel. The lower figure shows an integration along the  $y$  pixel axis. The small asymmetry of the peak comes from a slight misalignment of the instrument. No indication for strong diffuse scattering in  $x$ -direction (lateral) is observable.

## 8.4 Conclusion

The growth of  $\text{La}_{1/3}\text{Sr}_{2/3}\text{FeO}_3/\text{La}_{2/3}\text{Sr}_{1/3}\text{MnO}_3$  and  $\text{La}_{2/3}\text{Sr}_{1/3}\text{MnO}_3/\text{La}_{1/3}\text{Sr}_{2/3}\text{FeO}_3$  on the substrate  $\text{SrTiO}_3$  was investigated. Both types of samples exhibit a high crystallinity and good surface morphology. The samples are named LSMOfinal and LSFOfinal, corresponding to their second grown layer. Whereas  $\text{La}_{2/3}\text{Sr}_{1/3}\text{MnO}_3$  (LSMO) is a ferromagnetic layer, whose magnetic properties can be tuned by stoichiometry or epitaxial strain, the  $\text{La}_{1/3}\text{Sr}_{2/3}\text{FeO}_3$  (LSFO) layer features antiferromagnetism and a Verwey transition accompanied by a charge disproportionation and ordering of the Fe ions. The low strain between both layers helps one to study mainly the charge degrees of freedom at the interface.

Due to technical issues different deposition techniques had to be used for the different layers. LSMO was grown under high oxygen partial pressure by RF sputtering (HOPSA), whereas LSFO was grown by a state-of-the-art OMBE system using co-evaporation from effusion cells. Exposing the films to atmospheric conditions for the sample transport

between both growth chambers does not affect the growth as evidenced by in-situ and ex-situ methods like LEED, RHEED, XRD, and XRR.

The interface morphology and magnetic properties depend strongly on the used growth order of the layers. The sputtering deposition of LSMO on LSFO resulted in a strong interdiffusion of iron into the growing LSMO layer. The interdiffusion reaches at least nine monolayers into the LSMO layer. Ex-situ EDX analysis was crucial to elucidate the chemical structure as the X-ray reflectivity method exhibits a lack of sensitivity due to the vanishing contrast between manganese and iron ions. Polarized neutron reflectometry revealed an interface layer of similar thickness with a distinct magnetization as compared to the remaining part of the LSMO layer. The slight differences in  $T_C$  and the in-layer magnetic scattering length density might be attributed to small variations in the layer stoichiometry. LSMO<sub>final</sub> does not show any relevant field-cooling or temperature dependencies in  $M - H$ -curves. The LSFO<sub>final</sub> sample features a much narrower interface and interdiffusion is restricted to the first two monolayers at maximum. Furthermore, the EDX analysis confirms that iron does not diffuse into the LSMO layer, and also a diffusion of manganese into the LSFO could not be found. The sharper interface results in a reflectivity with more details due to the stronger contrast. The significantly sharper interface in sample LSFO<sub>final</sub> leads to an interlayer coupling and an exchange bias effect could be measured with magnetometry. The occurrence of the exchange bias effect verifies an existing ferromagnetic-antiferromagnetic interface coupling which is either ferromagnetic or antiferromagnetic. A direct proof of the antiferromagnetic ordering in the LSFO layer is still missing and needs further efforts in sample preparation. Furthermore field dependence of this sample varies strongly with temperature. Especially the occurrence of an inversed hysteresis is astonishing, because such behavior is only reported rarely in literature. However, the observed properties show the large diversity of transition metal oxides, which can be influenced and tuned in many ways.

One possible explanation of an inverted hysteresis can be found in competing anisotropy directions, for instance, shape and surface as well as magnetocrystalline anisotropies. Especially, in thin film systems the influence of shape and surface anisotropy can be significant and may change the magnetic properties.

The shape of the hysteresis loop at 10 K is different and changes its behavior with the applied magnetic field during field-cooling. An explanation for this behavior is still missing, but can also likely be attributed to the anisotropy conditions in the system. Magnetocrystalline, shape, and surface anisotropy determine the magnetic properties in thin film systems and can be easily influenced by strain, chemical interdiffusion, and oxygen vacancies, for instance. The difference of the magnetization in LSFO<sub>final</sub> could strengthen this assumption. While passing the cubic to tetragonal phase transition of STO, the influences of the magnetic properties of LSMO appear clearly as discussed earlier.

Polarized neutron reflectometry could not evidence an effect of electronic doping as anticipated at the beginning. The reason for the absence of the expected effect of electronic doping due to the resistivity change is not clear as several reasons are possible as discussed in the last sections. One crucial problem is the limitation of the accessible temperature range due to the structural phase transition of the used substrate, which also limits the probed resistivity range. Thus, the extent of the expected effect is also reduced, which probably makes an investigation problematic. Another reason is in the degree of the

interlayer interdiffusion resulting in no or only a weak coupling between both deposited layers.

From the field dependent reflectometry with polarization analysis the magnetization reversal process in LSMO<sub>final</sub> could be attributed to rotating rather than domain wall motion. The strong interdiffusion in this sample results in a featureless diffuse scattering showing no lateral magnetic correlations. Due to the small coercive field, the remagnetization process in LSFO<sub>final</sub> could not be studied. Temperatures below  $T_{\text{STO}}$  were not measured because of the appearance of increased surface roughness.

## 8.5 Outlook

Several questions remained after analyzing the data gained from MPMS, EDX, and PNR, for instance. One crucial point is the combination of two different growth methods, which were necessary due to technical problems. To avoid contamination and additional heating and cooling procedures it is planned to overcome the problems with the OMBE system in order to achieve perfect layers, which could show a better interlayer coupling as the interdiffusion and contamination can be reduced. Thus, technical problems concerning the manganese effusion cell have to be solved and the growth processes have to be optimized to achieve atomic sharp interface whose interlayer coupling is most likely more pronounced. Another important route is the substitution of the substrate. The used STO substrate with its structural phase transition influences the magnetization and the surface morphology of the grown samples. Thus, one can use a substrate, which exhibits a similar lattice constant that fits to the LSMO and LSFO lattice parameter, and does not show any structural transition from 350 K to 10 K. Possible candidates are  $\text{LaGaO}_3$  or scandates as  $\text{DyScO}_3$  as reported by Schlom et al. [136]. This enables the access to the full temperature range in PNR experiments. (as discussed, STO shows an increased roughness below  $T_{\text{STO}}$ , which makes a reflectivity measurement difficult). An additional point is the counting time for each temperature, which was quite short in order to measure enough temperature steps for both samples. An increase of the measurement time would increase the statistics especially for high  $Q_z$  values and a small effect can be found more reliably. Another growth related solution is the growth of thick single layers. As discussed in Sec. 6.3 the Verwey transition is smeared for thickness below a certain limit. Thicker layers could not be grown in order to avoid this problem. Additionally, a proof of the antiferromagnetic ordering in LSFO has to be done experimentally, which is quite challenging, because the mass of thin films is very small and lies in the region of  $\mu\text{g}$ . However, high resolution neutron diffractometer should be suitable to proof the antiferromagnetism properly.

It is also necessary to perform a systematic study of the magnetic anisotropies both in-plane and out-of-plane in order to achieve a sufficient understanding of the very interesting properties found in these samples and to understand how the different contributions influence the magnetization.



## 9 A quest for p-electron magnetism

A new mechanism for developing completely new devices is the so-called p- (or  $d^0$ )- magnetism. Conventionally, magnetism is based on partly filled shells of either 3d- or 4f-electrons, but the systems considered in this chapter the 3d shell is completely filled or empty ( $d^0$ ). The magnetism in the underlying systems is related to another mechanism, namely the magnetic polarization of p-electrons. The polarization of p-orbitals is quite unusual, because the p bands are broad and do not exhibit a high density of states at the Fermi level, which makes it unlikely to fulfill the Stoner criterion [137]. One has to mention that  $d^0$  is a necessary condition for ferroelectricity in perovskites. In a conventional picture of ferromagnetism partly filled d orbitals will never end in a ferroelectric state [138, 139], and thus the p or  $d^0$  magnetism will enable a new route to achieve a material where magnetoelectric coupling is present.

Here two different routes have been considered to fulfill the objective to create an unconventional magnetic system, either with doping of bulk materials or growing artificial thin film systems with the focus on the interface in between. The first section will focus on the p-electron magnetism in doped  $(\text{Ba}/\text{Sr})\text{TiO}_{3-x}\text{M}_x$ , where M can be carbon, nitrogen or boron. This system was calculated and described by Gruber et al. in 2012 [1]. Their theoretical work predicts a magnetically ordered ground state for each of the considered dopants.

Another approach is the second system, a thin film heterostructure of different non-magnetic perovskites like STO and KTO, for instance. It is suggested, that the combination leads to a charge imbalanced interface, which induces holes in the STO region of the interface. This leads to a  $d^0$  ferromagnetic half-metallic 2D electron gas due to the polarization of the oxygen 2p orbitals at the interface region. This theoretical and experimental work was also published in 2012 by Oja et al. [2].

The following sections will point out the ideas of the authors mentioned above and give an insight into the possibilities of a new approach of creating multifunctional materials for future applications.

### 9.1 The ideas behind p-electron magnetism

#### 9.1.1 $(\text{Ba}/\text{Sr})\text{TiO}_3$

Gruber et al. published results of a projected augmented plane-wave method calculation, as supported by the Vienna ab initio simulation package (VASP), concerning p-electron magnetism in doped  $(\text{Ba}/\text{Sr})\text{TiO}_{3-x}\text{M}_x$  [1, 140, 141]. The basis of the calculation is a

**Table 9.1:** Calculated parameters of a doped supercell including magnetic moment per dopant atom, cell volume,  $c/a$  ratio, and Ti-X distance  $d_{\text{Ti-X}}$ . Parameters from [1].

X =	B	C	N	O
Cell volume [ $\text{\AA}^3$ ]	64.99	64.70	64.32	63.76
$c/a$	1.019	1.012	1.009	1.000
$d_{\text{Ti-X}}$	2.170	2.096	2.015	1.998
$M$ [ $\mu_B$ ]	1	2	1	0

unit cell (supercell) with 40 atoms ( $\text{Ba}_8\text{Ti}_8\text{O}_{23}\text{X}$ ), where one oxygen atom is replaced by an atom X (C, N, or B). For all of these substituents they found a magnetically ordered ground state. This ground state is insulating for C and N, but half-metallic for B. Additionally they found that the cell parameters change after exchanging one oxygen atom through a dopant. The atomic size of the dopant causes a small tetragonal distortion of the assumed cubic perovskite structure, which increases the cell volume as shown in Tab. 9.1.

An exemplary C doping has been chosen in the following. Due to a tetragonal environment of the C atom the C p-states split locally into  $p_z$ , pointing to the Ti atoms and  $p_x, p_y$  mainly interact with oxygen.

A Molecular Orbital theory (MO) picture explains the magnetic ground state. The MO-picture and the Density of States (DOS) for C as dopant is shown in Fig. 9.1. In particular

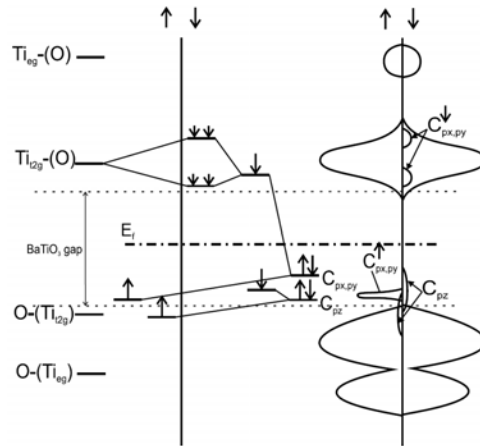


**Figure 9.1:** MO-diagram (left) and schematic DOS (right) for the case of C doping. The calculated DOS reveals differences if one considers the two different spin directions. Reprinted from [1], with the permission of EPL.

the calculated DOS shows a interesting behavior if spin polarization is allowed. The magnetic band splitting is different for the C  $p_x, p_y$  compared to the C  $p_z$  orbitals. For spin-up they found all  $p_x, p_y, p_z$  occupied with 3 electrons below the  $\text{BaTiO}_3$  (BTO) gap. The spin-down case shows that only the  $p_z$  orbitals remain occupied with 1 electron. In

contrast the  $p_x$ ,  $p_y$  states for the spin-down case lie above the gap and remain unoccupied, which leads to an insulating behavior. The magnetic moment caused by the 4 p-electrons in the occupied states can be calculated as  $2\mu_B$ , which is the strongest magnetic moment found for all dopants (Tab. 9.1).

As the whole idea is based on a calculation one has to provide proof of the concept experimentally (Section 9.2.1). In this work commercially available BTO powder was used in different annealing processes, where doping can be achieved.

### 9.1.2 $\text{KTaO}_3/\text{SrTiO}_3$ heterostructures

Ferromagnetism in the metallic band picture of electrons requires a large exchange energy  $J$  and high density of states at the Fermi level  $D(E_F)$ , which is described by the Stoner criterion  $JD(E_F) > 1$  [137]. Only in this case the exchange energy gained by spin-polarizing is larger than the increase of kinetic energy. The requirement of a high density of states at the Fermi level is usually attributed to materials with 3d orbitals. The Hund's coupling is also large in 2p orbitals, which is a common experimental observation for oxygen. The 2p orbitals exhibit a broad bandwidth and thus the high density of state, which is necessary to fulfill the Stoner criterion, is unlikely to be achieved [2, 142]. It is also known that holes in oxygen p orbitals result in magnetic moments and magnetic ordering of the holes is possible, if the hole density is high enough [143]. Especially, the oxygen  $t_{1g}$  band is an excellent candidate for realizing Stoner magnetism, because it does not show a hybridization with other bands [144]. As producing holes by vacancies at

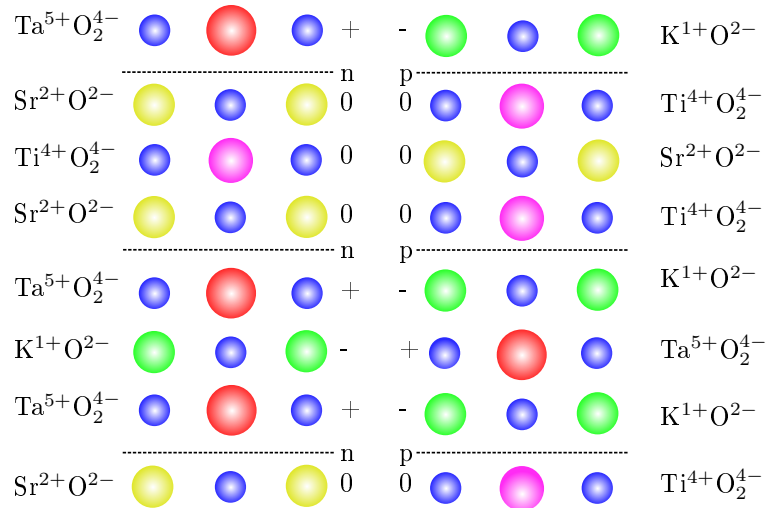


**Figure 9.2:** Used p- and n-type superlattices for calculation. The stacking sequence determines the charge at the interface. The charge arises from the charged  $\text{TaO}_2$  and  $\text{KO}$  layers. The  $\text{STO}$  layers are neutral. As the whole system has to be neutral, the interface has to compensate the surplus charges by introducing electrons or holes to the interface. Adapted from [2].

realistic concentrations is not sufficient to achieve a high hole density, Oja et al. showed a computational and experimental study of a charge imbalanced interface between non-magnetic perovskites [2]. They used a layered thin film system consisting of neutral (100)

and charged (100) layers of SrTiO<sub>3</sub>/KTaO<sub>3</sub>, SrTiO<sub>3</sub>/KNbO<sub>3</sub>, or SrTiO<sub>3</sub>/NaNbO<sub>3</sub>, respectively. For instance, the SrTiO<sub>3</sub> monolayers SrO and TiO<sub>2</sub> are both neutral, whereas the KTaO<sub>3</sub> monolayers KO and TaO<sub>2</sub> are charged either negatively or positively. Dependent on the stacking, as shown in Fig. 9.2, the charged layers exhibit an interface charge of  $\pm 0.5e$  per interface formula, because charge neutrality needs to be fulfilled for the complete structure [145]. The charge imbalance causes holes in the SrTiO<sub>3</sub> layer next to the surface. As a consequence a d<sup>0</sup> ferromagnetic 2D electron gas at the interface 2p orbitals can be found.

The group around Oja prepared their samples by using a PLD system under high oxygen pressure. They could achieve samples that exhibit sharp interfaces and high crystalline quality. The characterization of the magnetic properties revealed a ferromagnetic behavior at room temperature, which is shown in Fig. 9.3. The KTO/STO system shows the highest

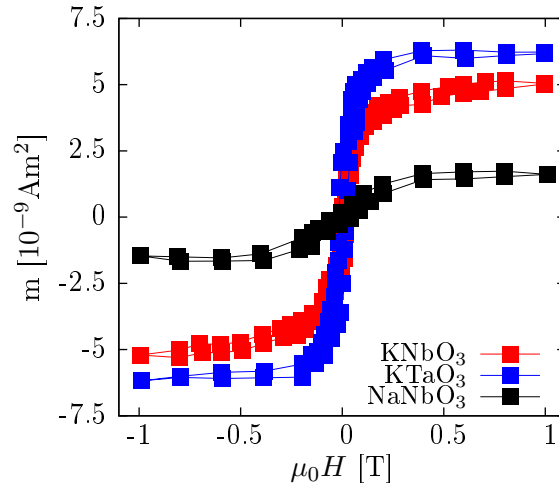


**Figure 9.3:** Magnetization measurements as a function of the external field at room temperature, where the diamagnetic contribution of the substrate is subtracted. The KTO/STO system shows the highest saturation magnetization. Adapted from [2].

saturation magnetization. Further annealing of the samples was performed in order to get rid of the influence of the oxygen vacancies, but they could not see an improvement. This means that the high pressure during the preparation is sufficient to saturate the samples properly.

## 9.2 Experimental work

This section treats the different ways of sample preparation and analysis of both systems introduced in the sections above in order to achieve a ferromagnetic material or interface which is usually non-magnetic.

### 9.2.1 BaTiO<sub>3</sub>

#### Untreated powder

For the experiment of doping, a commercially available powder (Sigma-Aldrich) with a grain size of less than  $2\ \mu\text{m}$  has been used. To start with powder experiments has one main advantage, the surface-to-volume ratio is large compared to any bulk material, so that it should be easier to dope the material. Furthermore the diffusion length of the dopant is in the same order of magnitude compared to the grain size, which makes a homogeneous doping more likely.

For the experiments nitrogen has been used as dopant. N<sub>2</sub> gas with a purity of 99.99 % was available and has been used in a microwave plasma generator with 2.45 GHz. The plasma generator helps to provide atomic nitrogen instead of molecular. Atomic nitrogen is more reactive and much smaller and thus it exhibits a higher probability to occupy an oxygen site in the perovskite structure, which is produced by prior annealing steps.

The generator is a commercially available microwave oven, which is modified for the special purpose of saturating or doping of materials with oxygen or nitrogen<sup>1</sup>. A heating during plasma treatment is not available, the plasma power was the only heat source, but powder temperature information is missing.

At first it is necessary to determine the structure of the untreated BTO, therefore in-house powder diffractometry (see 5.2.2) has been used. BTO undergoes several structural phase transitions while cooling or heating, which are shown in Fig. 9.4. Below 390 K a cubic to tetragonal transition occurs and thus the lattice parameter  $a$  and  $c$  split up.

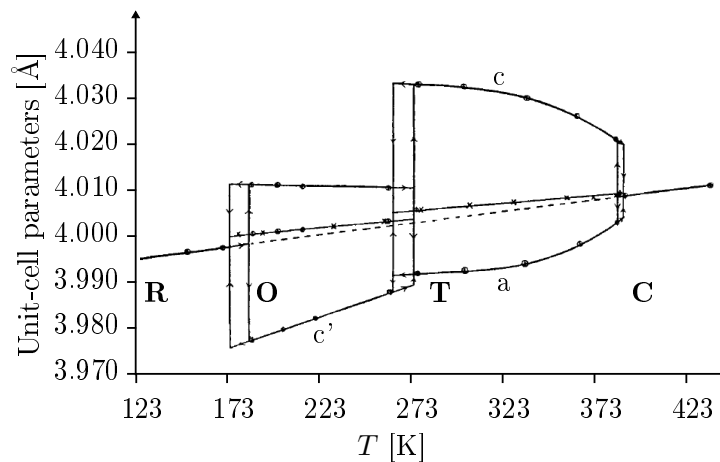


**Figure 9.4:** The structural phase diagram of bulk BTO . BTO has four different temperature dependent structural phases. A cubic (C) to tetragonal (T) phase transition sets in below approx. 390 K followed by a tetragonal (T) to orthorhombic (O) phase transition below 279 K. At 184 K the system undergoes a orthorhombic (O) to rhombohedral (R) phase transition. Reprinted from [146] with permission.

Fig. 9.5a shows the result of the BTO powder diffractometry measurement. As the powder measurement took place at room temperature the tetragonal structure was assumed for the

<sup>1</sup>With assistance of Ulrich Poppe, PGI-5, Forschungszentrum Jülich GmbH.

simulation. The cell parameters are deduced as  $a = b = 3.9977(4)$  Å and  $c = 4.0269(5)$  Å. The figure of merit of the profile function  $R_p$  and  $R_{wp}$  of the Le Bail fit is 5.3% and 7.6%, respectively. It seems that the simulation does not fit properly, especially for the peaks, where a splitting of reflections is expected due to the tetragonal distortion. A zoom on such reflections is shown in Fig. 9.5b. The overlap of the (002) and (200) reflections in the measured data indicates that the powder is not single phase as expected. A less distinct splitting of the (002) and (200) reflections gives rise to the assumption that a cubic phase is probably present in the powder.

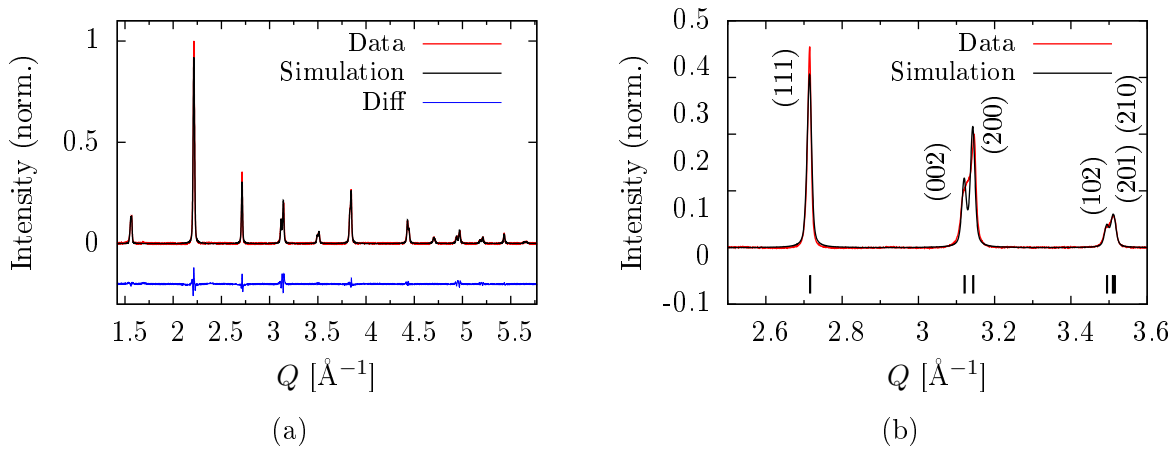


**Figure 9.5:** (a) Powder diffractometry measurement of untreated BTO and Le Bail refinement. Jana2006 [49] has been used for the Le Bail refinement. The data is normalized and the background is subtracted. (b) Zoom on reflections, where the Le Bail refinement does not fit perfectly due to an additional structural phase. The vertical black lines indicate the theoretical position of the peaks calculated with Jana2006 as well.

Since the sample preparation process of the used powder is unknown, one can attribute the non-single phase state to a rough sample treatment like fast cooling after the preparation. This fast cooling of the powder can possibly lead to an incomplete phase transition from the cubic high temperature phase to the tetragonal phase at room temperature (Fig. 9.4). Unfortunately, adding additional phases could not improve the  $R$  value of the profile function, which suggests that the structure is influenced by parameters, which are not known. Later on, it will be shown, that annealing improves the quality of the powder.

**Sample annealing** Two objectives have been pursued with sample annealing; on the one hand slow heating and cooling of the powder ends in a better quality of the powder due to a hopefully complete recrystallization into the tetragonal structure. On the other hand, annealing in a high vacuum or argon atmosphere as an inert gas at high temperature leads to oxygen vacancies, which has been shown for  $\text{La}_x\text{Sr}_{1-x}\text{MnO}_3$  thin films recently. While removing oxygen from the system the lattice relaxes and one gets lattice parameters, which are enlarged by several percent [113]. Those vacancies may enable doping of the BTO powder more efficiently, because the dopant can easily occupy a former oxygen position. Two different methods for sample annealing are available. At first the oven of the sputter high vacuum chamber has been used, where powder is heated in a platinum crucible up

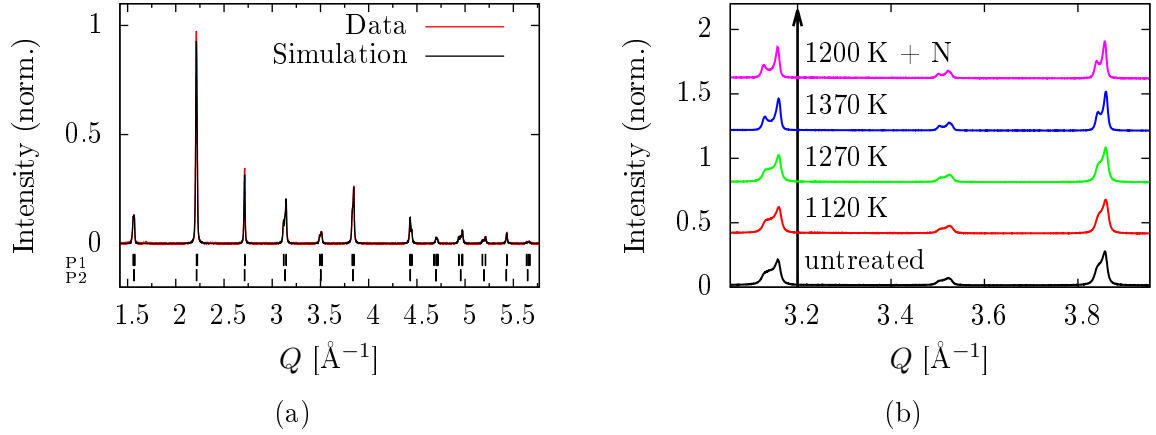


**Figure 9.6:** (a) A cubic phase has been introduced into the simulation of used BTO powder. Improvement of the refinement is visible, which means that the used and untreated powder is not a single phase powder. P1 and P2 indicate the calculated peak positions for phase 1 (tetragonal) and phase 2 (cubic). The simulation was calculated with Jana2006. (b) Plot of the annealing temperature dependency of the powder. One can easily see that an annealing process influences the structure of the powder, which becomes more single phase. The plasma treatment with nitrogen has not influenced the structure of the powder. The different data is shifted vertically by 0.4 for a better comparability.

**Table 9.2:** List of the annealing parameters for the used methods.

Environment	$T_{\text{an}}$ [K]	Ramp [K/min]	Duration [min]
Vacuum chamber	1120/1270	5	360
Tube furnace	1370	1.5	2170

to 1270 K. However, the exact powder temperature could not be measured, because the temperature sensor is located at the heater position, not at the powder position. Thus, the actual powder temperature is lower. The second way is to use an argon purged tube furnace for heating in a platinum crucible up to 1370 K.

An overview of the used parameters is given in Tab. 9.2. Analysis of the powder XRD data reveals that the room temperature powder structure changes with respect to the annealing temperatures. Fig. 9.6b shows selected peaks of the XRD measurements for different annealing procedures. The separation of the reflections becomes more pronounced, which means that the structure approaches a single phase tetragonal state. This effect is clearly observable at the reflection below  $3.2 \text{ \AA}^{-1}$  and above  $3.8 \text{ \AA}^{-1}$ , for instance. Sample annealing improves the crystal quality of the powder and lowers the fraction of impurity phases, which are clearly observable in the untreated powder as shown.

The annealing in a tube furnace enables the most significant change in the structure. The content of the impurity phases is lower compared to the untreated and vacuum annealed samples. It seems that the annealing in the tube furnace is most promising. The profile

function exhibit a  $R_p$  of 3.84% and a  $R_{wp}$  of 6.75%, which is an improvement with respect to the Le Bail simulation for the untreated powder. The simulation retrieved the lattice parameters  $a = b = 3.9945(3)$  Å and  $c = 4.0276(4)$  Å.

These heating methods have been used for further experimental steps in order to achieve an almost single phase BTO powder and to produce oxygen vacancies for doping reasons.

**N-plasma treatment** After the annealing steps shown before the powder has been treated in a microwave plasma. A microwave plasma cracks the  $N_2$  molecules to provide atomic nitrogen to the annealing process, which is necessary to make a doping process more likely. A sketch of the used instrument is shown in the inset of Fig. 9.7. The plasma annealing has been performed with a nitrogen partial pressure of 35 mbar without additional heating of the sample besides the microwave heating. A temperature measurement of the powder during plasma treatment was not possible. The plasma treatment

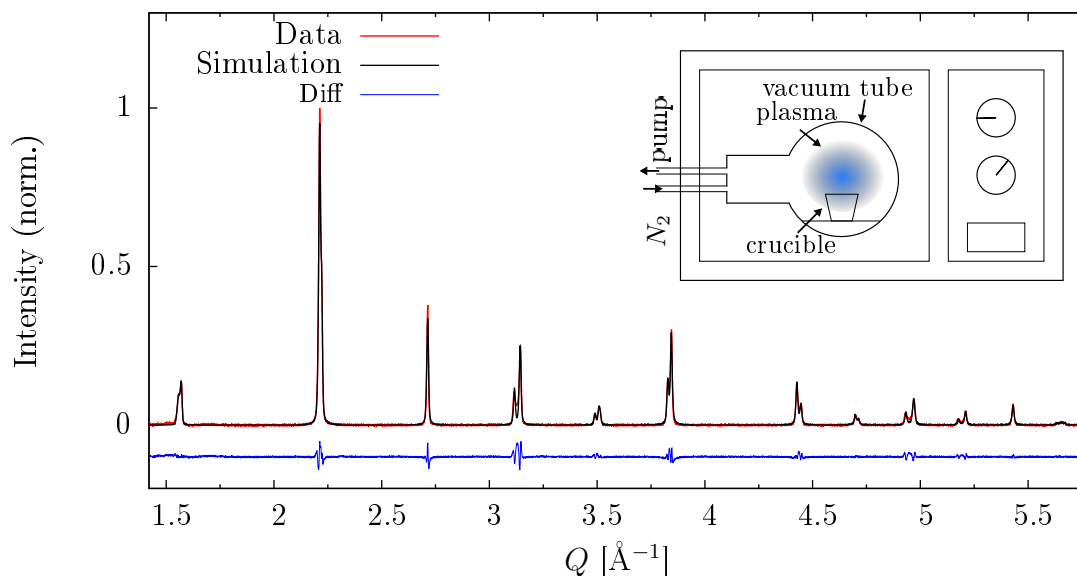


**Figure 9.7:** The XRD measurement after the N plasma treatment together with the Le Bail refinement done with Jana2006 [49]. The blue curve shows the difference between data and simulation. It is shifted by -0.1. A sketch of the used 2.45 GHz microwave plasma generator is shown in the inset. The plasma works with 800 W under 35 mbar nitrogen gas pressure and provides atomic nitrogen to the doping process.

was limited to 20 min due to stability problems. The used microwave oven was originally constructed and optimized for oxygen plasma annealing and it was not possible to keep the nitrogen plasma stable for longer time periods.

Fig. 9.7 shows the XRD measurement of the N treated powder. A Le Bail refinement in the tetragonal space group  $P4mm$  leads to a profile function with  $R_p = 3.95\%$  and  $R_{wp} = 6.47\%$ . The room temperature lattice parameters are shown in Tab. 9.3, where the results of the different powder treatments are summarized. In comparison to the change in structure calculated by Gruber et al. (Tab. 9.1, the relative change is 0.88% for the



**Table 9.3:** Comparison of lattice parameters after annealing and after nitrogen plasma treatment. The relative volume change is calculated with regard to the volume of the plasma treated.

	$a, b$ [Å]	$c$ [Å]	$V$ [Å <sup>3</sup> ]	$\Delta V$ [%]
Untreated	3.99559(29)	4.02979(40)	64.335(11)	-0.10
Annealed	3.99450(32)	4.02758(38)	64.264(12)	-0.20
N Plasma	3.99705(25)	4.03078(31)	64.397(10)	
Gruber et al.			64.32	

calculation and 0.20% in the experiments performed here, which is significantly lower than the ab initio calculation results.

A lot of external parameters affect changes of the lattice like further lattice relaxation due to the annealing procedure itself. Additionally the stoichiometry and the presence of oxygen deficiencies and on the other hand impurity phases in a real powder can lead to such deviations. The duration of the N plasma treatment was probably too short and the absence of a heater stage affected the sample preparation adversely. However, summing up, within the measurement errors one cannot exclude that a successful doping took place or not with regard to the structural analysis. Thus, it is necessary to do a magnetic characterization in order to confirm or exclude a magnetic phase reliably.

**Magnetization** The annealed and the plasma treated powder were measured to reveal the influences of the N plasma treatment on the magnetization. The field-cooled magnetization measurements of the annealed powder (Fig. 9.8a) and the N plasma treated powder (Fig. 9.8b) are shown. The magnetic field during cooling is 0.02 T. The measurement data was taken during the FC of the sample. Both samples show a pure diamagnetic behavior above 60 K for the annealed powder and 120 K for the N plasma treated powder. The diamagnetic contribution in both samples is not comparable due to the capsule and scotch tape diamagnetic signal. The paramagnetic response below approximately 60 K corresponds to paramagnetic transition of oxygen [147] of an oxygen contamination. The contamination occurs probably due to the usage of a capsule as a sample holder, which cannot be purged or pumped thoroughly even if holes are drilled into the capsule. The significant shift to a higher temperature for the nitrogen plasma annealed powder cannot be explained by a oxygen contamination. The origin of this paramagnetic phase is unknown, but may be attributed to an additional paramagnetic contamination. A verification is not possible as the contamination lies below the resolution limit and within the error of chemical analysis methods. Additionally, during the plasma annealing paramagnetic centres could be created, which are not distributed homogeneously over the powder and, thus, collective magnetism via exchange interaction is not present. A direct comparison of both measurements is not possible due to the unknown diamagnetic contributions from the used sample holders.

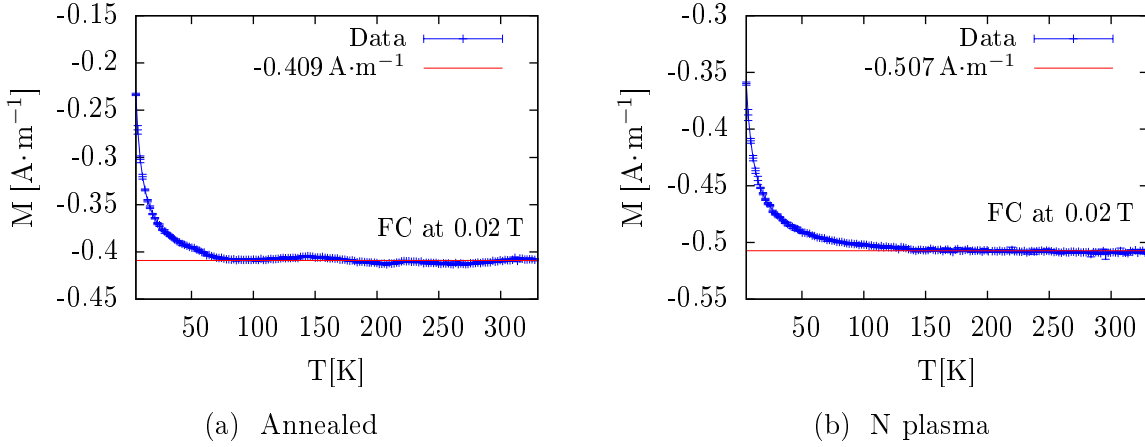


**Figure 9.8:** Magnetization from field-cooled measurements (to 10 K) of the annealed and the N plasma treated powder. The powder exhibits a diamagnetic behavior down to approximately 100 K. Then a paramagnetic behavior sets in, whose reason is a paramagnetic contamination of the used powder. The red curve indicates the diamagnetic behavior without consideration of the paramagnetic phase. The expected ferromagnetic behavior cannot be confirmed, but one cannot disprove it certainly unless the plasma annealing is improved.

Furthermore, the magnetization data does not fit to a Curie oder Curie-Weiss behavior. Possibly a superposition of several magnetic impurities causes the shown behavior. To overcome this problem it is necessary to prepare powder with in-house methods to ensure that the powder is not contaminated during the preparation process. But due to time reasons further efforts in sample preparation and analysis could not be done.

### 9.2.2 $\text{KTaO}_3$

The deposition of KTO on a STO substrate was done to create a charge imbalanced interface between KTO and STO. Tab. 9.4 shows the lattice parameters of both materials at room temperature. A lattice strain of 2% is not ideal, but can still lead to a successful epitaxial growth as reported in [2]. Choosing a STO substrate has the advantage, as shown, that it exhibits a very good crystalline quality and surface quality and thus is optimally suited to form a charge imbalanced interface with low roughness as demanded. The low

**Table 9.4:** Structural parameters at room temperature of  $\text{KTaO}_3$  [148] and  $\text{SrTiO}_3$  [21].

	$a$ [ $\text{\AA}$ ]	$V$ [ $\text{\AA}^3$ ]
KTO	3.9883(2)	63.44(2)
STO	3.901(1)	59.55(5)

melting point and high vapor pressure at low temperatures of potassium makes a controlled sample growth with the OMBE technique impossible. It would even be evaporated

during the bakeout process of the growth chamber, which is necessary to achieve low base pressures as mentioned before. Thus, the high oxygen pressure sputtering technique has been used for the KTO growth. One has to mention that the sputtering technique is also not ideal. It is a growth technique which also works close to the thermodynamical equilibrium as mentioned, and thus works with low growth rates of typically around 90 s per unit cell. The volatility of potassium requires rather high growth rates as provided by the PLD technique to avoid losing potassium during the growth process. The more promising PLD method was not available and the sputtering technique was used instead with a stoichiometric target which is commercially available from the Kurt J. Lesker company.

### Influences of growth temperature on growth

The growth temperature has the largest influence on the growth thermodynamics with respect to surface diffusion or desorption, respectively. Thus, it is the value which is considered here. The starting values used here are an oxygen partial pressure of 1.5 mbar, a plasma power of 120 W, and a growth temperature of 770 K. These values are empirical values from former perovskite thin film growth processes. For KTO it is necessary to find the lowest possible growth temperature due to the high volatility of potassium, which would end in a potassium depletion of the grown layer. The fixed stoichiometry of the target makes it impossible to correct the stoichiometry of the thin film in-situ. A self-preparation of a target was not successful and thus the option to use a target with a higher K content to compensate the loss could not be realized.

For the first samples the growth temperature was changed from 770 K to 1120 K and the growth time was constantly set to 7 h. XRR was performed to quantify the layer properties. The data and the simulation are shown in Fig. 9.9a. The vertical line indicates the critical value  $Q_t = \frac{4\pi}{\lambda} \cdot \sin \theta_t$  of total reflection for the lowest used growth temperature, which corresponds to the critical angle  $\theta_t$  introduced in section 3.5. The higher the growth temperature the larger is  $Q_t$ . As  $Q_t$  is dependent on the thin film scattering length density (SLD), which was shown in Sec. 3.1, this increase is related to an increase of the layer SLD and therefore also of the density. Higher temperatures provide more kinetic energy for diffusion processes on the surface and help to find atomic positions, which are energetically more favorable. These positions lead to a more dense structure. As a consequence the thickness of the layer decreases accordingly, and is indicated by the oscillation period, which becomes longer for higher growth temperatures. All the mentioned influences are considered in the shown simulation, which were done with GenX [52]. Fig. 9.9b shows the dependency between SLD and the layer thickness for the different growth temperatures. The optimal growth temperature can be estimated as 1020 K, where the SLD reaches the expected theoretically calculated value, which was desired to be achieved in order to get the expected KTO structure. Furthermore, the KTO roughness is 5.7(2) Å, which is roughly in the order of one unit cell. Both, the density and the roughness give rise to the assumption that a flat layer has been grown without any indication of island growth. This could also be shown with AFM.

Besides the layer density and thickness, crystalline growth was intended to be achieved. A proof of crystallinity in growth direction was not found for all grown samples, which means that most likely an amorphous layer has been grown for all used growth temperatures.

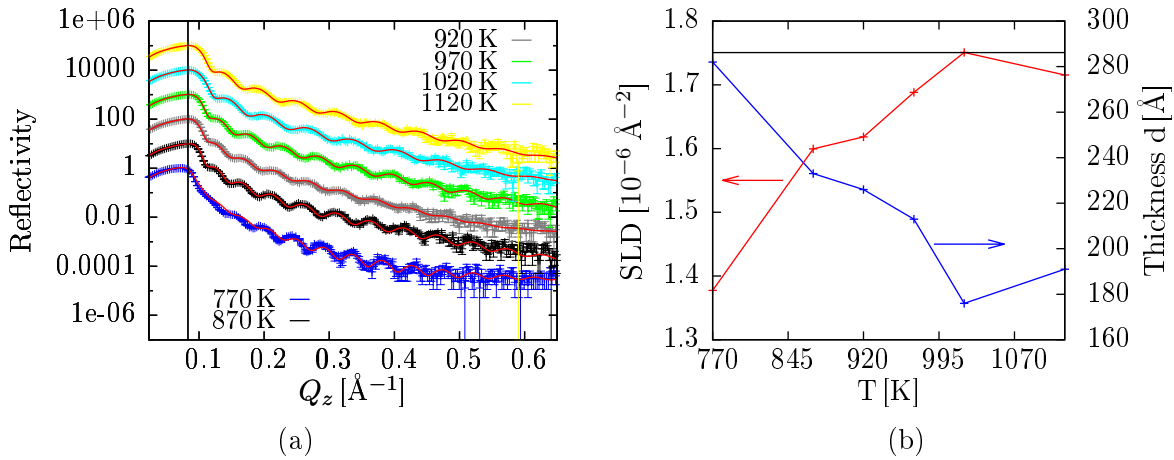


**Figure 9.9:** (a) Reflectivities measured at different temperatures. The vertical line points to the critical angle  $\theta_c$  ( $Q_c$ ) of total reflection. The higher the temperature the higher is this angle, which is related to the density of the sputtered film. For a better overview each curve is separated by a factor of 10. (b) Parameters, which one gets from the simulation of the measured reflectivity. The horizontal line describes the theoretically calculated SLD for a thin film with ideal stoichiometry and density.

To overcome this problem a further increase of the growth temperature from 1145 K to 1245 K was done in steps of 25 K, whereas the growth duration was reduced to 5 h and 2.5 h, respectively. The reduction of the growth duration helps to reduce the potassium depletion after further increase of the growth temperature by reducing the thickness accordingly. All other parameters stayed unchanged.

After each growth temperature the sample was characterized with XRD and the growth temperature was increased until a structural reflection of KTO appeared. The lowest temperature for a crystalline growth is 1195 K, where clear structural reflections appear.

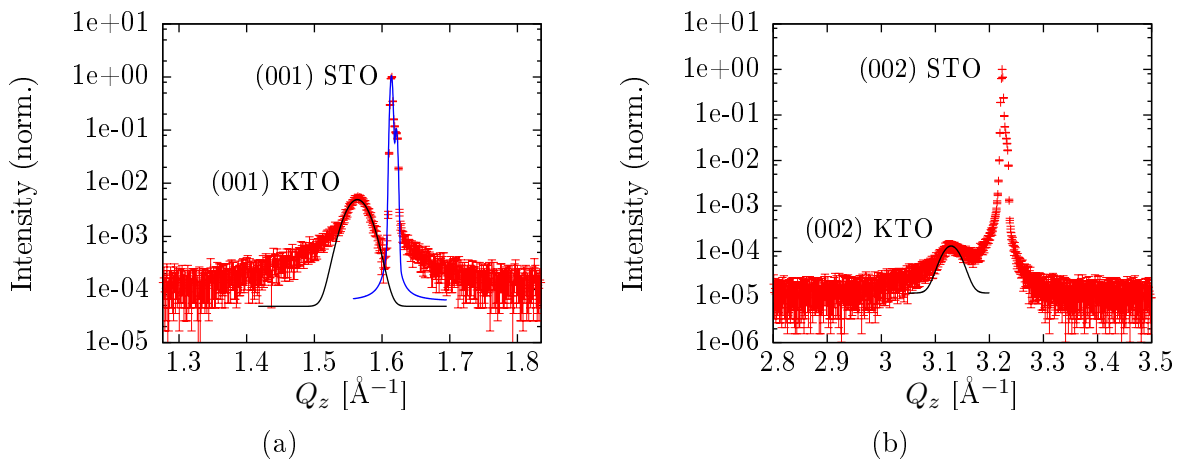


**Figure 9.10:** Room temperature XRD measurement of (001) (a) and (002) (b) reflection. Besides the Cu- $K_{\alpha_1}$  radiation a small Cu  $K_{\alpha_2}$  and Bremsstrahlung contribution is visible for the (001) and (002) STO reflection. Calculated parameters can be found in Tab. 9.5.

The XRD data is shown in Fig. 9.10, where one can find the (001) and the (002) reflections from both the KTO thin film and the STO substrate. A fit of a Gaussian to the data has been used to determine the position of each reflection.

**Table 9.5:** Position, FWHM, and out-of-plane lattice parameter of KTO and STO grown at 1195 K for the out-of-plane (001) and (002) reflections. A  $\theta$  correction has been done according to Eq. 9.2.

	(001)		(002)		$a$ [Å]
	$Q_z$ [Å <sup>-1</sup> ]	FWHM [Å <sup>-1</sup> ]	$Q_z$ [Å <sup>-1</sup> ]	FWHM [Å <sup>-1</sup> ]	
STO	1.6104(1)	0.003	3.2207(1)	0.004	3.9017(1)
KTO	1.5605(3)	0.035	3.1252(10)	0.038	4.0236(5)

A determination of the lattice parameter must contain the consideration of a  $\theta$  and  $Q_z$  shift which can be calculated with the condition

$$0 = \frac{l_1}{l_2} \sin(\theta_{r1}) - \sin(\theta_{r2}), \quad (9.1)$$

where  $l_1$  and  $l_2$  are the orders of the reflections according to  $(00l_i)$  and  $\theta_{ri}$  is the corresponding real angle, which is already corrected by  $\Delta\theta$ . The relation between real and measured angle is  $\theta_r = \theta_m + \Delta\theta$ . From Eq. 9.1 one gets

$$\tan \Delta\theta = \frac{\frac{l_1}{l_2} \sin \theta_2 - \sin \theta_1}{-\frac{l_1}{l_2} \cos \theta_2 + \cos \theta_1}. \quad (9.2)$$

Here  $\Delta\theta$  is calculated as  $-0.03^\circ$  and the corrected results of the XRD measurements are listed in Tab. 9.5. The calculated STO room temperature lattice parameter is  $3.9017(1)$  Å and in agreement with the literature value of  $a_{\text{STO}} = 3.901(1)$  Å found in [21]. The out-of-plane lattice parameter for KTO shows  $a_{\text{KTO}} = 4.0236(5)$  Å. If one assumes that the volume of the unit cells stays constant an in-plane compressive strain has been expected. The in-plane lattice parameter can be calculated to  $a = 3.9708(7)$  Å. Another explanation is the quality of the layer itself. The lattice parameter is an averaged value along the growth direction, thus the compressive strain applied by the substrate can be reduced and can explain the difference of the lattice parameter entirely. Information about the lattice relaxation in dependence of the layer thickness is not available. As introduced earlier, the FWHM of the layer reflections is inversely proportional to the total thickness of the layer and results in  $172(7)$  Å for the underlying sample, which is significantly lower compared to the layer thickness  $d = 273.5$  Å gained from XRR (Tab. 9.6). This is probably a hint to a layer which is separated into a crystalline and an amorphous part.

Potassium itself exhibits a high vapor pressure at the used growth temperature [149], which leads to an outgassing of the volatile potassium from the sample during growth, and in addition, the slow growth intensifies the effect of outgassing.

RBS revealed a strong depletion of potassium in the grown samples. One has to add, that the sensitivity of RBS to light atoms like potassium is low, and the error can be estimated

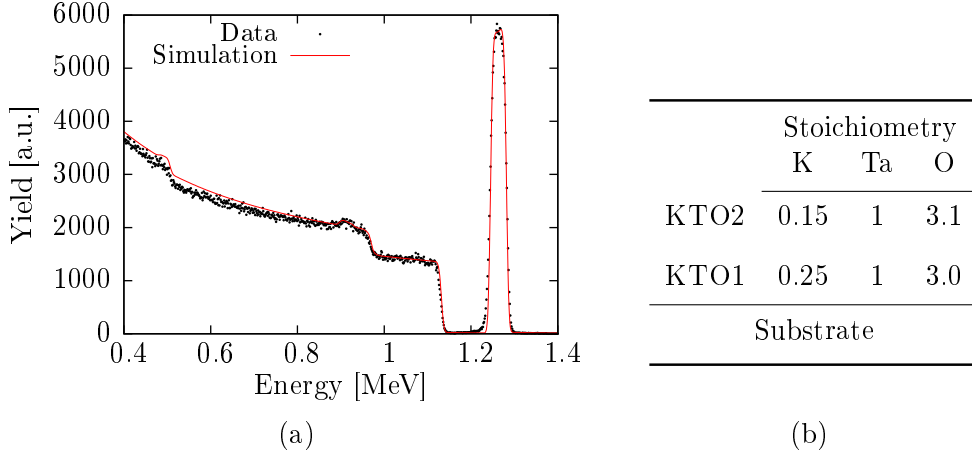


**Figure 9.11:** (a) RBS measurement of sputtered KTO on a STO substrate and its simulation. In (b) the parameters from the simulation (done with RUMP) are tabulated. At least two layers with different K content are necessary to simulate the data properly.

as higher than 10%. The results of the measurement of a sputtered KTO layer on STO at 1195 K are shown in 9.11, and nevertheless, it proves the depletion effect, which gradually increases while growing. RBS averages over the beam spotsize of a few  $\mu\text{m}$  and thus the lateral resolution is poor, which means that region with higher or lower potassium content could exist. This would explain the appearance of structural reflections due to stable perovskite regions within the layer, and also the large FWHM of the reflections, which are caused only from the crystalline part of the layer which is approximately  $173(7) \text{ \AA}$ . Additionally, the XRR measurement shown in Fig. 9.12a confirms the RBS results.

**Table 9.6:** Parameters from XRR simulation. To simulate the grown layer three different KTO sublayers are necessary with decreasing SLD as shown in Fig. 9.12b. KTO1 is the first assumed layer following the substrate, KTO2 and KTO3 are the further layers, which are necessary. The asymmetric parameter errors are calculated by GenX [52].

	thickness [ $\text{\AA}$ ]	roughness [ $\text{\AA}$ ]
Substrate		$9.0^{+1.0}_{-1.0}$
KTO 1	$184^{+4.0}_{-1.0}$	$7.5^{+0.1}_{-0.1}$
KTO 2	$66.8^{+2.0}_{-4.0}$	$4.2^{+0.1}_{-0.1}$
KTO 3	$22.7^{+2.0}_{-1.0}$	$7.5^{+0.2}_{-0.2}$

The simulation here has three different layers included with decreasing SLD, which is mainly a consequence of losing potassium during the growth process, and is in agreement with the RBS results. The corresponding SLD gained from the simulation is depicted in Fig. 9.12b.

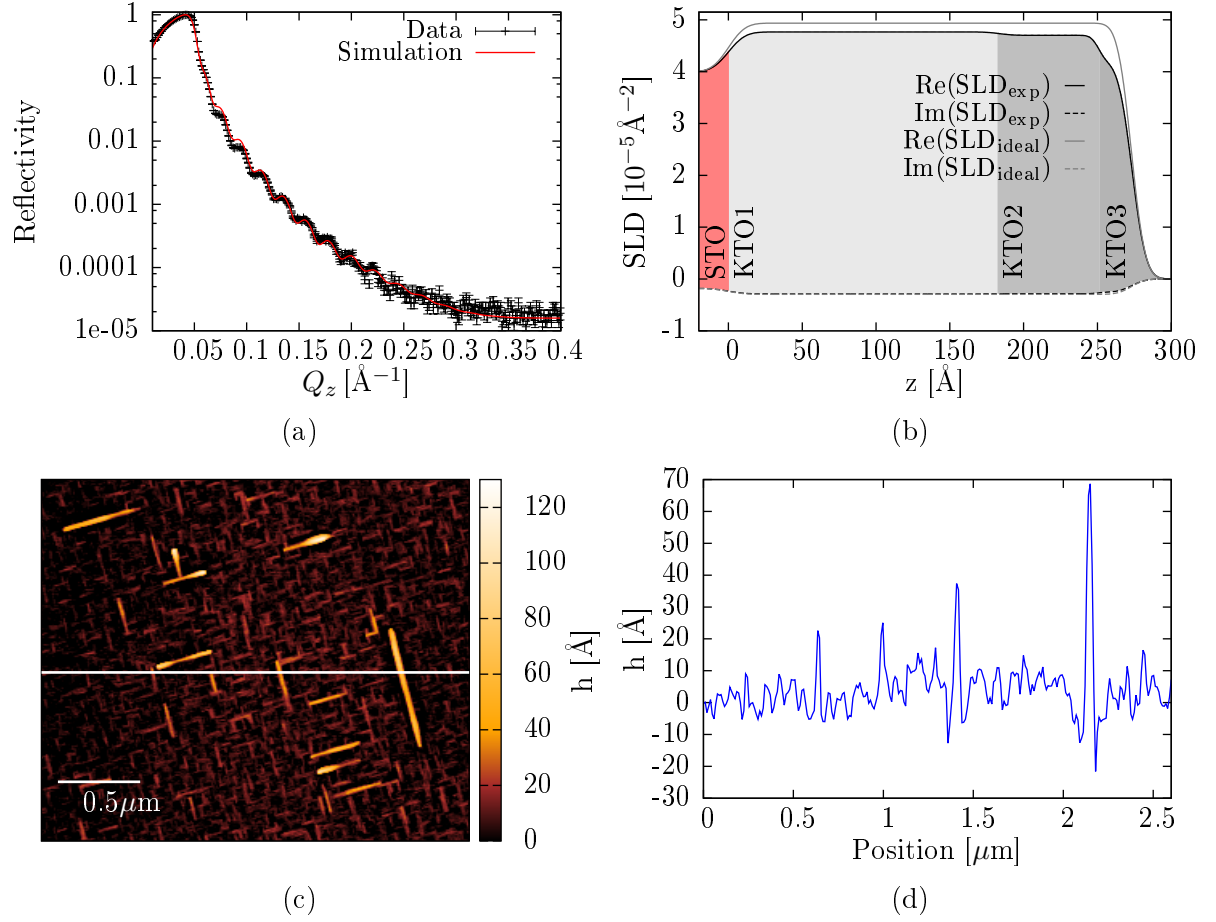


**Figure 9.12:** (a) XRR data and simulation. As the grown layer is inhomogeneous three different layers with decreasing SLD are necessary. The structural parameters of each layer are given in Tab. 9.6, whereas the SLD used is shown in (b). An ideal KTO layer is also shown here. (c)  $6 \mu\text{m}^2$  surface overview measured with an AFM. (d) is the height profile along the white line in (c). Data reduction and analysis was performed with Gwyddion [150].

An AFM measurement shows a drastically influenced surface and is shown in Fig. 9.12. It consists out of lengthy islands of different heights, which are aligned almost perpendicular to each other. Without verification, the lengthy islands are grown probably along the main cubic symmetry axis of the STO. Fig. 9.12d shows an extracted profile along the white horizontal line in Fig. 9.12c. In between rather small needles high islands can be seen. The averaged roughness for the measured region is  $10.45 \text{\AA}$ . Considering that AFM in contrast to XRR only measures a small region ( $\mu\text{m}^2$  vs.  $\text{mm}^2$ ), the roughness is in agreement with X-ray measurement. Unfortunately, AFM does not give information about the composition of these islands, which would prove the concept of a non-homogeneous distribution of potassium within the sample.

The growth of island instead of a smooth surface is usually caused by two different influences in the system. Either the growth temperature is not high enough or the stoichiometry of the growing thin film is not the expected one and thus the structure is not stable. Here it seems that the reason for this kind of growth mode is the non-stoichiometry of the

layer. The used temperature 1195 K is the lowest temperature, where one can observe a crystalline structure. Unfortunately, this growth temperature is high enough to influence the stoichiometry and thus the surface morphology negatively. This is somehow a predicament and HOPSA does not seem to be the appropriate growth method. As expected, the high oxygen pressure sputtering technique is not applicable for the growth of KTO layers on STO due to the influences of a high growth temperature together with a rather slow growth process.

### 9.3 Discussion

The two introduced rather unconventional magnetic systems are handled as promising candidates for new materials in functional devices for information technology. Especially the first one (BTO) needs experimental confirmation of the theory published by Gruber et al. However, during this work it was not possible to confirm a spontaneous magnetic polarization in powder. The publication predicted a strong magnetization for all doping materials. The reason for that is speculative, because a direct measurement of the doping concentration was not possible. The determination of concentrations of a very small amount of light atoms like carbon and nitrogen is not straight forward. A ferromagnetic behavior of the system cannot be found. It is possible that either the doping was not successful or the effect is dominated by other effects in real systems like strain or crystalline imperfections, which destroy the collective polarization of the p-orbitals. Gruber et al. calculated the case of a dopant atom on an oxygen position. According to their calculations a replacement of oxygen by dopant atoms is energetically possible and stable at the ground state. However, they could not model what happens at higher temperatures and, especially, if it is possible to introduce dopant atoms at higher temperatures. Furthermore one has to consider that the size of all dopants is smaller than oxygen, and especially carbon and boron tend to have positive oxidation numbers compared to -2 of oxygen, which could lead to instabilities.

By the way, the natural occurrence of nitrogen in the earth's atmosphere is about 80% and it contaminates oxygen supplies or vacuum chambers. In recent years lots of research was done on bulk or thin film perovskites, especially on BTO or STO. Why nobody found a doping effect by accident?

Secondly, a try to grow KTO on STO along the second route with HOPSA was done. The idea is based on a theoretical and experimental work from Oja et al. As explained the sputtering technique is not a suitable method to achieve the objective of obtaining stoichiometric and crystalline thin films. Low growth temperatures led to smooth surfaces, but epitaxial and crystalline growth could not be found. In contrast high growth temperatures result in a crystallinity, which is obviously incomplete, and in a high depletion of potassium and highly structured surface. The strong depletion of potassium may destabilize the perovskite structure and thus the layer is not homogeneous. Some regions may exhibit crystallinity and stoichiometry, whereas amorphous regions with strong potassium depletion dominate the sample. To overcome the stoichiometry problem targets with higher potassium content are necessary. The preparation of KTO targets was not successful, which also cancels out the option to grow samples on a PLD system from



a neighboring group, which is definitely the method of choice, because of its rather fast growth.

As both systems are interesting and promising one should continue working on them to achieve magnetoelectric materials that can revolutionize information technology with respect to storage efficiency in both the power consumption and storage density case. Especially for the KTO systems an exchange of STO with BTO was planned. BTO also exhibits neutral layers, which is a requirement to the system to get a charge imbalanced interface between KTO and BTO. The ferroelectric BTO may couple to the ferromagnetic interface, which enables an additional route to a multiferroic storage device.



## 10 General outlook

In this thesis metal oxides in different compounds were investigated with respect to their structural, electronic, and magnetic properties. Due to their sensitivity to external and internal parameters, transition metal ions are perfect candidates for the development of new storage device concepts, especially for  $\text{La}_{2/3}\text{Sr}_{1/3}\text{MnO}_3$ , where the magnetic properties are highly sensitive to structural and electronic changes in its environment.

Especially, the materials, where p-electrons mediate the magnetism instead of the usually magnetic 3d- or 4f- electrons are very interesting. In such materials, carbon doped  $\text{BaTiO}_3$ , for instance, ferroelectric and ferromagnetic properties can coexist and, potentially, both properties are coupled. Thus, a storage device with low energy consumption is imaginable due to the possibility of switching the magnetic states with an applied electric field. Furthermore, the second type of a p-electron system is quite promising. Here the functional device is the interface between  $\text{BaTiO}_3$  and  $\text{KTaO}_3$  thin layers, where a coupling of the ferromagnetic interface and the ferroelectric  $\text{BaTiO}_3$  layer is expected. However, the preparation of these systems is difficult and was not successful and further efforts are necessary to achieve a proof of concept.



# Acknowledgments

Special thanks for supporting my thesis go to

**Prof. Dr. Thomas Brückel** for giving me the opportunity to work at JCNS, for fruitful discussions, and for reviewing my thesis.

**Prof. Dr. Larissa Juschkin** for reviewing my thesis.

**Dr. Jörg Voigt** and **Dr. Alexander Weber** for helping me during my thesis and for many fruitful discussions which I have really appreciated.

**Dr. Jörg Voigt** for proofreading my thesis.

**Dr. Paul Zakalek**, **Dr. Markus Schmitz**, **Dr. Alexander Weber**, and **Dr. Sonja Schröder**, the MBE Team, for supporting my sample preparation and for thousands of interesting discussions, and for helping me through hard times at the touchy OMBE.

**PD Dr. Oleg Petravic** for discussing a lot of stuff concerning magnetism and MPMS.

**Jörg Perßon** for his support during powder and target preparation.

**Paul Hering** and **Dr. Karen Friese** for their help during analysis of powder data, especially for their help with Jana2006.

**Frank Gossen** and **Berthold Schmitz** for technical assistance in all ways.

**Dr. Juri Barthel** for the STEM and EDX measurements and data analysis.

**Dr. Jürgen Schubert**, **Willi Zander**, **Dr. Bernd Holländer**, and **Dr. René Heller** for performing the RBS measurements and data analysis which were an essential part of the development of thin film growth processes.

**Dr. Brian Kirby** and **Dr. Hui Wu** for the beamline support at PBR and BT-1 and I acknowledge the support of the National Institute of Standards and Technology, U. S. Department of Commerce, in providing the neutron research facilities used in this work.

**Dr. Sabine Pütter** and **Dr. Alexandra Steffen** for their support during the sample preparation at the oxide MBE at the MLZ in Garching.

**Dr. Stefan Matauch** for the beamline support at MARIA.

**Dr. Kirill Nemkovskiy**, **Dr. Yixi Su**, and **Dr. Sultan Demirdis** for the beamline support at DNS and for their help during data analysis.

**11-BM staff at APS** for performing the powder synchrotron experiment at the Powder Diffractometer at the Advanced Photon Source at Argonne National Laboratory.

**Dr. Thomas Breuer** for providing me his recipes for LSFO powder preparation.

**Xiao Sun**, **Alice Hanke**, and **Tobias Cronert** for being great office mates.

**My family and friends** for their continuous support and patience.

Last but not least I need to thank all other colleagues at the JCNS for the great support and help, and for the beers we had during conferences and stimulating discussions.

## Acknowledgments

---

Without you all, my work would not have been successfully finished. The time here was awesome and I have enjoyed every single minute.

## Bibliography

- [1] C. Gruber, P. O. Bedolla-Velazquez, J. Redinger, P. Mohn, and M. Marsman. p-electron magnetism in doped  $\text{BaTiO}_{3-x}\text{M}_x$  ( $\text{M}=\text{C},\text{N},\text{B}$ ). *EPL (Europhysics Letters)*, 97(6):67008, 2012.
- [2] R. Oja, M. Tyunina, L. Yao, T. Pinomaa, T. Kocourek, A. Dejneka, O. Stupakov, M. Jelinek, V. Trepakov, S. van Dijken, and R. M. Nieminen.  $d^0$  Ferromagnetic Interface between Nonmagnetic Perovskites. *Physical Review Letters*, 109:127207, Sep 2012.
- [3] S. Blügel, T. Brückel, R. Waser, and C. M. Schneider, editors. *Electronic Oxides - Correlation Phenomena, Exotic Phases and Novel Functionalities*. 41st IFF Springschool, Forschungszentrum Jülich, Institut für Festkörperforschung, 2010.
- [4] J. G. Bednorz and K. A. Müller. Possible high  $T_c$  superconductivity in the Ba-La-Cu-O system. *Zeitschrift für Physik B Condensed Matter*, 64(2):189–193, 1986.
- [5] A.-M. Haghiri-Gosnet and J.-P. Renard. CMR manganites: physics, thin films and devices. *Journal of Physics D: Applied Physics*, 36(8):R127, 2003.
- [6] M. Fiebig. Revival of the magnetoelectric effect. *Journal of Physics D: Applied Physics*, 38(8):R123–R152, 2005.
- [7] W. Eerenstein, N. D. Mathur, and J. F. Scott. Multiferroic and magnetoelectric materials. *Nature*, 442(7104):759–765, August 2006.
- [8] N. Reyren, S. Thiel, A. D. Caviglia, L. Fitting Kourkoutis, G. Hammerl, C. Richter, C. W. Schneider, T. Kopp, A.-S. Rüetschi, D. Jaccard, M. Gabay, D. A. Muller, J.-M. Triscone, and J. Mannhart. Superconducting Interfaces Between Insulating Oxides. *Science*, 317(5842):1196–1199, 2007.
- [9] A. Brinkman, M. Huijben, M. van Zalk, J. Huijben, U. Zeitler, J. C. Maan, W. G. van der Wiel, G. Rijnders, D. H. A. Blank, and H. Hilgenkamp. Magnetic effects at the interface between non-magnetic oxides. *Nature Materials*, 6(7):493–496, July 2007.
- [10] S. J. May, A. B. Shah, S. G. E. te Velthuis, M. R. Fitzsimmons, J. M. Zuo, X. Zhai, J. N. Eckstein, S. D. Bader, and A. Bhattacharya. Magnetically asymmetric interfaces in a  $\text{LaMnO}_3/\text{SrMnO}_3$  superlattice due to structural asymmetries. *Physical Review B*, 77:174409, May 2008.

- [11] Nicola A. Hill. Why are there so few magnetic ferroelectrics? *The Journal of Physical Chemistry B*, 104(29):6694–6709, 2000.
- [12] R. Ramesh and Nicola A. Spaldin. Multiferroics: progress and prospects in thin films. *Nature Materials*, 6(1):21–29, January 2007.
- [13] J. Hemberger, A. Krimmel, T. Kurz, H.-A. Krug von Nidda, V. Yu. Ivanov, A. A. Mukhin, A. M. Balbashov, and A. Loidl. Structural, magnetic, and electrical properties of single-crystalline  $\text{La}_{1-x}\text{Sr}_x\text{MnO}_3$  ( $0.4 < x < 0.85$ ). *Physical Review B*, 66:094410, Sep 2002.
- [14] Koichi Momma and Fujio Izumi. VESTA: a three-dimensional visualization system for electronic and structural analysis. *Journal of Applied Crystallography*, 41(3):653–658, June 2008.
- [15] S. Sasaki, C. T. Prewitt, J. D. Bass, and W. A. Schulze. Orthorhombic perovskite  $\text{CaTiO}_3$  and  $\text{CdTiO}_3$ : structure and space group. *Acta Crystallographica Section C*, 43(9):1668–1674, Sep 1987.
- [16] V.M. Goldschmidt. Die Gesetze der Krystallochemie. *Naturwissenschaften*, 14(21):477–485, 1926.
- [17] FIZ Karlsruhe. Inorganic Crystal Structure Database (ICSD). <https://icsd.fiz-karlsruhe.de>, 2015. [Online; accessed 05-August-2015].
- [18] Yu-ping Cai, Dai-Zhao Han, and Ru-Yun Ning. Theoretical Study of Antiferrodistortive Phase Transition in Strontium Titanate. *Chinese Journal of Chemical Physics*, 23(2):237–240, 2010.
- [19] D. A. Mota, Y. Romaguera Barcelay, A. M. R. Senos, C. M. Fernandes, P. B. Tavares, I. T. Gomes, P. Sá, L Fernandes, B. G. Almeida, F. Figueiras, P. Mirzadeh Vaghefi, V. S. Amaral, A. Almeida, J. Pérez de la Cruz, and J. Agostinho Moreira. Unravelling the effect of  $\text{SrTiO}_3$  antiferrodistortive phase transition on the magnetic properties of  $\text{La}_{0.7}\text{Sr}_{0.3}\text{MnO}_3$  thin films. *Journal of Physics D: Applied Physics*, 47(43):435002, 2014.
- [20] S. A. Hayward and E. K. H. Salje. Cubic-tetragonal phase transition in  $\text{SrTiO}_3$  revisited: Landau theory and transition mechanism. *Phase Transitions*, 68(3):501–522, 1999.
- [21] Yu. A. Abramov, V. G. Tsirelson, V. E. Zavodnik, S. A. Ivanov, and Brown I. D. The chemical bond and atomic displacements in  $\text{SrTiO}_3$  from X-ray diffraction analysis. *Acta Crystallographica Section B*, 51(6):942–951, Dec 1995.
- [22] Safa Mnefgui, Abdessalem Dhahri, Jemai Dhahri, and El-Kebir Hlil. Effects of Transition-Metal V-Doping on the Structural, Magnetic and Transport Properties in  $\text{La}_{0.67}\text{Sr}_{0.33}\text{MnO}_3$  Manganite Oxide. *Journal of Superconductivity and Novel Magnetism*, 26(2):251–260, 2013.



- 
- [23] J. Blasco, M. C. Sánchez, J. García, J. Stankiewicz, and J. Herrero-Martín. Growth of  $\text{Sr}_{2/3}\text{Ln}_{1/3}\text{FeO}_3$  (Ln=La, Pr, and Nd) single crystals by the floating zone technique. *Journal of Crystal Growth*, 310(13):3247 – 3250, 2008.
- [24] Marjana Ležaić and Martin Schlipf. Crystal Field Effects and Excitations. In Manuel Angst, Thomas Brückel, Dieter Richter, and Reiner Zorn, editors, *Scattering Methods for Condensed Matter Research: Towards Novel Applications at Future Sources*, volume 33. Forschungszentrum Jülich GmbH, 2012.
- [25] E. Teller H. A. Jahn. Stability of Polyatomic Molecules in Degenerate Electronic States. I. Orbital Degeneracy. *Proceedings of the Royal Society of London. Series A, Mathematical and Physical Sciences*, 161(905):220–235, 1937.
- [26] E. J. W. Verwey and P. W. Haayman. Electronic conductivity and transition point of magnetite ( $\text{Fe}_3\text{O}_4$ ). *Physica*, 8(9):979 – 987, 1941.
- [27] J. Hubbard. Electron correlations in narrow energy bands. *Proceedings of the Royal Society of London. Series A, Mathematical and Physical Sciences*, 276(1365):238–257, 1963.
- [28] James R. Cullen and Earl R. Callen. Multiple ordering in magnetite. *Physical Review B*, 7:397–402, Jan 1973.
- [29] Philip Hofmann. *Solid State Physics: An Introduction*. Wiley-VCH Verlag, 2nd edition, 2015.
- [30] A. J. Millis. Orbital ordering and superexchange in manganite oxides. *Physical Review B*, 55:6405–6408, Mar 1997.
- [31] P. W. Anderson. Antiferromagnetism. Theory of Superexchange Interaction. *Physical Review*, 79:350–356, Jul 1950.
- [32] John B. Goodenough. Theory of the Role of Covalence in the Perovskite-type Manganites  $[\text{La},\text{M}(\text{II})]\text{MnO}_3$ . *Physical Review*, 100:564–573, Oct 1955.
- [33] John B. Goodenough. An interpretation of the magnetic properties of the perovskite-type mixed crystals  $\text{La}_{1-x}\text{Sr}_x\text{CoO}_{3-\lambda}$ . *Journal of Physics and Chemistry of Solids*, 6(2):287 – 297, 1958.
- [34] Junjiro Kanamori. Superexchange interaction and symmetry properties of electron orbitals. *Journal of Physics and Chemistry of Solids*, 10(2):87 – 98, 1959.
- [35] Clarence Zener. Interaction between the  $d$ -shells in the Transition Metals. ii. Ferromagnetic Compounds of Manganese with Perovskite Structure. *Physical Review*, 82:403–405, May 1951.
- [36] J. Nogués and Ivan K. Schuller. Exchange bias. *Journal of Magnetism and Magnetic Materials*, 192(2):203 – 232, 1999.

- [37] A. E. Berkowitz and Kentaro Takano. Exchange anisotropy — a review. *Journal of Magnetism and Magnetic Materials*, 200(1–3):552 – 570, 1999.
- [38] J. M. D. Coey. *Magnetism and Magnetic Materials*. Cambridge University Press, 2009.
- [39] I. G. Austin and N. F. Mott. Polarons in crystalline and non-crystalline materials. *Advances in Physics*, 50(7):757–812, 2001.
- [40] R. C. Devlin, A. L. Krick, R. J. Sichel-Tissot, Y. J. Xie, and S. J. May. Electronic transport and conduction mechanism transition in  $\text{La}_{1/3}\text{Sr}_{2/3}\text{FeO}_3$  thin films. *Journal of Applied Physics*, 115(23), 2014.
- [41] Thomas Brückel. A Neutron Primer. In Thomas Brückel, Dieter Richter, Georg Roth, Andreas Wischnewski, and Reiner Zorn, editors, *Neutron Scattering Lectures*, volume key technologies 106. Zentralbibliothek des Forschungszentrum Jülich GmbH, 2015.
- [42] D. S. Sivia. *Elementary Scattering Theory*, volume 14. Oldenburg Verlag, 2011.
- [43] John David Jackson. *Classical Electrodynamics*, volume 3. Wiley, 1998.
- [44] Charles Kittel. *Einführung in die Festkörperphysik*, volume 1. Oxford University Press, 2006.
- [45] Ulrich Rücker and Emmanuel Kentzinger. Thin film systems: Scattering under grazing incidence. In Knut Urban, Claus M. Schneider, Thomas Brückel, Stefan Blügel, Karsten Tillmann, Werner Schweika, Markus Lentzen, and Lutz Baumgarten, editors, *Probing the nanoworld*, volume 34. Zentralbibliothek des Forschungszentrum Jülich GmbH, 2009.
- [46] G. Roth. Diffraction. In Thomas Brückel, Dieter Richter, Georg Roth, Andreas Wischnewski, and Reiner Zorn, editors, *Neutron Scattering Lectures*, volume key technologies 106. Zentralbibliothek des Forschungszentrum Jülich GmbH, 2015.
- [47] H. M. Rietveld. A profile refinement method for nuclear and magnetic structures. *Journal of Applied Crystallography*, 2(2):65–71, June 1969.
- [48] V. K. Pecharsky and P. Y. Zavalij. *Fundamentals of Powder Diffraction and Structural Characterization of Materials*. Springer Science+Business Media, 2009.
- [49] Václav Petříček, Michal Dušek, and Lukáš Palatinus. Crystallographic Computing System JANA2006: General features. *Zeitschrift für Kristallographie - Crystalline Materials*, 229(5):345–352, 2014.
- [50] John Lekner. *Theory of Reflection*, volume 87. Springer Series on Atomic, Optical, and Plasma Physics, 2016.
- [51] L. G. Parratt. Surface Studies of Solids by Total Reflection of X-Rays. *Physical Review*, 95:359–369, Jul 1954.

- 
- [52] Matts Björck and Gabriella Andersson. *GenX: an extensible X-ray reflectivity refinement program utilizing differential evolution*. *Journal of Applied Crystallography*, 40(6):1174–1178, Dec 2007.
- [53] G. L. Squires. *Introduction to the theory of Thermal Neutron Scattering*. Cambridge University Press, New York, 1978.
- [54] Hartmut Zabel. Spin polarized neutron reflectivity of magnetic films and superlattices. *Physica B: Condensed Matter*, 198(1):156 – 162, 1994.
- [55] J. F. Ankner and G. P. Felcher. Polarized-neutron reflectometry. *Journal of Magnetism and Magnetic Materials*, 200:741 – 754, 1999.
- [56] M. P. Seah and W. A. Dench. Quantitative electron spectroscopy of surfaces: A standard data base for electron inelastic mean free paths in solids. *Surface and Interface Analysis*, 1(1):2–11, 1979.
- [57] Hans Lüth. *Solid Surfaces, Interfaces and Thin Films*. Springer-Verlag Berlin Heidelberg, 5 edition, 2010.
- [58] M. A. Herman and H. Sitter. *Molecular Beam Epitaxy - Fundamentals and Current Status*. Springer-Verlag, 1989.
- [59] R. Dittmann. Thin film deposition techniques. In S. Blügel, T. Brückel, R. Waser, and C. M. Schneider, editors, *Electronic Oxides - Correlation Phenomena, Exotic Phases and Novel Functionalities*. 41st IFF Springschool, Forschungszentrum Jülich, Institut für Festkörperforschung, 2010.
- [60] P. Ehrhart. Präparation dünner Schichten: Molekularstrahl-Epitaxie. In P.H. Dederichs, P. Grünberg, and R. Hölzle, editors, *Magnetische Schichtsysteme*. 30. IFF Ferienkurs, Forschungszentrum Jülich GmbH, Institut für Festkörperforschung, 1999.
- [61] W. Schweika. Schichtpräparation mit Sputterverfahren. In P.H. Dederichs, P. Grünberg, and R. Hölzle, editors, *Magnetische Schichtsysteme*. 30. IFF Ferienkurs, Forschungszentrum Jülich GmbH, Institut für Festkörperforschung, 1999.
- [62] L. B. Freund and S. Suresh. *Thin Film Materials*. Cambridge University Press, 2004. Cambridge Books Online.
- [63] Günter Sauerbrey. Verwendung von Schwingquarzen zur Wägung dünner Schichten und zur Mikrowägung. *Zeitschrift für Physik*, 155(2):206–222, 1959.
- [64] Ulrich Poppe. Herstellung von Oxidschichten mit physikalischen Methoden: Sputtern, reaktives Aufdampfen, Laserablation. In Rainer Hölzle, editor, *Elektrokeramische Methoden*, volume 1. Forschungszentrum Jülich GmbH - Institut für Festkörperforschung, 1995.

- [65] J. M. Vila-Funqueiriño, C. T. Bui, B. Rivas-Murias, E. Winkler, J. Milano, J. Santiso, and F. Rivadulla. Thermodynamic conditions during growth determine the magnetic anisotropy in epitaxial thin-films of  $\text{La}_{0.7}\text{Sr}_{0.3}\text{MnO}_3$ . *Journal of Physics D: Applied Physics*, 49(31):315001, 2016.
- [66] K. Oura, V. G. Lifshits, A. Saranin, A.V. Zotov, and M. Katayama. *Surface Science: An Introduction*, volume 1. Springer-Verlag Berlin Heidelberg, 2003.
- [67] W. Braun. *Applied RHEED: Reflection High-Energy Electron Diffraction During Crystal Growth*, volume 1. Springer-Verlag Berlin Heidelberg, 1999.
- [68] Ayahiko Ichimiya and Philip I. Cohen. *Reflection High-Energy Electron Diffraction*, volume 1. Cambridge University Press, 2004.
- [69] Markus Schmitz. *Strain and electric field mediated manipulation of magnetism in  $\text{La}_{1-x}\text{Sr}_x\text{MnO}_3/\text{BaTiO}_3$  heterostructures*. PhD thesis, RWTH Aachen, Forschungszentrum Jülich, 2015.
- [70] G. Binnig, C. F. Quate, and Ch. Gerber. Atomic Force Microscope. *Physical Review Letters*, 56:930–933, Mar 1986.
- [71] J. E. Jones. On the Determination of Molecular Fields. ii. From the Equation of State of a Gas. *Proceedings of the Royal Society of London A: Mathematical, Physical and Engineering Sciences*, 106(738):463–477, 1924.
- [72] Boris Chesca, Reinhold Kleiner, and Dieter Koelle. SQUID Theory. In J. Clarke and A. I. Braginski, editors, *The SQUID Handbook*, volume 1. WILEY-VCH Verlag GmbH & Co. KGaA, 2004.
- [73] Mike McElfresh. *Fundamentals of Magnetism and Magnetic Measurements featuring Quantum Design’s Magnetic Property Measurement System*. Quantum Design, 1994.
- [74] R. L. Fagaly. Superconducting quantum interference device instruments and applications. *Review of Scientific Instruments*, 77(10), 2006.
- [75] 1. *Physical Property Measurement System: Heat Capacity Option User’s Manual*. Quantum Design, 2004.
- [76] Lawrence R. Doolittle. Algorithms for the rapid simulation of Rutherford backscattering spectra. *Nuclear Instruments and Methods in Physics Research Section B: Beam Interactions with Materials and Atoms*, 9(3):344 – 351, 1985.
- [77] David B. Williams and C. Barry Carter, editors. *Transmission Electron Microscopy - Part 1 - Basics*, volume 2. Springer Science+Business Media, 2009.
- [78] Ernst Ruska-Centre for Microscopy and Spectroscopy with Electrons (ER-C). FEI Helios Nanolab 400S FIB-SEM. *Journal of large-scale research facilities*, 2(A60), 2016. <http://dx.doi.org/10.17815/jlsrf-2-106>.

- [79] Ernst Ruska-Centre for Microscopy and Spectroscopy with Electrons (ER-C). FEI Helios Nanolab 460F1 FIB-SEM. *Journal of large-scale research facilities*, 2(A59), 2016. <http://dx.doi.org/10.17815/jlsrf-2-106>.
- [80] Ernst Ruska-Centre for Microscopy and Spectroscopy with Electrons (ER-C). FEI Titan G2 80-200 CREWLEY. *Journal of large-scale research facilities*, 2(A43), 2016. <http://dx.doi.org/10.17815/jlsrf-2-106>.
- [81] P. Schlossmacher, D. O. Klenov, B. Freitag, S. von Harrach, and A. Steinbach. Nanoscale Chemical Compositional Analysis with an Innovative S/TEM-EDX System. *Microscopy and Analysis*, 24(7):S5–S8, 2010.
- [82] Jun Wang, Brian H. Toby, Peter L. Lee, Lynn Ribaud, Sytle M. Antao, Charles Kurtz, Mohan Ramanathan, Robert B. Von Dreele, and Mark A. Beno. A dedicated powder diffraction beamline at the Advanced Photon Source: Commissioning and early operational results. *Review of Scientific Instruments*, 79(8), 2008.
- [83] Heinz Maier-Leibnitz Zentrum. DNS: Diffuse scattering neutron time-of-flight spectrometer. *Journal of large-scale research facilities*, 1(A27), 2015. <http://dx.doi.org/10.17815/jlsrf-1-33>.
- [84] Yixi Su. DNS: Neutron Polarization Analysis. In Thomas Brückel, Dieter Richter, Georg Roth, Andreas Wischnewski, and Reiner Zorn, editors, *Laboratory Course Neutron Scattering Experiment Manual*, volume key technologies 107. Zentralbibliothek des Forschungszentrum Jülich GmbH, 2015.
- [85] R. M. Moon, T. Riste, and W. C. Koehler. Polarization Analysis of Thermal-Neutron Scattering. *Physical Review*, 181:920–931, May 1969.
- [86] O. Schärpf and H. Capellmann. The XYZ-Difference Method with Polarized Neutrons and the Separation of Coherent, Spin Incoherent, and Magnetic Scattering Cross Sections in a Multidetector. *physica status solidi (a)*, 135(2):359–379, 1993.
- [87] NIST Centre for Neutron Research. High Resolution Powder Diffractometer - BT1. <https://www.ncnr.nist.gov/instruments/bt1/index.html>, 2016. [Online; accessed 14-July-2016].
- [88] Heinz Maier-Leibnitz Zentrum. MARIA: Magnetic reflectometer with high incident angle. *Journal of large-scale research facilities*, 1(A8), 2015. <http://dx.doi.org/10.17815/jlsrf-1-29>.
- [89] NIST Centre for Neutron Research. Polarized Beam Reflectometer (PBR). <https://www.ncnr.nist.gov/instruments/pbr/>, 2016. [Online; accessed 14-July-2016].
- [90] P. D. Battle, T. C. Gibb, and S. Nixon. A study of charge disproportionation in the nonstoichiometric perovskite  $\text{Sr}_2\text{LaFe}_3\text{O}_{8+y}$  by Mössbauer spectroscopy. *Journal of Solid State Chemistry*, 77(1):124 – 131, 1988.

- [91] J. B. Yang, X. D. Zhou, Z. Chu, W. M. Hikal, Q. Cai, J. C. Ho, D. C. Kundaliya, W. B. Yelon, W. J. James, H. U. Anderson, H. H. Hamdeh, and S. K. Malik. Charge disproportionation and ordering in  $\text{La}_{1/3}\text{Sr}_{2/3}\text{FeO}_{3-\delta}$ . *Journal of Physics: Condensed Matter*, 15(29):5093, 2003.
- [92] M. Takano and Y. Takeda. Electronic State of  $\text{Fe}^{4+}$  Ions in Perovskite-Type Oxides. *Bulletin of the Institute for Chemical Research, Kyoto University*, 61(5-6):406–425, 1983.
- [93] J. Matsuno, T. Mizokawa, A. Fujimori, K. Mamiya, Y. Takeda, S. Kawasaki, and M. Takano. Photoemission and hartree-fock studies of oxygen-hole ordering in charge-disproportionated  $\text{La}_{1-x}\text{Sr}_x\text{FeO}_3$ . *Physical Review B*, 60:4605–4608, Aug 1999.
- [94] P. D. Battle, T. C. Gibb, and P. Lightfoot. The structural consequences of charge disproportionation in mixed-valence iron oxides. i. the crystal structure of  $\text{Sr}_2\text{LaFe}_3\text{O}_{8.94}$  at room temperature and 50 K. *Journal of Solid State Chemistry*, 84(2):271 – 279, 1990.
- [95] J. Q. Li, Y. Matsui, S. K. Park, and Y. Tokura. Charge Ordered States in  $\text{La}_{1-x}\text{Sr}_x\text{FeO}_3$ . *Physical Review Letters*, 79:297–300, Jul 1997.
- [96] Jie Ma. *Neutron Scattering Study of Charge-Ordering in  $R_{1/3}\text{Sr}_{2/3}\text{FeO}_3$  ( $R=\text{La, Pr, Nd, Sm, Y}$ )*. PhD thesis, Iowa State University Paper 11490, 2010.
- [97] K. Ueno, A. Ohtomo, F. Sato, and M. Kawasaki. Field-effect modulation of transport properties of charge-ordered  $\text{La}_{1/3}\text{Sr}_{2/3}\text{FeO}_3$  thin films. *Physical Review B*, 73:165103, Apr 2006.
- [98] R. J. McQueeney, J. Ma, S. Chang, J.-Q. Yan, M. Hehlen, and F. Trouw. Stabilization of Charge Ordering in  $\text{La}_{1/3}\text{Sr}_{2/3}\text{FeO}_{3-\delta}$  by Magnetic Exchange. *Physical Review Letters*, 98:126402, 2007.
- [99] N. F. Mott and L. Friedman. Metal-insulator transitions in  $\text{VO}_2$ ,  $\text{Ti}_2\text{O}_3$  and  $\text{Ti}_{2-x}\text{V}_x\text{O}_3$ . *Philosophical Magazine*, 30(2):389–402, 1974.
- [100] T. Mizokawa and A. Fujimori. Description of Spin and Charge Domain Walls in Doped Perovskite-Type 3d Transition-Metal Oxides Based on Superexchange Interaction. *Physical Review Letters*, 80:1320–1323, Feb 1998.
- [101] P. M. Woodward, D. E. Cox, E. Moshopoulou, A. W. Sleight, and S. Morimoto. Structural studies of charge disproportionation and magnetic order in  $\text{CaFeO}_3$ . *Physical Review B*, 62:844–855, Jul 2000.
- [102] Rebecca J. Sichel-Tissot, Robert C. Devlin, Philip J. Ryan, Jong-Woo Kim, and Steven J. May. The effect of oxygen vacancies on the electronic phase transition in  $\text{La}_{1/3}\text{Sr}_{2/3}\text{FeO}_3$  films. *Applied Physics Letters*, 103(21), 2013.

- 
- [103] Makoto Minohara, Miho Kitamura, Hiroki Wadati, Hironori Nakao, Reiji Kumai, Youichi Murakami, and Hiroshi Kumigashira. Thickness-dependent physical properties of  $\text{La}_{1/3}\text{Sr}_{2/3}\text{FeO}_3$  thin films grown on  $\text{SrTiO}_3$  (001) and (111) substrates. *Journal of Applied Physics*, 120(2), 2016.
- [104] Y. J. Xie, M. D. Scafetta, E. J. Moon, A. L. Krick, R. J. Sichel-Tissot, and S. J. May. Electronic phase diagram of epitaxial  $\text{La}_{1-x}\text{Sr}_x\text{FeO}_3$  films. *Applied Physics Letters*, 105(6), 2014.
- [105] S. K. Park, T. Ishikawa, Y. Tokura, J. Q. Li, and Y. Matsui. Variation of charge-ordering transitions in  $\text{R}_{1/3}\text{Sr}_{2/3}\text{FeO}_3$  (r=La, Pr, Nd, Sm, and Gd). *Physical Review B*, 60:10788–10795, Oct 1999.
- [106] A. Banerjee, S. Pal, E. Rozenberg, and B. K. Chaudhuri. Adiabatic and non-adiabatic small-polaron hopping conduction in  $\text{La}_{1-x}\text{Pb}_x\text{MnO}_{3+\delta}$  ( $0.0 \leq x \leq 0.5$ )-type oxides above the metal–semiconductor transition. *Journal of Physics: Condensed Matter*, 13(42):9489, 2001.
- [107] Artur Glavic. Plot.py: direct data plotting and evaluation. <https://sourceforge.net/projects/plotpy/>, 2017. [Online; accessed 18-April-2017].
- [108] A. J. Dianoux and G. Lander, editors. *Neutron Data Booklet*. Institut Laue-Langevin, OCP Science imprint, 2003.
- [109] M. I. Aroyo, J. M. Perez-Mato, D. Orobengoa, E. Tasci, G. De La Flor, and A. Kirov. Crystallography online: Bilbao crystallographic server. *Bulgarian Chemical Communications*, 43(2):183–197, 2011.
- [110] J. M. Perez-Mato, S.V. Gallego, E.S. Tasci, L. Elcoro, G. de la Flor, and M.I. Aroyo. Symmetry-Based Computational Tools for Magnetic Crystallography. *Annual Review of Materials Research*, 45(1):217–248, 2015.
- [111] Peter W. Stephens. Phenomenological model of anisotropic peak broadening in powder diffraction. *Journal of Applied Crystallography*, 32(2):281–289, 1999.
- [112]  $\text{SrTiO}_3$  for Research and Development. <http://crystec.de/daten/srtio3.pdf>, 2017. [Online; accessed 17-May-2017].
- [113] Paul Zakalek. *Magnetic Interface Effects in Thin Film Heterostructures*. PhD thesis, RWTH Aachen, Forschungszentrum Jülich, 2016.
- [114] N. D. Mermin and H. Wagner. Absence of Ferromagnetism or Antiferromagnetism in One- or Two-Dimensional Isotropic Heisenberg Models. *Physical Review Letters*, 17:1133–1136, Nov 1966.
- [115] J. Okamoto, D. J. Huang, K. S. Chao, S. W. Huang, C.-H. Hsu, A. Fujimori, A. Masuno, T. Terashima, M. Takano, and C. T. Chen. Quasi-two-dimensional  $d$ -spin and  $p$ -hole ordering in the three-dimensional perovskite  $\text{La}_{1/3}\text{Sr}_{2/3}\text{FeO}_3$ . *Physical Review B*, 82:132402, Oct 2010.

- [116] T. Holstein. Studies of polaron motion. *Annals of Physics*, 8(3):343 – 389, 1959.
- [117] J. H. Haeni, C. D. Theis, and D. G. Schlom. RHEED Intensity Oscillations for the Stoichiometric Growth of  $\text{SrTiO}_3$  Thin Films by Reactive Molecular Beam Epitaxy. *Journal of Electroceramics*, 4(2):385–391, 2000.
- [118] Myron B. Salamon and Marcelo Jaime. The physics of manganites: Structure and transport. *Review of modern Physics*, 73:583–628, Aug 2001.
- [119] C. Adamo, X. Ke, H. Q. Wang, H. L. Xin, T. Heeg, M. E. Hawley, W. Zander, J. Schubert, P. Schiffer, D. A. Muller, L. Maritato, and D. G. Schlom. Effect of biaxial strain on the electrical and magnetic properties of (001)  $\text{La}_{0.7}\text{Sr}_{0.3}\text{MnO}_3$  thin films. *Applied Physics Letters*, 95(11), 2009.
- [120] Masahito Mochizuki and Nobuo Furukawa. Microscopic model and phase diagrams of the multiferroic perovskite manganites. *Physical Review B*, 80:134416, Oct 2009.
- [121] Andrius Miniotas, Arturas Vailionis, Eric B. Svedberg, and Ulf O. Karlsson. Misfit strain induced lattice distortions in heteroepitaxially grown  $\text{La}_x\text{Ca}_{1-x}\text{MnO}_3$  thin films studied by extended x-ray absorption fine structure and high-resolution x-ray diffraction. *Journal of Applied Physics*, 89(4):2134–2137, 2001.
- [122] R. Heller and J. Schubert. private communication.
- [123] Joonghoe Dho, N. H. Hur, I. S. Kim, and Y. K. Park. Oxygen pressure and thickness dependent lattice strain in  $\text{La}_{0.7}\text{Sr}_{0.3}\text{MnO}_3$  films. *Journal of Applied Physics*, 94(12):7670–7674, 2003.
- [124] J.-L. Maurice, F. Pailloux, A. Barthélémy, O. Durand, D. Imhoff, R. Lyonnet, A. Rocher, and J.-P. Contour. Strain relaxation in the epitaxy of  $\text{La}_{2/3}\text{Sr}_{1/3}\text{MnO}_3$  grown by pulsed-laser deposition on  $\text{SrTiO}_3$  (001). *Philosophical Magazine*, 83(28):3201–3224, 2003.
- [125] H Boschker, M Huijben, A Vailionis, J Verbeeck, S van Aert, M Luysberg, S Bals, G van Tendeloo, E P Houwman, G Koster, D H A Blank, and G Rijnders. Optimized fabrication of high-quality  $\text{La}_{0.67}\text{Sr}_{0.33}\text{MnO}_3$  thin films considering all essential characteristics. *Journal of Physics D: Applied Physics*, 44(20):205001, 2011.
- [126] D. Pesquera, V. Skumryev, F. Sánchez, G. Herranz, and J. Fontcuberta. Magnetoelastic coupling in  $\text{La}_{2/3}\text{Sr}_{1/3}\text{MnO}_3$  thin films on  $\text{SrTiO}_3$ . *Physical Review B*, 84:184412, Nov 2011.
- [127] Richard D. Deslattes, Ernest G. Kessler, P. Indelicato, L. de Billy, E. Lindroth, and J. Anton. X-ray transition energies: new approach to a comprehensive evaluation. *Review of modern Physics*, 75:35–99, Jan 2003.
- [128] R. Peng, H. C. Xu, M. Xia, J. F. Zhao, X. Xie, D. F. Xu, B. P. Xie, and D. L. Feng. Tuning the dead-layer behavior of  $\text{La}_{0.67}\text{Sr}_{0.33}\text{MnO}_3/\text{SrTiO}_3$  via interfacial engineering. *Applied Physics Letters*, 104(8):081606, 2014.



- 
- [129] F. Y. Bruno, J. Garcia-Barriocanal, M. Varela, N. M. Nemes, P. Thakur, J. C. Cezar, N. B. Brookes, A. Rivera-Calzada, M. Garcia-Hernandez, C. Leon, S. Okamoto, S. J. Pennycook, and J. Santamaria. Electronic and Magnetic Reconstructions in  $\text{La}_{0.7}\text{Sr}_{0.3}\text{MnO}_3/\text{SrTiO}_3$  Heterostructures: A Case of Enhanced Interlayer Coupling Controlled by the Interface. *Physical Review Letters*, 106:147205, Apr 2011.
- [130] M. Ziese, I. Vrejoiu, and D. Hesse. Inverted hysteresis and giant exchange bias in  $\text{La}_{0.7}\text{Sr}_{0.3}\text{MnO}_3/\text{SrRuO}_3$  superlattices. *Applied Physics Letters*, 97(5):052504, 2010.
- [131] M. R. Fitzsimmons, P. Yashar, C. Leighton, Ivan K. Schuller, J. Nogués, C. F. Majkrzak, and J. A. Dura. Asymmetric Magnetization Reversal in Exchange-Biased Hysteresis Loops. *Physical Review Letters*, 84:3986–3989, Apr 2000.
- [132] Amitesh Paul, Emmanuel Kentzinger, Ulrich Rücker, and Thomas Brückel. Symmetry and asymmetry during magnetization reversal in exchange biased multilayers and bilayers. *Physical Review B*, 73:092410, Mar 2006.
- [133] S. M. Valvidares, L. M. Álvarez-Prado, J. I. Martín, and J. M. Alameda. Inverted hysteresis loops in magnetically coupled bilayers with uniaxial competing anisotropies: Theory and experiments. *Physical Review B*, 64:134423, Sep 2001.
- [134] Wei Zhang. *Competing anisotropies in epitaxial exchange biased thin films and patterned nanostructures*. PhD thesis, University of Washington, 2013.
- [135] Wajdi Chérif, Mohamed Ellouze, Abdel-Fatah Lehlooh, Sami H. Mahmood, and Foued Elhalouani. Structure, magnetic properties and mössbauer spectra of  $\text{La}_{0.67}\text{Sr}_{0.33}\text{Fe}_x\text{Mn}_{1-x}\text{O}_3$  manganites oxide prepared by mechanical ball milling method. *Hyperfine Interactions*, 211(1):153–164, 2012.
- [136] Darrell G. Schlom, Long-Qing Chen, Xiaoqing Pan, Andreas Schmehl, and Mark A. Zurbuchen. A Thin Film Approach to Engineering Functionality into Oxides. *Journal of the American Ceramic Society*, 91(8):2429–2454, 2008.
- [137] Edmund C. Stoner. Collective Electron Ferromagnetism. *Proceedings of the Royal Society of London A: Mathematical, Physical and Engineering Sciences*, 165(922):372–414, 1938.
- [138] D. I. Khomskii. Multiferroics: Different ways to combine magnetism and ferroelectricity. *Journal of Magnetism and Magnetic Materials*, 306(1):1 – 8, 2006.
- [139] R. E. Cohen. Origin of ferroelectricity in perovskite oxides. *Nature*, 358(6382):136–138, July 1992.
- [140] C. Gruber, P. O. Bedolla, and P. Mohn. Covalent magnetism and magnetic impurities. *Journal of Physics: Condensed Matter*, 25(18):186002, 2013.
- [141] G. Kresse and J. Furthmüller. Efficient iterative schemes for *ab initio* total-energy calculations using a plane-wave basis set. *Physical Review B*, 54:11169–11186, Oct 1996.

- [142] O. Volnianska and P. Boguslawski. Magnetism of solids resulting from spin polarization of p orbitals. *Journal of Physics: Condensed Matter*, 22(7):073202, 2010.
- [143] Guntram Fischer, Nadiezhda Sanchez, Waheed Adeagbo, Martin Lüders, Zdzisława Szotek, Walter M. Temmerman, Arthur Ernst, Wolfram Hergert, and M. Carmen Muñoz. Room-temperature  $p$ -induced surface ferromagnetism: First-principles study. *Physical Review B*, 84:205306, Nov 2011.
- [144] T. Wolfram and S. Ellialtıođlu. *Electronic and optical properties of d-band perovskites*. Cambridge University Press, 2006.
- [145] N. C. Bristowe, P. B. Littlewood, and Emilio Artacho. The net charge at interfaces between insulators. *Journal of Physics: Condensed Matter*, 23(8):081001, 2011.
- [146] H. F. Kay and P. Vousden. XCV. Symmetry changes in barium titanate at low temperatures and their relation to its ferroelectric properties. *The London, Edinburgh, and Dublin Philosophical Magazine and Journal of Science*, 40(309):1019–1040, 1949.
- [147] *Oxygen contamination*. Quantum Design, April 1997. MPMS Application Note 1014-210.
- [148] Elizabeth A. Zhurova, Yury Ivanov, Valery Zavodnik, and Vladimir Tsirelson. Electron density and atomic displacements in  $\text{KTaO}_3$ . *Acta Crystallographica Section B*, 56(4):594–600, Aug 2000.
- [149] W. Edmondson and A. Egerton. The Vapour Pressures and Melting Points of Sodium and Potassium. *Proceedings of the Royal Society of London A: Mathematical, Physical and Engineering Sciences*, 113(765):520–533, 1927.
- [150] David Nečas and Petr Klapetek. Gwyddion: an open-source software for SPM data analysis. *Central European Journal of Physics*, 10:181–188, 2012.

## A Acronyms

**AES** Auger Electron Spectroscopy.

**AFM** Atomic Force Microscopy.

**APS** Advanced Photon Source of the Argonne National Laboratory.

**BTO** BaTiO<sub>3</sub>.

**CTO** CaTiO<sub>3</sub>.

**DNS** Diffuse Neutron Scattering Spectrometer.

**DOS** Density of States.

**EDX** Energy Dispersive X-ray Spectroscopy.

**HAADF** High-Angle Annular Dark-Field.

**HOPSA** High Oxygen Pressure Sputtering Automat.

**HV** High Vacuum.

**HZDR** Helmholtz Zentrum Dresden-Rossendorf.

**KTO** KTaO<sub>3</sub>.

**LEED** Low Energy Electron Diffraction.

**LSFO** La<sub>1/3</sub>Sr<sub>2/3</sub>FeO<sub>3</sub>.

**LSMO** La<sub>2/3</sub>Sr<sub>1/3</sub>MnO<sub>3</sub>.

**MLZ** Heinz Maier-Leibnitz Zentrum.

**MO** Molecular Orbital theory.

**MPMS** Magnetic Property Measurement System.

**NCNR** NIST Centre for Neutron Research.

**OMBE** Oxide Molecular Beam Epitaxy.

**PBR** Polarized Beam Reflectometer.

**PID** Proportional-Integral-Derivative.

**PLD** Pulsed Laser Deposition.

**PNR** Polarized Neutron Reflectometry.

**PPMS** Physical Property Measurement System.

**QMB** Quartz Microbalance.

**RBS** Rutherford Backscattering Spectrometry.

**RHEED** Reflection High Energy Electron Diffraction.

**SLD** Scattering Length Density.

**SQUID** Superconducting Quantum Interference Device.

**STEM** Scanning Transmission Electron Microscopy.

**STO** SrTiO<sub>3</sub>.

**UHV** Ultra High Vacuum.

**XRD** X-Ray Diffraction.

**XRR** X-Ray Reflectometry.

## B Physical quantities

List of frequently used quantities:

$\tau$	Goldschmidt tolerance factor
$a, b, c$ also $a_i, b_i, c_i$	crystal lattice parameter
$J_H$	Hund's exchange energy
$\Delta$	crystal field splitting
$T$	temperature (subscripts: Verwey V, Curie C, Néel N, charge ordering CO)
$M_i$	molar mass for element $i$
$\vec{B}$	magnetic flux density
$\vec{H}$	magnetic field
$M =  \vec{M} $	magnetization (normalized to mass)
$K$	anisotropy constant
$\sigma_N$	uniaxial strain
$\mu$	mobility of a particle (i.e. electron, polaron)
$\sigma_s$	specific conductivity
$\rho_r$	specific resistivity
$\lambda$	wavelength
$\vec{k}', \vec{k}$	wavevector (incident, outgoing)
$k =  \vec{k} $	absolute value of wavevector
$\vec{Q} = \vec{k}' - \vec{k},  \vec{Q}  = Q$	scattering vector
$\sigma$	total cross section
$f(\vec{Q})$	scattering amplitude
$\vec{G}$ or $\vec{G}_{hkl}$	reciprocal lattice vector ( $hkl$ : Miller indices)
$d_{hkl}$	lattice plane distance for different $h, k, l$
$I$	Intensity
$R_p, R_{wp}$	(weighted) reliability factor
$n_i$	refractive index of material $i$
$b_j$	scattering length
$\hat{\sigma}$	spin operator
$V$	volume
$p, p_i$	pressure (for gas species $i$ )
$C_p, C_V$	specific heat for $p = \text{const}$ or $V = \text{const}$
$R_i$	Reflectivity with neutron channel $i$

## Physical quantities

---

- $d_{\langle \text{name} \rangle}$  thickness of layer  $\langle \text{name} \rangle$
- $\sigma_{\langle \text{name} \rangle}$  roughness parameter of layer  $\langle \text{name} \rangle$  (Reflectivity simulations)
- $\rho_{\langle \text{name} \rangle}$  density of layer  $\langle \text{name} \rangle$

## C Physical constants

$c = 299792458 \text{ m} \cdot \text{s}^{-1}$	speed of light in vacuum
$N_A = 6.022140857(74) \cdot 10^{23} \text{ mol}^{-1}$	Avogadro constant
$k_B = 1.38064852(79) \cdot 10^{-23} \text{ J} \cdot \text{K}^{-1}$	Boltzmann constant
$R = N_A \cdot k_B = 8.3144598(48) \text{ J} \cdot \text{mol}^{-1} \cdot \text{K}^{-1}$	gas constant
$h = 6.626070040(81) \cdot 10^{-34} \text{ J} \cdot \text{s}$	Planck constant ( $\hbar = h/2\pi$ )
$m_n = m_p = 1.672621898(21) \cdot 10^{-27} \text{ kg}$	proton and neutron mass
$m_e = 9.10938356(11) \cdot 10^{-31} \text{ kg}$	electron mass
$e = 1.6021766208(98) \cdot 10^{-19} \text{ C}$	elementary charge
$\mu_0 = 4\pi \cdot 10^{-7} \text{ N} \cdot \text{A}^{-2}$	magnetic constant
$\epsilon_0 = \frac{1}{\mu_0 c^2}$	electric constant
$r_0 = \frac{e^2}{4\pi\epsilon_0 m_e c^2}$	classical electron radius
$\mu_B = \frac{e\hbar}{2m_e}$	Bohr magneton
$\mu_N = \frac{e\hbar}{2m_n}$	nuclear magneton
$\phi_0 = \frac{h}{2e}$	magnetic flux quantum





## D Supplementary information

Parameters are shown which were used for powder and both bilayer samples. Additional measurements are also shown.

### D.1 Definition of fitting parameters

#### D.1.1 Jana2006

Profile parameters are defined in D.2,  $R$  values are defined in Sec. 3.4.

---

$a, b, c$	lattice parameter in $\text{\AA}$
$M_1$	magnetic moment of $\text{Fe}^{5+}$ in $\mu_B$
$M_2$	magnetic moment of $\text{Fe}^{3+}$ in $\mu_B$
shift	parameter for $\theta_0$ correction
scale	profile scale factor
GOF	Goodness of fit: $R_{w,profile}/R_w$

---

#### D.1.2 GenX

---

$d_{(\text{layer})}$	thickness of corresponding layer in $\text{\AA}$
$\sigma_{(\text{layer})}$	roughness parameter in $\text{\AA}$
$c_{\text{oxygen,top}}$	oxygen content top layer
$\rho_{(\text{layer})}$	density in $\text{\AA}^{-3}$
$m_{\text{MLx}}$	magnetization for magnetic layer x in $\mu_B$ per formula unit (Fig. 8.14)
$c_{\text{Mn,inter}}$	Mn content in interlayer
$c_{\text{Fe,inter}}$	Fe content in interlayer
FOM	figure of merit as defined in Sec. 3.6

---

## D.2 LSFO powder sample

Normalized Gaussians and Lorentzians exhibit angle (or  $Q$ ) dependent parameters as follows:

**normalized Gaussian:**

$$G(\Delta T, \Gamma_G) = \sqrt{\frac{4 \ln 2}{\pi \Gamma_G^2}} \exp\left(-\frac{4 \ln 2 (\Delta T)^2}{\Gamma_G^2}\right),$$

where  $\Gamma_G$  is defined as

$$\Gamma_G = GU \tan^2 \theta + GV \tan \theta + GW + \frac{GP}{\cos^2 \theta}.$$

**normalized Lorentzian:**

$$L(\Delta T, \gamma_L) = \frac{2}{\pi \gamma_L} \frac{1}{1 + \left(\frac{2\Delta T}{\gamma_L}\right)^2}$$

with

$$\gamma_L = \frac{LX}{\cos \theta} + LY \tan \theta.$$

### D.2.1 BT-1 refinement parameters

300 K			
GU	76.33	$a, b$ [Å]	5.4846(4)
GV	-137.01	$c$ [Å]	13.4032(13)
GW	157.41	$M_1$ [ $\mu_B$ /f.u.]	N/A
LX	0	$M_2$ [ $\mu_B$ /f.u.]	N/A
LY	16.23725	shift (1/1000)	2.33
$R_{w, \text{profile}}$ [%]	6.28	scale	0.73
$R_w$ [%]	3.83		
GOF	2.50		

<b>5K</b>			
GU	231.81	$a, b$ [Å]	5.4762(7)
GV	-173.81	$c$ [Å]	13.3598(26)
GW	158.98	$M_1$ [ $\mu_B$ /f.u.]	3.53(23)
LX	6.03	$M_2$ [ $\mu_B$ /f.u.]	2.51(36)
LY	2.89	shift (1/1000)	5.50
$R_{w,profile}$ [%]	7.92	scale	0.75
$R_w$ [%]	6.22		
GOF	2.65		

### D.2.2 11-BM refinement parameters

<b>100 K</b>			
GU	15.32	$a, b$ [Å]	5.4797(2)
GV	-21.64	$c$ [Å]	13.3727(6)
GW	1.37	shift (1/1000)	0.06
LX	0.33	scale	0.16
LY	13.72		
$R_{w,profile}$ [%]	13.40		
$R_w$ [%]	5.32		
GOF	2.48		

### D.2.3 DNS refinement additional data and parameters

**Measurement at 4.5 Å** The top of Fig. D.1 shows a DNS measurement performed at 5K with a wavelength of 4.5 Å. Due to problems occurred during the beamtime only the 5K measurement is available. The following measurement (see next paragraph) was then performed at 3.3 Å. The bottom of this figure depicts the simulation and data of the magnetic signal. As low angles are influenced by the beam stop of the unscattered neutron beam, the lowest reflection was ignored. The table contains the parameters from the Rietveld refinement. The listed scale factor was not refined. It was taken from the refinement of the nuclear signal and kept constant during the refinement of the magnetic contribution (indicated by \*).

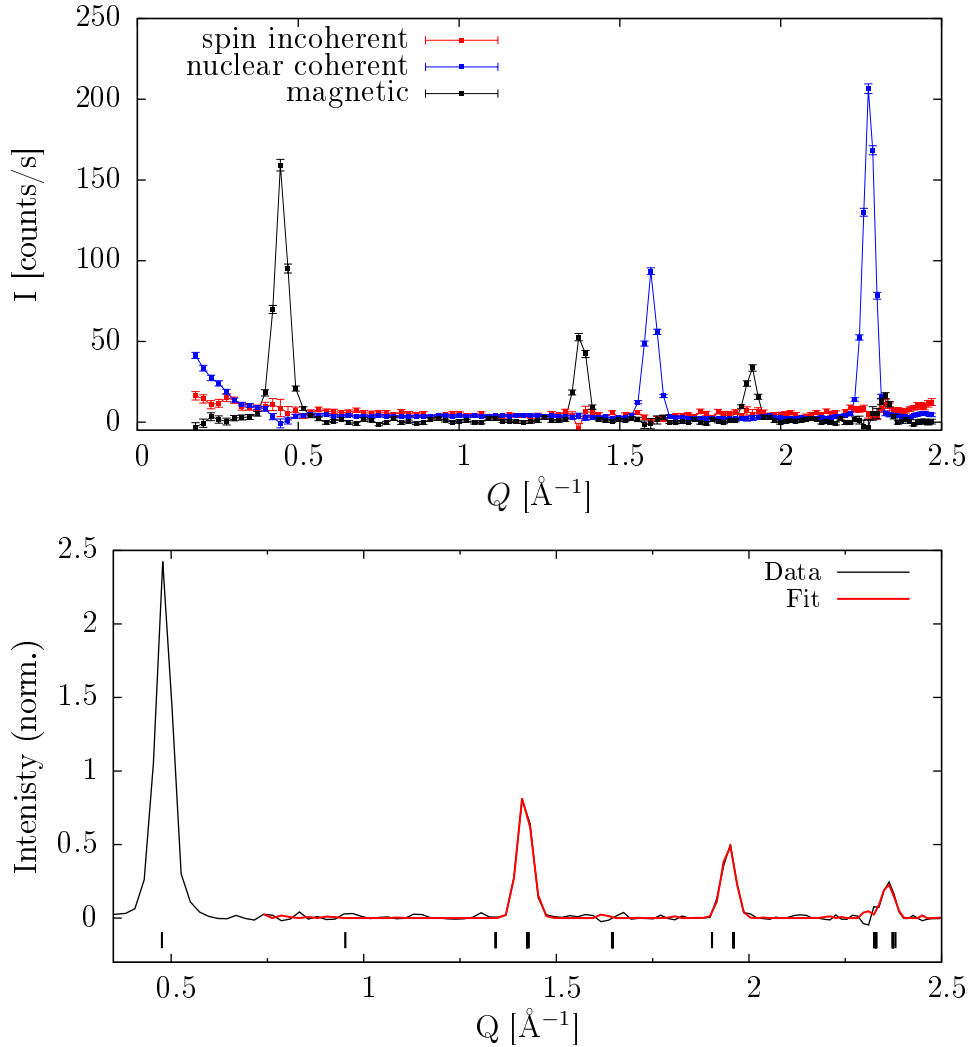


**Figure D.1:** Top figure shows 5K powder measurement performed at the DNS instrument with a wavelength of  $4.5 \text{ \AA}$ . Bottom figure shows refinement of the magnetic signal. The lowest reflections was omitted due to a shadowing effect of the beamstop at low angles.

GU	2346.58	$a, b \text{ [}\text{\AA}\text{]}$	5.402(29)
GV	-13372.58	$c \text{ [}\text{\AA}\text{]}$	13.194(102)
GW	892.6253	$M_1 \text{ [}\mu_{\text{B}}/\text{f.u.}\text{]}$	3.12(43)
LX	1.353764	$M_2 \text{ [}\mu_{\text{B}}/\text{f.u.}\text{]}$	4.26(22)
LY	0	shift (1/1000)	192.24
$R_w \text{ [%]}$	2.99	scale*	0.87

### Measurement at $3.3 \text{ \AA}$

The \* indicates that the parameter is used from the refinement of the nuclear contribution and kept fixed during the magnetic signal refinement.

GU	43871.35	$a, b$ [Å]	5.491(9)
GV	-65328.29	$c$ [Å]	13.5068(15)
GW	12992.81	$M_1$ [ $\mu_B$ /f.u.]	1.73(34)
LX	3.14	$M_2$ [ $\mu_B$ /f.u.]	1.34(23)
LY	0	shift (1/1000)	40.8249
$R_{w,profile}$ [%]	7.92	scale*	1.9429
$R_w$ [%]	0.08	1	1

## D.3 LSMOfinal

### D.3.1 Substrate

SrTiO<sub>3</sub> substrate from CrysTec GmbH [112].

Cleaning 3 min with acetone and 3 min with ethanol in an ultrasonic bath before using

### D.3.2 LSFO growth with OMBE

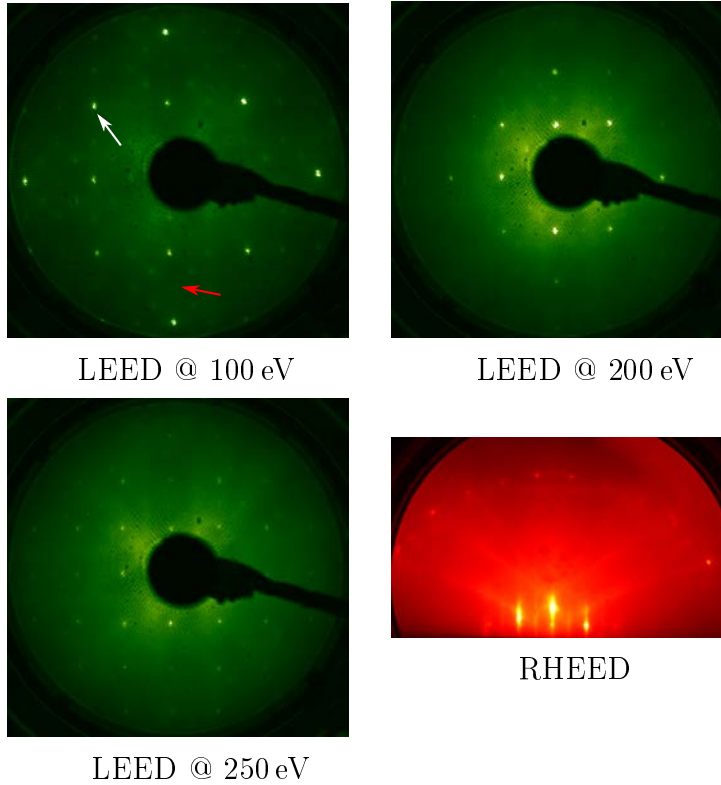
#### Frequency changes of quartz microbalance

	before growth	after 14 h	difference / 1 h [%]
$-\Delta f_{Sr}$ [ $\frac{Hz}{s}$ ]	0.076	0.079	0.3
$-\Delta f_{La}$ [ $\frac{Hz}{s}$ ]	0.056	0.050	0.8
$-\Delta f_{Fe}$ [ $\frac{Hz}{s}$ ]	0.091	0.091	0.0

#### Growth procedure

Plasma	300 W / 0.15 sccm
O <sub>2</sub> partial pressure $p_{O_2}$	1.3E-7 mbar
Growth duration	4500 s
Substrate annealing	1320 K (1h)
Growth temperature $T_{growth}$	1240 K
Post-annealing	5400 s at $T_{growth}$
Cooling procedure	to 470 K with 3K/min
Second annealing	470 K (0.5 h)

### LEED and RHEED after LSFO growth



### D.3.3 LSMO growth with HOPSA

#### Growth procedure

Note: The growth rates of HOPSA and OMBE are comparable. Thus, the same growth time has been used for both.

Plasma	120 W
O <sub>2</sub> partial pressure $p_{O_2}$	2.05 mbar
Growth duration	4500 s
Pre-annealing	1250 K (0.25 h)
Growth temperature $T_{\text{growth}}$	1250 K
Cooling procedure	to 870 K with 5K/min
Annealing	870 K (0.5 h)

### D.3.4 Parameters from PNR simulations

110K		FOM: 1.23	
Parameter	Value	asymmetric errors	
$d_{\text{LSFO}}$ [Å]	215.4014	-2.114e+00, 9.784e-01	
$d_{\text{LSMO}}$ [Å]	153.9441	-6.642e-01, 2.475e+00	
$\sigma_{\text{LSMO}}$ [Å]	29.9971	-8.560e+00, 2.893e-03	
$\sigma_{\text{LSFO}}$ [Å]	20.5946	-5.425e+00, 6.709e-01	
$\sigma_{\text{Sub}}$ [Å]	8.3648	-1.618e+00, 1.555e+00	
$d_{\text{TOP}}$ [Å]	22.1035	-2.416e+00, 7.510e-02	
$\sigma_{\text{TOP}}$ [Å]	2.0252	-2.510e-02, 3.377e+00	
$d_{\text{Inter}}$ [Å]	30.5713	-4.189e-01, 2.618e+00	
$\sigma_{\text{Inter}}$ [Å]	4.1034	-1.034e+00, 2.643e-01	
$c_{\text{oxygen,top}}$	2.6298	-8.667e-02, 2.913e-01	
$\rho_{\text{Top}}$ [Å <sup>-3</sup> ]	0.01399	-1.055e-03, 2.575e-04	
$\rho_{\text{LSMO}}$ [Å <sup>-3</sup> ]	0.01682	-3.923e-05, 2.641e-04	
$\rho_{\text{LSFO}}$ [Å <sup>-3</sup> ]	0.01690	-3.255e-05, 1.000e-05	
$\rho_{\text{Inter}}$ [Å <sup>-3</sup> ]	0.01649	-1.718e-04, 5.396e-04	
$m_{\text{ML1}}$ [ $\mu\text{B}/\text{uc}$ ]	0.0000	-	
$m_{\text{ML2}}$ [ $\mu\text{B}/\text{uc}$ ]	0.0000	-	
$m_{\text{ML3}}$ [ $\mu\text{B}/\text{uc}$ ]	1.7462	-6.925e-02, 7.850e-02	
$m_{\text{ML4}}$ [ $\mu\text{B}/\text{uc}$ ]	3.3136	-5.451e-02, 3.818e-02	
$m_{\text{ML5}}$ [ $\mu\text{B}/\text{uc}$ ]	1.0344	-3.430e-02, 5.086e-01	
$c_{\text{Mn,inter}}$	0.9565	-2.563e-02, 3.275e-02	

200K		FOM: 1.32	
Parameter	Value	asymmetric errors	
$d_{\text{LSFO}}$ [Å]	220.3728	-1.321e+00, 7.411e-01	
$d_{\text{LSMO}}$ [Å]	141.5174	-1.601e+00, 4.062e+00	
$\sigma_{\text{LSMO}}$ [Å]	29.9959	-5.055e+00, 4.118e-03	
$\sigma_{\text{LSFO}}$ [Å]	20.4938	-2.242e+00, 8.842e-01	
$\sigma_{\text{Sub}}$ [Å]	9.2691	-7.456e-01, 5.638e-01	
$d_{\text{TOP}}$ [Å]	26.3155	-2.621e+00, 1.360e+00	
$\sigma_{\text{TOP}}$ [Å]	2.1508	-1.473e-01, 1.460e+00	
$d_{\text{Inter}}$ [Å]	34.2162	-1.305e+00, 1.061e+00	
$\sigma_{\text{Inter}}$ [Å]	4.0777	-5.755e-01, 1.731e-01	
$c_{\text{oxygen,top}}$	2.4717	-7.596e-02, 9.466e-02	
$\rho_{\text{Top}}$ [Å <sup>-3</sup> ]	0.01485	-5.991e-04, 6.439e-04	
$\rho_{\text{LSMO}}$ [Å <sup>-3</sup> ]	0.01705	-2.059e-04, 9.195e-05	
$\rho_{\text{LSFO}}$ [Å <sup>-3</sup> ]	0.01687	-4.385e-05, 1.487e-05	
$\rho_{\text{Inter}}$ [Å <sup>-3</sup> ]	0.01511	-3.668e-04, 9.365e-04	
$m_{\text{ML1}}$ [ $\mu\text{B}/\text{uc}$ ]	0.0000	-	
$m_{\text{ML2}}$ [ $\mu\text{B}/\text{uc}$ ]	0.0000	-	
$m_{\text{ML3}}$ [ $\mu\text{B}/\text{uc}$ ]	1.6693	-1.239e-01, 8.865e-02	
$m_{\text{ML4}}$ [ $\mu\text{B}/\text{uc}$ ]	3.0011	-1.074e-03, 9.991e-02	
$m_{\text{ML5}}$ [ $\mu\text{B}/\text{uc}$ ]	1.2251	-2.212e-01, 2.037e-01	
$c_{\text{Mn,inter}}$	0.9067	-6.697e-02, 4.528e-02	

250K	FOM: 1.23	
Parameter	Value	asymmetric errors
$d_{\text{LSFO}} [\text{Å}]$	220.6374	-1.944e+00, 9.346e-01
$d_{\text{LSMO}} [\text{Å}]$	127.2262	-2.761e+00, 4.838e+00
$\sigma_{\text{LSMO}} [\text{Å}]$	34.9428	-1.085e+01, 5.712e-02
$\sigma_{\text{LSFO}} [\text{Å}]$	23.9258	-2.800e+00, 2.963e-01
$\sigma_{\text{Sub}} [\text{Å}]$	11.7558	-1.027e+00, 1.962e+00
$d_{\text{TOP}} [\text{Å}]$	33.1244	-3.097e+00, 3.477e+00
$\sigma_{\text{TOP}} [\text{Å}]$	2.0282	-2.816e-02, 4.175e+00
$d_{\text{Inter}} [\text{Å}]$	41.0035	-4.029e+00, 1.585e+00
$\sigma_{\text{Inter}} [\text{Å}]$	2.5867	-3.028e-01, 2.713e-01
$c_{\text{oxygen,top}}$	2.4803	-9.740e-02, 3.614e-02
$\rho_{\text{Top}} [\text{Å}^{-3}]$	0.01624	-1.960e-04, 6.205e-04
$\rho_{\text{LSMO}} [\text{Å}^{-3}]$	0.01724	-2.462e-04, 2.348e-04
$\rho_{\text{LSFO}} [\text{Å}^{-3}]$	0.01709	-4.807e-05, 5.622e-05
$\rho_{\text{Inter}} [\text{Å}^{-3}]$	0.01587	-4.326e-04, 2.917e-04
$m_{\text{ML1}} [\mu_{\text{B}}/\text{uc}]$	0.0000	-
$m_{\text{ML2}} [\mu_{\text{B}}/\text{uc}]$	0.0000	-
$m_{\text{ML3}} [\mu_{\text{B}}/\text{uc}]$	1.5282	-1.176e-01, 4.622e-02
$m_{\text{ML4}} [\mu_{\text{B}}/\text{uc}]$	2.6073	-9.029e-02, 4.262e-02
$m_{\text{ML5}} [\mu_{\text{B}}/\text{uc}]$	1.5246	-5.978e-02, 3.493e-01
$c_{\text{Mn,inter}}$	0.9977	-6.305e-02, 2.283e-03



## D.4 LSFOfinal

### D.4.1 Substrate

SrTiO<sub>3</sub> substrate from Crystec GmbH [112].

Cleaning 3 min with acetone and 3 min with ethanol in an ultrasonic bath before using.

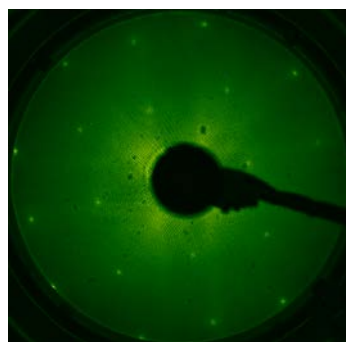
### D.4.2 LSMO growth

#### Growth procedure

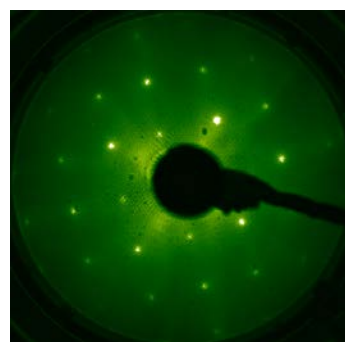
Plasma	120 W
O <sub>2</sub> partial pressure $p_{\text{O}_2}$	2.05 mbar
Growth duration	4500 s
Pre-annealing	1320 K (1.4 h)
Growth temperature $T_{\text{growth}}$	1250 K
Post-annealing	1120 K (0.5 h)
Cooling procedure	to 270 K with 5K/min

#### LEED and RHEED after LSMO growth

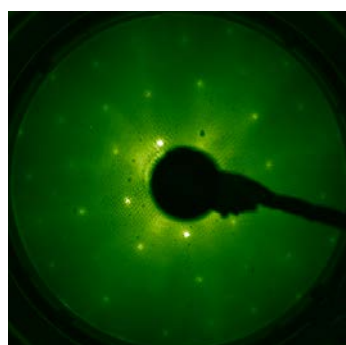
LEED and RHEED measurement after transfer from HOPSA to OMBE.



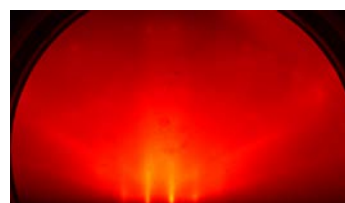
LEED @ 100 eV



LEED @ 200 eV



LEED @ 250 eV



RHEED

### D.4.3 LSFO growth

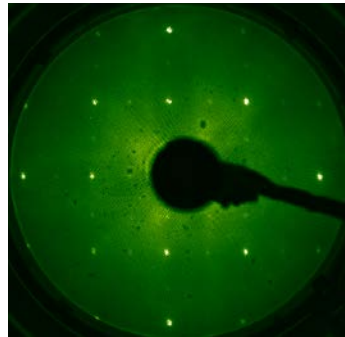
#### Frequency changes of quartz microbalance

	before growth	after 14 h	difference / 1 h [%]
$-\Delta f_{\text{Sr}} \left[ \frac{\text{Hz}}{\text{s}} \right]$	0.076	0.072	0.4
$-\Delta f_{\text{La}} \left[ \frac{\text{Hz}}{\text{s}} \right]$	0.056	0.050	0.8
$-\Delta f_{\text{Fe}} \left[ \frac{\text{Hz}}{\text{s}} \right]$	0.091	0.091	0.0

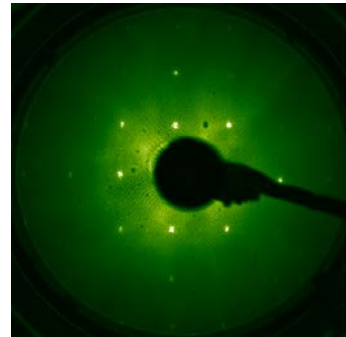
#### Growth procedure

Plasma	300 W / 0.15 sccm
O <sub>2</sub> partial pressure $p_{\text{O}_2}$	1.3E-7 mbar
Growth duration	4500 s
Pre-annealing	1240 K (0.25 h)
Growth temperature $T_{\text{growth}}$	1240 K
Post-annealing	900 s at $T_{\text{growth}}$
Cooling procedure	3K/min
Second annealing	770 K (0.5 h)
Third annealing	470 K (0.5 h)

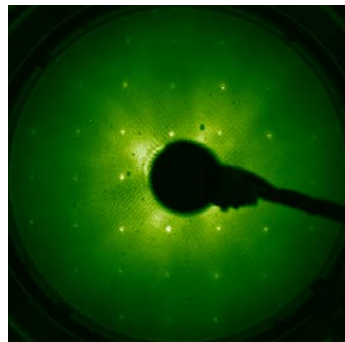
LEED and RHEED after LSFO/LSMO growth



LEED @ 100 eV



LEED @ 200 eV



LEED @ 250 eV



RHEED

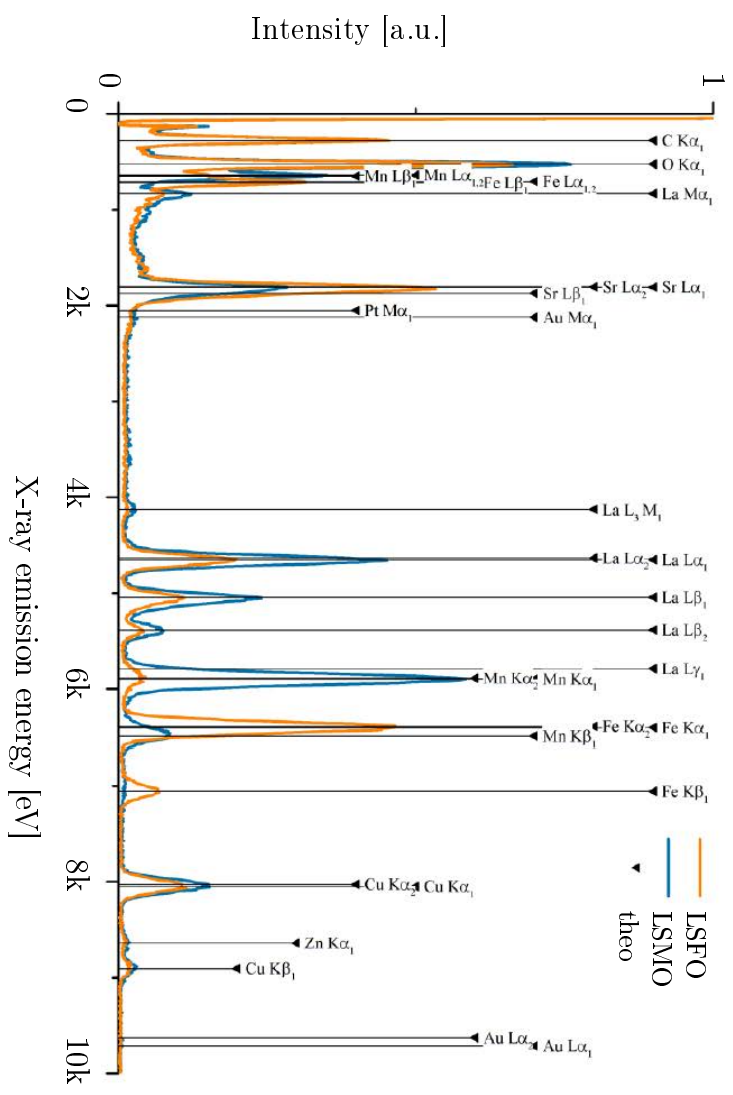
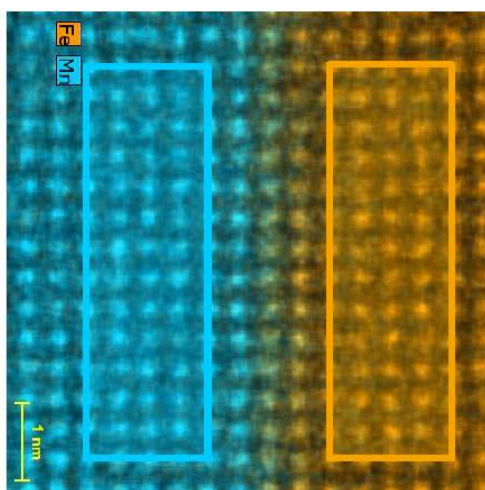


**Figure D.2:** EDX spectra taken at the marked areas in the left-hand figure. The reversal of the approximate 2:1 ration of Sr and La can be found from the respective intensities. The theoretical position are taken from Deslattes et al. [127]. Plot and analysis done by Juri Barthel, ER-C.



#### D.4.4 PNR measurements: additional temperatures

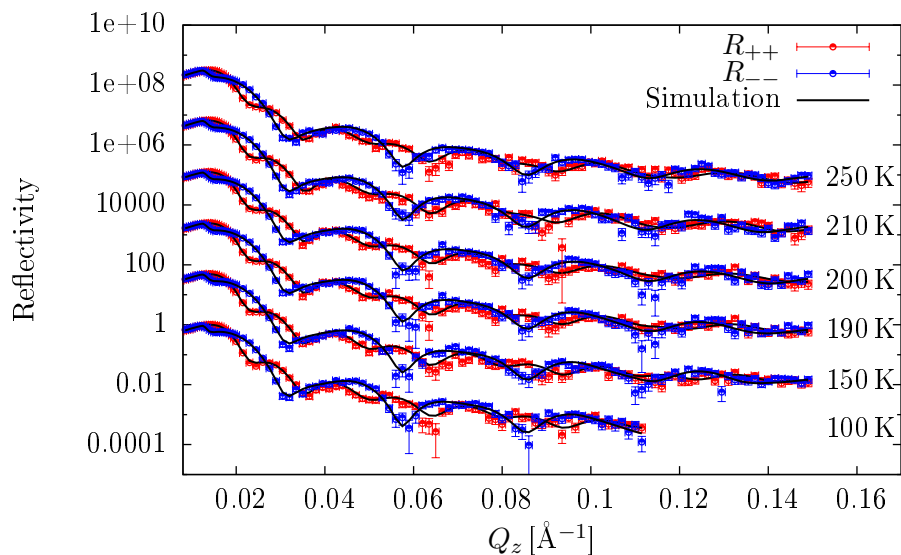


**Figure D.3:** Additional PNR measurements and simulations of sample LSFOfinal for both non-spin-flip channels.

#### D.4.5 Parameters from PNR simulations

The following tables contain all parameters gained from the simulation done in this thesis.

100K	FOM: 1.00	
Parameter	Value	asymmetric errors
$d_{\text{LSFO}} [\text{\AA}]$	215.0968	-4.561e+00, 3.355e+00
$d_{\text{LSMO}} [\text{\AA}]$	173.8870	-1.587e+00, 5.618e+00
$\sigma_{\text{LSMO}} [\text{\AA}]$	16.9650	-6.956e+00, 3.495e-02
$\sigma_{\text{LSFO}} [\text{\AA}]$	4.1839	-1.182e+00, 1.078e+01
$\sigma_{\text{Sub}} [\text{\AA}]$	14.3727	-3.628e+00, 2.187e+00
$d_{\text{TOP}} [\text{\AA}]$	6.7699	-1.664e+00, 2.594e+00
$\sigma_{\text{TOP}} [\text{\AA}]$	4.8339	-1.061e+00, 9.895e-01
$d_{\text{Inter}} [\text{\AA}]$	8.4516	-1.834e+00, 3.109e+00
$\sigma_{\text{Inter}} [\text{\AA}]$	9.0716	-4.387e+00, 9.150e-01
$c_{\text{oxygen,top}}$	3.0000	-
$\rho_{\text{Top}} [\text{\AA}^{-3}]$	0.01859	-3.452e-03, 4.068e-04
$\rho_{\text{LSMO}} [\text{\AA}^{-3}]$	0.01734	-2.533e-04, 2.544e-04
$\rho_{\text{LSFO}} [\text{\AA}^{-3}]$	0.01736	-7.456e-05, 7.791e-05
$\rho_{\text{Inter}} [\text{\AA}^{-3}]$	0.01594	-1.811e-03, 1.685e-03
$m_{\text{ML1}} [\mu_{\text{B}}/\text{uc}]$	3.1076	-1.816e-01, 7.563e-02
$m_{\text{ML2}} [\mu_{\text{B}}/\text{uc}]$	0.0000	-
$m_{\text{ML3}} [\mu_{\text{B}}/\text{uc}]$	0.0000	-
$m_{\text{ML4}} [\mu_{\text{B}}/\text{uc}]$	0.0000	-
$c_{\text{Fe,inter}}$	0.5298	-1.481e-01, 6.129e-02

150K		FOM: 0.95		190K		FOM: 0.85		
Parameter	Value	asymmetric errors	Parameter	Value	asymmetric errors	Parameter	Value	asymmetric errors
$d_{\text{LSFO}}$ [Å]	199.5102	-4.534e+00, 5.078e+00	$d_{\text{LSFO}}$ [Å]	209.5130	-4.095e+00, 4.497e+00	$d_{\text{LSFO}}$ [Å]	209.5130	-4.095e+00, 4.497e+00
$d_{\text{LSMO}}$ [Å]	174.6823	-4.744e+00, 4.770e+00	$d_{\text{LSMO}}$ [Å]	171.5622	-2.621e+00, 4.745e+00	$d_{\text{LSMO}}$ [Å]	171.5622	-2.621e+00, 4.745e+00
$\sigma_{\text{LSMO}}$ [Å]	4.3759	-1.149e+00, 1.671e+00	$\sigma_{\text{LSMO}}$ [Å]	8.8426	-1.915e+00, 1.145e+00	$\sigma_{\text{LSMO}}$ [Å]	8.8426	-1.915e+00, 1.145e+00
$\sigma_{\text{LSFO}}$ [Å]	5.4366	-1.133e+00, 6.937e-01	$\sigma_{\text{LSFO}}$ [Å]	7.5011	-6.782e-01, 8.515e-01	$\sigma_{\text{LSFO}}$ [Å]	7.5011	-6.782e-01, 8.515e-01
$\sigma_{\text{Sub}}$ [Å]	9.8945	-7.260e-01, 9.894e-01	$\sigma_{\text{Sub}}$ [Å]	14.0246	-6.040e+00, 9.682e-01	$\sigma_{\text{Sub}}$ [Å]	14.0246	-6.040e+00, 9.682e-01
$d_{\text{TOP}}$ [Å]	15.3279	-2.033e+00, 3.199e+00	$d_{\text{TOP}}$ [Å]	10.5780	-4.230e+00, 3.829e+00	$d_{\text{TOP}}$ [Å]	10.5780	-4.230e+00, 3.829e+00
$\sigma_{\text{TOP}}$ [Å]	2.0000	-3.455e+00, 1.755e+00	$\sigma_{\text{TOP}}$ [Å]	2.0007	-6.810e-04, 2.446e+00	$\sigma_{\text{TOP}}$ [Å]	2.0007	-6.810e-04, 2.446e+00
$d_{\text{Inter}}$ [Å]	15.8474	-3.455e+00, 1.755e+00	$d_{\text{Inter}}$ [Å]	12.5460	-2.018e+00, 1.427e+00	$d_{\text{Inter}}$ [Å]	12.5460	-2.018e+00, 1.427e+00
$\sigma_{\text{Inter}}$ [Å]	5.0196	-6.758e-01, 6.222e-01	$\sigma_{\text{Inter}}$ [Å]	5.1692	-9.950e-01, 1.246e+00	$\sigma_{\text{Inter}}$ [Å]	5.1692	-9.950e-01, 1.246e+00
$c_{\text{oxygen,top}}$	3.0000	-	$c_{\text{oxygen,top}}$	3.0000	-	$c_{\text{oxygen,top}}$	3.0000	-
$\rho_{\text{Top}}$ [Å <sup>-3</sup> ]	0.01702	-3.615e-04, 6.703e-04	$\rho_{\text{Top}}$ [Å <sup>-3</sup> ]	0.01596	-7.710e-04, 4.430e-04	$\rho_{\text{Top}}$ [Å <sup>-3</sup> ]	0.01596	-7.710e-04, 4.430e-04
$\rho_{\text{LSMO}}$ [Å <sup>-3</sup> ]	0.01764	-2.962e-04, 2.628e-04	$\rho_{\text{LSMO}}$ [Å <sup>-3</sup> ]	0.01756	-2.348e-04, 1.981e-04	$\rho_{\text{LSMO}}$ [Å <sup>-3</sup> ]	0.01756	-2.348e-04, 1.981e-04
$\rho_{\text{LSFO}}$ [Å <sup>-3</sup> ]	0.01703	-1.036e-04, 1.084e-04	$\rho_{\text{LSFO}}$ [Å <sup>-3</sup> ]	0.01723	-6.821e-05, 8.562e-05	$\rho_{\text{LSFO}}$ [Å <sup>-3</sup> ]	0.01723	-6.821e-05, 8.562e-05
$\rho_{\text{Inter}}$ [Å <sup>-3</sup> ]	0.01537	-8.083e-04, 1.695e-03	$\rho_{\text{Inter}}$ [Å <sup>-3</sup> ]	0.01547	-9.766e-04, 5.030e-04	$\rho_{\text{Inter}}$ [Å <sup>-3</sup> ]	0.01547	-9.766e-04, 5.030e-04
$m_{\text{ML1}}$ [ $\mu_{\text{B}}$ /uc]	2.75087	-1.202e-01, 9.134e-02	$m_{\text{ML1}}$ [ $\mu_{\text{B}}$ /uc]	2.7519	-1.324e-01, 1.672e-01	$m_{\text{ML1}}$ [ $\mu_{\text{B}}$ /uc]	2.7519	-1.324e-01, 1.672e-01
$m_{\text{ML2}}$ [ $\mu_{\text{B}}$ /uc]	0.0000	-	$m_{\text{ML2}}$ [ $\mu_{\text{B}}$ /uc]	0.0000	-	$m_{\text{ML2}}$ [ $\mu_{\text{B}}$ /uc]	0.0000	-
$m_{\text{ML3}}$ [ $\mu_{\text{B}}$ /uc]	0.0000	-	$m_{\text{ML3}}$ [ $\mu_{\text{B}}$ /uc]	0.0000	-	$m_{\text{ML3}}$ [ $\mu_{\text{B}}$ /uc]	0.0000	-
$m_{\text{ML4}}$ [ $\mu_{\text{B}}$ /uc]	0.0000	-	$m_{\text{ML4}}$ [ $\mu_{\text{B}}$ /uc]	0.0000	-	$m_{\text{ML4}}$ [ $\mu_{\text{B}}$ /uc]	0.0000	-
$c_{\text{Fe,inter}}$	0.17444	-2.442e-02, 2.297e-01	$c_{\text{Fe,inter}}$	0.3924	-4.977e-02, 2.747e-02	$c_{\text{Fe,inter}}$	0.3924	-4.977e-02, 2.747e-02

200K			210K		
Parameter	Value	asymmetric errors	Parameter	Value	asymmetric errors
FOM: 0.88					
$d_{\text{LSFO}}$ [Å]	208.9935	-8.543e-01, 3.271e+00	$d_{\text{LSFO}}$ [Å]	212.3297	-1.247e+00, 3.662e+00
$d_{\text{LSMO}}$ [Å]	172.1845	-4.844e+00, 3.045e+00	$d_{\text{LSMO}}$ [Å]	167.7343	-4.261e+00, 6.464e+00
$\sigma_{\text{LSMO}}$ [Å]	11.9999	-6.997e+00, 4.718e-05	$\sigma_{\text{LSMO}}$ [Å]	7.2568	-1.589e+00, 1.723e+00
$\sigma_{\text{LSFO}}$ [Å]	7.1279	-3.126e+00, 8.720e-01	$\sigma_{\text{LSFO}}$ [Å]	9.9797	-6.960e+00, 2.030e-02
$\sigma_{\text{Sub}}$ [Å]	16.6545	-7.965e+00, 3.419e-01	$\sigma_{\text{Sub}}$ [Å]	16.7042	-7.491e+00, 2.953e-01
$d_{\text{TOP}}$ [Å]	11.9877	-1.977e+00, 2.266e+00	$d_{\text{TOP}}$ [Å]	12.2881	-4.834e+00, 3.263e-01
$\sigma_{\text{TOP}}$ [Å]	2.0054	-5.363e-03, 2.906e+00	$\sigma_{\text{TOP}}$ [Å]	2.0083	-8.275e-03, 3.481e+00
$d_{\text{inter}}$ [Å]	11.2072	-3.357e+00, 8.386e-01	$d_{\text{inter}}$ [Å]	11.4650	-3.225e+00, 1.721e-01
$\sigma_{\text{inter}}$ [Å]	4.3281	-2.303e+00, 3.635e+00	$\sigma_{\text{inter}}$ [Å]	6.7007	-4.512e-01, 9.806e-01
Coxy <sub>gen,top</sub>					
$\rho_{\text{Top}}$ [Å <sup>-3</sup> ]	3.0000	-	$\rho_{\text{Top}}$ [Å <sup>-3</sup> ]	3.0000	-
$\rho_{\text{LSMO}}$ [Å <sup>-3</sup> ]	0.01573	-6.868e-04, 1.332e-03	$\rho_{\text{LSMO}}$ [Å <sup>-3</sup> ]	0.01519	-1.085e-03, 3.159e-03
$\rho_{\text{LSFO}}$ [Å <sup>-3</sup> ]	0.01765	-2.157e-04, 1.841e-04	$\rho_{\text{LSFO}}$ [Å <sup>-3</sup> ]	0.01770	-2.710e-04, 1.588e-04
$\rho_{\text{inter}}$ [Å <sup>-3</sup> ]	0.01724	-7.870e-05, 4.310e-05	$\rho_{\text{inter}}$ [Å <sup>-3</sup> ]	0.01728	-1.497e-04, 7.180e-05
$m_{\text{ML1}}$ [μB/uc]	0.01405	-7.373e-04, 1.280e-03	$m_{\text{ML1}}$ [μB/uc]	0.01441	-6.111e-04, 1.670e-03
$m_{\text{ML2}}$ [μB/uc]	2.7731	-9.874e-02, 1.275e-01	$m_{\text{ML2}}$ [μB/uc]	2.75036	-1.924e-01, 9.279e-02
$m_{\text{ML3}}$ [μB/uc]	0.0000	-	$m_{\text{ML3}}$ [μB/uc]	0.0000	-
$m_{\text{ML4}}$ [μB/uc]	0.0000	-	$m_{\text{ML4}}$ [μB/uc]	0.0000	-
$c_{\text{Fe,inter}}$	0.3509	-1.399e-01, 3.471e-01	$c_{\text{Fe,inter}}$	0.6679	-3.071e-01, 3.197e-02



250K		FOM: 0.93
Parameter	Value	asymmetric errors
$d_{\text{LSFO}}$ [Å]	209.3108	-4.164e+00, 3.227e+00
$d_{\text{LSMO}}$ [Å]	171.9685	-4.677e+00, 4.929e+00
$\sigma_{\text{LSMO}}$ [Å]	5.0000	-
$\sigma_{\text{LSFO}}$ [Å]	5.0000	-
$\sigma_{\text{Sub}}$ [Å]	15.8473	-5.175e+00, 1.138e+00
$d_{\text{TOP}}$ [Å]	10.4659	-1.628e+00, 3.623e+00
$\sigma_{\text{TOP}}$ [Å]	2.2782	-2.778e-01, 1.733e+00
$d_{\text{Inter}}$ [Å]	13.5230	-2.642e+00, 1.454e+00
$\sigma_{\text{Inter}}$ [Å]	2.9449	-6.404e-01, 5.376e-01
$c_{\text{oxygen,top}}$	3.0000	-
$\rho_{\text{Top}}$ [Å <sup>-3</sup> ]	0.01625	-8.101e-04, 8.073e-04
$\rho_{\text{LSMO}}$ [Å <sup>-3</sup> ]	0.01760	-3.472e-04, 3.092e-04
$\rho_{\text{LSFO}}$ [Å <sup>-3</sup> ]	0.01724	-1.057e-04, 8.159e-05
$\rho_{\text{Inter}}$ [Å <sup>-3</sup> ]	0.01380	-7.538e-04, 1.693e-03
$m_{\text{ML1}}$ [ $\mu_{\text{B}}/\text{uc}$ ]	2.3909	-1.995e-01, 2.182e-01
$m_{\text{ML2}}$ [ $\mu_{\text{B}}/\text{uc}$ ]	0.0000	-
$m_{\text{ML3}}$ [ $\mu_{\text{B}}/\text{uc}$ ]	0.0000	-
$m_{\text{ML4}}$ [ $\mu_{\text{B}}/\text{uc}$ ]	0.0000	-
$c_{\text{Fe,inter}}$	0.1544	-1.385e-01, 2.079e-01

# List of Figures

2.1	Cubic perovskite structure of STO. The A-site is occupied by Sr atoms, the B-site by Ti atoms. The blue marked octahedron specifies the oxygen environment, which is characteristic for the perovskite structure. The dedicated space group is $Pm\bar{3}m$ . The figure was made with VESTA [14]. . . . .	5
2.2	Antiferrodistortive transition at 105K of STO. The oxygen octahedron rotates around the cubic $c$ -axis with the rotation angle $\phi$ which leads to a transition from cubic to tetragonal. The rotation of the octahedra in two adjacent cells is opposite. Adapted from [18]. . . . .	6
2.3	<b>(a)</b> Hexagonal unit cell of LSFO with space group $R\bar{3}c$ , which contains six chemical formula units. The A-site is occupied statistically with 33 % Lanthanum and 67 % Strontium which is indicated by two different green tones. <b>(b)</b> Rhombohedral (pseudo cubic) unit cell, which is a slightly distorted cubic perovskite structure. The blue polyhedron indicates the octahedral oxygen environment. One can easily see that the [111] direction of the pseudo cubic structure is equivalent to the $c$ -axis of the hexagonal unit cell. Both figures were created with VESTA [14]. . . . .	7
2.4	Crystal field splitting of a transition metal ion with different oxygen environments. The crystal field splitting energy $\Delta$ separates the $e_g$ and $t_{2g}$ energy level. . . . .	9
2.5	Two different spin configurations for the four electrons of $Fe^{4+}$ in a cubic oxygen environment, which is depicted in Fig. 2.1, for instance. . . . .	9
2.6	Illustration of the double-exchange mechanism between two manganese atoms with different valences. Black indicates the state before the electron hopping occurs, whereas red is the end state. As double exchange is a real hopping process the valance of the manganese atom changes. . . . .	11
2.7	A simplified illustration of the exchange coupling between a ferromagnetic and an antiferromagnetic thin film. Adapted from [36]. . . . .	12
3.1	Scattering experiment within the Fraunhofer approximation. An incident plane wave is scattered towards a detector. Adapted from [41]. . . . .	16
3.2	Definition of the scattering cross-section. The scattered intensity is proportional to the cross-section. Adapted from [41]. . . . .	17
3.3	Ewald construction to visualize the Laue condition. The scattering condition is only fulfilled for lattice points which lie on the Ewald sphere (or Ewald circle in the 2D projection). . . . .	19

3.4	Construction of 2D projection of a crystal lattice. The crystal lattice is a convolution of a basis consisting of atoms and a mathematical point lattice.	20
3.5	Scattering geometry of a typical reflectometry experiment. In the case of specular scattering <b>(a)</b> , where $\alpha_i$ and $\alpha_s$ are equal, $\vec{Q}$ is perpendicular to the sample's surface and thus only $Q_z \neq 0$ . The blue arrow is the refracted beam with the angle $\alpha_r$ . In case of $\alpha_i \neq \alpha_s$ the off-specular scattering or diffuse scattering occurs and lateral structures can be probed <b>(b)</b> . The scattering vector $\vec{Q}$ has a non-vanishing lateral component. . . . .	23
3.6	The reflectivity $R$ <b>(a)</b> and the transmittance $T$ <b>(b)</b> for the case of vanishing absorption. In both $\theta_t$ is the key angle. For $R$ below $\theta_t$ total reflection takes place. $T$ shows a different behavior. At $\theta_t$ the incident and scattered wave interfere constructively, which means that the amplitudes can be added. From a doubled amplitude $T = 4$ follows, because it is the square value of the amplitude. Adapted from [41]. . . . .	25
3.7	Sketch of the scattering geometry for PNR. The incident neutrons have a polarization $\vec{P}$ parallel to the $y$ -direction. Dependent on the magnetic field within the sample $\vec{B}$ non-spin-flip (NSF) and spin-flip (SF) processes can be observed. The sample is assumed to be single domain. Adapted from [54].	27
3.8	Ewald construction for two-dimensional surface scattering on a cut along $k_x$ . Lattice rods appear instead of lattice points. These lattice points always intersect with the Ewald sphere and thus the Laue condition is fulfilled easily for an incoming beam with the wavevector $\vec{k}$ and the scattered wavevector $\vec{k}'$ . This sketch is adapted from [57]. . . . .	28
4.1	The upper sketch explains the different mechanism that occur during thin film growth. The bottom figure shows the different heteroepitaxial growth modes, which are caused by the surface thermodynamics. For a smooth layer it is necessary to achieve the Frank-van der Merwe growth mode <b>(a)</b> , which indicates a perfect layer-by-layer growth. . . . .	32
4.2	<b>(a)</b> Bird's eye view of the used system. The system is divided into three sections. The load lock, the buffer line, and the main chamber. A transfer system allows one to move the sample within the system. The main chamber, or growth chamber, is equipped with two electron beam evaporaters and six effusion cells. In total up to eight elements can be evaporated simultaneously. <b>(b)</b> depicts a cross section of the main chamber to see the arrangement of the equipment that is necessary for sample growth. The substrate is mounted upside-down on a heater. The oxygen source and the evaporaters can be closed with shutters. Both sketches are not true to scale. AES: Auger electron spectroscopy, QMB: quartz microbalance, LEED: low energy electron diffraction, RHEED: reflection high energy electron diffraction, RGA: residual gas analyzer. . . . .	35

4.3	Sketch of the used high oxygen pressure sputtering automat. Two targets can be used simultaneously to grow multilayer systems and the movable target arm is necessary to start and stop the growth as well as switching between two targets. The target size is ca 5cm, the distance between substrate and target can vary within a few centimeters. The zoom shows a detailed view on the target, heater, and substrate. . . . .	36
5.1	Sketch of a LEED system. The electrons are accelerated towards the sample and impinge perpendicular to the sample surface and are then diffracted in direction of the LEED screen. Inelastically scattered electrons are filtered by an energy filter. The grid is used to further accelerate the elastically scattered electrons to trigger fluorescence on the screen. . . . .	39
5.2	RHEED scattering geometry. The grazing incidence electron beam is only scattered from the 2D surface, which leads to lattice rods instead of lattice points (see. 3.8). The scattered electrons become visible after impinging on a fluorescence screen and are detected by a video camera. . . . .	40
5.3	<b>(a)</b> is a RHEED pattern of a cleaned silicon substrate. Point-like reflections on higher Laue ring indicate a very smooth surface. Kikuchi lines are an indication of a perfectly shaped surface. In contrast <b>(b)</b> depicts an obviously island growth of manganate on STO, where a 3D diffraction pattern overlies. . . . .	41
5.4	Sketch of the Bruker D8 Advanced X-ray reflectometer. This instrument has been used for the structural characterization of the thin films. Only the tube and the detector can be moved. Thus only out-of-plane information is provided by specular scattering. However, off-specular scattering gives informations on lateral correlations. Sketch taken from [69]. . . . .	42
5.5	Sketch of the in-house powder diffractometer Huber Guinier G670. A monochromatized and collimated X-ray beam is scattered by a powder sample. The primary beam is blocked with a beam stop. An image plate detects the scattered intensity. This geometry is called Guinier technique and is commonly used. . . . .	43
5.6	<b>(a)</b> shows the AFM measurement technique which is based on the interaction between sample and tip. The tip is oscillating near its resonant frequency and the amplitude is measured with a laser and a detector. <b>(b)</b> depicts the underlying Lennard-Jones potential, which is a good approximation to describe the interaction between surface atoms and tip atoms. $V$ and $r$ are normalized to constants $\epsilon$ and $\sigma_L$ , respectively. The AFM has been used in non-contact (NC) mode. FO is the range, where the tip can freely oscillate. . . . .	44
5.7	Measurement technique of the used Quantum Design MPMS. The sample is mounted in a straw and is moved through a second order gradiometer. The gradiometer is thus coupled inductively to the sample. The pick-up system is then coupled to a rf SQUID. . . . .	45
5.8	Heat capacity measurement option of the PPMS. The puck will be connected to the PPMS dewar. Adapted from [75]. . . . .	46

5.9	Sketch of a RBS experiment. An ion source provides helium ions that are accelerated towards the sample and then backscattered under the scattering angle $\theta$ . The backscattered ions are detected with an energy sensitive detector. . . . .	47
5.10	Overview of a TEM measurement of a sample after preparation. . . . .	49
5.11	Schematic drawing of the DNS. Adapted from [83]. . . . .	50
5.12	DNS scattering geometry. $\vec{Q}$ lies in the x-y-plane and $\alpha$ is the angle between the x-axis and $\vec{Q}$ . . . . .	51
5.13	<b>(a)</b> Sketch of the MARIA reflectometer. The velocity selector determines the wavelength of the neutrons. Slits collimate the neutron beam before scattering from the sample. Polarization of the neutrons occurs in a polarizer, whereas the analyzer is used for polarization analysis after the scattering event. A cryostat for cooling applications and a magnet are available. Adapted from [88]. <b>(b)</b> A drawing of the PBR experiment. The neutron beam is monochromatized and then polarized by a supermirror. A spin flipper allows one to flip the spin direction. After being scattered from the sample the neutrons are detected with a $^3\text{He}$ detector. A supermirror is used for analyzing the polarization of the neutron beam. Taken from [89]. . . . .	54
5.14	Half-hysteresis measurement performed with MARIA. To maintain the neutron polarization only the part shown by the solid line is accessible. . . . .	54
6.1	<b>(a)</b> Charge ordering of LSFO along the [111]-direction (red arrow) of the pseudo cubic unit cell. The ordering vector for the charge ordered phase is $\vec{q}_{\text{CO}} = (1/3, 1/3, 1/3)$ . The colored planes perpendicular to the [111]-direction indicate the position of the $\text{Fe}^{3+}$ and $\text{Fe}^{5+}$ , respectively. <b>(b)</b> depicts the charge and magnetic ordering in space group $R\bar{3}c$ projected onto the (010) plane. The arrows show the different spin states of $\text{Fe}^{3+}$ and $\text{Fe}^{5+}$ . Adapted from [94]. Sketches are generated with VESTA [14]. . . . .	58
6.2	Resistivity measurement of polycrystalline LSFO. The measurement was performed while cooling the sample from room temperature to 10 K. Data taken from [96]. . . . .	59
6.3	<b>(a)</b> depicts the thickness dependence of the resistivity measured on a LSFO thin film grown on STO. Reprinted from [103], with the permission of AIP publishing. Above the critical thickness of 200 Å a transition can be observed. In contrast <b>(b)</b> shows resistivity measurements of $\text{La}_{1-x}\text{Sr}_x\text{FeO}_3$ grown on STO. Reprinted figure with permission from [104]. Copyright (2014) by the American Physical Society. A clear effect of the stoichiometry is visible, already a small deviation from $x = 0.65$ leads to a smearing of the Verwey transition. . . . .	61
6.4	Process steps for powder preparation. To prepare high quality powder several calcination and sintering steps are necessary. The calcination took place under ambient pressure, whereas the sintering was done under a continuous oxygen flow. . . . .	62

---

6.5	(a) Measured X-ray powder data after each calcination step. For a better visibility the data sets are shifted along the $y$ -axis. The vertical markers indicate the theoretically calculated peak positions of the expected space group $R\bar{3}c$ . (b) A zoom on the (2-24) reflection in order to see the changes of each calcination step in detail. . . . .	63
6.6	Powder XRD measurement at room temperature and the Le Bail fit (see section 3.4) after sintering. The preparation process leads to a single phase crystalline powder with the expected space group $R\bar{3}c$ . The parameters obtained from the fit are listed in the table. They confirm the goodness of the fit. The lattice parameters are also shown. . . . .	64
6.7	Specific heat of 1 mg LSFO. For temperatures above 215 K, the used Apiezon <sup>®</sup> N grease influenced the measurement. At 201.7(1) K a clear peak is visible, which is typical for a first order phase transition. . . . .	66
6.8	4-wire measurement principle for determination of the resistivity of the sample. The measurement has been performed with the PPMS. The dimension of the measured sample is $2.5 \times 4.5 \times 1.5 \text{ mm}^3$ . . . . .	67
6.9	(a) shows two resistivity measurements. The red is measured during cooling, whereas the blue was measured during warming (b) depicts the fit to the measured data of the non-adiabatic polaron model for $T > T_V$ . The colored arrows point to the determined transition temperatures. . . . .	68
6.10	(a) shows a set of magnetization measurements. The blue curve has been measured during field-cooling (FC) in 7 mT. After field-cooling in 7 mT the red curve was measured during field-warming (FCW) in the same field. A thermal hysteresis is present with transition temperature 197.8(5) K and 204.7(5) K, respectively. (b) is measured with an applied field while warming after zero-field cooling (ZFC-FW). . . . .	69
6.11	$M - H$ - measurements at different temperatures after zero-field cooling. (a) shows a measurement right above (204 K) and below (194 K) the phase transition. (b) shows a measurement at 50 K for high magnetic fields, but saturation of the magnetization cannot be reached. . . . .	70
6.12	DNS measurement performed at 5 K without self-normalization. Separation of the different contributions has been done with dnsplot. Additionally, the two labeled reflections are Al (111) and (200). Aluminium has been used as sample holder and sample environment. . . . .	72
6.13	Temperature dependency of the differential magnetic cross section. The higher order reflections are not shown for a better clarity. The measurement was performed upon warming after cooling to 5 K. . . . .	73
6.14	The temperature dependency of the sublattice magnetization, which is defined as the square root of the magnetic scattering cross section, is given. It has been determined by intensity integration of the reflections within $1.27 < Q < 2.42 \text{ \AA}$ . For the integration a background subtraction was done. The measurement was performed while warming from 5 K to 250 K. A smoothed curve is shown as a guide to the eye. . . . .	73

6.15	Neutron powder diffraction and Rietveld refinement measured at 5 K. The intensity and peak shape of the first reflection at $0.5 \text{ \AA}^{-1}$ is influenced by the beam block and thus not considered during refinement. Additionally, the reflections above $2.5 \text{ \AA}^{-1}$ are also not reliable, as discussed, and were not considered for the refinement as well. The used magnetic space group is $P\bar{1}$ . The vertical lines indicate the position of calculated peaks, but for some of them the modeled intensity is zero. . . . .	75
6.16	100 K powder X-ray diffractometry measurement performed on 11-BM @ APS. <b>(a)</b> gives an overview and includes the Rietveld refinement data. The difference of data and simulation is also depicted, but shifted by -0.3. The symmetry space group is $R\bar{3}c$ . <b>(b)</b> is a zoom in on the region around the $(2\bar{1}0)$ and $(104)$ reflection. Refinement parameters are listed in Appendix D.2.	76
6.17	Subgroup graph under the assumption, that the number of chemical formula units per unit cell stays constant. Data taken from [109]. . . . .	77
6.18	Temperature dependence of the lattice parameter measured with 11-BM. . . . .	78
6.19	$(\frac{2}{3}\frac{2}{3}\frac{2}{3})$ charge ordering reflection. A clear difference can be seen for the measurement above compared to below the charge ordering transition. . . . .	79
6.20	Neutron powder diffractometry measurements and Rietveld refinements at 300 K and 5 K. The 5 K measurement is shifted by 0.25 along the intensity axis. At -0.2 and -0.1 the difference between measurement and refinement is plotted. At 5 K clear additional reflections can be observed and are attributed to the magnetic scattering. The $R$ values of the refinements can be seen in Tab. 6.5, further refinement parameters are listed in Appendix D.2.	80
6.21	The difference between 300 K and 5 K measurement. The peaks with negative intensity are uncompensated nuclear reflections due to a shrinking of the crystal lattice upon cooling. . . . .	80
6.22	Zoom on a small $Q$ -range to illustrate problems of the calculated profile function. The vertical lines show the positions of calculated reflections. . . . .	81
6.23	Sketch of the OMBE thin film growth process optimization. The frequency changes can be roughly calculated as shown in Eq. 6.4 and 6.5. The start values are empirical experiment values. After the growth of the first layer the structure was analyzed with LEED, RHEED, XRR and XRD, and RBS. If, with regard to surface morphology, crystalline structure, and stoichiometry, a good sample has been reached, the growth process optimization is completed. If not, the growth parameter have to be adjusted until a good quality sample has been achieved. . . . .	84
6.24	Evaluation of Eq. 6.4 with $c_{\text{La}}$ . $C_{\text{La}}/C_{\text{Fe}}$ is the ratio between La and Fe from RBS measurements. All thin films were grown under comparable growth conditions. . . . .	84
6.25	Frequency change observation caused by deposited Fe prior growth over 120 min with each data point averaged over 5 min. The frequency change is $0.090(2) \frac{\text{Hz}}{\text{s}}$ and is stable within the measurement error. . . . .	85
6.26	LEED image of a STO substrate taken at 100 eV after annealing. Clear and sharp reflections indicate a crystalline and clean surface. . . . .	86

6.27	<b>(a)</b> A RHEED image of sample $\text{LSFO}_{\text{na}}$ . <b>(b)</b> An image of sample $\text{LSFO}_{\text{a}}$ . Both measurements are done at room temperature. . . . .	87
6.28	<b>(a)</b> Reflectivity and dedicated simulations. The curve for $\text{LSFO}_{\text{a}}$ is shifted by a factor of 10. All simulation parameters can be found in Tab. 6.7. <b>(b)</b> The SLD for sample $\text{LSFO}_{\text{a}}$ and of a calculated layer. . . . .	89
6.29	<b>(a)</b> The (002) reflection of sample $\text{LSFO}_{\text{na}}$ . <b>(b)</b> is the same reflection for the annealed sample $\text{LSFO}_{\text{a}}$ . The measurement was performed at room temperature. The arrows in <b>(b)</b> point to the position of thickness oscillations, which are overlain by the substrate reflection. The position of the thickness oscillations has been determined with a sum of Gaussians. . . . .	90
6.30	<b>(a)</b> RBS data and simulation. The measured sample exhibits the composition $\text{La}_{0.33}\text{Sr}_{0.66}\text{Fe}_{1.03}\text{O}_{3-\delta}$ . <b>(b)</b> Measurement of the (002) reflection. The black line is the fit for each oscillation. The thickness oscillations are clearly visibly up to high orders, which also confirms the smoothness and crystallinity of the layer. . . . .	91
6.31	<b>(a)</b> XRR data and simulation. The parameters are shown in Tab. 6.7. <b>(b)</b> LEED image taken at 80 eV. Very sharp reflections confirm the good surface morphology of the sample. . . . .	92
6.32	<b>(a)</b> Magnetization measurement of a LSFO single layer. The measurement has been taken during field-warming after field-cooling in 20 mT along [100]. The red error bars describe the error of the MPMS, whereas the black lines are the maximum and minimum error, which follows from the imprecise determination of the mass of the thin layer, but has the same magnitude for all measurement points. <b>(b)</b> First derivative of the data. The zero of the derivative, which corresponds to a maximum in the data, is at 196(10) K. . . . .	93
6.33	Schematic explanation of the temperature dependence of the susceptibility of an antiferromagnet. . . . .	94
6.34	A $M-H$ - curve measured at 110 K after field-cooling in 20 mT along [100]. The dotted lines are describing the coercive field $H_C$ . The opening of the hysteresis hints a ferromagnetic component. . . . .	94
6.35	Four-wire contacting for resistivity measurement. Optionally magnetic fields are applied perpendicular to the sample surface. . . . .	95
6.36	<b>(a)</b> Resistivity measurement of a sample during cooling prepared without post-growth annealing. In contrast <b>(b)</b> shows a resistivity measurement of a LSFO single layer prepared with post-growth annealing with and without an applied field. To extend the measurement range, a PPMS-DynaCool instrument with a 2-point measurement technique has been used for low temperatures. Both layers exhibit the desired stoichiometry and a layer thickness of 309 Å. The first derivative of this measurement is shown in Fig. 6.37. . . . .	96
6.37	First derivative of measurement shown in Fig. 6.36b. The minimum of the derivative corresponds to the Verwey transition temperature. The less significant minima are measurement artifacts. A moving window derivative has been used. . . . .	97



6.38	(a) Replot of the data in order to fit the non-adiabatic small polaron model. The vertical line indicates the position of the transition temperature $T_V$ . (b) Double ln plot to determine the power law eq. 6.7 according to [40]. The used temperature range was selected to be far below the transition temperature. . . . .	98
7.1	Structural, magnetic, and electronic phase diagram of $\text{La}_{1-x}\text{Sr}_x\text{MnO}_3$ from Hemberger et al.. The concentration used here is $x = \frac{1}{3}$ , which exhibit a rhombohedral crystal structure, and is a metallic-like ferromagnetic material with a bulk $T_c$ of 370 K. The symbols in the diagram are orthorhombic O, rhombohedral R, tetragonal T, monoclinic Mc, hexagonal H; insulating I, metallic M; ferromagnetic FM, antiferromagnetic AFM, paramagnetic PM. Reprinted from [13], with the permission of AIP publishing. . . . .	102
7.2	Image of a closed pBN crucible after two weeks of usage. . . . .	102
7.3	(a) XRR data and simulation. The corresponding simulation parameters can be found in Tab. 7.1. (b) XRD measurement around the (002)-substrate (STO) reflection. Besides a clear substrate and thin film reflection, thickness oscillations are visible, which indicate a good surface and crystalline quality. The structure parameters are listed in Tab. 7.1. . . . .	104
7.4	Field-cooling magnetization measurements at different fields. A linear regression has been used to determine the transition temperature $T_C = 330(2)$ K for the 10 mT measurement, because the measurement ends at 320 K. The vertical line indicates the substrate's antiferrodistortive transition at 105 K, which significantly influences the magnetization. . . . .	106
8.1	LEED image measured at 80 eV after transferring sample from HOPSA to the OMBE system. Clear and sharp reflections indicate a good surface morphology. . . . .	109
8.2	Different sample stacking and connected sample names. . . . .	110
8.3	XRR measurement and simulation of LSMOfinal (a) and LSFOfinal (c), respectively. (b), (d) Corresponding SLD obtained from the simulation. The data analysis was done with GenX [52]. Both samples exhibit neglecting diffuse scattering. Thus, a correction of the specular reflectivity was not done. Insets show a LEED image measured at 80 eV after LSFO deposition, and for LSMOfinal before the deposition of LSMO. . . . .	111
8.4	(002) - measurement of sample LSMOfinal (a) and LSFOfinal (b). A $\theta_0$ correction was applied. The thickness oscillations were analyzed by applying a sum of Gaussians, which consider the distance between oscillations as a parameter. The thickness oscillations are attributed to the total thickness. However, in (a) a second period was found (see arrows), which is identified as oscillations caused by the single layers. The arrows point to the minima of the second oscillations indicating a destructive interference which extinct the bilayer oscillation significantly. . . . .	112

8.5	HAADF-STEM image of the well-ordered interface region of sample LSFO-final in <b>(a)</b> . The interface is not sharp, but is slightly waved and buckled. The inset <b>(b)</b> is a magnification to identify the perovskite structure with its A- and B-sites as indicated by colored spheres. . . . .	114
8.6	<b>(a)</b> HAADF-STEM image of sample LSMOfinal including EDX information. Mn ions are colored light blue, Fe ions dark blue. The dashed line estimates the interface between LSMO and LSFO. <b>(b)</b> laterally integrated EDX signal. A clear diffusion of Fe into the LSMO layer is observable. <b>(c)</b> HAADF-STEM image of sample LSFOfinal including EDX information. Mn ions are colored blue, Fe ions orange. The dashed line estimates the interface between LSMO and LSFO. <b>(d)</b> Corresponding EDX signal. Only little interdiffusion nearby the interface can be observed. . . . .	115
8.7	Sample holder shadowing during LSFO growth. . . . .	116
8.8	Magnetization measurement of LSMOfinal <b>(a)</b> , which exhibits high Fe interdiffusion to the LSMO layer, and LSFOfinal <b>(b)</b> during field-warming after field-cooling. The field was applied parallel to a [100] direction of STO. . . . .	117
8.9	$M - H$ - measurements of LSMOfinal. <b>(a)</b> shows hysteresis loops at different temperature after field-cooling at 3 mT. <b>(b)</b> depicts hysteresis loops measured at 10 K after field-cooling in different fields. A slight shift of the loop towards negative fields indicates an exchange bias effect at 10 K. To ensure saturation all measurements were done up to $\pm 1$ T. The field was applied parallel to a [001] direction of the substrate. . . . .	119
8.10	$M - H$ - measurement of the high-temperature region of sample LSFOfinal. Even at 380 K a ferromagnetic hysteresis is present which lies well above $T_C$ of LSMO. This is an indication of an additional ferromagnetic phase with high coercive field $H_C$ (dashed line) and high $T_C$ . Measurements were performed at PPMS-VSM. . . . .	119
8.11	$M - H$ - measurements of LSFOfinal after zero-field-cooling and field-cooling in 1 T applied along [001] at 110 K. The measurement was done between $\pm 1$ T as shown in <b>(a)</b> . The closer look depicted in <b>(b)</b> revealed an unusual behavior, known as inversed magnetic hysteresis. . . . .	120
8.12	$M - H$ - measurements at 10 K of LSFOfinal after field-cooling. The measurement was done from $\pm 1$ T starting from positive field. A zoom on an interesting region is given in <b>(a)</b> . <b>(b)</b> shows field-cooling field dependence in the exchange bias field and coercive field, respectively. The coercive field is defined as $H_C = (H_{C2} - H_{C1})/2$ and is used to compare the different measurements. . . . .	121
8.13	One possible explanation of the inverted hysteresis in the system, where an antiferromagnetic interlayer coupling is assumed. The interface is indicated by a dashed line. Red arrows are magnetic spins in LSFO, black arrows indicate the spins in LSMO. . . . .	123
8.14	Sample model for LSMOfinal. It is divided into a nuclear and magnetic part. Due to intermixing effects between LSMO and LSFO an interlayer was introduced which considers a Fe loaded LSMO phase as seen from EDX measurements. . . . .	124

8.15	PNR measurements and simulations of sample LSMOfinal <b>(a)</b> and LSFOfinal <b>(b)</b> at different temperatures for both non-spin-flip channels. The red dotted line indicates the $Q_z$ position used for the MARIA experiment. The measurements were performed at the PBR instrument after field-cooling in 110 mT. Due to the STO structural phase transition, which causes a significantly increased roughness, the measurement was started above this phase transition. The reflectivity curves are shifted by a factor of 100. The errorbars are scaled with respect to the lowest measurement. All parameters gained from the refinements are listed in appendix D.3.4 and D.4.5. Additional temperatures for LSFOfinal are shown in appendix D.4.4. . . .	126
8.16	Real part of nuclear and magnetic scattering length densities (NSLD and MSLD) from simulation of LSMOfinal <b>(a)</b> and LSFOfinal <b>(b)</b> for different temperatures. A height of 0 Å is calibrated to the surface of the substrate. LSMOfinal shows a reduced magnetization in the interface region and top region, whereas LSFOfinal exhibit a homogeneously magnetized LSMO layer. The expansion of the interface region corresponds to the TEM measurements as shown. . . . .	127
8.17	<b>(a)</b> 110 K PNR hysteresis measurement with polarization analysis of LSMOfinal. The coercive field was recalibrated with respect to the MPMS measurements. <b>(b)</b> Sketch which describes the reversal process in three steps found in sample LSMOfinal. . . . .	131
8.18	MARIA detector image of one single measurement of the non-spin-flip uu channel. The lower figure shows an integration along the $y$ pixel axis. The small asymmetry of the peak comes from a slight misalignment of the instrument. No indication for strong diffuse scattering in $x$ -direction (lateral) is observable. . . . .	132
9.1	MO-diagram (left) and schematic DOS (right) for the case of C doping. The calculated DOS reveals differences if one considers the two different spin directions. Reprinted from [1], with the permission of EPL. . . . .	136
9.2	Used p- and n-type superlattices for calculation. The stacking sequence determines the charge at the interface. The charge arises from the charged TaO <sub>2</sub> and KO layers. The STO layers are neutral. As the whole system has to be neutral, the interface has to compensate the surplus charges by introducing electrons or holes to the interface. Adapted from [2]. . . . .	137
9.3	Magnetization measurements as a function of the external field at room temperature, where the diamagnetic contribution of the substrate is subtracted. The KTO/STO system shows the highest saturation magnetization. Adapted from [2]. . . . .	138
9.4	The structural phase diagram of bulk BTO . BTO has four different temperature dependent structural phases. A cubic (C) to tetragonal (T) phase transition sets in below approx. 390 K followed by a tetragonal (T) to orthorhombic (O) phase transition below 279 K. At 184 K the system undergoes a orthorhombic (O) to rhombohedral (R) phase transition. Reprinted from [146] with permission. . . . .	139

9.5 **(a)** Powder diffractometry measurement of untreated BTO and Le Bail refinement. Jana2006 [49] has been used for the Le Bail refinement. The data is normalized and the background is subtracted. **(b)** Zoom on reflections, where the Le Bail refinement does not fit perfectly due to an additional structural phase. The vertical black lines indicate the theoretical position of the peaks calculated with Jana2006 as well. . . . . 140

9.6 **(a)** A cubic phase has been introduced into the simulation of used BTO powder. Improvement of the refinement is visible, which means that the used and untreated powder is not a single phase powder. P1 and P2 indicate the calculated peak positions for phase 1 (tetragonal) and phase 2 (cubic). The simulation was calculated with Jana2006. **(b)** Plot of the annealing temperature dependency of the powder. One can easily see that an annealing process influences the structure of the powder, which becomes more single phase. The plasma treatment with nitrogen has not influenced the structure of the powder. The different data is shifted vertically by 0.4 for a better comparability. . . . . 141

9.7 The XRD measurement after the N plasma treatment together with the Le Bail refinement done with Jana2006 [49]. The blue curve shows the difference between data and simulation. It is shifted by -0.1. A sketch of the used 2.45 GHz microwave plasma generator is shown in the inset. The plasma works with 800 W under 35 mbar nitrogen gas pressure and provides atomic nitrogen to the doping process. . . . . 142

9.8 Magnetization from field-cooled measurements (to 10 K) of the annealed and the N plasma treated powder. The powder exhibits a diamagnetic behavior down to approximately 100 K. Then a paramagnetic behavior sets in, whose reason is a paramagnetic contamination of the used powder. The red curve indicates the diamagnetic behavior without consideration of the paramagnetic phase. The expected ferromagnetic behavior cannot be confirmed, but one cannot disprove it certainly unless the plasma annealing is improved. . . . . 144

9.9 **(a)** Reflectivities measured at different temperatures. The vertical line points to the critical angle  $\theta_c$  ( $Q_c$ ) of total reflection. The higher the temperature the higher is this angle, which is related to the density of the sputtered film. For a better overview each curve is separated by a factor of 10. **(b)** Parameters, which one gets from the simulation of the measured reflectivity. The horizontal line describes the theoretically calculated SLD for a thin film with ideal stoichiometry and density. . . . . 146

9.10 Room temperature XRD measurement of (001) **(a)** and (002) **(b)** reflection. Besides the Cu- $K_{\alpha 1}$  radiation a small Cu  $K_{\alpha 2}$  and Bremsstrahlung contribution is visible for the (001) and (002) STO reflection. Calculated parameters can be found in Tab. 9.5. . . . . 146

9.11 **(a)** RBS measurement of sputtered KTO on a STO substrate and its simulation. In **(b)** the parameters from the simulation (done with RUMP) are tabulated. At least two layers with different K content are necessary to simulate the data properly. . . . . 148

---

9.12	(a) XRR data and simulation. As the grown layer is inhomogeneous three different layers with decreasing SLD are necessary. The structural parameters of each layer are given in Tab. 9.6, whereas the SLD used is shown in (b). An ideal KTO layer is also shown here. (c) $6 \mu\text{m}^2$ surface overview measured with an AFM. (d) is the height profile along the white line in (c). Data reduction and analysis was performed with Gwyddion [150]. . . .	149
D.1	Top figure shows 5K powder measurement performed at the DNS instrument with a wavelength of $4.5 \text{ \AA}$ . Bottom figure shows refinement of the magnetic signal. The lowest reflections was omitted due to a shadowing effect of the beamstop at low angles. . . . .	178
D.2	EDX spectra taken at the marked areas in the left-hand figure. The reversal of the approximate 2:1 ration of Sr and La can be found from the respective intensities. The theoretical position are taken from Deslattes et al. [127]. Plot and analysis done by Juri Barthel, ER-C. . . . .	186
D.3	Additional PNR measurements and simulations of sample LSFOfinal for both non-spin-flip channels. . . . .	187

# List of Tables

2.1	Values of tolerance factor for different perovskite coordinations. . . . .	7
2.2	Room-temperature lattice parameter and their relative deviations of cubic STO [21] and pseudocubic LSMO [22] as well as pseudocubic LSFO [23]. . . . .	8
6.1	Lattice parameters of LSFO with space group $R\bar{3}c$ at room temperature from [23]. . . . .	57
6.2	Calculated molar masses and weight percent of the required starting materials. . . . .	62
6.3	The weight percent results are listed in <b>(a)</b> . The measurement was performed by ZCH-3:Analytics. Pt and Zr could be found as impurities which obviously arise from the preparation process, but are small enough to be neglected. <b>(b)</b> shows the result calculated for one chemical formula unit normalized to Fe. . . . .	65
6.4	Model and profile $R$ values from refinement. Explanation of these values is given in section 3.4. Further refinement parameters are listed in Appendix D.2. . . . .	76
6.5	300 K and 5 K model and profile $R$ values from refinement done with Jana2006 [49]. . . . .	81
6.6	Summary of different growth parameters used for growth process optimization. Post-growth sample annealing analysis was done with samples which exhibit a slightly increased strontium content. The final sample was grown with an adjusted strontium rate, which further improved the sample quality. . . . .	88
6.7	Parameters from simulation shown in Fig. 6.28 and Fig. 6.31a, respectively, in order to compare samples with different growth parameters (Tab. 6.6). The final sample ( $LSFO_{\text{final}}$ ) is a further optimized layer, with respect to stoichiometry, after the investigation of the annealing influences. . . . .	89
6.8	Measured out-of-plane lattice parameter $c$ and calculated in-plane values $a$ . The substrate was used as a reference (*) (Sec. 9.2.2) to correct the scattering angle $\theta$ . . . . .	90
7.1	The left-hand table shows the parameters from simulation shown in Fig. 7.3a. The right-hand table contains the structural parameters as gained from XRD data shown in Fig. 7.3b. The layer's in-plane lattice constant has been calculated from the bulk volume found in [22]. . . . .	104

---

8.1	Parameters (thickness $d$ , roughness $\sigma$ ) from simulation shown in Fig. 8.3 concerning both samples, LSMOfinal and LSFOfinal, respectively. . . . .	112
8.2	Out-of-plane lattice parameter calculated from (002) - reflection of the respective sample is shown. . . . .	113
8.3	Averaged magnetization per unit cell of the LSMO layer in sample LSMOfinal and LSFOfinal for different measured temperatures. . . . .	129
8.4	Magnetization in saturation obtained from a $M - H$ -measurement at 110 K discussed in Sec. 8.2. . . . .	129
9.1	Calculated parameters of a doped supercell including magnetic moment per dopant atom, cell volume, $c/a$ ratio, and Ti-X distance $d_{\text{Ti-X}}$ . Parameters from [1]. . . . .	136
9.2	List of the annealing parameters for the used methods. . . . .	141
9.3	Comparison of lattice parameters after annealing and after nitrogen plasma treatment. The relative volume change is calculated with regard to the volume of the plasma treated. . . . .	143
9.4	Structural parameters at room temperature of $\text{KTaO}_3$ [148] and $\text{SrTiO}_3$ [21].	144
9.5	Position, FWHM, and out-of-plane lattice parameter of KTO and STO grown at 1195 K for the out-of-plane (001) and (002) reflections. A $\theta$ correction has been done according to Eq. 9.2. . . . .	147
9.6	Parameters from XRR simulation. To simulate the grown layer three different KTO sublayers are necessary with decreasing SLD as shown in Fig. 9.12b. KTO1 is the first assumed layer following the substrate, KTO2 and KTO3 are the further layers, which are necessary. The asymmetric parameter errors are calculated by GenX [52]. . . . .	148